

Uncovering the neural encoding of behavior in the adult *Drosophila* motor system

Présentée le 27 juin 2022

Faculté des sciences de la vie
Unité du Prof. Ramdya
Programme doctoral en neurosciences

pour l'obtention du grade de Docteur ès Sciences

par

Chin-Lin CHEN

Acceptée sur proposition du jury

Prof. C. Petersen, président du jury
Prof. P. P. Ramdya, directeur de thèse
Prof. E. Chiappe, rapporteuse
Prof. A. Cardona, rapporteur
Prof. B. McCabe, rapporteur

夫大道不稱，大辯不言，大仁不仁，大廉不謙，大勇不伎。道昭而不道，言辯而不及，
仁常而不成，廉清而不信，勇伎而不成。

摘自《莊子·齊物論》

Acknowledgements

First of all, I would like to thank Prof. Pavan Ramdya for giving me the opportunity to join the team as the first Ph.D. student. I always think that I am lucky to have such a unique experience of working with a lab from starting point and learning how to coordinate and align targets step by step in the early stage that aims for the lab to grow stronger. I also appreciate that you encourage the collaboration between colleagues with different expertise and forage us as interdisciplinary scientists after the group gets bigger. Here, I learned how a group can be managed, how efficient communication should be made, and how a project should be visioned and progresses. Though it is expected that the direction is not always clear during the investigation stage, it comes as a nice discovery after the clash of different ideas. That's how science progress, I guess.

Next, I am very grateful to have the first lab mate and friend—Laura Hermans, to share the pressure and the fun in the early stage of the lab. Thanks to her for being proactive and problem-solving, we can manage to push our first collaborative project to publication during a fun over-time period. Also, I would like to thank Victor Lobato for being in the late-person-for-coffee-break brotherhood with me so that I can go through the breathtaking and exciting large-scale screen experiments when finishing lately in the evening. In addition, I want to thank Florian Aymanns for supporting analytical and technical parts where I feel I learn solid knowledge even though easy to forget. Nevertheless, I am sure that I have developed more concepts and experience when starting practicing the newly learned tools with the experimental data. Last but not least, I would like to acknowledge Semih Günel for the joy and the coins you share, Victor Vasquez Matsuda and Nicolas Talabot's excellent works to make our project successful and your humble spirit, and the newly coming members for giving more diverse input to our research and make more fun in the lab. Overall, it has been a very stimulating and inspiring journey in my life.

Outside the lab, I want to thank my family for letting me explore any possibility in life without too many worries and always being there to support and recharge my energy when back home to allow me to continue the journey. Next, I would like to thank Taiwanese friends in Lausanne, especially 沈慈賢(Tzu-Hsien), 孫益強(Yi-Chiang), 邱彥綺(Yen-Chi), 黃建霖(Jian-Lin), 游紹祺(Henry), 曾柏仁(Po-Jen), and 王祥舉(Hsiang-Chu) for having fun, jokes, and mental therapy together, and advice and helps during downtime like failing the candidacy and getting

Acknowledgements

COVID-19. Also, I would like to thank 美子 (Yoshiko) for introducing me to the tennis family, so I can enjoy the summertime on the court with good tennis players.

I would like to thank my jury members– Prof. Eugenia Chiappe, Prof. Albert Cardona, and Prof. Brian McCabe for agreeing and taking your time helping the last piece of my Ph.D. work, and as well Prof. Carl Petersen for agreeing to be the president of my private defense.

Lastly, I would like to thank 土地公, 媽祖, 文昌君, and 天 for keeping everything bright and smooth.

Lausanne, April 24th 2022

Chin-Lin Chen

Abstract

One of the most important goals in neuroscience research has always been to understand how animals control their behavior. However, the long focus on the role of brain neurons in behavioral control might be missing the full story. In fact, brain-wide fluctuations in neural activity are highly correlated to the behavioral state, suggesting a closed-loop system where the behavioral command and the body state interact to interpret sensory inputs and dynamically guide action selection. However, to date, little is known about how and where information about the behavioral state is generated. In principle, information about the behavioral state is a relatively high-level encoding of the body state derived from the integration of signals from primary sensors and the local network. Local motor circuits residing in the spinal cord of mammals or the ventral nerve cord (VNC) of insects may give rise to the behavioral state and pass to the brain via brain-projecting interneurons—termed ascending neurons (ANs). However, what information ANs carry and where this information originates is still a mystery due to the technical challenges in measuring these signals in behaving animals. Therefore, it is critical to develop tools to track neuron identity and record neuronal activity during behavior to crack the functional network.

In this work, a method is introduced for imaging the motor circuit in the VNC of *Drosophila melanogaster*. This preparation demonstrates how to retain fly limb function after dissection and allows simultaneous recording of a tethered fly's behavior and its neural activity in the VNC. Incorporating this methodology with other approaches can verify the conclusions from the experiments such as those manipulating neuronal excitability, and motivate further investigation into neuronal function in specific types of behavior.

Since it has long been theorized that ANs are the cellular basis of the behavioral state information sent in the brain, the technique introduced in this work was designed to resolve questions relating to what type of information ANs convey. Here, a large-scale functional screen was performed to relate neural activity, behavior, and neuronal morphology for 247 genetically identified ANs in the adult fly. This is the first large-scale screen of neural activity in a behaving animal, and this work uncovered three fundamental features of AN populations. First, rather than low-level limb movements, ANs encode high-level behaviors like walking, grooming, and resting. Second, ANs project nearly exclusively to an integrative sensory center (AVLP) and an action selection hub (GNG). Remarkably, the encodings projected to these

Abstract

distinct areas reflect their potential roles in contextualizing sensory cues (AVLP) and guiding future actions (GNG). Third, the behavioral encodings of ANs are closely linked to their motor system patterning.

In conclusion, this work provides an indispensable tool to study the motor system beyond the brain network by overcoming a major technical barrier in *in-vivo* recording of the VNC of a behaving fly. This tool was used to help resolve what is encoded by ANs as a higher-level behavioral state, suggesting that the primary cellular origin of the behavioral information that is used to modulate brain function comes from the VNC. Overall, the technique and the findings on AN encoding should inspire follow-up studies to uncover additional neural mechanisms used in adaptive behavior generation.

Keywords: ascending neurons, behavioral state, motor system, brain, ventral nerve cord, two-photon microscopy, functional imaging, *Drosophila melanogaster*

Résumé

Comprendre comment le comportement animal est contrôlé a toujours été l'un des objectifs les plus importants de la recherche en neurosciences. Cependant, l'accent mis depuis longtemps sur le rôle des neurones du cerveau dans le contrôle du comportement pourrait ne pas suffire à trouver la réponse. Récemment, plusieurs résultats ont montré que l'activité en arrière-plan à travers tout le cerveau est corrélée à l'état comportemental, suggérant un système en boucle fermée où la commande comportementale et l'état corporel interagissent l'un avec l'autre pour interpréter les entrées sensorielles et guider la sélection des actions de manière dynamique. Pourtant, à ce jour, on sait peu de choses sur la manière dont les informations sur l'état comportemental sont générées et sur l'endroit où elles le sont. En principe, l'information sur l'état du comportement est un codage d'ordre relativement supérieur de l'état du corps, résultant de l'intégration des signaux provenant des capteurs primaires et du réseau de neurones local. Les circuits moteurs locaux qui résident dans la moelle épinière des mammifères ou dans le cordon nerveux ventral (VNC) des insectes pourraient générer l'information sur l'état comportemental et la transmettre au cerveau par l'intermédiaire d'interneurones appelés neurones ascendants (AN). Cependant, la manière dont elle est générée et son contenu restent mystérieux en raison de la barrière technique. Pour comprendre le fonctionnement de ces réseaux de neurones, il est essentiel de disposer d'outils permettant de suivre l'identité des neurones et de les enregistrer pendant le comportement.

Dans ce travail, une méthode qui permet d'imager le circuit moteur dans le VNC de la *Drosophila melanogaster* est présentée. La préparation démontre comment conserver la fonction des membres de la mouche lors de la dissection pour permettre l'enregistrement simultané du comportement d'une mouche attachée et de son activité neuronale dans le VNC. L'incorporation avec d'autres expériences montre en outre qu'il s'agit d'un outil indispensable pour consolider la conclusion des résultats, par exemple, de la manipulation de l'excitabilité neuronale, ou pour motiver un examen plus approfondi afin d'élaborer la déduction de la fonction du neurone dans un comportement spécifique.

Puisqu'il a longtemps été théorisé que les ANs sont la base cellulaire de l'information sur l'état comportemental envoyée au cerveau, ce qu'ils véhiculent peut alors être étudié avec la technique introduite dans ce travail. Ici, un enregistrement fonctionnel à grande échelle a été réalisé pour mettre en relation l'activité neuronale, le comportement et la morphologie

Abstract

neuronale pour 247 ANs identifiés génétiquement chez la mouche adulte. C'est le premier enregistrement à grande échelle de l'activité neuronale chez un animal qui se comporte et grâce auquel, trois caractéristiques fondamentales des populations d'AN ont été découvertes. Premièrement, elles codent des comportements de haut niveau comme la marche, le toilettage et le repos plutôt que des informations de bas niveau telles que les mouvements des membres. Deuxièmement, elles projettent presque exclusivement à deux endroits du cerveau : un centre sensoriel intégratif (AVLP) et un centre de sélection des actions (GNG). Il est remarquable de noter que les encodages des ANs qui projettent vers ces zones distinctes reflètent leurs rôles potentiels dans la contextualisation des signaux sensoriels (AVLP) et dans l'orientation des actions futures (GNG). Troisièmement, nous constatons que les encodages comportementaux des ANs sont étroitement liés à la configuration de leur système moteur. De façon plus intrigante, nous identifions des ANs qui intègrent le nombre d'extensions du proboscis (PE) sur des dizaines de secondes. Ces ANs sont entrelacés, ce qui est cohérent avec les connexions récurrentes qui peuvent calculer cette mémoire des PEs.

En conclusion, ce travail fournit d'abord un outil indispensable pour étudier le système moteur au-delà du réseau cérébral en surmontant la barrière technique de l'enregistrement *in-vivo* dans le VNC d'une mouche qui se comporte. Cette préparation permet de mieux comprendre ce que les ANs encodent comme état comportemental de plus haut niveau, ce qui montre que l'origine cellulaire principale de la modulation comportementale dans la fonction cérébrale provient du VNC. Dans l'ensemble, la technique et les résultats de l'encodage des ANs peuvent être une source d'inspiration pour les études futures visant à découvrir d'autres mécanismes neuronaux pour la génération de comportements adaptatifs.

Mots-clés : neurones ascendants, état comportemental, système moteur, cerveau, cordon nerveux ventral, microscopie à deux photons, imagerie fonctionnelle, *Drosophila melanogaster*

Contents

Acknowledgements	v
Abstract (English/Français)	vii
List of figures	xvii
List of tables	xxi
List of videos	xxiii
1 Introduction	1
1.1 Motor system for behavior control	1
1.1.1 Motor-related modulation on brain modules	1
1.1.2 Body-state informing module	5
1.2 Challenges and gaps	9
1.3 Potential solutions from current resources	11
1.3.1 The fly as a model organism to study motor system	11
1.3.2 Experimental techniques	16
1.4 Aims	19
2 Imaging neural activity in the ventral nerve cord of behaving adult <i>Drosophila</i>	21
2.1 Abstract	22
2.2 Introduction	22
2.3 Results	23
2.3.1 A dissection for accessing the ventral nerve cord	23
2.3.2 Imaging the activity of populations of neurons in the VNC	23
2.3.3 Imaging the activity of sparse sets of neurons in the VNC	25
2.3.4 Activity patterns of moonwalker ascending neurons	25
2.3.5 Activity patterns of moonwalker descending neurons	27
2.3.6 Activity patterns of novel descending neurons	28
2.3.7 Facilitating access to the VNC by inducing cell death in IFMs	29
2.4 Discussion	30
2.5 Materials and methods	32

Contents

2.5.1	<i>Drosophila</i> lines	32
2.5.2	Generation of Act88F:Rpr construct and flies	32
2.5.3	Fluorescence imaging of indirect flight muscles	33
2.5.4	Immunofluorescence imaging of whole-mount brains and ventral nerve cords	33
2.5.5	Imaging GFP expression in leg muscles	34
2.5.6	Thoracic dissection for VNC imaging	34
2.5.7	2-photon microscopy during behavior	35
2.5.8	Comparing walking behaviors in dissected or non-dissected animals	36
2.5.9	Infrared laser antennal stimulation	36
2.5.10	Statistics	37
2.5.11	Data analysis	37
2.6	Code availability	42
2.7	Data availability	42
2.8	Acknowledgments	42
2.9	Author contributions	42
2.10	Declaration of Interests	43
2.11	Supplementary information	44
2.11.1	Supplementary Figures	44
2.11.2	Supplementary Videos	51
3	Ascending neurons convey behavioral state to integrative sensory and action selection centers in the brain	55
3.1	Abstract	56
3.2	Introduction	57
3.3	Results	59
3.3.1	A large-scale screen of ascending neuron movement encoding, brain targeting, and motor system patterning	59
3.3.2	Ascending neurons encode high-level behaviors	62
3.3.3	Ascending neurons target integrative sensory, or action selection brain regions as a function of their encoding	63
3.3.4	Distinct rest- and puff-encoding by morphologically similar ANs	65
3.3.5	Walk- or turn- encoding correlates with the laterality of VNC projections	68
3.3.6	Foreleg-dependent actions are encoded by ANs in the anterior VNC	71
3.3.7	Temporal integration of proboscis extensions by a cluster of ANs	74
3.4	Discussion	74
3.4.1	Encoding of high-level behavioral states	76
3.4.2	Predominant projection to the brain's AVLP and GNG	77
3.4.3	Patterning within the VNC is predictive of behavioral encoding	78
3.4.4	Future work	79
3.5	Materials and Methods	80

3.5.1	Key resource table	80
3.5.2	Fly husbandry	81
3.5.3	<i>In vivo</i> two-photon calcium imaging experiments	82
3.5.4	Immunofluorescence tissue staining and confocal imaging	82
3.5.5	Two-photon image analysis	83
3.5.6	Behavioral data analysis	83
3.5.7	Regression analysis of PE integration time	85
3.5.8	Linear modeling of neural fluorescence traces	85
3.5.9	Behavior-based neural activity analysis	86
3.5.10	Neural fluorescence-triggered averages of spherical treadmill rotational velocities	86
3.5.11	Brain and VNC confocal image registration	87
3.5.12	Analysis of individual AN innervation patterns	87
3.5.13	AxoID: a deep learning-based software for tracking axons in imaging data	88
3.5.14	Overall workflow	95
3.6	Code availability	96
3.7	Data availability	97
3.8	Acknowledgments	97
3.9	Author contributions	97
3.10	Declaration of Interests	97
3.11	Supplementary Information	98
3.11.1	Supplementary Figures	98
3.11.2	Supplementary Tables	105
3.11.3	Supplement Videos	114
4	Serotonergic Modulation of Walking in <i>Drosophila</i>	115
4.1	Abstract	116
4.2	Introduction	116
4.3	Results	117
4.3.1	VNC Serotonergic Neurons Arborize within the Leg Neuropils	117
4.3.2	Activation of VNC Serotonergic Neurons Slows Walking Speed	118
4.3.3	Inhibition of 5-HT ^{VNC} Neurons Increases Walking Speed	120
4.3.4	5-HT ^{VNC} Neurons Are Active in Walking Flies Neurons Increases Walking Speed	122
4.3.5	5-HT ^{VNC} Activation Does Not Disrupt Walking Coordination	122
4.3.6	5-HT ^{VNC} Neuron Inactivation Slows Walking in Multiple Contexts	123
4.3.7	Silencing 5-HT ^{VNC} Neurons Alters the Response to Sudden Changes in the Environment	125
4.3.8	Different Serotonin Receptor Mutants Alter the Startle Response in Different Ways	127
4.3.9	Serotonin Receptors Are Expressed in Distinct Cell Types	130

Contents

4.4	Discussion	130
4.4.1	A Common Role for Serotonin in Modulating Walking Speed across Species	130
4.4.2	Serotonergic Modulation of the Startle Response	131
4.4.3	A Model for Serotonin-Mediated Modulation of Walking in Flies	131
4.5	Materials and Methods	133
4.5.1	Key Resources Table	133
4.5.2	Fly Husbandry	134
4.5.3	Animal Rearing for Behavioral Experiments	135
4.5.4	Immunostaining Brain and VNC	135
4.5.5	Immunostaining Brain and VNC	136
4.5.6	Cell Counting and Quantification	136
4.5.7	Leg Dissection, Imaging, and Image Processing	136
4.5.8	Arena Experiments	137
4.5.9	Flywalker Experiments	139
4.5.10	Functional Imaging Experiments	140
4.5.11	Quantification and Statistical Analysis	140
4.5.12	Arena Experiments	140
4.5.13	Flywalker Experiments	143
4.5.14	Functional Imaging Experiments	144
4.6	Data and Code Availability	146
4.7	Acknowledgments	146
4.8	Author contributions	146
4.9	Declaration of Interests	146
4.10	Supplementary Information	148
4.10.1	Supplementary Figures	148
5	Extensive and Diverse Patterns of Cell Death Sculpt Neural Networks in Insects	157
5.1	Abstract	158
5.2	Introduction	158
5.3	Results	161
5.3.1	An early and rapid mode of developmental cell death eliminates significant numbers of newly born neurons throughout postembryonic development in <i>Drosophila</i>	161
5.3.2	Blocking PCD in <i>Drosophila</i> generates identifiable, differentiated populations of undead neurons	165
5.3.3	Undead neurons are functional and integrate into motor networks	167
5.3.4	Hemilineage-specific cell death in the MNB lineage correlates with loss of flight in the swift lousefly <i>Crataerina pallida</i>	170
5.3.5	Increased hemilineage-specific PCD in flightless dipterans may be responsible for adaptive modifications to neural circuits	175
5.4	Discussion	177

5.4.1	Hemilineage-specific cell death occurs in newly born neurons	177
5.4.2	Blocking death results in functional neurons that integrate into adult networks	179
5.4.3	Cell death during neurogenesis is widespread across insects	179
5.4.4	Midline neurons show hemilineage-based variations in different species	180
5.4.5	Hemilineage-specific reductions in fibre diameter in the bee lousefly . .	180
5.4.6	Conclusions	181
5.5	Materials and Methods	182
5.5.1	Key resources table	182
5.5.2	Animals	184
5.5.3	Construction of UAS-SR4VH	184
5.5.4	Immunohistochemistry and chemical staining	185
5.5.5	EdU treatment	186
5.5.6	Generation of undead neuron MARCM clones	186
5.5.7	Thermogenetic activation and video recordings	186
5.5.8	Two-photon calcium imaging in behaving intact flies	187
5.5.9	Data analysis for 2-photon imaging in behaving <i>Drosophila</i>	187
5.5.10	Confocal imaging and image processing	188
5.5.11	Fluorescence intensity plots	188
5.5.12	Analysis of thermogenetic activation	188
5.5.13	Quantification of 3A/3B bundle diameters	188
5.5.14	Statistical analysis	189
5.6	Data availability	189
5.7	Acknowledgments	190
5.8	Author contributions	190
5.9	Declaration of Interests	190
5.10	Supplementary Information	191
5.10.1	Supplementary Figures	191
5.10.2	Supplement Videos	198
6	Conclusion and perspectives	199
6.1	A plausible parallel system for efficiently interpreting body state	200
6.2	The role of VNC neurons in neural dynamics	201
6.3	Limitations	202
6.4	Future works	203
6.4.1	Scientific part	203
6.4.2	Technical part	205
	Bibliography	207
	List of abbreviations	239

Contents

Curriculum Vitae

241

List of Figures

1.1	A diagram depicting the adaptive behavior hypothesis portraying the motor system as a closed-loop.	2
1.2	The neuronal population in the visual cortex of the rat is more active in the awake state than under anesthesia.	3
1.3	Behavioral variables can explain the variance of spontaneous activity across the brain.	4
1.4	Mammalian sensory organs.	6
1.5	Insect sensory organs.	7
1.6	Proprioceptive hardware.	8
1.7	Schematic comparison of somatosensory pathways in flies and mammals. . . .	10
1.8	Anatomy of the ventral nerve cord (VNC) of a fly.	12
1.9	GAL4-UAS driver system.	15
1.10	Split-GAL4 expression system.	15
1.11	Principle of one-photon and two-photon excitation.	17
1.12	Genetically encoded calcium indicator—GCaMP.	17
1.13	Two-photon laser scanning microscopy and photomultiplier tube	19
1.14	Experimental setups for recording neural activity in behaving flies	20
2.1	Dissection for imaging the adult <i>Drosophila</i> ventral nerve cord (VNC).	24
2.2	Recording populations of neurons in the VNC during behavior	26
2.3	Recording the activity of dorsal Moonwalker Ascending Neurons (dMANs) in the thoracic cervical connective during behavior.	27
2.4	Recording the activity of Moonwalker Descending Neurons (MDNs) in the thoracic cervical connective during behavior.	28
2.5	Recording the activity of A1 neurons in the thoracic cervical connective during behavior.	29
2.6	Indirect flight muscle degradation in <i>Act88F:Rpr</i> animals.	31
S2.1	Illustration of dorsal dissection to access the VNC.	44
S2.2	Locomotion in flies with or without thoracic dissection.	45
S2.3	System for VNC imaging.	45
S2.4	Optimization of λ and γ values for image registration.	46
S2.5	ovariance in fluorescence signals between bilateral pairs of neurons.	47
S2.6	GFP expression in the central nervous system.	48

List of Figures

S2.7 GFP expression in leg muscles.	49
S2.8 Locomotor behaviors in control and <i>Act88F:Rpr</i> animals.	50
3.1 Large-scale functional and morphological screen of ascending neuron movement encoding and nervous system targeting	60
3.2 Ascending neurons encode high-level behaviors.	64
3.3 Ascending neurons principally project to the brain's AVLP and GNG and the VNC's leg neuromeres.	66
3.4 Functional and anatomical properties of ascending neurons that encode resting, or responses to puffs.	67
3.5 Functional and anatomical properties of ascending neurons that encode walking, or turning.	70
3.6 Functional and anatomical properties of ascending neurons that encode multiple foreleg behaviors, or only eye grooming.	72
3.7 Functional and anatomical properties of ascending neurons that integrate the number of proboscis extensions over time.	75
3.8 Summary of ascending neuron functional encoding, brain targeting, and VNC patterning.	77
S3.1 Semi-automated tracking of proboscis extensions, and the accuracy of the behavioral classifier.	98
S3.2 AxoID, a deep learning-based algorithm that detects and tracks axon cross-sections in two-photon microscopy images.	99
S3.3 Correlations among and between low-level joint angles and high-level behavioral states.	100
S3.4 Normalized mean activity ($\Delta F/F$) of ascending neurons during high-level behaviors, and a summary of their behavioral encoding, brain targeting, and VNC patterning.	101
S3.5 Puff-ANs do not encode backward walking and respond similarly to puffs of air, or CO ₂	102
S3.6 The bilaterality of an ascending neuron pair's VNC patterning correlates with the synchrony of their activity.	103
S3.7 Ascending neurons that become active only when the spherical treadmill is removed.	104
4.1 Neuromodulators in the <i>Drosophila</i> CNS.	119
4.2 5-HT ^{VNC} Neurons Modulate Walking Speed.	121
4.3 5-HT ^{VNC} Neurons Modulate Walking Speed.	124
4.4 Changes in Walking Behavior When 5-HT ^{VNC} Neurons Are Silenced.	126
4.5 Phenotype of the Startle Response of Trh and Serotonin Receptor Mutants.	128
4.6 Differential Expression of Serotonin Receptors in Locomotor Circuit Components.	147
S4.1 Trh-Gal4 accurately drives expression in serotonergic VNC neurons.	148

S4.2	Activation and inactivation of 5-HT ^{VNC} neurons shifts locomotor behavior.	149
S4.3	Imaging 5-HT ^{VNC} neurons in actively behaving flies.	151
S4.4	5-HT ^{VNC} activation reduces variance in foot placement.	152
S4.5	5-HT ^{VNC} inactivation, mutation of Trh, and mutation of 5-HT receptors shifts behavioral responses to startling stimuli.	153
S4.6	5-HT receptors are expressed in both flexor- and extensor-like muscles in the leg.	154
5.1	Early neurogenesis in insects.	160
5.2	Early neuronal cell death occurs throughout postembryonic development.	163
5.3	Blocking death results in differentiated undead neurons in the medial neuroblast (NB) lineage.	166
5.4	Undead neurons are functional: thermogenetic activation of undead neurons induces walking in decapitated <i>Drosophila</i>	168
5.5	Undead neurons integrate into VNC networks: undead neurons are active during naturalistic behaviours in intact adult <i>Drosophila</i>	171
5.6	Median neuron numbers vary between insect species.	172
5.7	Hemilineage-specific cell death may be responsible for reduced octopaminergic neurons in the swift lousefly.	173
5.8	Cell death during neurogenesis in the ‘primitive’ wingless firebrat.	175
5.9	Neuronal cell death sculpts the wing circuitry of wingless dipterans.	176
S5.1	SR4VH reveals successive stages of cell death in lineages with doomed hemilineages.	191
S5.2	Postembryonic development of lineage 0B in wild-type and H99/XR38 flies.	192
S5.3	Examples of postembryonic MARCM clones in which cell death is blocked.	194
S5.4	Quantification of undead neuron morphology.	195
S5.5	Wild-type octopaminergic neurons are active during walking in intact adult <i>Drosophila</i>	196
S5.6	Subregion analysis of calcium signals along the width of a primary neurite in a H99/XR38 animal.	197

List of Tables

S3.1 Sparse AN driver lines and associated properties.	105
S3.2 Activation (AD) and DNA-binding Domains (DBD) of split-GAL4 lines used in this study.	111

List of videos

S2.1 VNC imaging volume.	51
S2.2 Horizontal VNC imaging.	51
S2.3 Coronal VNC imaging.	51
S2.4 Coronal cervical connective imaging.	51
S2.5 Motion and deformation correction.	52
S2.6 Semi-automated behavioral classification.	52
S2.7 Coronal cervical connective imaging of dorsal Moonwalker Ascending Neurons.	52
S2.8 Behavioral responses associated with dorsal Moonwalker Ascending Neuron activity events.	52
S2.9 Coronal cervical connective imaging of Moonwalker Descending Neurons	52
S2.10 Behavioral responses associated with Moonwalker Descending Neuron activity events.	52
S2.11 Coronal cervical connective imaging of A1 neurons.	53
S2.12 Behavioral responses associated with left A1 neuron activity events.	53
S2.13 Behavioral responses associated with right A1 neuron activity events.	53
S2.14 Behaviors and neural activity in <i>Act88F:Rpr</i> and control animals.	53
S2.15 Coronal and horizontal section imaging of A1 neurons in the VNC.	53
S2.16 Long-term behavior in animals used to image dMAN activity.	53
S2.17 Long-term behavior in animals used to image MDN activity.	53
S2.18 Long-term behavior in animals used to image A1 activity.	54
S3.1 High-level behaviors, their associated 3D poses, and spherical treadmill rotational velocities.	114
S3.2 Representative data for 50 comprehensively analyzed, AN-targeting sparse driver lines.	114
S3.3 - S3.52 Representative data for 50 comprehensively analyzed, AN-targeting sparse driver lines.	114
S5.1 Video recordings of control and ‘undead’ decapitated flies during thermogenetic activation.	198
S5.2 Recording of 2-photon calcium imaging in undead neurons.	198
S5.3 Z-stack of the imaging area for GCaMP6s activity in undead neurons.	198
S5.4 Subregion neuronal activity patterns during walking.	198

1 Introduction

1.1 Motor system for behavior control

Animals navigating in a complex environment must process overwhelming information, such as when predators approach or they are chasing prey, and generate the appropriate behavior to ensure their continued survival. These behaviors can be seen as sequences of similar types of actions, such that a general behavior can always be broken down into individual actions. For example, grooming behavior can be seen as a sequence of legs scratching and walking can be seen as a coordinated sequence of leg swing cycles. As such, individual actions within a behavior can be more precisely adjusted to help the animal adapt appropriately at every moment, and these adapting action sequences require the continuous sensation of external cues and body-state awareness to be well-orchestrated. A plausible way to generate this adaptation in behavior is to use the body state caused by the current behavior to instantly correct the next action. This suggests a dynamic behavioral model consisting of a closed loop formed by the mutual connection between the commanding and informing modules (**Figure 1.1**). As far as we know, this information about the body state is sent from primary sensory neurons (SNs) and ascending neurons (ANs) in the spinal cord of mammals or the ventral nerve cord (VNC) of insects to the brain for higher-order computation (**Figure 1.1**). Then, behavior generation requires the brain to compute this information and send commands back down, where the local circuits within the spinal cord or VNC function as central pattern generators (CPGs) [1, 2] and reflex arcs [2] (**Figure 1.1**). Hence, to understand how the brain selects the next action, it is essential to know what information SNs and ANs encode and pass on to the brain.

1.1.1 Motor-related modulation on brain modules

In line with the hypothesis of the dynamic loop for adaptive behavior generation, evidence has been found supporting bottom-up motor signaling to the brain modules. This may have

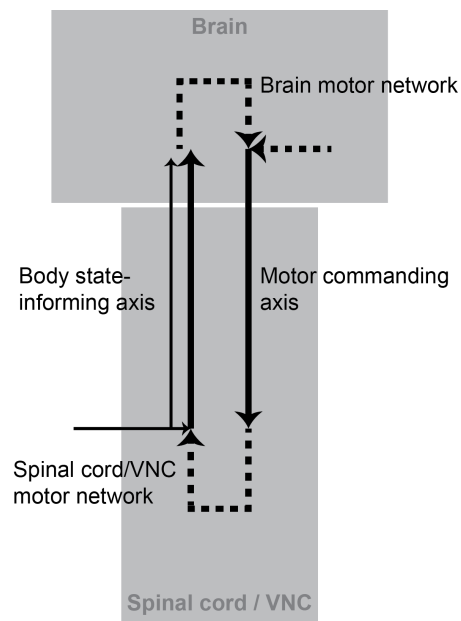


Figure 1.1: **A diagram depicting the adaptive behavior hypothesis portraying the motor system as a closed-loop.** The local networks in the brain and spinal cord in mammals or the ventral nerve cord (VNC) in insects are the centers of the motor system that generate the appropriate actions required for an animal adapt to different situations. The neural mechanism of dynamic behavior modification requires information exchange, which can be achieved by wiring together information about the body state, which ascends from the spinal cord/VNC to the brain, with the motor commanding module, which descends from the brain to the spinal cord/VNC. The thin line along the body-state-informing axis additionally represents the direct signal from sensors. The dash lines represent information flow within local networks, either in the brain or the spinal cord/VNC.

been missed previously, as to date, most conventional experiments have been performed with anesthetized animals, which pre-excludes the behavioral effect and allows observation of only the stimulus-related response. Therefore, activity events that could not be explained by the corresponding manipulation were mistakenly considered "background noise". However, as such background activity increases in recordings from awake animals (Figure 1.2) [3], it must be physiologically meaningful.

More recent findings indicate that the cause of baseline fluctuations in neural activity across brain regions in awake mice can be linked to behavior. In the visual cortex, spontaneous neural activity, which can be observed without any visual input, is significantly correlated to spontaneous behavior, such as pupil dilation, whisking, or running [4, 5]. It has also been shown that the behavioral state can modulate the neural response to visual stimuli [5]. Moreover, such behavioral correlation is brain-wide (Figure 1.3) [4, 6]. Similar results were also found in insects, primarily in *Drosophila melanogaster*. Behavior such as flight and walking

can modulate the response to visual motion stimuli [7–10]. When a fly engages in flight or walking, there is an increase of gain in response to the visual stimulus in horizontal (HS) and vertical system (VS) visual neurons, which might help process high-frequency visual motion during movement [7, 8]. Moreover, HS neurons have been found to encode the speed of turning and translation independent of the visual cue, thus potentially playing a role in the

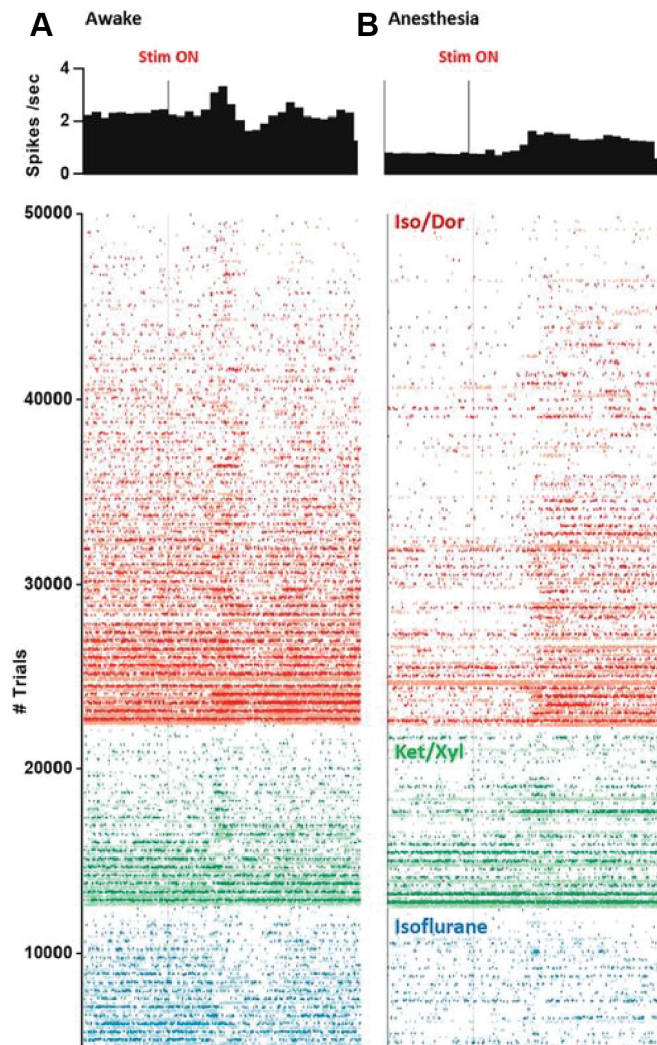


Figure 1.2: **The neuronal population in the visual cortex of the rat is more active in the awake state than under anesthesia.** Average firing rate (top) and the raster plot (bottom) of all trials of all single units recorded from the neuronal population in an (A) awake versus (B) anesthetized rat. One line represents one trial (96 trials per unit). Trials are ranked according to firing rates from high to low rate (bottom-up) for each anesthetic. Visual stimulation onset is indicated as "Stim ON". The type of anesthesia is indicated as isoflurane (Iso; blue), isoflurane-dormicum (Iso/Dor; orange), and ketamine/xylazine (Ket/Xyl; green). Both panels are modified from Aesobø et al., 2017 [3].

fly’s navigation when walking [9]. Similar to this behavioral modulation on the visual system in *Drosophila*, the moth *Manduca sexta* displays an increase in odor sensibility with wing beat [11]. In addition to these linked behaviors, the behavioral state can also affect which following action is chosen. For example, the speed at which a fly walks can determine whether it will flee or freeze when approached by a predator [12]; they usually choose to run or jump away when walking at high speeds, whereas they tend to freeze when moving slow [12].

Overall, these findings indicate that the behavioral state modulates brain activity and may change perception by integrating external stimuli to select an appropriate action for each circumstance. Hence, knowing the origin of behavioral state signals can help reveal the neural mechanism of context-dependent action selection—otherwise known as adaptive behaviors.

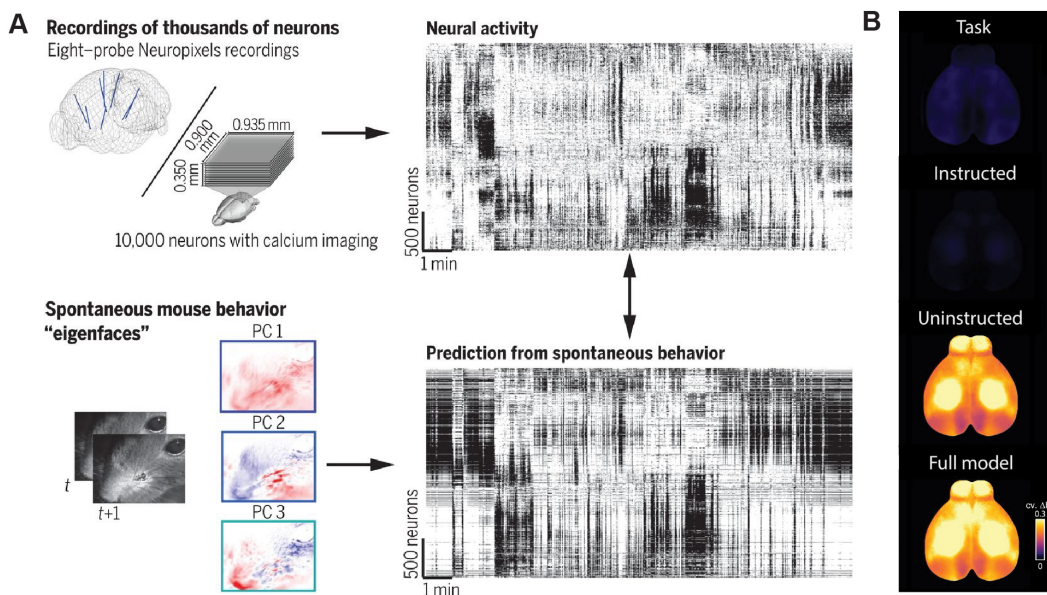


Figure 1.3: **Behavioral variables can explain the variance of spontaneous activity across the brain.** (A) Large-scale neural population activity of 10,000 neurons recorded by Neuropixels probes (top left) can be predicted by principal components (PCs) of a series of spontaneous mouse facial motions (bottom left). The prediction from spontaneous facial behavior (top right) has a similar population activity pattern as the experimental recordings (bottom right). Adapted from Stringer et al., 2019 [4]. (B) The signal variance indicated by calcium indicator GCaMP6s across the entire brain of the mouse can be uniquely explained by the spontaneous behavior (uninstructed) rather than experimental task events (task) or the task-consequent behavior (instructed). Modified from Musall et al., 2019 [6].

1.1.2 Body-state informing module

Sensory neurons (SNs)

SNs throughout the skin, muscles, and bones enable the sensing of external cues such as the feeling of the breeze and the sting of the bee, and generate the corresponding proprioception like the force for lifting stones. To transform stimuli into signals, diverse sensory organs located at the nerve ending of these neurons detect a range of stimuli including touch, muscle force, pain, and temperature [13, 14]. Among those, the sense of muscle and tendon tension, which is also called proprioception, is detected by muscle spindles, Golgi tendon organs and joint receptors and is believed to be the basis of self-body sensation [15], while tactile sensation and nociception are encoded via diverse cutaneous sensors, such as Merkel cells, Ruffini endings, Meissner corpuscles, Pacinian's corpuscles, and free endings, each with a different activation threshold in response to different intensities of stimuli (Figure 1.4) [13, 14].

Notably, this sensory system is also conserved in insects. Despite the difference in the mechanistic nature of their muscles and exoskeleton, the proprioceptive and somatosensory neurons function in the same way. In insects, the joint angle and limb position are detected via stretch receptors (sr), chordotonal organs (co), and hair cells (hc) [16–18], whereas external stimuli encoding touch, pressure, and nociception are detected via external sensilla (es), campaniform sensilla (cs), and multidendritic neurons (md), respectively (Figure 1.5) [17, 18].

Sensory information is critical for the integrity of behavior, with a clinical case showing that the absence of this peripheral information impairs limb control. Due to an autoimmune disease, Ian Waterman lost primary sensory neurons below the neck and struggled to generate smooth and precise limb movements [19]. Without this sensory feedback to the CNS, he could not feel any of his body parts, which required him to use visual guidance to plan each limb movement for even simple actions such as reaching. In parallel, animal studies with mice or flies also showed that loss of proprioception decreases the precision of limb coordination [20, 21]. In short, coordinated action requires top-down motor commands from the brain and subsequent peripheral feedback. Furthermore, primary sensory neurons also branch at the spinal cord or the VNC (Figure 1.6) [17, 22], suggesting additional local signal computation.

Ascending neurons (ANs)

Along with SNs, the afferent source to the brain also contains ANs, which are long-range interneurons that project to the brain with dendritic innervation from the spinal cord or VNC. Thus, besides the motor neurons in both mammals and insects, ANs are the final output neurons of local preprocessed signals (Figure 1.7), suggesting that they can carry information that is more diverse and complicated than that of SNs. Due to their higher complexity, current studies of ANs are discrete and topic-specific; hence, the understanding of ANs is not as comprehensive as for SNs.

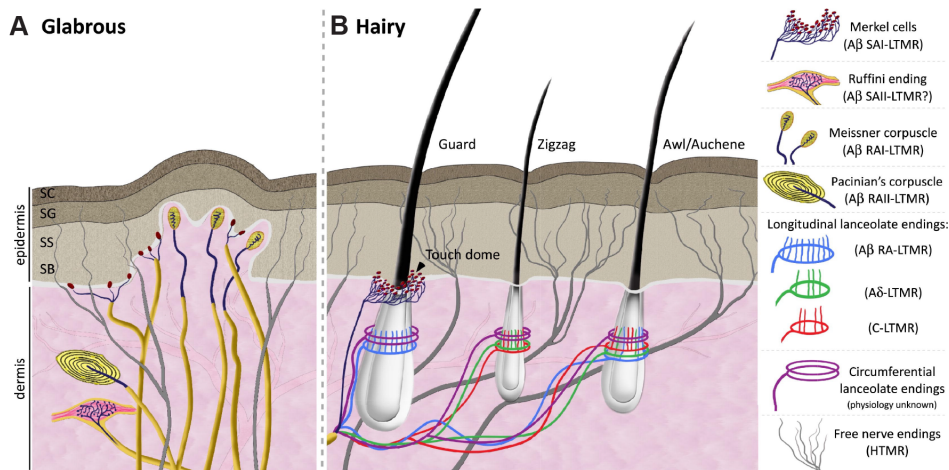


Figure 1.4: Mammalian sensory organs. (A) In skin regions lacking hair, termed glabrous, innocuous touch is mediated by four types of mechanoreceptors. The Merkel cell-neurite complex in the basal layer of the epidermis consists of clusters of Merkel cells that make synapse-like associations with enlarged nerve terminals branching from a single $A\beta$ fiber. This complex and its associated SAI-LTMR responses help us reconstruct acute spatial images of tactile stimuli. Meissner corpuscles are localized in the dermal papillae and consist of horizontal lamellar cells embedded in connective tissue. Their characteristic RAI-LTMR responses detect movement across the skin. Ruffini endings are localized deep in the dermis and are morphologically similar to the Golgi tendon organ, a large, thin spindle-shaped cylinder composed of layers of perineural tissue. Historically, Ruffini endings have been associated with SAI-LTMR responses, which respond best to skin stretch, though such correlations remain highly controversial. Lastly, Pacinian corpuscles are located in the dermis of glabrous skin where their characteristic onion-shaped lamellar cells encapsulate a single $A\beta$ ending. Their well-recognized RAI-LTMR responses detect high-frequency vibration. (B) In hairy skin, tactile stimuli are transduced through three types of hair follicles, defined in the mouse as guard, awl/auchenne, and zigzag. The longest hair type, guard hair, is associated with touch domes at the apex and $A\beta$ -LTMR longitudinal lanceolate endings at the base. Zigzag hair follicles are the shortest and are innervated by both C- and $A\delta$ -LTMR longitudinal lanceolate endings. Awl/auchenne hairs are triply innervated by C-LTMR, $A\delta$ -LTMR, and $A\beta$ -LTMR longitudinal lanceolate endings. In addition, all three hair follicle types are innervated by circumferential lanceolate endings whose physiological properties remain unknown. Noxious touch is detected by free nerve endings found in the epidermis of both glabrous and hairy skin and are characterized by both $A\delta$ - and C-HTMR responses. Abbreviations: SA, slowly adapting; RA, rapidly adapting; LTMR, low-threshold mechanoreceptor; HTMR, high-threshold mechanoreceptor; SC, stratum corneum; SG, stratum granulosum; SS, stratum spinosum; SB, stratum basalis; SA, slow adapting; IA, intermediate adapting; RA, rapidly adapting. Both panels and captions are adapted from Abaira and Ginty, 2013 [13].

Various functions of ANs in local signal processing have been shown. First, ANs relay primary sensory signals. For example, it is well established that primary nociceptive neurons terminate at downstream ANs, where the signal is contralaterally relayed to the thalamus in

1.1 Motor system for behavior control

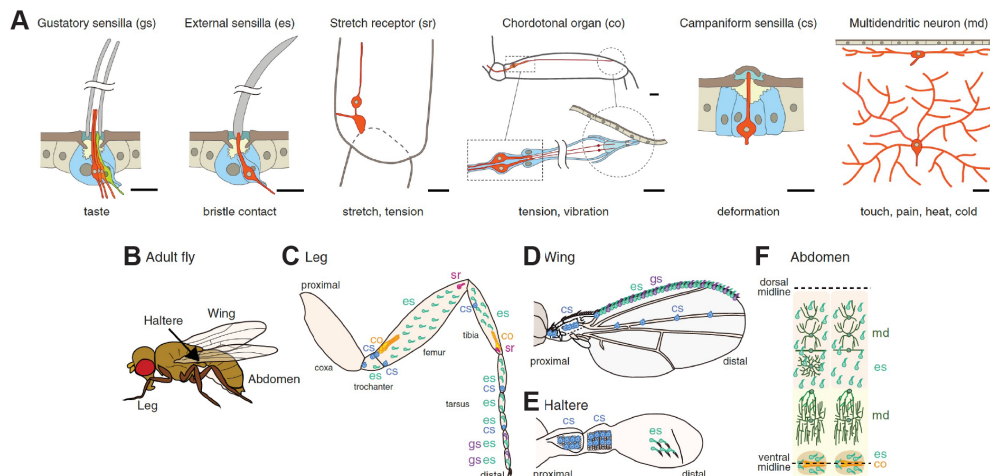


Figure 1.5: **Insect sensory organs.** (A) Schematics of the mechanosensory receptors of *Drosophila* and the gustatory sensilla, the latter of which chemically senses via taste receptors. External sensilla are the low threshold tactile sensors for detecting touch while the campaniform sensilla is the high threshold sensor for detecting pressure. Stretch receptors and chordotonal organs are the proprioceptors for detecting the joint and muscle tension. Multidendritic neurons are the nociceptors. The schematics are depicted as cross-sectional views, except for the multidendritic neurons, which are depicted using a planar view (rightmost panel). Red and blue indicate neurons and support cells, respectively. Scale bars are 10 μ m. The distribution of the mechanosensory organs in (B) an adult fly are indicated by focused views of the (C) leg, (D) wing, (E) haltere, and (F) abdomen. All panels modified from Tsubouchi et al., 2017 [18].

A δ and C fibers via the spinothalamic tract in the spinal cord [24]. Second, ANs form a local circuit to help distinguish self-motion-induced sensory inputs and external perturbations to maintain ongoing behavior. A known circuit called corollary discharge (CD) has been identified [25,26]. For example, ascending interneurons (aIN) in the *Xenopus* tadpole suppress the sensory interneurons to maintain the swimming pattern [26]. Similar networks are also found in invertebrates. For instance, cricket wing chirping uses CD to suppress motor-induced auditory stimuli [26]; nematodes and sea slugs use it to eliminate the self-motion-induced somatosensory input for maintaining locomotion [25]. In the mammalian spinocerebellar tract, ANs also help to eliminate the perturbation of external stimuli during locomotion, which is possible because the efferent copy of the signal from the central pattern generator that they transmit dominates the discrete external sensory input [27]. The activation of Moonwalker Ascending Neurons (MANs) has also been found to prolong backward walking in flies, even though the cellular mechanism is unknown [28]. Third, spinobulbar ANs of the lamprey activate rhythmically with nearby ventral roots during locomotion to form monosynaptic connections to descending neurons [29]. Fourth, a type of AN (R13D11) that is responsible for the computation between touch and proprioception via the a network of a inhibitory neurons between both types of SNs [30]. Additionally, an AN-AN connection has been uncovered [31],

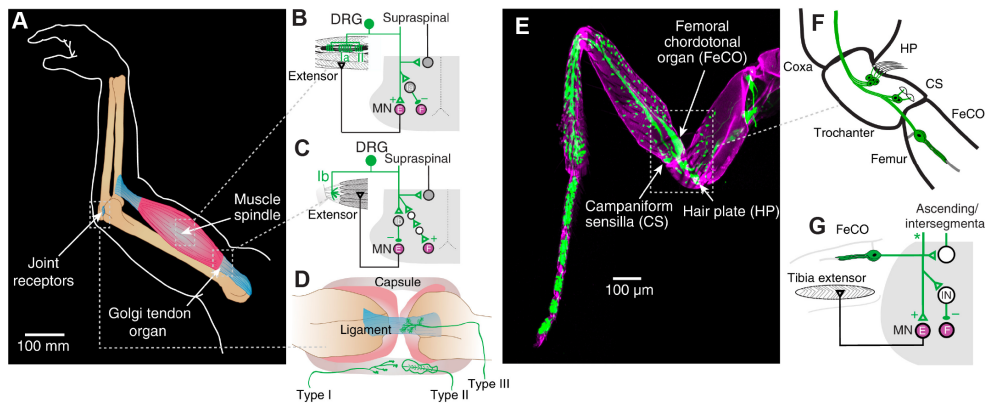


Figure 1.6: **Proprioceptive hardware.** (A) Location of proprioceptive organs in a mammalian limb. (B) Schematic of muscle spindle afferent spinal connectivity, highlighting homonymous motor pool activation and antagonist inhibition, via Ia inhibitory interneurons. MN, motor neuron; E, extensor; F, flexor; DRG, dorsal root ganglion. (C) Schematic of Golgi tendon organ group Ib afferent connectivity in the spinal cord. Note the opposite effects on extensor and flexor activity as compared to muscle spindle afferents, in part mediated by inhibitory Ib interneurons that innervate homonymous motor neurons. (D) Schematic of receptor types in the joint capsule and ligament that could convey proprioceptive information. Three major types are: type I, slowly adapting receptors in the outer layers of the fibrous joint capsule; type II, rapidly adapting receptors in the deeper layers of the joint capsule; and type III, slowly adapting receptors embedded in the ligaments and terminal regions of the tendons near the joint capsule. (E) Distribution of mechanosensory neurons on the *Drosophila* leg. Image shows ChAT-Gal4 driving UAS-GFP. (F) Schematic of proprioceptor distribution on proximal regions of the *Drosophila* leg. For clarity, only a subset of proprioceptors are shown. (G) Example wiring schematic of sensory neuron targets in the insect VNC, based on data from the locust (note that not all connections are shown). Flexion-sensitive proprioceptors from the femoral chordotonal organ directly excite tibial extensor motor neurons and indirectly inhibit flexor motor neurons. FeCO neurons also synapse on intersegmental and ascending interneurons. The direct afferent from sensory neurons to the brain are labelled with asterisk, based on the data from Tsubouchi et al., 2017 [18]. All panels and captions modified from Tuthill and Azim, 2018 [23].

suggesting that signals carried within AN can be further sculpted. Overall, our understanding of the role of ANs in local processing is discrete and functionally specific.

The function of ANs in the brain has also been shown in a few cases, with the overall current findings suggesting that ANs participate in behavioral state-dependent modulation on the brain modules. First, the brain contains axon terminals of walking-response ANs Lco2N1 and Les2N1D (R85A11) [18]. Second, ANs can convey behavioral signals that affect the activity of other brain neurons. As examples, the walking signal from LAL-PS-ANs is transmitted to HS cells in visual system [32], reafference can occur from the motor center to the visual center [33], and the activity of PER_{in} neurons affects the choice of action between feeding initiation and walking [34]. Third, non-behavioral information is also conveyed to the brain, such as the

encoding of gustatory information by the gustatory-encoding AN of 2nd order taste projection neurons (TPNs).

A plausible network of information flow to ANs has been depicted. Burrow proposed a model of the connectivity structure from SNs to ANs based on the findings from different types of VNC neurons in the locust [35]. In this model, the origin of AN-encoded information arising from SNs was consistent with findings in Tuthill and Wilson, 2016 [30] and locust studies [35]. However, recent findings such as AN-AN connectivity [31] and the sensory channel comparison [30] cannot be explained by this model, suggesting that the connectivity is much more complicated. However, the neurons in this model lack genetical identity for repeatedly access by modern genetical tools and thus make it hard to elaborate further from this model.

Overall, all these findings suggest that behavioral state modulation in the brain can be affected by the information transmitted by ANs, which contains both motor copy as well as integrated primary information. In particular, this is consistent with the findings relating to AN modulation on the perception and prevention of sensory confusion between states. Findings from flies and mice indicate that a certain degree of similarity exists in the organization and function of SNs and ANs (Figure 1.7). In general, SNs from both animals lack the morphological structure as of ANs to receive locally computed outputs. Thus, SNs are less likely to distinguish sensory signals from different behavioral states.

1.2 Challenges and gaps

As discussed in section 1.1, findings from insects and mammals indicate a degree of similarity in the organization and function of their motor systems. For example, SNs and ANs' general structure and function shown in Tsubouchi et al., 2017 [18], and behavior control is modularized and mediated either by distinct types of brainstem neurons in mice [36, 37] or descending neurons (DNs) in flies [38]. Therefore, the progress made in one system is potentially informative to the other and could be used to expand our knowledge about the neural mechanism of adaptive behavior and guide neuro-inspired technological applications. According to anatomical and functional studies in these organisms, the closed-loop circle proposed here in Figure 1.1 depicts the four potential parts of the neural substrate and can be used to generate and modulate an action plan. However, there are large differences in insects and mammals in the availability of resources to tackle the unanswered questions and the difficulty of experimental design needs to be addressed. Hence, the understanding of how these modules cooperate is still limited.

Technical barrier Brain function and the corresponding circuit of motor function have always attracted more attention than the spinal cord or VNC and have thus been more inten-

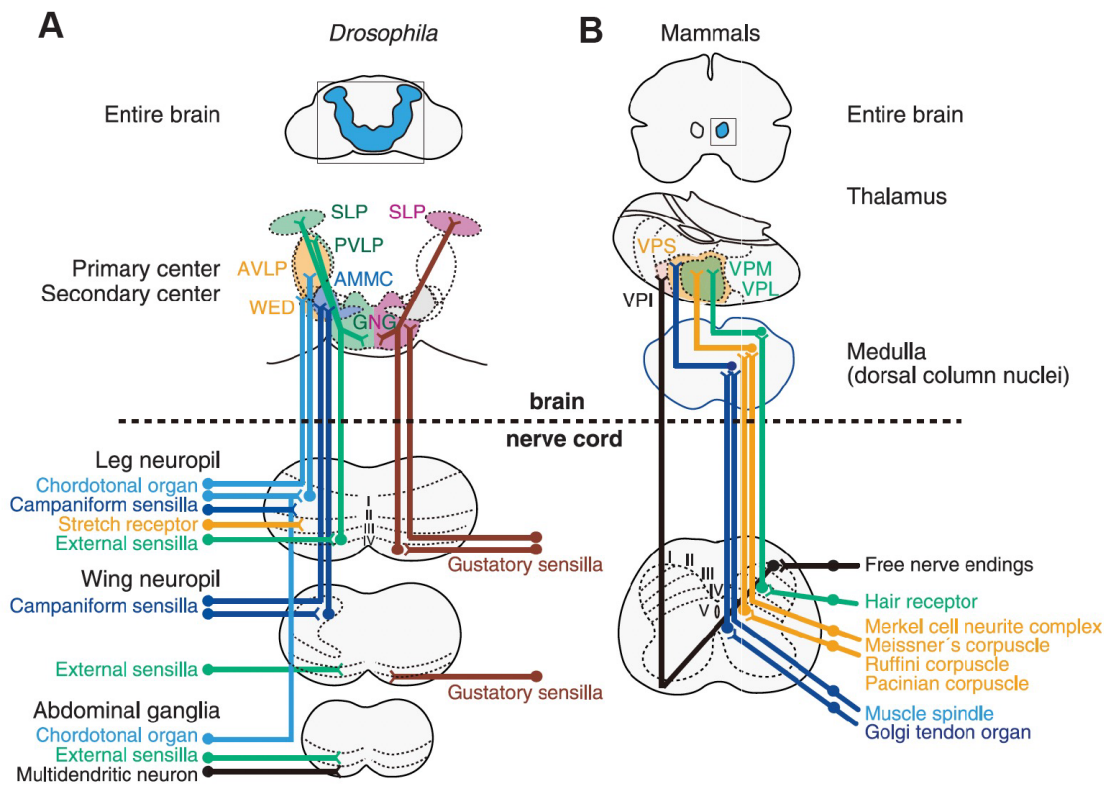


Figure 1.7: **Schematic comparison of somatosensory pathways in flies and mammals.** (A) Sensory pathways in *Drosophila* from each type of mechanosensory neuron. Note that the direct transmission from external sensilla to the brain was not found in this study [18]. (B) Known pathways in mammals. All panels and captions modified from Tsubouchi, 2017 [18].

sively studied in both flies and mice. Therefore, there are relatively more resources, such as analysis tools, experimental reagents, and techniques, available for topics related to brain function. For example, there are established techniques for *in vivo* imaging/electrophysiology in the brain of behaving animals for mice [39] and flies [7, 40, 41], extensive reagents for optogenetics [42], and an existing connectome database [43]. Hence, investigations to elaborate the understanding of brain circuits or DN function can be quickly established with a handful of ready-to-use tools.

On the contrary, the spinal cord or VNC has been explored much less due to its limited accessibility and the challenges related to recording conditions in behaving animals. For instance, efforts have been made for imaging the spinal cord in a tethered mouse [44, 45], though the required removal of the vertebral column and pia to expose the spinal cord may impair behavior, and the motion-induced movement often disrupts the recording. In insects, the current techniques are also not fully capable of studying the motor circuit in the VNC of a behaving insect. Here, intracellular recording has been demonstrated with large tethered

insects, but without the ability to track cell identity that is required to reproduce the results [35, 46, 47]. In addition, recording in the VNC requires the dissection from a fly's ventral thorax, though this sacrifices the leg function [30]. Thus, to study neural function that resides outside the brain, it will be critical to have a technical breakthrough in *in vivo* recording from the spinal cord or the VNC during behavior.

Scientific gaps After the technical breakthrough that has just been described, it will be possible to ask numerous questions regarding the function of the spinal cord or the VNC. For instance, one of the core questions in understanding adaptive behavior is how an animal generates the appropriate action in different situations. Since it has been reported that behavioral state can modulate sensory perception, the information sent from the motor system in the spinal cord or the VNC must play an important role here. Apart from the SNs, which are well known for encoding signals from a variety of sensors, the final output of locally processed information in the spinal cord or the VNC comes from ANs, which might consequently encode behavioral state [18, 32, 34]. These first insights motivate a further comprehensive investigation on what neural representation of a spectrum of behavioral states exists in AN population. Therefore, this work attempts to push current understanding by asking: (i) What information do ANs transmit to the brain? (ii) Where does that information go in the brain? (iii) Where do ANs sample the input signal? Answers to these questions can, in turn, inspire future studies focusing on neural dynamics in specific behavioral states and could potentially improve the existing algorithm for robot control, such as by modifying the subsumption architecture with a more novel representation of the robot's state [48].

1.3 Potential solutions from current resources

1.3.1 The fly as a model organism to study motor system

As discussed in [section 1.1](#), the degree of similarity in the organization and function of the motor systems in flies and mice means that, theoretically, conceptual advances in mammals can be made from a fly VNC, which is the functional equivalent to the spinal cord. Therefore, as the purpose of this work is to investigate the cellular basis of behavioral state information, *Drosophila melanogaster* was chosen to be the model animal mainly due to (i) functional and anatomical similarity to the nervous system to mammals, (ii) traceable cell identity across animals, and (iii) the smaller sized CNS is more efficient for anatomical mapping of behavioral state encoding from the VNC to the brain in comparison to a mammalian spinal cord.

Chapter 1. Introduction

Anatomy of fly ventral nerve cord (VNC)

Drosophila melanogaster is an insect with six legs, a pair of wings, and three body segments, including the head, thorax, and abdomen (Figure 1.8A). Each body part has its corresponding neuromere in the VNC, including six leg regions divided into the prothoracic, mesothoracic, metathoracic neuromere pairs located on the ventral side; one abdominal neuromere located at the posterior tip; one wing neuromere located at the dorsal side above the mesothoracic neuromeres; one haltere neuromere; and one neck neuromere (Figure 1.8B-F). The cervical connective is located at the dorsoanterior part of the VNC that connects to the brain (Figure 1.8B). Besides the neuromeres directly linked to body appendages, there are other associative regions, including the intermediate and lower tectulums and associative mesothoracic neuromere (AMN) (Figure 1.8C,E). Compared to the mouse, a higher degree of freedom with more movable body parts, such as the six legs, might indicate that fly behavior is more diverse and extensive.

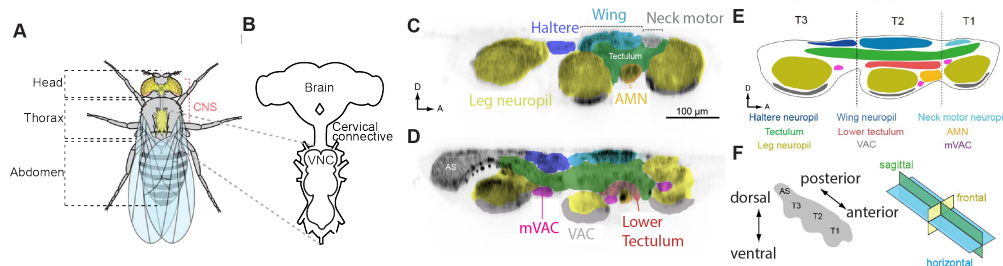


Figure 1.8: **Anatomy of the ventral nerve cord (VNC) of a fly.** (A,B) The central nervous system (CNS) of a fly consists of the brain, cervical connective, and VNC. The main body segments are indicated on the left side. A sagittal view of VNC confocal images through a (C) lateral and (D) medial plane. The colors represent our divisions of the recognized domains in the VNC: AMN, accessory mesothoracic neuropil; AS, abdominal segment; mVAC, medial ventral association center; VAC, ventral association center. (E) Schematic of the neuropils in the VNC. T1 (prothoracic segment), T2 (mesothoracic segment), T3 (metathoracic segment). (F) The body axis and sections used to describe VNC anatomy. Panel A,C-F and the corresponding captions are modified from Namiki et al, 2017 [38], and Panel B and the caption are modified from Chen et al., 2018 [49].

Fruit fly behavior and the measurement techniques

To assess the effect of neural manipulation on behavior in a fly, normally exhibited behaviors are first set as the baseline. In general, animal behavior represents a variety of actions ranging from discrete movements such as raising a limb to general states like walking. Thus, behavior can be understood as a spectrum of actions. Flies also exhibit a repertoire of behavior when alone versus when interacting in social situations. When alone, they show spontaneous behavior. In addition to resting (also called standing or posing), they spend most of their

time in locomotor behavior, which can be divided into straightforward walking, turning [49], backward walking [28, 49], and occasionally discrete and rapid exploratory motions [50]. They also spend time grooming their eyes and antennae with their forelegs, grooming their abdomen and wings with their hindlegs, and grooming their legs by rubbing against each other [51]. When necessary, they also maneuver during flight, which represents a distinct behavior from terrestrial animals.

Flies also exhibit other behaviors as part of spectrum of actions in response to external cues or during particular situations. For example, they jump or freeze when sensing the looming stimulus [12]. When interacting with other individuals, they exhibit social behavior such as approaching, limb touching, or avoiding other individuals. Moreover, they might engage in a more complex scenario like reproduction. During courtship behavior, the male fly orients to the female, performs a courtship song, taps the female with his forelegs, contacts her genitalia with his mouthparts, and then bends his abdomen to copulate [52]. The female fly may repel the approach of the male by escaping or kicking with her hindlegs [53]. Aggressive behavior is also observed in flies. Here, they combine different actions, including approaching, wing erection, foreleg lunging [54, 55], and female-specific head butting [54]. This ability to rapidly optimize the choice of reaction among various available combat skills in response to instant and overwhelming cues presented in a fighting situation also makes the fly a good model for study action selection.

However, it is still difficult to categorize behavior based on the animal's perception of what it is doing. To date, an experimenter can divide behavior into smaller action steps or group a sequence of actions into a more general behavior, though this can be arbitrary and is not necessarily physiologically meaningful [51, 56]. Hence, the way in which animal behavior is dissected is important, though remains an open question. Recent studies of descending neurons (DNs) suggest that behavioral commands function as modules [38]. In other words, the commanding signal from the brain triggers a sequence of actions grouped as one behavior rather than individual steps, such as forelimb-related grooming [57] and backward walking [28] observed in flies or tapping, grasping, and reaching observed in mice [36, 37] as opposed to controlling the individual joint angle changes required to perform these behaviors. These motion states are reported to the necessary brain regions by an efferent copy of the motor command that stems either locally from DN's in the brain [25] or from the motor center in the spinal cord [25, 27, 29] or VNC [25, 34]. However, the way in which these behavior states are reported is organized in the behavior-commanding space, which can differ from the behavioral states informed by ANs. Because what is encoded by reporting neurons—ANs might range from detailed actions, such as leg reaching during exploratory walking, to a general behavioral state, such as any movement during walking, there may be a hierarchical structure of behavioral encoding in the reporting axis of the motor system. For example, general foreleg movement encoding might also cover foreleg-rubbing encoding, which does not make sense to have a general foreleg movement command in DN's to actuate the leg without specific aim.

Chapter 1. Introduction

To study spontaneous behavior on the ground, experimental setups usually consist of an arena equipped with a camera that records video from a bird's-eye view. The video can then be used to quantify the action to be measured or the travel distance. This design can be extended to a high-throughput pipeline with a multi-chamber platform, such as Janelia's Flybowl [58]. Additionally, detailed studies on limb dynamics in spontaneous behavior can be performed on a tethered fly in a space equipped with side cameras [56]. With deep learning tools such as DeepFly3D [56] and Deeplabcut [59], joint position can be traced through video, triangulated into joint location in 3D space, and further analyzed. However, if the fly is tethered, then it might not be able to perform certain behaviors, such as wing grooming. When studying flight behavior, the fly is usually tethered to observe the dynamics of wing beat [7]. For studying the 3D trajectory of flight, a tunnel equipped with top and side cameras has also been used [60].

Overall, the complexity of fly behavior has been observed and studied in situations ranging from solitary to social. Through this progress, the relevant experimental apparatuses and analysis pipelines have also been established. However, the scientific question of how an animal perceives its body state during behavior remains open. Here, *Drosophila* can serve as a model animal because of the diversity of available genetic toolkits allow for studies quantifying the relevant neural activity and behavioral manipulation for different ethological topics.

***Drosophila* driver system**

Currently, there are three types of driver systems for tissue-specific manipulation in *Drosophila melanogaster*, among which the GAL4-UAS system is the most common. GAL4 is a transcription activator protein in yeast that comes from the GAL gene family [61]. In principle, it recognizes a specific upstream activation sequence (UAS) in the genome and binds to it via its DNA-binding domain (DBD) to allow its activation domain (AD) to initiate transcription of the downstream DNA sequence (Figure 1.9A) [62–64]. This transcription tool has been randomly inserted into the *Drosophila* genome [64], where GAL4 gene is a downstream to an enhancer or promoter to enhance tissue-specific gene expression. Using this genetical engineered flies to examine neuron expression patterns has led to the creation of a library of nervous-system-specific driver systems for neurobiology research [65]. With the same manipulation, UAS can be conjugated with any target gene and then inserted into genome to enable the tissue-specific expression driven by GAL4. For example, UAS-RNAi [66] has been used in a loss-of-function study [66], UAS-GFP [67] for cell labelling, UAS-GCaMP [68] for monitoring calcium intensity, and UAS-ChR2 [42] or UAS-CsChrimson [69] for rapidly manipulating the excitability of a cell. In practice, the GAL4 strain and the UAS strain are kept separate and thus can be immediately crossed in various combinations to yield the desired GAL4-UAS offspring (Figure 1.9B).

To further restrict the labeling pattern, a split-GAL4 system can create driver lines with cleaner labeling patterns for long-term use [63]. In this system, the AD and DBD of the GAL4 gene are split and inserted at downstream from two different tissue-specific promoters (Figure 1.10).

1.3 Potential solutions from current resources

Therefore, the GAL4 can only restore transcription function at the UAS site in cells expressing both enhancer genes, restricting the labeling pattern to the intersection between the two original GAL4 lines. Cells can also be sparsely targeted via random expression, such as with the Multi-Color Flip-out (MCFO) [70] or Mosaic Analysis with a Repressive Cell Marker (MARCM) [71] labelling systems.

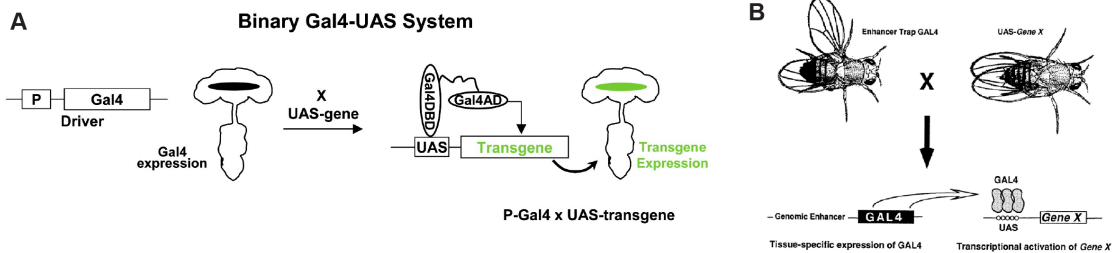


Figure 1.9: **GAL4-UAS driver system.** (A) Diagram showing the simplified working principle of the GAL4-UAS system. GAL4 gene is inserted downstream to a tissue-specific promoter (P) and is thus expressed in a distinct sub-population of brain neurons. After the UAS is introduced into the genome, GAL4 can recognize the sequence and bind to it via the DNA-binding domain (DBD). The downstream transgene transcription can then be initiated by the activation domain (AD). Thus, the expression of the transgene is constrained by the specificity of the promoter. Modified from Luan et al., 2006 [63]. (B) Practical example of the GAL4-UAS system used to set up a cross between GAL4 male and UAS female flies to collect their offspring, which inherit both GAL4 and UAS in their genome. Hence, the targeted cells can express the transgene product of interest. Modified from Brand and Perrimon, 1993 [64].

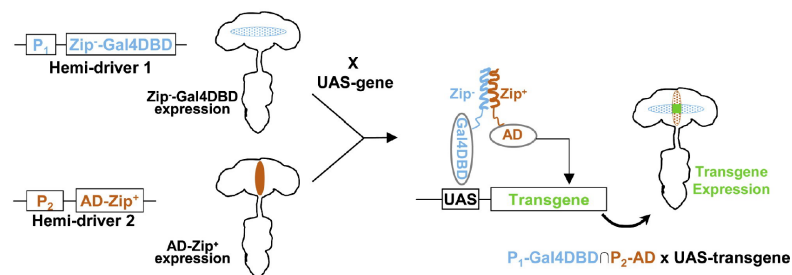


Figure 1.10: **Split-GAL4 expression system.** A diagram showing the working principle of the split-GAL4/UAS system. The split-GAL4 gene is engineered such that the Zip tag is inserted downstream from two different promoters (P₁ and P₂). After UAS is introduced into the genome, split-GAL4DBD binds to UAS. To initiate the downstream transgene expression, the Zip tag recruits AD to the DBD to form a functional GAL4. Therefore, only cells expressing both promoters can assemble the AD and DBD at the UAS site, and this activation occurring only in the intersection of expression patterns between two promoters ensures the sparsity of the labeling. Modified from Luan et al., 2006 [63].

Finally, GAL4-UAS is not the only driver system. Similar expression tools are available as alternatives and enable orthogonal expression to study the interaction between cells with different enhancers. These other known systems are *lex-lexAOP* [72] and *QF-QUAS* [73].

1.3.2 Experimental techniques

Two-photon functional imaging

A standard method for measuring the neural dynamics in a behaving fly is *in vivo* imaging of neural activity-related fluorescence, which was invented in 1990 [74]. Two-photon microscopy mainly consists of three elements: (i) two-photon laser excitation, (ii) fluorophore reflection of neural activity, and (iii) laser scanning microscopy.

Two-photon absorption is a phenomenon wherein two photons of the same frequency are absorbed simultaneously by a fluorophore, which then reaches a higher excited state than would occur from the absorption of a single photon (**Figure 1.11A,B**) [75, 76]. Returning to the ground state from the excited state then causes a photon to be released, which generates the fluorescence [75]. Hence, fluorophore excitation occurs only at the focal volume, where there is a much higher probability of two-photon absorption. In contrast, one-photon excitation excites all molecules along the path of the laser beam (**Figure 1.11C,D**) [75, 76]. To balance waveform distortion through the tissue and maximize the chance of two-photon absorption, a Ti:sapphire laser is usually used to generate laser pulses at ≈ 100 MHz with an optimized length of 100 fs. In general, the conventional technique of two-photon excitation relies on infrared or near-infrared lasers to generate localized excitation, hence it is less susceptible to tissue-scattering and phototoxicity [76].

As a reporter to reflect the neural activity-related signal, genetically encoded calcium indicator (GECIs) is commonly used. When a neuron is excited, an action potential opens the calcium channels, leading to electrochemical gradient-induced calcium influx due to the concentration, which is higher outside and lower inside the cell [77]. Thus, the signal reflected by GECIs is an indirect readout of neural activity. A popular GECI is GCaMP, which is a fusion protein assembled from a calcium chelator complex and a circularly permuted EGFP (cpEGFP) domain (**Figure 1.12**) [68, 78–80]. The calcium chelator complex, consisting of an M13 peptide and a calmodulin domain, can bind to calcium ions to trigger a conformation change of the indicator. The conformation change then restores the fluorescence ability of the cpEGFP, which can be excited at 488 nm to emit green fluorescence (**Figure 1.12**). In general, GCaMP has slow dynamics, which result in low temporal resolution. Compared to the length of an action potential, which is ≈ 2 ms [81], GCaMP6f takes ≈ 0.2 s to rise to the peak with a decay half-life of ≈ 0.2 s [68]. An alternative for more accurately capturing the dynamics of membrane potential is genetically encoded voltage indicators (GEVIs), though these tend to have a lower signal-to-noise-ratio (SNR) than GECIs [82].

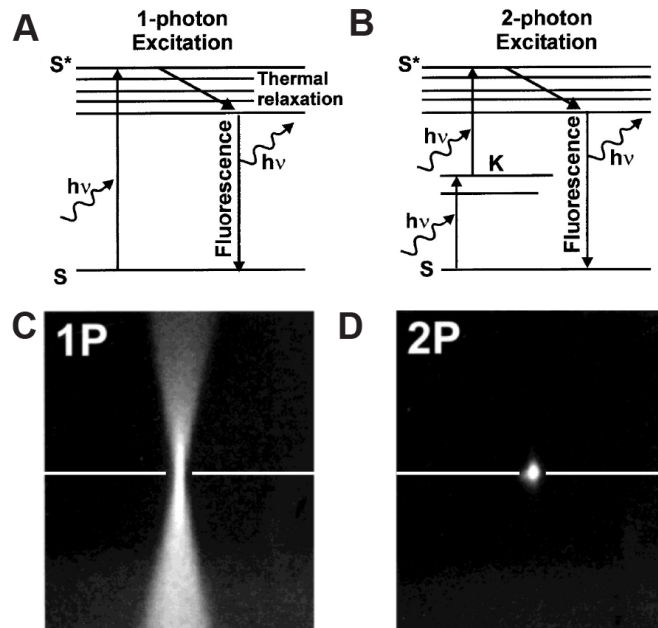


Figure 1.11: **Principle of one-photon and two-photon excitation.** The diagram shows the simplified working principle of (A) one-photon and (B) two-photon excitation from the ground state (s) to the excited state (s^*) by the energy ($h\nu$), such as that from a laser. Energy loss during the return to the ground state results in the emission of a photon with a longer wavelength than the excited photon. Fluorescence emission in a solution of fluorescein induced by (C) one-photon and (D) two-photon excitation. Note that in the latter, the fluorescence is only generated at the focal volume where the two-photon absorption occurs, in contrast to the former, wherein fluorescence is generated along the light path of the laser beam for one-photon excitation. The white line depicts the assumed focal plane. Modified from Soeller and Cannel, 1999 [75].

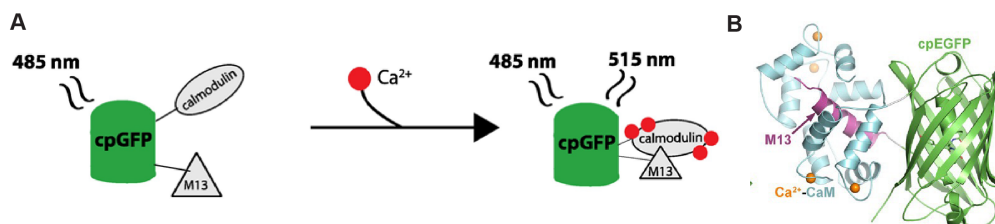


Figure 1.12: **Genetically encoded calcium indicator—GCaMP.** (A) Schematic of the fluorescence mechanism of GCaMP. When the calcium-binding domain calmodulin binds to calcium ions, a conformational change is induced within the M13 domain, restoring the fluorescence ability of cpGFP and allowing it to emit green light. Modified from Girven and Sparta, 2016 [79]. (B) Molecular structure of GCaMP. Modified from Akerboom et al., 2019 [80]

Laser scanning microscopy has several key features that enable the accurate imaging of fluorescent specimens. To start, the scanning modules of the microscope enable signal acquisition

across a region-of-interest (ROI). In principle, these modules move the focal volume across the area, and the corresponding fluorescence signal is recorded to reconstruct the image. The key components of laser scanning microscopy include XY-scanning mirrors to change the angle of the laser, the dichroic mirror to segregate the excitation and emission light, and a photomultiplier tube (PMT) to convert photons into an electric current (**Figure 1.13A**) [76, 83]. The XY-scanning mirrors rotate to change the angle of the reflection of the laser beam, which in turn translocates the focal volume across the sample. The machinery to rotate the scanning mirror can be modified by different motors, for example, Galvo-Galvo or Galvo-Resonance, to reach different scanning speeds in a trade-off between scanning speed and duration of photon accumulation on the PMTs, a measurement termed pixel dwell time. As long as two-photon absorption occurs, the emitted photons scatter into either epi-fluorescence, which are the photons that travel towards the sides of the objective lens, or trans-fluorescence, which are photons that move away from the objective lens and cross the specimen. Because the signal is weak, both epi- and trans-fluorescence are passed to the PMTs. Here, the dichroic mirror in the light path of the excitation laser selectively reflects epi-fluorescence to the PMT from the mixed light path. Within the PMTs, primary electrons are generated via the photoelectric effect at the photocathode. Then their number is multiplied through secondary electron emission, a cascade of interactions between electrons and the dynode to generate more electrons at each impact. Finally, this amplified number of electrons arrive at the anode to induce a sharp current pulse that can be detected by, for example, the oscilloscope (**Figure 1.13B**) [84].

In summary, two-photon scanning microscopy can produce signals with a higher SNR compared to one-photon imaging. The signal's waveform and SNR can also differ based on the properties of the fluorophore, such as sensitivity or kinetics of conformation change.

Spherical treadmill and mounting stage

To image the neural dynamics in flies via two-photon scanning microscopy with cellular resolution, it is typical to tether the animal. Seelig et al., 2010 [40] introduced a setup wherein a head-fixed fly can walk on an air-supported foam ball with an optically accessible window to the brain (**Figure 1.14A,B**). Therefore, two-photon imaging in the brain can be performed while simultaneously recording the fly's behavior. The foam ball is dotted with ink, so the movement of the markers can be detected by optical flow sensors and translated into ball rotation and travel path.

To expose the brain for imaging, the dorsal cuticle of the head is removed before mounting the fly to the two-photon setup. The fly is fixed at the ventral side of the holder, with the dorsal part of the head passing through the dissection window. The dissection side of the holder contains a solution that mimics the ion composition of the extracellular fluid in the nervous system (**Figure 1.14B,C**) [7, 40]. Because both dissection and imaging are performed in the

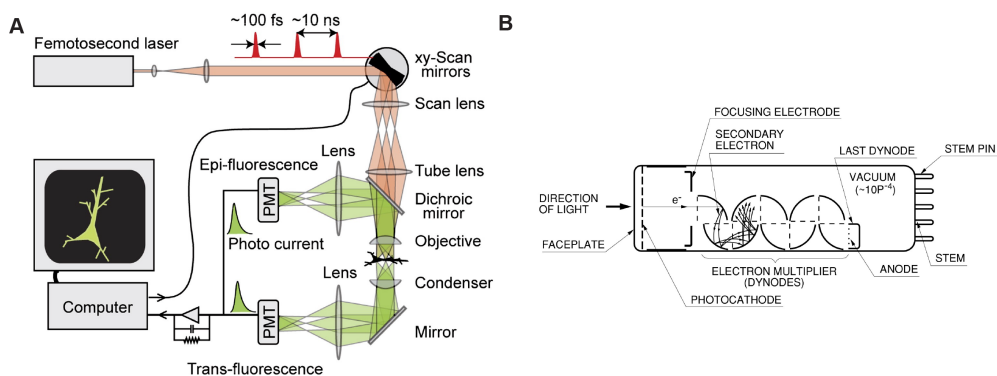


Figure 1.13: **Two-photon laser scanning microscopy and photomultiplier tube.** (A) Schematic of a two-photon microscope with epi- and trans-fluorescence detection. High instantaneous intensities of excitation light (≈ 100 fs length and ≈ 10 ns interval) are generated. The reflection angle of the scanning mirror translocates the focal point position on the specimen. The emitted fluorescence is directed to the PMT for photon-electron conversion and amplification. A dichroic mirror is implemented at the light path of the excitation laser to isolate epi-fluorescence. Modified from Svoboda and Yasuda, 2006 [76]. (B) Schematics of working principle of a photomultiplier tube. Light enters from the input window and strikes the photocathode to release electrons into the vacuum via the photoelectric effect. The emitted photoelectrons then arrive at the first dynode, where the number of electrons is multiplied by secondary electron emission. The amplification carries on through the dynode chain and finally reaches the anode to induce a detectable current as the readout. Modified from Hamamatsu Photonics K.K, 2007 [84].

ion solution to maintain neurophysiological function, a water-immersion objective should be used.

1.4 Aims

Apart from the enormous progress made in quantifying fly behavior, there is still no technique for recording neural activity in the VNC of a fly during behavior that is comparable to that used in the brain. This lack of appropriate tools constrains further understanding of how the thoracic circuit orchestrates limb movements. Hence, this work aims to overcome this gap by:

Aim1: Developing a preparation method to obtain optical access to the VNC of a tethered fly for imaging neural activity while behaving ([chapter 2](#)) that can be adapted for two-photon microscopy [76] and the spherical treadmill [40].

The application of this novel preparation to other experiments is also demonstrated via two collaborative projects discussed in [chapter 4](#) and [chapter 5](#).

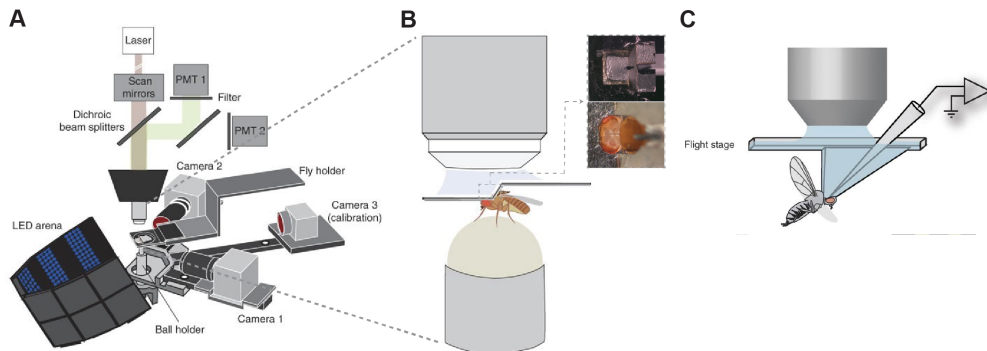


Figure 1.14: **Experimental setups for recording neural activity in behaving flies.** (A) A setup equipped with optical flow sensors (cameras 1 and 2), two-photon microscopy, and a spherical treadmill for imaging brain activity in a fly behaving on an air-supported ball (B). The LED screen visually induces the movement of the fly. The inset shows the view from the dissection window of the mounting stage. Modified from Seelig et al., 2010 [40] (C) The fly brain recording chamber coupled with patch-clamp technique to study flight. Modified from Maimon et al., 2010 [7]

To understand adaptive behavior generation in the context of the motor dynamic closed loop, it is critical to understand how information integrates with behavioral state signals in the brain. However, the operation of the key players in the motor system, including the content, the origin, and the downstream receivers, remains unclear. Compared to SNs, ANs have a more complex morphology and connectivity and thus might encode behavioral states arising from local signal processing. Thus, with the technological breakthrough from **Aim1**, this work also uses a systemic approach to answer existing questions about the functionality of ANs via:

Aim2: A large-scale screen to investigate the functional encoding of ANs in the behaving fly and the corresponding morphological characteristics (**chapter 3**).

2 Imaging neural activity in the ventral nerve cord of behaving adult *Drosophila*

Disclaimer: This chapter is reproduced from the following article with permissions of all co-authors and journal.

Chin-Lin Chen¹, Laura Hermans¹, Meera C. Viswanathan, Denis Fortun, Florian Aymanns, Michael Unser, Anthony Cammarato, Michael H. Dickinson, Pavan Ramdya. "Imaging neural activity in the ventral nerve cord of behaving adult *Drosophila*", *Nature Communications*, vol.9, pp.4390, 2018. <https://doi.org/10.1038/s41467-018-06857-z>

¹These authors contribute equally.

My contribution: Performing experiments for (i) comparing the locomotion in flies with and without thoracic dissection to confirm that dissected flies still exhibit behavior with comparable quality within 30 minutes after dissection, (ii) summarizing the success rate of the dissection for two-photon imaging calculated from all operations, (iii) examining the expression pattern of *MDN*, *MAN*, and *A1-GAL4* lines in the brain and the VNC, (iv) examining the GFP expression driven by flight muscle promoter in the central nervous system and the legs to ensure that the programmed cell death only occurs in flight muscles, (v) checking the locomotion in flies with and without genetic removal of flight muscles by laser heat-induced locomotion to confirm that behavior of both groups is comparable. Developing analysis pipelines for (i) semi-auto segmenting regions-of-interest in two-photon image stacks from recordings of *MDN*, *MAN*, and *A1-GAL4* lines and extracting their fluorescence value, (ii) synchronizing the fluorescence data, ball rotation, and behavioral photos to generate a dataset for further quantification, and (iv) visualizing the experimental recordings in videos. Overall, my contribution mainly focused on the control experiments to prove that this novel method is feasible and of good quality in the imaging data and flies behavior and on developing the analysis pipeline for this experimental setup.

2.1 Abstract

To understand neural circuits that control limbs, one must measure their activity during behavior. Until now this goal has been challenging, because limb premotor and motor circuits have been largely inaccessible for large-scale recordings in intact, moving animals – a constraint that is true for both vertebrate and invertebrate models. Here, we introduce a method for 2-photon functional imaging from the ventral nerve cord (VNC) of behaving adult *Drosophila melanogaster*. We use this method to reveal patterns of activity across nerve cord populations during grooming and walking and to uncover the functional encoding of moonwalker ascending neurons (MANs), moonwalker descending neurons (MDNs), and a novel class of locomotion-associated A1 descending neurons. Finally, we develop a genetic reagent to destroy the indirect flight muscles and to facilitate experimental access to the VNC. Taken together, these new approaches enable the direct investigation of circuits associated with complex limb movements.

2.2 Introduction

Limbs allow animals to rapidly navigate complex terrain, groom, manipulate objects, and communicate. In vertebrates, neural circuits in the spinal cord coordinate the actions of each arm or leg. Thoracic circuits perform comparable tasks in insects [85]. The thoracic segments of the fruit fly, *Drosophila melanogaster*, house the ventral nerve cord (VNC) which is a fusion of three thoracic and eight abdominal ganglia. The VNC contains six spherical neuromeres, each controlling one leg, a flat dorsal neuropil associated with the neck, wing, and halteres, and a set of intermediate neuropils including the tectulum that may coordinate the action of the legs and wings [86]. Also within the thoracic VNC are descending [38] and ascending [18] axons that connect the VNC and the brain. These tracts run through the neck or cervical connective, which – like the VNC – is inaccessible in most preparations.

In recent years, the VNC of adult *Drosophila* has gained attention as the site where some higher-order decisions are transformed into actions. Adult flies engage in complex limbed behaviors including walking [21,87], reaching [88], escape jumping [89], courtship tapping [90], aggressive boxing [91], and grooming [92]. Our current understanding of how thoracic circuits coordinate these actions is entirely based on behavioral genetics or recordings from a few neurons in tissue explants [34], immobilized animals [30,93,94], or sharp electrode studies in larger insects [46,47].

To fully understand how thoracic circuits orchestrate limb movements, it is necessary to record the activity of individual cells and populations of neurons during behavior. To date, these experiments have not been performed in *Drosophila* due to the difficulty of accessing the VNC in intact, behaving animals. Here we describe a preparation that overcomes this obstacle and makes it possible to record the dynamic activity of populations and sparse sets of individual

neurons within adult thoracic circuits during walking, grooming, and other actions involving limb movement.

2.3 Results

2.3.1 A dissection for accessing the ventral nerve cord

The VNC lies on the thoracic sternum – a cuticular structure that anchors the leg muscles and the proximal leg segments to the thorax (**Figure 2.1**). Consequently, it is difficult to access the VNC by removing ventral thoracic cuticle without destroying musculoskeletal elements required for limb movement. We chose instead to access the VNC dorsally at the expense of flight-related behaviors [7]. This approach requires removing the prescutum and scutum of the dorsal thoracic cuticle, the indirect flight muscles (IFMs), and transecting the proventriculus, crop, and salivary glands of the gut (**Figure 2.1**, **Figure S2.1**, see Methods).

Using this technique, it is possible to uncover the VNC for functional imaging in flies that are still capable of exhibiting robust behavior, such as walking and grooming, for up to at least 4 h. In one round of studies ($n = 46$ flies) by a newly trained experimenter 46% of animals produced behaviors, 26% had limb movement deficiencies, and 28% were incapacitated. When comparing walking behaviors between flies with or without a thoracic dissection, we found that dissected flies generate locomotor bouts with likelihoods and velocities within the range of those observed in non-dissected animals (**Figure S2.2**; $n = 20$ dissected and 20 non-dissected flies). We note, however, that there are more examples of highly active non-dissected animals. We also found that, on average, dissected animals generate longer bouts (**Figure S2.2b**; $P < 0.05$ Mann-Whitney U -test). This may be due to the fact that we only recorded from dissected animals that produced limb movements in response to touch or puffs of air. Therefore, they may also have been among those in a higher state of arousal.

Next, to illustrate the extent of optical access, we drove expression of the genetically encoded calcium indicator, GCaMP6s [68], together with tdTomato [95] — a fluorophore that serves as an anatomical fiduciary — throughout the entire nervous system ($GMR57C10 > GCaMP6s; tdTomato$) [65], (**Figure 2.1b, d-g** and **Video S2.1**). To perform 2-photon microscopy in semi-intact, behaving animals, we constructed a customized fly holder and spherical treadmill (**Figure S2.3**) that, in contrast to previous methods used to record neural activity in the brain [7, 40, 96], permits optical access to the VNC along with unobstructed videography of limb movements.

2.3.2 Imaging the activity of populations of neurons in the VNC

By scanning horizontal x-y image planes in animals expressing GCaMP6s and tdTomato pan-neuronally ($GMR57C10 > GCaMP6s; tdTomato$), we could record the detailed time course of

Chapter 2. Imaging neural activity in the ventral nerve cord of behaving adult *Drosophila*

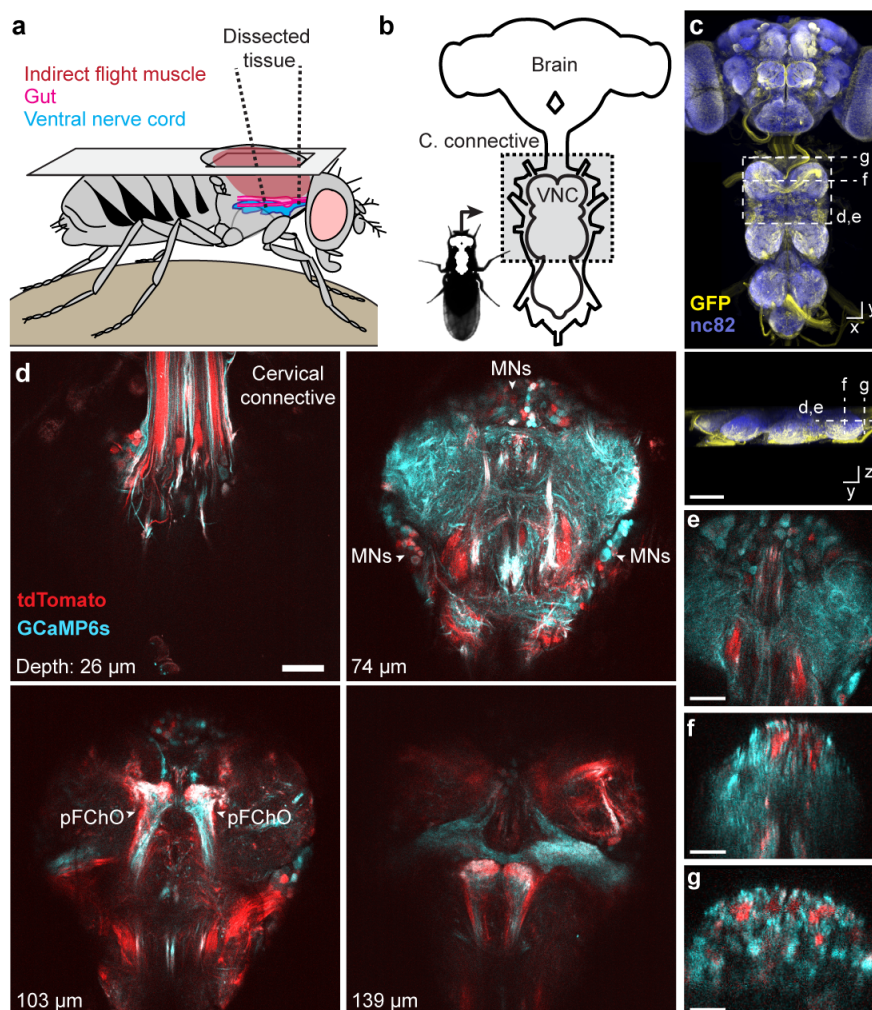


Figure 2.1: **Dissection for imaging the adult *Drosophila* ventral nerve cord (VNC).** (a) Schematic of the dorsal thoracic dissection. (b) Overview of newly accessible nervous tissue following thoracic dissection. (c) Confocal image of pan-neuronal driver line expression in the brain and VNC. Scale bar is 90 μm . GFP (yellow) and neuropil (nc82, blue) are labelled. Dashed lines highlight the horizontal and coronal imaging modalities used in this study. (d) Horizontal sections of the VNC imaged at different depths in an animal expressing GCaMP6s (cyan) and tdTomato (red) throughout the nervous system (*GMR57C10>GCaMP6s; tdTomato*). Motor neuron (MNs) cell bodies and prothoracic femoral chordotonal organ (pFChO) axon terminals are indicated (white arrowheads). Scale bar is 30 μm . (e) Horizontal section imaging of the VNC. Scale bar is 35 μm . (f) Coronal section imaging of the prothoracic neuromere. Scale bar is 50 μm . (g) Coronal section imaging of the cervical connective. Scale bar is 35 μm . Images in e-g were taken from flies expressing GCaMP6s and tdTomato throughout the nervous system (*GMR57C10>GCaMP6s; tdTomato*).

neural activity in the prothoracic neuromere during walking and grooming (Figure 2.1c, e and Video S2.2). Alternatively, we could use a piezo-driven objective to scan coronal x-z image

planes. These coronal sections allowed us to simultaneously record neural activity across different depths of the VNC corresponding to distinct layers housing sensory neuron axons [18], interneurons [30], and motor neuron dendrites [97] (Figure 2.1c, f and [or to monitor activity patterns across populations of descending [28, 38] and ascending fibers [18, 28, 34] within the thoracic cervical connective (Figure 2.1c, g and Video S2.4). Thus, we confirmed that our new preparation provides optical access to previously inaccessible thoracic neural populations in behaving adult flies.

During behavior, the VNC moves and deforms. To overcome these image analysis obstacles, we used a non-parametric, variational image registration approach, designed to model arbitrarily complex deformations (Figure S2.4 and Video S2.5, see Methods). After successful image registration, we used a semi-automated approach to annotate walking and grooming behaviors (Video S2.6, see Methods) and regressed these two datasets to identify VNC regions whose activities correlated with walking and grooming (Figure 2.2). We anticipate that further improvements in image registration will make it possible to build similar behavior-function maps from dense neural population imaging data in which the activity patterns of individual neurons can be identified.

2.3.3 Imaging the activity of sparse sets of neurons in the VNC

Using *Drosophila*, it is possible to repeatedly and systematically investigate the functional properties of sparse sets of genetically-identifiable neurons. In a recent study, a thermogenetic activation screen was used to identify a pair of descending neurons – Moonwalker Descending Neurons (MDNs) – that cause flies to walk backwards [28]. Additionally, concurrent thermogenetic activation of ascending neurons that project from the VNC to the brain – Moonwalker Ascending Neurons (MANs) – resulted in even more sustained backwards walking, perhaps by arresting forward walking [28]. Although these activation experiments show that MDNs and MANs play an important role in the control of backwards walking, their native activity patterns and the means by which they regulate or encode limb movements remain unknown.

Because MAN and MDN axons terminate in the gnathal ganglia (GNG) and the VNC – both relatively inaccessible regions of the nervous system – it is difficult to record the activity of these cells during behavior. We used our functional imaging approach to overcome this challenge and recorded the activity of ascending and descending neurons within the VNC. To overcome vertical movement artifacts associated with walking, we performed coronal section imaging of their axons within the cervical connective (e.g., Figure 2.3a).

2.3.4 Activity patterns of moonwalker ascending neurons

Using this approach, MAN axons are visible as small ellipses (Figure 2.3b). The MAN split-GAL4 line we used drives expression of GCaMP6s and tdTomato (*MAN>GCaMP6s; tdTomato*)

Chapter 2. Imaging neural activity in the ventral nerve cord of behaving adult *Drosophila*

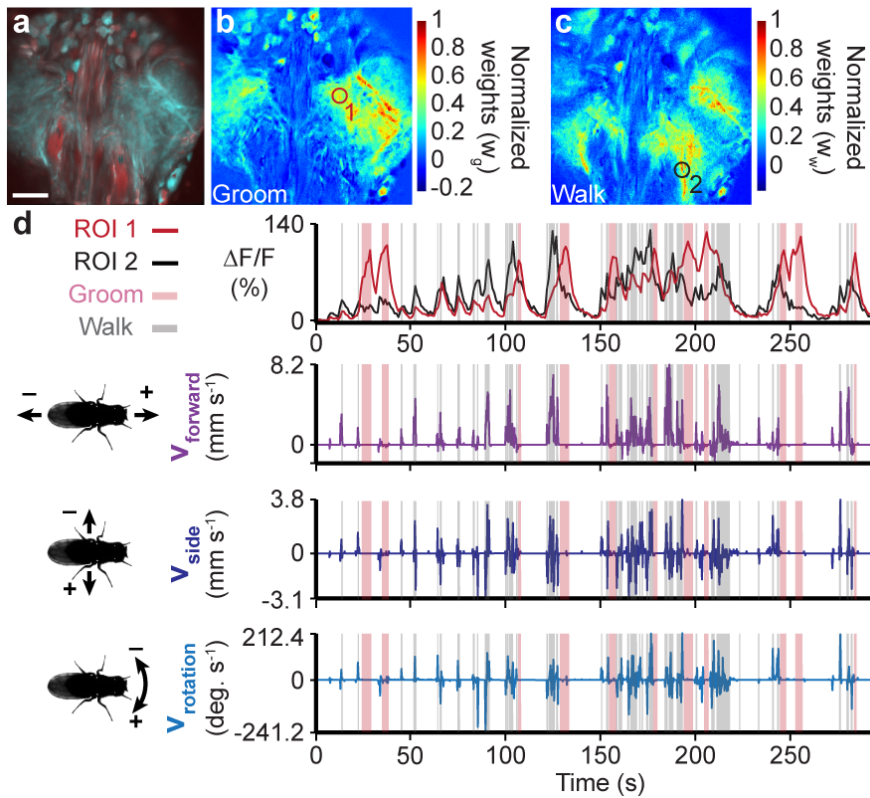


Figure 2.2: Recording populations of neurons in the VNC during behavior. (a) Standard deviation time projection for an experiment performing horizontal section imaging of the VNC. Scale bar is 35 μm . (b-c) Heat maps of linear regression weights w_g and w_w showing the pixel-wise relationships between fluorescence traces and (b) grooming or (c) walking, respectively. Weights are normalized to the maximum for each image. Data are from the experiment shown in panel a. (d) ROI-associated fluorescence traces (red from panel b, black from panel c) (**top**). Shaded regions indicate semi-automatically detected bouts of grooming (pink) or walking (gray). Corresponding forward, sideways, and rotational velocities of the fly (**bottom**).

in a pair of dorsal and a pair of ventral neurons. We focused our analysis on the dorsal pair of neurons – hereafter referred to as dMANs – because they showed conspicuous changes in activity (Figure 2.3c). The activity of left and right dMANs were strongly correlated (Figure S2.5a; Pearson’s $r = 0.96 \pm 0.01$, $n = 5$ flies), allowing us to study their collective response properties. Specifically, we automatically identified the occurrence of transient increases in dMAN fluorescence – referred to as ‘events’ – and examined corresponding behaviors reflected by rotations of the spherical treadmill (see Methods). Our analysis revealed that dMAN events were associated with rapid bimodal anterior-posterior rotations of the spherical treadmill (Figure 2.3d, $n = 746$ left and 748 right dMAN events from 9773 s of data from 5 flies). Through close inspection of the video data, we observed that these rotations occur when flies extend all six legs to push down on the spherical treadmill (Video S2.7 and Video S2.8).

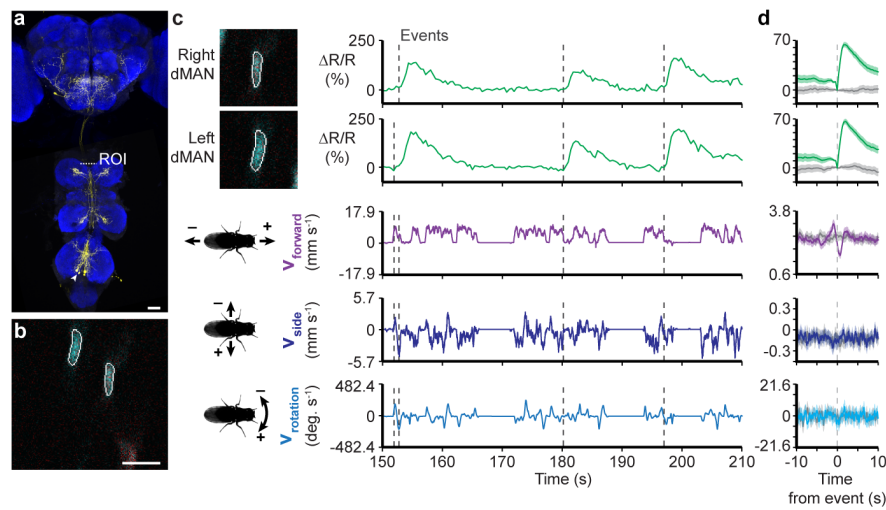


Figure 2.3: **Recording the activity of dorsal Moonwalker Ascending Neurons (dMANs) in the thoracic cervical connective during behavior.** (a) Confocal image of *MAN-GAL4* driver line expression in the brain and VNC. Scale bar is $40\ \mu\text{m}$. Neuronal GFP (yellow) and neuropil (nc82, blue) are labelled. A dashed white line highlights the thoracic x-z plane imaged. (b) Coronal section of the thoracic cervical connective in an animal expressing GCaMP6s (cyan) and tdTomato (red) in MANs (*MAN>GCaMP6s; tdTomato*). Scale bar is $3.5\ \mu\text{m}$. (c) Separated ROIs (**top-left**) and associated fluorescence signals from right and left dMANs (**top-right**). Corresponding forward, sideways, and rotational velocities of the fly (**bottom-right**). Events are indicated as dashed gray lines. (d) Summary of dMAN activity and spherical treadmill rotations with respect to fluorescence events aligned to 0 s (dashed gray line). Control data in which events are time-shuffled are overlaid in gray. Shown are the means (solid line) and bootstrapped 95% confidence intervals (transparencies).

2.3.5 Activity patterns of moonwalker descending neurons

Next, we asked to what extent MDNs are active during periods of backwards walking, a possibility suggested by behavioral responses to thermogenetic [28] and optogenetic [98] MDN stimulation. To address this question, we performed coronal section imaging of the thoracic cervical connective in flies expressing GCaMP6s and tdTomato in MDNs (*MDN-1>GCaMP6s; tdTomato*) (Figure 2.4a-b). As for dMANs, left and right MDN activity patterns were strongly correlated (Figure 2.4c), allowing us to study their collective response properties (Figure S2.5b; Pearson's $r = 0.93 \pm 0.001$, $n = 3$ flies). As predicted, MDNs became active prior to anterior rotations of the spherical treadmill, corresponding to brief episodes of backward walking (Figure 2.4c-d, $n = 900$ left and 900 right MDN events from 3 flies and 7790 s of data; Video S2.9 and Video S2.10).

Chapter 2. Imaging neural activity in the ventral nerve cord of behaving adult *Drosophila*

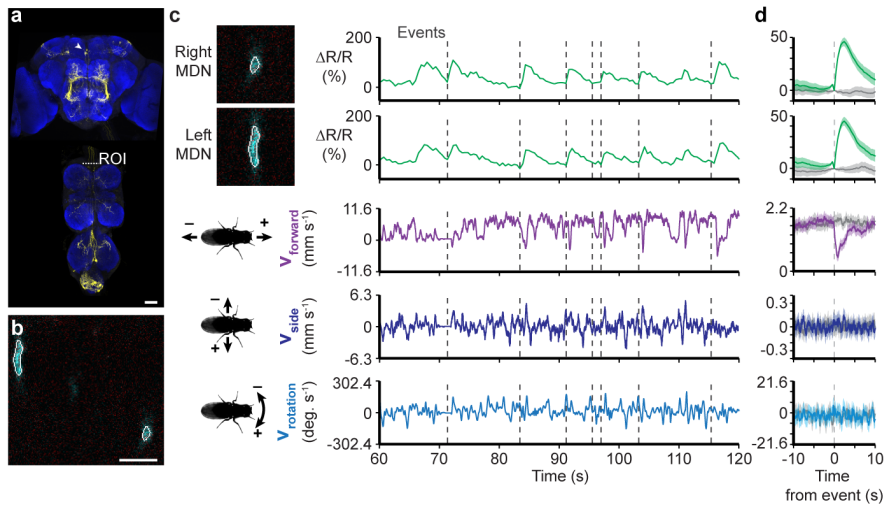


Figure 2.4: Recording the activity of Moonwalker Descending Neurons (MDNs) in the thoracic cervical connective during behavior. (a) Confocal image of *MDN-1-GAL4* driver line expression in the brain and VNC. Scale bar is $40 \mu\text{m}$. Neuronal GFP (yellow) and neuropil (nc82, blue) are labelled. A dashed white line highlights the thoracic x-z plane imaged. (b) Coronal section of the thoracic cervical connective in an animal expressing GCaMP6s (cyan) and tdTomato (red) in Moonwalker Descending Neurons (*MDN-1>GCaMP6s; tdTomato*). Scale bar is $6 \mu\text{m}$. (c) Separated ROIs (top-left) and associated fluorescence signals from right and left MDNs (top-right). Corresponding forward, sideways, and rotational velocities of the fly (bottom-right). Events are indicated as dashed gray lines. (d) Summary of MDN activity and spherical treadmill rotations with respect to fluorescence events aligned to 0 s (dashed gray line). Control data in which events are time-shuffled are overlaid in gray. Shown are the means (solid line) and bootstrapped 95% confidence intervals (transparencies).

2.3.6 Activity patterns of novel descending neurons

In addition to resolving the functional properties of previously identified neurons, our method can facilitate the discovery of novel cell classes that are active during walking, grooming, and other behaviors involving the limbs or abdomen. As a proof-of-concept, we selected four split-GAL4 lines [63] that drive sparse expression in pairs of descending neurons [38] whose axons project to leg neuromeres in the VNC (classes DNa01, DNb06, DNg10, and DNg13). We did not observe fluorescence responses during grooming or locomotion in DNg10, or DNg13 cells. DNb06 activity appeared to be only partially correlated with locomotion. By contrast, we observed that DNa01 neurons – hereon referred to as A1 cells – had activity patterns that were clearly linked to locomotor behaviors (*A1>GCaMP6s; tdTomato*) (Figure 2.5a-b and Video S2.11). The activity of left and right A1 neurons were not highly correlated (Figure 2.5c and Figure S2.5c; Pearson's $r = 0.53 \pm 0.17$, $n = 4$ flies). Therefore, we investigated the response properties of the left and right cells separately. We found that although the activities of both cells are linked to forward walking, events associated only with left A1 activity were correlated

with negative medial-lateral and yaw rotations, or leftward turning by the fly (Figure 2.5d and Video S2.12; $n = 1644$ events from 4 flies and 8784 s of data). As expected from bilateral symmetry, activity in the right \neg A1 neuron coincided with positive medial-lateral and yaw rotations, or rightward turning (Figure 2.5e and Video S2.13; $n = 1651$ events from 4 flies and 8784 s of data).

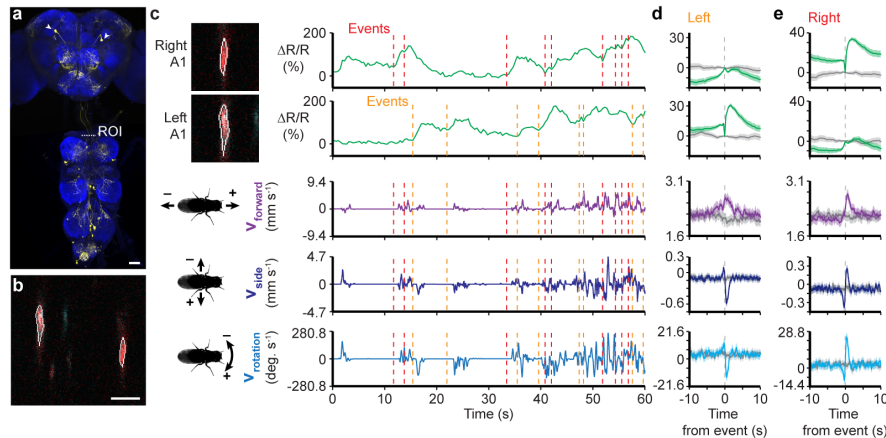


Figure 2.5: **Recording the activity of A1 neurons in the thoracic cervical connective during behavior.** (a) Confocal image of *DN0a1-GAL4* driver line expression in the brain and VNC. Scale bar is $40 \mu\text{m}$. Neuronal GFP (yellow) and neuropil (nc82, blue) are labelled. A dashed white line highlights the thoracic x-z plane imaged. (b) Coronal section of the thoracic cervical connective in an animal expressing GCaMP6s (cyan) and tdTomato (red) in A1 neurons (*A1>GCaMP6s; tdTomato*). Scale bar is $5 \mu\text{m}$. (c) Separated ROIs (top-left) and associated fluorescence signals from right and left A1 neurons (top-right). Corresponding forward, sideways, and rotational velocities of the fly (bottom-right). Events are indicated as dashed red and orange lines for right and left A1 neuron events, respectively. (d-e) Summary of A1 neural activity and spherical treadmill rotations with respect to (d) left or (e) right A1 neuron fluorescence events aligned to 0 s (dashed gray line). Control data in which events are time-shuffled are overlaid in gray. Shown are the means (solid line) and bootstrapped 95% confidence intervals (transparencies).

2.3.7 Facilitating access to the VNC by inducing cell death in IFMs

Our approach for recording neural activity in the VNC of behaving *Drosophila* opens up many new avenues for studying premotor and motor circuits. Nevertheless, we can envision further improvements that will accelerate the study of the thoracic nervous system. For example, in our preparation we found it challenging and time-consuming to remove indirect flight muscles (IFMs) that fill most of the thorax. Although large, these muscles are quite fragile and tend to disintegrate over several hours after the cuticle of the notum is removed. However, to increase the speed and efficiency of our dissection, we devised a transgenic strategy to selectively ablate IFMs. We drove the expression of Reaper – a protein involved in apoptosis [99] – in IFMs using a 5' *Act88F* promoter sequence [100]. This loss results in highly elevated or slightly

Chapter 2. Imaging neural activity in the ventral nerve cord of behaving adult *Drosophila*

depressed wings – phenotypes seen in IFM developmental mutants [101]. Act88F:Rpr animals show a nearly complete loss of IFMs after 7 days post-eclosion (dpe) when raised at 25°C (Figure 2.6a-b). The heterozygous *Act88F:Rpr* transgenic background greatly accelerated the dorsal thoracic dissection. Immediately following eclosion (0 dpe), we observed prominent degradation of IFMs (Figure 2.6c). For imaging, *Act88F:Rpr* was most effective at up to 3 dpe; after this stage, the abdominal gut often entered the thoracic cavity. *Act88F:Rpr* also increased the success of dissections: in one round of studies (n = 15 flies) 73% of animals produced behaviors, only 13% had limb movement deficiencies, and only 13% were incapacitated.

We next assessed the degree to which *Act88F:Rpr* might negatively impact tissues beyond the IFMs, including neurons and muscles. Due to the difficulty of identifying regions with Rpr-driven cell death, we instead measured fluorescence in transgenic animals expressing GFP driven by the same promoter sequence (*Act88F:eGFP*) [100]. We observed green fluorescence very rarely and at very low levels outside – but not within – the central nervous system (Figure S2.6). We also did not observe any fluorescence in the leg muscles of *Act88F:eGFP* animals (Figure S2.7). These anatomical observations were further supported by behavioral responses to antennal infrared laser stimulation: Act88F:Rpr (*Act88F:Rpr; UAS-GCaMP6s-p2A-tdTomato; R57C10-GAL4*) and control (+; *UAS-GCaMP6s-p2A-tdTomato; R57C10-GAL4*) animals exhibited qualitatively indistinguishable walking behaviors at 7 dpe. However, we did observe very small, quantitative differences in walking speed near the end of the stimulation pulse (Figure S2.8), n = 15 *Act88F:Rpr* animals and n = 15 control animals; n = 10 responses per animal; $P < 0.001$ Friedman test, then $P < 0.05$ Mann-Whitney *U*-test with Holm-Bonferroni correction). Finally, we recorded neural activity in Act88F:Rpr flies and observed no qualitative differences between these animals (*Act88F:Rpr; elav-GAL4/+; UAS-GCaMP6s/+*) and their control counterparts (*elav-GAL4/+; UAS-GCaMP6s/+*) (Video S2.14).

2.4 Discussion

Several additional modifications might increase the power of our VNC imaging approach. First, we used coronal section imaging to record from sparse sets of descending and ascending neurons. This strategy was chosen to overcome movement issues observed during horizontal section imaging (Video S2.15). Technologies for reducing axial resolution to achieve video-rate 2-photon imaging could be used to overcome this problem [102]. Second, we currently resect the gut to gain access to the VNC. Although this intervention does not profoundly impact limb movements and we can consistently record behaviors for at least 40 minutes (Video S2.16, Video S2.17, Video S2.18), we predict that efforts to leave the gut intact will permit even longer recordings.

We have shown that we can record the activity of large VNC neural populations (Figure 2.2) as well as sparse cell classes with known (Figure 2.3 and Figure 2.4), or unexplored functional properties (Figure 2.5). Our findings have been confirmatory – MDN activity correlates with

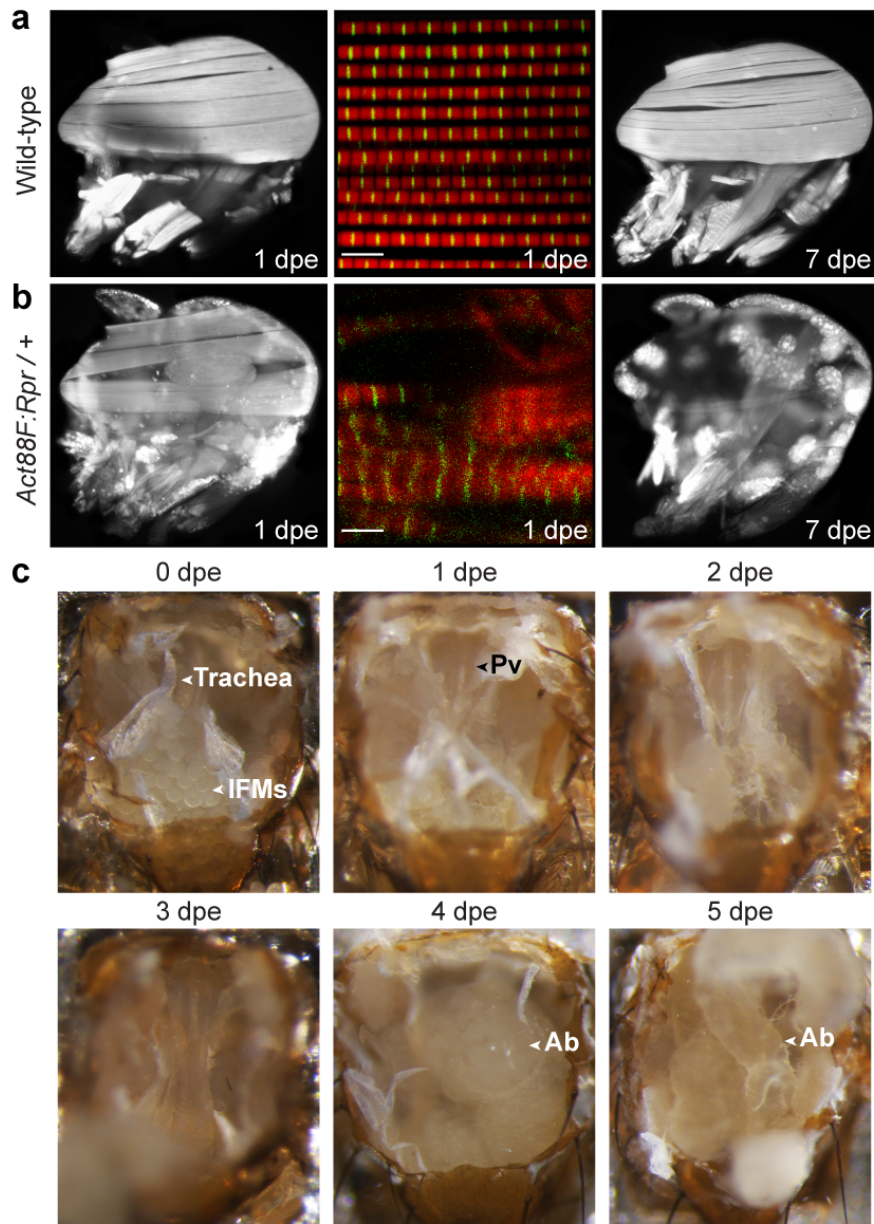


Figure 2.6: **Indirect flight muscle degradation in *Act88F:Rpr* animals.** Confocal images of dorsal longitudinal IFMs (DLMs) stained with TRITC-Phalloidin at 1 dpe (**left**), 7 dpe (**right**), or whole-mount confocal micrographs of myofibrillar structure (**middle**) for (**a**) wild-type, or (**b**) *Act88F:Rpr* heterozygous flies. Scale bars are 5 μm . (**c**) IFM degradation over time in heterozygous *Act88F:Rpr* animals (*Act88F:Rpr/elav-GAL4; UAS-GCaMP6s/+*). IFMs are already absent at 1 dpe, revealing the underlying proventriculus (Pv). At 4 dpe and later, abdominal gut (Ab) invades the thoracic cavity.

Chapter 2. Imaging neural activity in the ventral nerve cord of behaving adult *Drosophila*

backward walking – as well as unexpected – dMAN activity correlates with limb pushdown behaviors. With fluorescence decay transients ($t_{1/2}$) on the order of 1s [68], we cannot currently establish whether these signals precede these behaviors. However, based on previous observations [28], MDNs and perhaps A1 descending neurons likely drive locomotor behaviors. By contrast, MAN activity may report behavioral signals to higher-order decision-making centers in the brain. These first results suggest that our recording method, in conjunction with genetic behavioral screens [28, 103, 104], will become an indispensable tool for unraveling how signaling between the brain and VNC gives rise to complex motor actions.

2.5 Materials and methods

2.5.1 *Drosophila* lines

Several lines (*GMR57C10-GAL4*, *elav-GAL4*, *UAS-GCaMP6s*, *UAS-GCaMP6f*, *UAS-CD4:tdGFP*, and *UAS-tdTomato*) were obtained from the Bloomington Stock Center. *MAN-GAL4* (VT50660-AD; VT14014-DBD) and *MDN-1-GAL4* (VT44845-DBD; VT50660-AD) were provided by B. Dickson (Janelia Research Campus). *DNa01-GAL4* (SS00731: *GMR22C05-AD*; *GMR56G08-DBD*), *DNb06-GAL4* (SS02631: *GMR20C04-AD*; *BJD113E03-DBD*), *DNg13-GAL4* (SS02538: *BJD118A10-AD*; *BJD123E03-DBD*), and *DNg16-GAL4* (SS01543: *BJD104A07-AD*; *BJD107F12-DBD*) were provided by G. Rubin (Janelia Research Campus). *Act88F:GFP* was obtained from R. Benton (University of Lausanne). *Actin88F:Rpr* strains (*Act88F:Rpr* flies) were generated using the *Actin88F:eGFP* construct described previously [100] and injected (BestGene, Chino Hills, CA, USA) with the phiC31-based integration system using the attP18 (X chromosome) landing site [105]. For some experiments, this transgene was combined with *UAS-GCaMP6s-p2A-tdTomato* (generated in the laboratory of M.H.D.).

2.5.2 Generation of *Act88F:Rpr* construct and flies

Actin88F:Rpr strains (*Act88F:Rpr* flies) were generated using an *Actin88F:eGFP* construct²⁹. The *Act88F:GFP* line, which houses an *eGFP* construct driven by a 2053bp region of the *actin88F* promoter, was obtained from R. Benton (University of Lausanne). An *Act88F:Rpr* construct was generated by first using the following primer pair, to add a KpnI restriction site to the 5' end of a *rpr* cDNA clone (IP02530, Drosophila Genomics Resource Center, Bloomington, IN) and an XbaI site to the 3' end of the open reading frame, via a QuikChange Site-directed mutagenesis kit (Agilent Technologies):

Forward primer 5' AGACGGTACCATGGCAGTGGCATTC 3'

Reverse primer 5' GCCGCGTCTAGATCATTGCGATGGCTT 3'

The *Rpr* construct was then spliced into the *Act88F:eGFP* construct behind the *Act88F* promoter in place of the *eGFP* sequence. The *Act88F:Rpr* construct was injected into atp18 *Drosophila* embryos for PhiC31 integrase-mediated site-specific transgenesis³⁵ (transgene landing site cytolocation 6C12) by BestGene Inc. (Chino Hills, CA). For some experiments, this transgene was combined with *UAS-GCaMP6s-p2A-tdTomato* (generated in the laboratory of M.H.D.).

2.5.3 Fluorescence imaging of indirect flight muscles

Fluorescent microscopy of hemi-thoraces was performed as described previously [106, 107]. Briefly, flies were anesthetized and their heads and abdomens were then removed. Thoraces were fixed overnight in 4% paraformaldehyde at 4°C and rinsed in 1x phosphate buffered saline (PBS) the following day. The specimens were arranged on a glass slide, snap frozen in liquid nitrogen and bisected down the midsagittal plane using a razor blade. IFMs were stained with Alexa-Fluor 568 Phalloidin (1:100 in PBS with 0.1% Triton-X (PBST)) overnight at 4°C, rinsed with PBS and visualized using EVOS® FL Cell Imaging System (Life Technologies) at 4x magnification. For whole mount imaging of IFM myofibrils, flies were prepared and thoraces bisected as described above. Hemi-thoraces were stained with Alexa-Fluor 568 Phalloidin (1:100 in PBST) overnight at 4°C. Samples were rinsed in PBS, mounted with Vectashield (Vector Laboratories) and visualized using a Leica TCS SPE RGBV confocal microscope (Leica Microsystems) at 100x magnification.

2.5.4 Immunofluorescence imaging of whole-mount brains and ventral nerve cords

Brains and VNCs were dissected out of 2-3 dpe female flies in PBS. Tissues were then fixed for 20 min in 4% paraformaldehyde in PBS at room temperature. After fixation, brains and VNCs were washed 2-3 times in PBS with 1% Triton-X-100 (PBST) for 10 min each and then incubated at 4°C overnight in PBST. Samples were then placed in PBST with 5% normal goat serum (PBSTS) for 20 min at room temperature. They were then incubated with primary antibodies (rabbit anti-GFP at 1:500, Thermofisher RRID: AB_2536526; mouse anti-Bruchpilot/nc82 at 1:20, Developmental Studies Hybridoma Bank RRID: AB_2314866) diluted in PBSTS for 48 h at 4°C. Brains and VNCs were rinsed 2-3 times in PBST for 10 min each before incubation with secondary antibodies (goat anti-rabbit secondary antibody conjugated with Alexa 488 at 1:500; Thermofisher; goat anti-mouse secondary antibody conjugated with Alexa 633 at 1:500; Thermofisher) diluted in PBSTS for 48 h at 4°C. Finally, brains and VNCs were rinsed 2-3 times for 10 min each in PBST and mounted onto slides with bridge coverslips in Slowfade mounting-media (Thermofisher).

Chapter 2. Imaging neural activity in the ventral nerve cord of behaving adult *Drosophila*

Samples were imaged using a Carl Zeiss LSM 700 Laser Scanning Confocal Microscope with the following settings: 20x magnification, 8-bit dynamic range, 2x image averaging, $0.52 \times 0.52 \mu\text{m}$ pixel size, $0.57 \mu\text{m}$ z-step interval. Standard deviation z-projections of imaging volumes were made using Fiji [108]. To compare GFP expression in the central nervous system, laser intensity and PMT gains for the green channel were kept constant across wild-type, *A1>GFP*, and *Act88F:GFP* samples.

2.5.5 Imaging GFP expression in leg muscles

Legs were manually dissected at the body-coxa joint and mounted onto glass slides using double-sided tape. Slowfade mounting-media (Thermofisher) was then added to the space between the cover slip and the slide. We then recorded GFP fluorescence in the green channel using an LSM 700 Laser Scanning Confocal Microscope (Zeiss). Laser intensity, PMT gains, and scanning parameters were kept constant across wild-type, *MHC>GFP* and *Act88F:GFP* animals: 20x magnification, 8-bit dynamic range, 8x image averaging, $0.63 \times 0.63 \mu\text{m}$ pixel size, and $10 \mu\text{m}$ z-step interval. Cuticular auto-fluorescence was also recorded in the red channel.

2.5.6 Thoracic dissection for VNC imaging

Custom holders used to mount flies during imaging were fabricated as described previously [109]. For VNC imaging, these stages were modified to have (i) flat rather than folded steel shims, and (ii) chamfered vertices to make the spherical treadmill visible to optic flow sensors (Shapeways, <https://github.com/NeLy-EPFL/Imaging-Drosophila-VNC-and-CC/blob/master/VNC-CC-Imaging-stage/vnc-cc-imaging-stage.STL>). Steel shims were fabricated from 0.001" Stainless Steel, type 316 soft annealed (McMaster-Carr, part #2317K11). Shims were etched (Etchit, Buffalo, MN) to generate rectangular holes as described in <http://ptweir.github.io/flyHolder/>. The shim design file can be found here: <https://github.com/NeLy-EPFL/Imaging-Drosophila-VNC-and-CC/blob/master/VNC-CC-Imaging-stage/shims.DXF>.

All experiments were performed on 1-3 dpe female flies raised at 25°C on standard cornmeal food on a 12 h light:12 h dark cycle. Flies were anesthetized at 4°C. A female fly was selected and, in some cases, its wings were clipped to simplify the mounting process. The fly's dorsal thorax was then pushed through a hole in the steel shim of the imaging stage. The stage was then flipped over, UV-curing glue (Bondic, Aurora, ON Canada) was carefully applied around the perimeter of the thorax and cured by UV illumination (LED-200, Electro-Lite Co. Bethel, CT USA). UV glue was then used to fix the head and abdomen to the underside of the stage. The stage was then filled with extracellular saline as described previously [7]. Under a high-magnification dissection microscope (Leica M165C), a hypodermic needle (30G, BD PrecisionGlide, Franklin Lakes, NJ USA) was used to slice and lift the cuticle off the dorsal thorax [110], being careful not to sever the neck connective. Subsequently, in

non-*Act88F:Rpr* animals, a pair of dull forceps was used to remove IFMs, predominantly from the anterior-medial region of the thorax overlying the gut (this step is unnecessary in *Act88F:Rpr* animals). This process exposes the dorsal surface of the proventriculus – a large bulbous gut structure. With great care, a pair of super-fine forceps was then used to grasp and lift the proventriculus to displace much of the gut (including the crop and salivary glands) from the more ventrally located nervous tissue. With the gut thus elevated, ultra-fine clipper scissors (Fine Science Tools, Foster City, CA USA) were used to transect it at its anterior-most section. The proventriculus was then peeled back and a posterior incision was made to completely remove these portions of the gut, revealing the underlying nervous tissue. Notably, this dissection also removes the aorta, restricting hemolymph flow from the abdominal dorsal vessel. Nevertheless, we found that flies were viable and behaved for up to 4 h. In some cases, we observed that gut or muscle tissue would begin to obscure the VNC during imaging. Therefore, loose tissue should be removed at this stage while taking great care not to sever the VNC. After each dissection, we examined the extent to which the animal moved its legs in response to a puff of air or grabbed an object with each of its legs. This proved to be an accurate predictor of the success of the preparation. To evaluate the quality of a dissection, we examined the movements of each leg on the spherical treadmill. If a fly could walk in a coordinated manner, the dissection was considered successful. Otherwise, the animal was categorized as having a limb movement deficiency. Animals with multiple dysfunctional legs were categorized as incapacitated.

2.5.7 2-photon microscopy during behavior

Experiments were performed in the evening Zeitgeber time (Z.T.) and animals were typically imaged 30-60 min following dissection. Fly holders were secured to a raised platform over the spherical treadmill ([Figure S2.3a](#)). The VNC was then located using microscope oculars and positioned in the center of the field-of-view by 2-photon imaging.

The spherical treadmill is an aluminum rod with a ball-shaped hole milled at one end [40]. We fabricated 10 mm diameter foam balls (Last-A-Foam FR-7106, General Plastics, Burlington Way, WA USA) and manually spotted them using a Rapidograph pen (Koh-I-Noor, Leeds, MA USA) to provide high-contrast features for optic flow measurements. A 500-600 mL min⁻¹ stream of filtered and humidified air was passed through the holder using a digital flow controller (Sierra Instruments, Monterey, CA USA). Movements of the ball were measured using two optical flow sensors (ADNS3080) outfitted with zoom lenses (Computar MLM3X-MP, Cary, NC USA). The ball and fly were illuminated using a pair of IR LEDs (850-nm peak wavelength) coupled to optic fibers and collimator lenses (ThorLabs, Newton, NJ USA). Optic flow measurements were passed to a microcontroller board (Arduino Mega2560) to be recorded using custom Python code. Simultaneously, video recordings of animals behaving on the ball were made using an IR-sensitive firewire camera (Basler, Ahrensburg, Germany) at approximately 30 fps.

Chapter 2. Imaging neural activity in the ventral nerve cord of behaving adult *Drosophila*

We performed 2-photon microscopy using a Bergamo II microscope (ThorLabs) outfitted with two GaAsP PMT detectors for GCaMP6 and tdTomato imaging and coupled to a Ti:Sapphire laser (MaiTai DeepSee, Newport Spectra-Physics, Santa Clara, CA USA) tuned to 930 nm. We used an Olympus 20x water-immersion objective lens with 1.0 NA (Olympus, Center Valley, PA USA). The microscope was controlled using ThorImage software (ThorLabs). Coronal section imaging experiments were performed in Galvo-Galvo imaging mode at 6 - 9 Hz. This framerate varied with image size which ranged between $26.58 \mu\text{m} \times 26.58 \mu\text{m}$ and $53.15 \mu\text{m} \times 53.15 \mu\text{m}$. Laser power ranged between 3 mW and 5.7 mW. Volumetric imaging is also possible with appropriate hardware (e.g., Galvo-Resonance scanner and Piezo-driven objective collar).

Occasionally, a puff of air was used to elicit walking behaviors. These puffs were digitally encoded (Honeywell AWM 3300V, Morris Plains, NJ USA). Custom ROS software interfaced through an analog output device (Phidgets, Calgary, Canada) to ThorSync software (ThorLabs) was used to synchronize optic flow measurements, behavior videography, air puff measurements, and 2-photon image acquisition. For coronal section imaging, a Piezo collar (Physik Instrumente, Karlsruhe, Germany) was used to control rapid z-axis movements of the microscope objective lens.

To compare neural activity between control and *Act88F:Rpr* animals, we acquired 512×512 pixel images at 1.7 fps using a constant laser intensity and PMT gain. Selected imaging regions were empirically chosen as horizontal sections consisting of landmarks observed at $61\text{-}65 \mu\text{m}$ depth in [Video S2.1](#).

2.5.8 Comparing walking behaviors in dissected or non-dissected animals

To evaluate the effects of dissection on locomotion, wild-type flies were subjected to the following procedure. Flies were mounted onto imaging stages and saline was added to each stage. A random subset of animals was dissected. All mounted flies were then placed onto the spherical treadmill for 30 min. Optic flow was recorded as described. To increase the likelihood of locomotion, a 500 ms pulse of 100% CO₂ was directed at the fly's antennae with a one min inter-pulse interval ($0.05 I_n \text{ min}^{-1}$ using a mass flow controller; Vögtlin Instruments, Switzerland).

2.5.9 Infrared laser antennal stimulation

To compare walking behaviors between *Act88F:Rpr* and control animals, we stimulated their antennae with an 830nm near infrared laser (Schäfter+Kirchhoff, Germany). We first anesthetized 7-8 dpe female animals at 4°C and mounted them on imaging stages. Flies were then acclimated for 10 min. For each experiment, an animal received ten 2 s laser stimulation pulses (18.1 mW) to its right antenna at a 60 s inter-pulse interval. Control and *Act88F:Rpr*

animals were tested in alternation to minimize the effects of circadian time on behavioral comparisons.

2.5.10 Statistics

Sample sizes for animal experiments were chosen as follows: we performed at least three experiments to illustrate population and sparse neural recordings and performed more than ten experiments per group when performing statistical comparisons. A pre-established criteria of low signal-to-noise fluorescence signals resulted in the removal of two MDN experiments from our dataset. No randomization or blinding was used. For antennal laser stimulation, data were not normally distributed, thus Friedman and Mann-Whitney U-tests were performed. Estimates of variation are presented as mean and bootstrapped 95% confidence intervals.

2.5.11 Data analysis

We analyzed all data using custom Python scripts. Because the data acquisition frequency differed for optic flow, behavior videography, and 2-photon imaging we interpolated signals to match those of the highest frequency. Subsequently, optic flow data were smoothed using a running average (window = 200 ms) and then translated into rotations s^{-1} for anterior-posterior, medial-lateral, and yaw axes as described in [40]. To make these measurements more intuitive, rotations s^{-1} were then converted into $mm\ s^{-1}$ ($1\ rot\ s^{-1} = 31.42\ mm\ s^{-1}$ for anterior-posterior ($v_{forward}$) and medial-lateral (v_{side}) movements and into $degrees\ s^{-1}$ ($1\ rot\ s^{-1} = 360^\circ\ s^{-1}$ for yaw ($v_{rotation}$) movements [40].

Evaluation of locomotion in dissected animals (related to [Figure S2.2](#))

The analysis of locomotion in dissected animals ([Figure S2.2](#)) was performed as follows. $V_{forward}$ optic flow data for 20 dissected and 20 non-dissected flies were downsampled to 1500 points s^{-1} and smoothed using a running average of duration 0.2 s. To compute the percentage of time walking forward/backward, or walking sideways two thresholds, $-0.31\ mm\ s^{-1}$ and $+0.31\ mm\ s^{-1}$, were empirically defined to differentiate between standing still and forward (rightward) or backward (leftward) walking, respectively. Values above $0.31\ mm\ s^{-1}$ were considered moments of forward (rightward) walking and values below $0.31\ mm\ s^{-1}$ were considered moments of backward (leftward) walking. Optic flow values between these thresholds were considered moments of standing still. The percentage of time walking was calculated as the proportion of data points in which an animal was not considered standing still. Similarly, thresholds of 10.8 and $-10.8\ degree\ s^{-1}$ were used to defined moments of turning. A bout was defined as a continuous period of walking or turning.

Pan-neuronal image registration, ROI identification, and fluorescence processing (related to Figure 2.2)

Large tissue deformations could occur during behavior. Therefore, we performed post-hoc registration of pan-neuronal imaging data. To do this, we registered all frames of an imaging experiment to one reference image. Because the complexity of deformations could not be captured using simple parametric motion models (e.g., affine transformations), we used a non-parametric, variational approach, designed to model arbitrarily complex deformations. We computed the motion field \mathbf{w} between the reference image, denoted I_r , and the image at time t , denoted I_t , by solving the minimization problem

$$\hat{\mathbf{w}} = \underset{\mathbf{w}}{\operatorname{argmin}} D(\mathbf{w}) + \lambda \sum_{x \in \Omega} \|\nabla \mathbf{w}(\mathbf{x})\|_2^2, \quad (1)$$

where $D(\mathbf{w})$ is a data fitting term, the second term is a regularization promoting smoothness of \mathbf{w} by penalizing its gradient $\nabla \mathbf{w}$ [111], Ω is the discrete image domain, and the parameter λ balances the contributions of the two terms.

GCaMP6s images present a challenge for motion estimation because neural activity produces large local intensity changes. Therefore, we used an additional activity independent fluorophore, tdTomato, and defined a data term of the form

$$D(w) = \rho(w, I_r, I_t) + \gamma \phi(w, I_r, I_t). \quad (2)$$

The first term models the standard assumption of conservation of intensity along the trajectory of each pixel. It is defined by

$$\rho(w, I_r, I_t) = \sum_{x \in \Omega} |I_t(x + w(x)) - I_r(x)|, \quad (3)$$

where we use an l_1 norm to gain partial robustness to intensity changes [112]. The second term in (2) is a feature matching constraint inspired by Revaud and co-workers [113], written as

$$\phi(w, I_r, I_t) = \sum_{x \in \Omega} \|w(x) - m(x, I_r, I_t)\|_1. \quad (4)$$

In equations (2) to (4), I_r and I_t are from the tdTomato channel. Minimizing the function ϕ favors motion vectors $\mathbf{w}(\mathbf{x})$ to be close to feature correspondences $\mathbf{m}(\mathbf{x}, I_r, I_t)$, computed on a sparse set of relevant keypoints. We obtain \mathbf{m} with the feature matching algorithm proposed by Revaud and co-workers [113], which is specifically designed to handle large image deformations. We compute \mathbf{m} using the tdTomato imaging channel, such that the correspondences are also insensitive to the intensity changes between I_r and I_t . As a result,

the estimation is guided by reliable feature matches. The parameter γ balances the two terms in (2).

For each experiment, we optimized the values for λ and γ using a grid search to register horizontal section images of the VNC (**Figure S2.4**). As an objective function for optimization, we used the gradient of the temporal mean image [114]. Small values of λ (i.e. $\lambda < 1000$), occasionally led to artifacts in the registered images. These artifacts were associated with strong convergence in the vector field $\mathbf{w}(\mathbf{x})$ (**Figure S2.4c**). Therefore, we empirically defined artifacts as clusters of pixels with $div \mathbf{w}(\mathbf{x}) < -1.2$ and cardinality > 20 (we obtained similar results with cardinality > 5). Finally, we selected λ and γ values as those with no artifacts and the highest gradient of the mean image. Sample unregistered images, transformation vector fields, and registered images of the three optimized examples are shown in **Video S2.5**.

We solved the optimization problem (1) with an alternated direction method of multiplier (ADMM) algorithm [115]. We introduced two splitting variables, associated with the regularization and the feature matching terms, respectively. Each sub-problem of the algorithm was solved analytically. We used parts of the inverse problems library described in [116]. A post processing based on weighted median filtering was applied using the method from [117].

In **Figure 2.2**, behaviors were semi-automatically annotated, using a custom Python module. This module allows the user to select two ROIs on the video's first frame. The first ROI is used to detect walking and must be positioned over the metathoracic and mesothoracic legs. The second ROI is responsible for detecting prothoracic leg grooming and must be positioned in front of the fly. To detect motion in those regions, consecutive frames are subtracted. Resulting differential images are then median blurred (radius = 5 pixels), to reduce noise. Based on this blurred image, a threshold on the number of non-zeros pixels in each of the two ROIs is applied to extract binary sequences of grooming and walking bouts. Note that prothoracic leg movements observed during walking are ignored (i.e., grooming classification is subservient to walking classification). A hysteresis filter was then applied to low-pass filter binary behavioral sequences and to remove transitions that occur over too few frames to be biologically plausible. Example ROIs and behavioral annotations are illustrated in **Video S2.6**. This behavior data was used in **Figure 2.2** as shown in **Video S2.2**. It was annotated using the following parameters: threshold for walking = 400, threshold for grooming = 5, hysteresis length for walking = 8, hysteresis length for grooming = 10.

For **Figure 2.2b-c**, we used linear regression to find regions in the VNC associated with either walking or grooming. Regressors X_w and X_g (for walking and grooming, respectively) were constructed from the two behavioral sequences, S_w and S_g , using equation (5) by convolution with an exponentially decaying Calcium signal Impulse Response (CIR) derived from the time constant measured for GCaMP6s ($t_{1/2}=1.1448s$) [68].

$$X_w = S_w \otimes CIR$$

Chapter 2. Imaging neural activity in the ventral nerve cord of behaving adult *Drosophila*

$$X_g = S_g \otimes CIR, \quad (5)$$

Target functions were pixel-wise $\Delta F/F$ traces, where $\Delta F = F_t - F$. F_t is the fluorescence at time, t . F is a baseline fluorescence signal measured as the average pixel value for the first ten sequential GCaMP6s images in which no cellular activity was observed (i.e., minimal and unchanging GCaMP6s fluorescence). The regressor weights were calculated using equation (6).

$$w_w = (X_w^T X_w)^{-1} X_w^T y$$
$$w_g = (X_g^T X_g)^{-1} X_g^T y, \quad (6)$$

where y is the pixel-wise $\Delta F/F$ trace.

Figure 2.2b-c shows heat maps of the regressor weights, w_w for walking and w_g for grooming, normalized to their respective maxima. ROI 1 was chosen as a region of the heat map with a high weight for grooming but a low weight for walking. ROI 2 was chosen as the spatial location with the highest value of w_w . Each ROI encompasses a region with a 15 pixel radius.

Sparse neuron ROI identification, and fluorescence processing (related to [Figure 2.3](#), [Figure 2.4](#), [Figure 2.5](#))

For single-neuron fluorescence data, ROIs were selected using custom Python scripts that depended on OpenCV and Numpy libraries. First, a reference frame was selected for which the software identified all potential ROIs. To do this, the GCaMP6s image was smoothed to reduce background noise and then an Otsu filter threshold was applied to the image. An erosion factor was then applied on all objects detected within the image. Contours of all detected objects were then presented to the user for manual selection. Once these reference ROIs were selected for left and right neurons, we used a cross-correlation-based image registration algorithm [118] to identify the most likely left and right ROIs for each image frame based on those manually selected on the reference frame. A second script was used to manually verify automatically selected ROIs and, if incorrect, to display all potential ROIs within the frame for manual selection. If erosion values yielded malformed ROIs, another script was used to manually position elliptical ROIs of arbitrary orientation on any given frame. Finally, binary ROI images were used as an image mask to extract mean fluorescence signals from the original GCaMP6s or tdTomato images. These signals were reported as $\% \Delta R/R$ as in [119] to reduce the effects of motion on our measurements. Due to the absence of stimuli, the baseline R was calculated as the minimum ratio of GCaMP6s/tdTomato within a 2.5 s bin.

To detect transient increases in activity, we developed an algorithm based partly on [120]. We first determined when the first derivative of the $\% \Delta R/R$ signal crossed a threshold, which was determined by examining all derivative values for a given neuron class (MDN, MAN, or A1).

We reasoned that threshold values should be characteristic and potentially different for each type of neuron because fluorescence dynamics are related to intrinsic physiological properties that can differ across neuron classes but not across experiments for a single class. We set this threshold as the 97.5th percentile for MDNs and dMANs and the 90th percentile for A1 neurons. A lower threshold value was selected for A1 neurons because many more fluorescence transients were observed in A1 traces. These transients would have been overlooked using a 97.5th percentile threshold. To identify the onset of fluorescence increases we found the nearest preceding time point where the derivative crossed zero. This zero-crossing is considered the time-point of an ‘event’ associated with the identified fluorescence increase. Events detected close to one another with no intervening derivative zero-crossing were compressed into one event associated with the first time-point. There were 10 separate experiments per animal. Events in the first and last 10 s of each experiment were not considered since the data presentation window encompassed 10 s before and 10 s after each event.

Because left and right MDN and dMAN activities strongly covaried ([Figure S2.5](#)), an additional step was performed for event detection: if events were detected in both left and right neurons within 2 s of one another, both events were retained; otherwise, an event identified for neuron A (e.g., left MDN) and not neuron B (e.g., right MDN) was also added to neuron B’s event library. By contrast, left and right A1 activities did not strongly covary. Therefore, events were associated with one and not the other neuron. To accomplish this, if an event was detected for both left and right A1 neurons within a time window of 0.25 s, neither of the events were used for analysis.

$\% \Delta R/R$ and optic flow traces linked to each event were aligned by setting the event time points to 0 s. We then computed the mean and bootstrapped 95% confidence intervals for these aligned traces using the Python Seaborn library. Optic flow and $\% \Delta R/R$ measurements were downsampled to 500 values s⁻¹ for this analysis. To increase clarity, $\% \Delta R/R$ traces were baseline-subtracted to make them zero at the time of the event in the summary panels ([Figure 2.3d](#), [Figure 2.4d](#), [Figure 2.55d-e](#)). Control, shuffled data (gray traces) were computed by instead assigning random time-points in place of real, identified events. These random time points were treated as real events and their mean and bootstrapped 95% confidence intervals were computed and plotted for comparison.

Covariance analysis (related to [Figure S2.5](#))

Covariance analysis was performed using a custom Python script that depended on the Matplotlib and Numpy libraries. Scatter plots were computed to compare left and right neuron $\% \Delta R/R$ values from all experiments for each fly separately. Pearson’s *r* values are reported as mean \pm standard deviation.

Chapter 2. Imaging neural activity in the ventral nerve cord of behaving adult *Drosophila*

Event-related behaviors (related to [Video S2.8](#), [Video S2.10](#), [Video S2.12](#), and [Video S2.13](#))

Events for behavioral summary movies were manually selected from automatically detected events as described above. For dMANs, events were selected from among those that maximized the difference in anterior-posterior ball rotations between 1 s before and 2 s after the event. For MDNs, events were selected from among those that minimized anterior-posterior ball rotations up to 2 s after the event. For A1 neurons, events were selected from among those that maximized the average yaw ball rotations (positive for left A1 neuron examples and negative for right A1 neuron examples) for up to 2 s after the events.

Laser-stimulated walking (related to [Figure S2.8](#))

Responses to near infrared laser stimulation were averaged across 10 trials for each animal. Optic flow was downsampled to 500 values s^{-1} . Mean and 95% bootstrapped confidence intervals for optic flow traces were measured and plotted using the Python Seaborn library. The Python Scipy library was used to perform Friedman and Mann-Whitney U -tests.

2.6 Code availability

Code and sample datasets used for this study are available at: <https://github.com/NeLy-EPFL/Imaging-Drosophila-VNC-and-CC>

2.7 Data availability

The data used in this study is available from the authors on reasonable request.

2.8 Acknowledgments

We thank B.J. Dickson (Janelia Research Campus, VA) for MDN-1-GAL4 and MAN-GAL4 fly strains. We thank G. Rubin (Janelia Research Campus, VA) for DNa01-GAL4, DNb06-GAL4, DNg13-GAL4, and DNg16-GAL4 fly strains. AC acknowledges support from the National Institutes of Health (R01HL124091). MHD acknowledges support from the National Institute of Neurological Disorders and Stroke of the National Institutes of Health (U01NS090514). PR acknowledges support from the Swiss National Science Foundation (31003A_175667).

2.9 Author contributions

C.L.C. generated strains; performed experiments; analyzed data **L.H.** performed experiments; analyzed data **M.C.V.** generated strains; performed experiments; analyzed data **D.F.** wrote

analysis code **FA.** analyzed data **A.C.** designed and supervised the project **M.H.D.** designed and supervised the project **P.R.** conceived of, designed, and supervised the project; performed experiments; analyzed data All authors contributed to writing the paper

2.10 Declaration of Interests

The authors declare no competing interests.

2.11 Supplementary information

2.11.1 Supplementary Figures

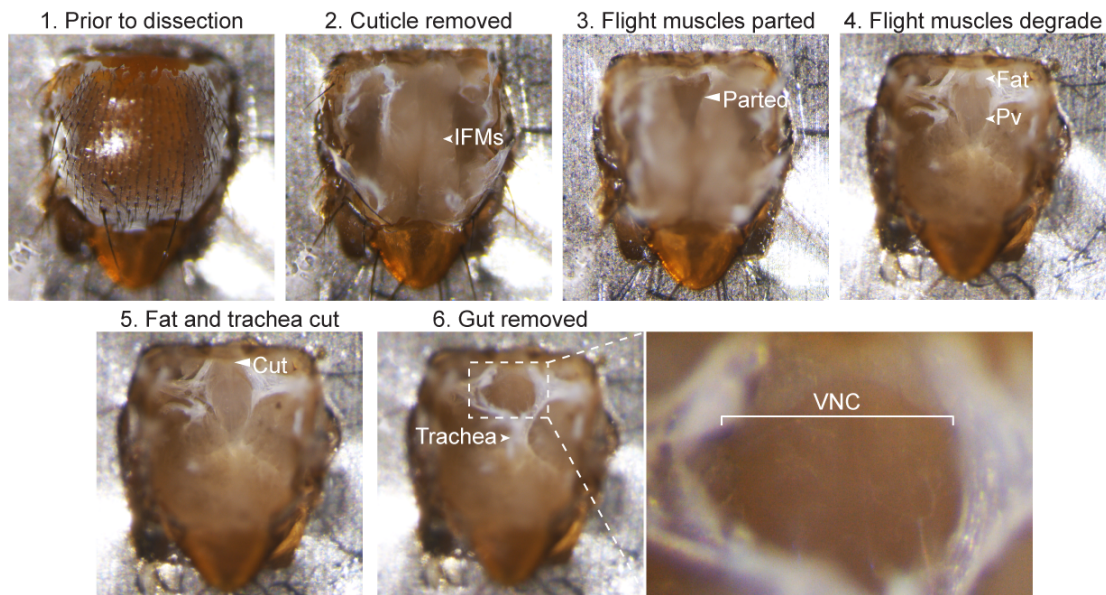


Figure S2.1: **Illustration of dorsal dissection to access the VNC.** First, the dorsal cuticle is removed, revealing indirect flight muscles (IFMs) (**steps 1-2**). The IFMs are then parted at the anterior midline (**step 3**). After >1hr, the IFMs degrade, exposing midline trachea, fat bodies (Fat), and the proventriculus (Pv) (**step 4**). After removing these structures (**steps 5-6**), the prothoracic and mesothoracic VNC (**inset**) become accessible for 2-photon microscopy.

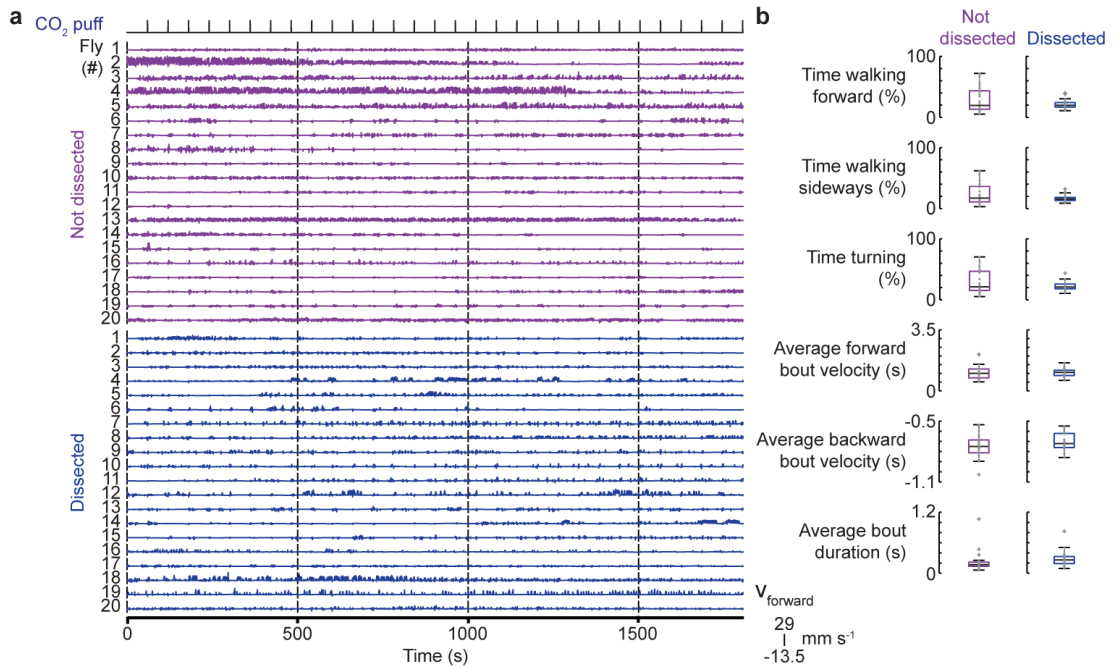


Figure S2.2: **Locomotion in flies with or without thoracic dissection.** (a) Raw spherical treadmill traces showing forward velocity for animals without (**top, purple**), or following the thoracic dissection revealing the VNC (bottom, blue). Timing of CO₂ pulses delivered to the antennae are indicated. (b) Locomotor parameters from animals without (**left, purple**) or with (**right, blue**) the thoracic dissection. Parameters include percent of time walking forward, walking sideways, or turning, as well as the average forward bout velocity per animal, average backward bout velocity per animal, and average bout duration per animal. Box plots show the median, upper, and lower quartiles.

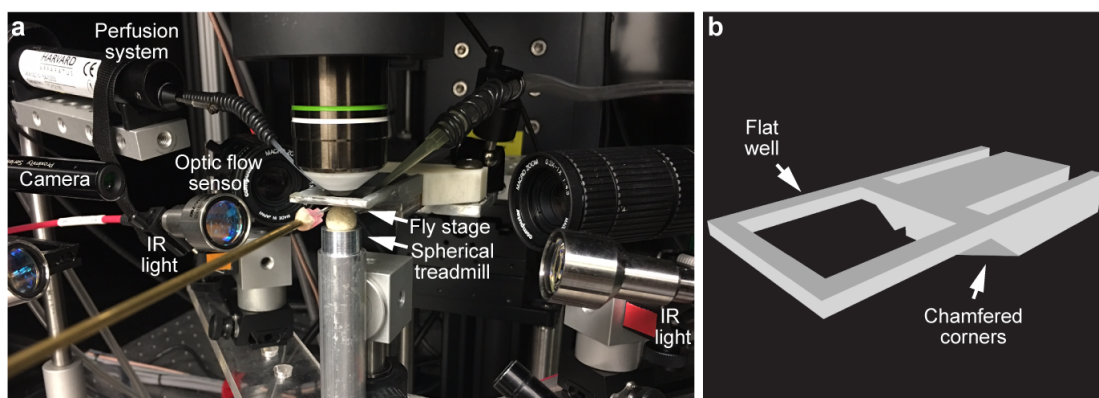


Figure S2.3: **System for VNC imaging.** (a) Photograph of the experimental system and (b) a CAD schematic of the custom fly stage used in this study.

Chapter 2. Imaging neural activity in the ventral nerve cord of behaving adult *Drosophila*

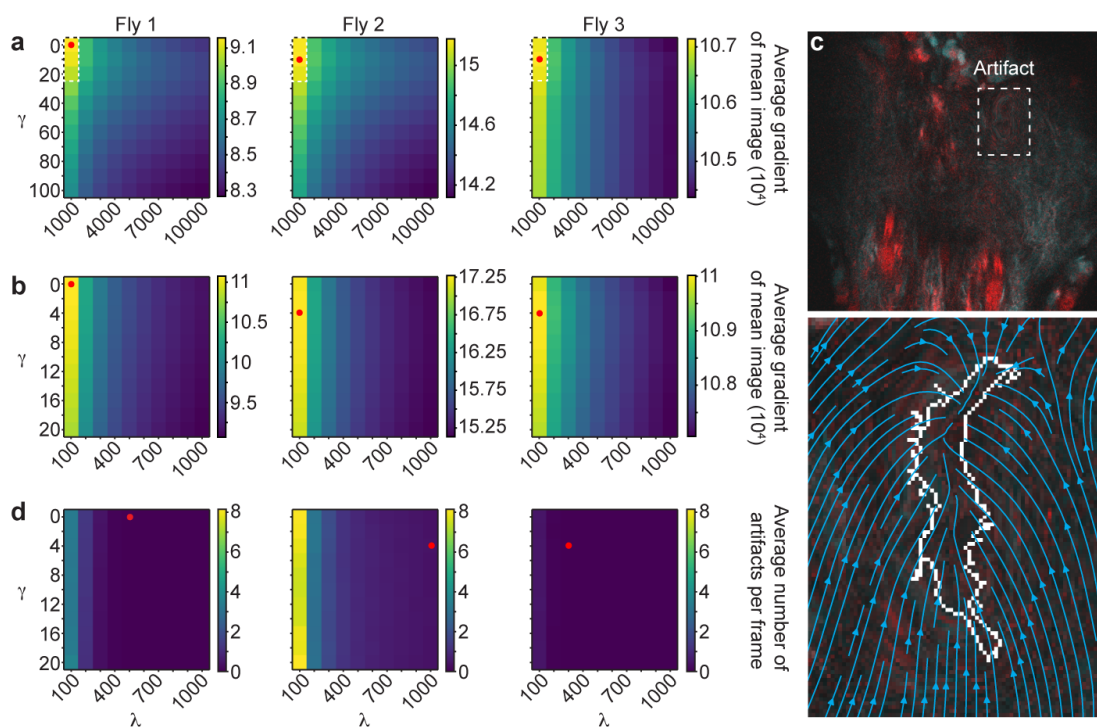


Figure S2.4: **Optimization of λ and γ values for image registration.** (a-b) The average gradient of the mean image for (a) a coarse grid search of λ and γ values for three horizontal section VNC imaging datasets ($n = 3$ flies; same data and ordering as in [Video S2.5](#)). Red dots indicate the maximum value. White dashed boxes indicate the regions explored using (b) a finer-scale grid search. (c) Illustration of an image registration artifact observed for data from fly 2 when using $\lambda = 100$ and $\gamma = 0$ (top). The region in the white inset magnified and overlaid with the transformation vector field (blue arrows) and the boundary (white outline) of the artifact as determined using a threshold on divergence (bottom). (d) Average number of artifacts per frame. Red dots indicate the final λ and γ values used to register the data shown in [Video S2.5](#). These values result in images with no artifacts but a maximal average gradient of the mean image.

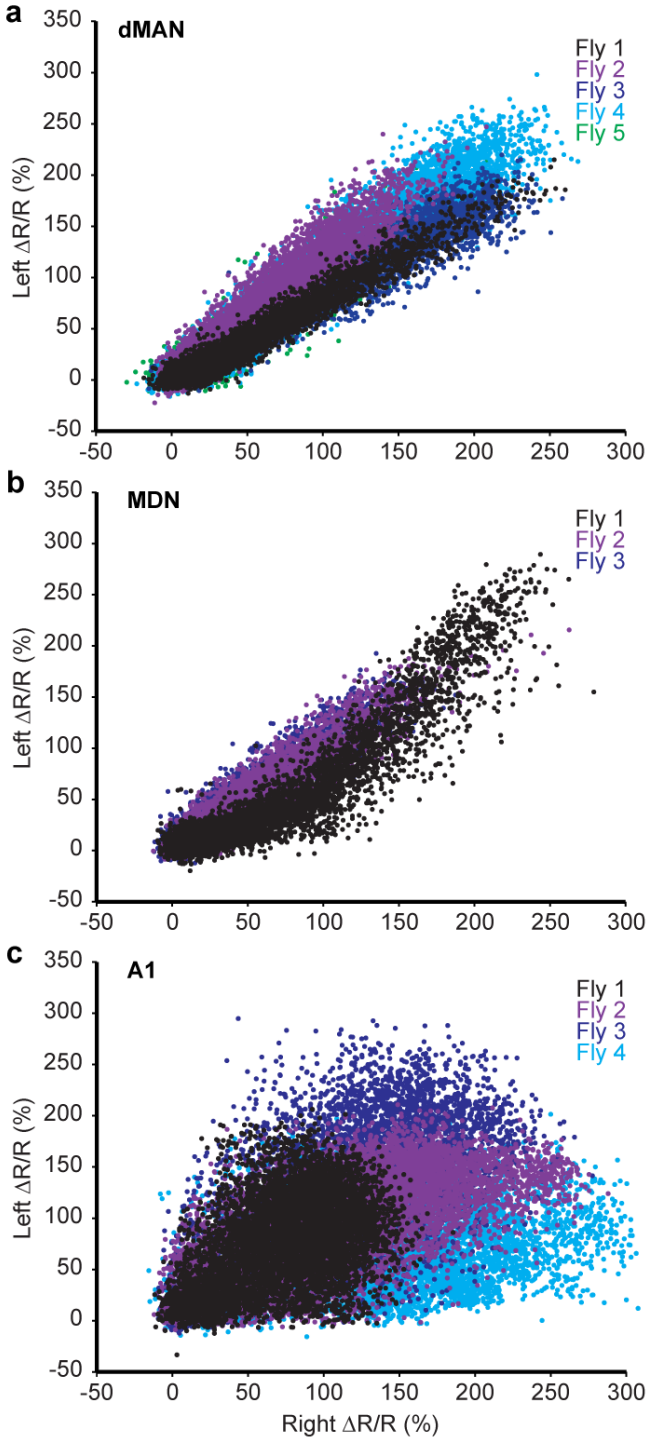


Figure S2.5: **Covariance in fluorescence signals between bilateral pairs of neurons.** Scatter plots comparing % $\Delta R/R$ signals recorded from right and left (a) dMAN, (b) MDN, or (c) A1 neuron pairs.

Chapter 2. Imaging neural activity in the ventral nerve cord of behaving adult *Drosophila*

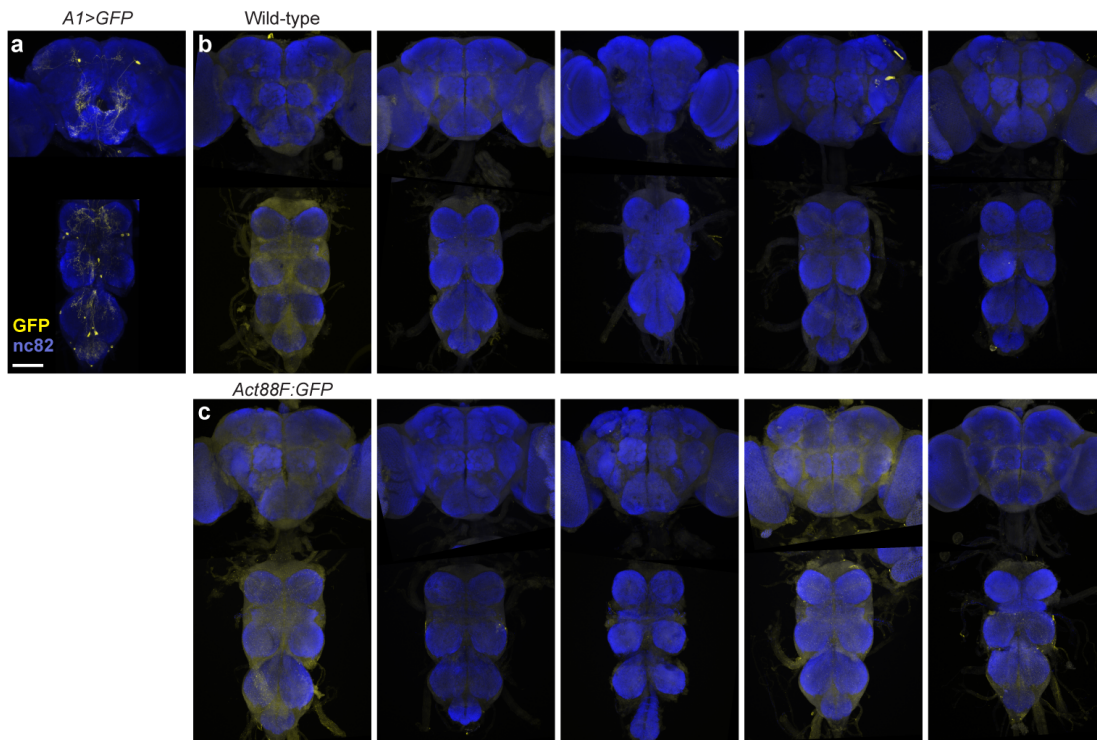


Figure S2.6: **GFP expression in the central nervous system.** Representative confocal images of brains and VNCs from (a) one *A1>GFP* fly: a positive control with sparse GFP expression, (b) five wild-type flies: negative controls without GFP expression, or (c) five *Act88F:GFP* flies. Immunostaining is against GFP (yellow) and nc82 (blue). Scale bar is 180 μm .

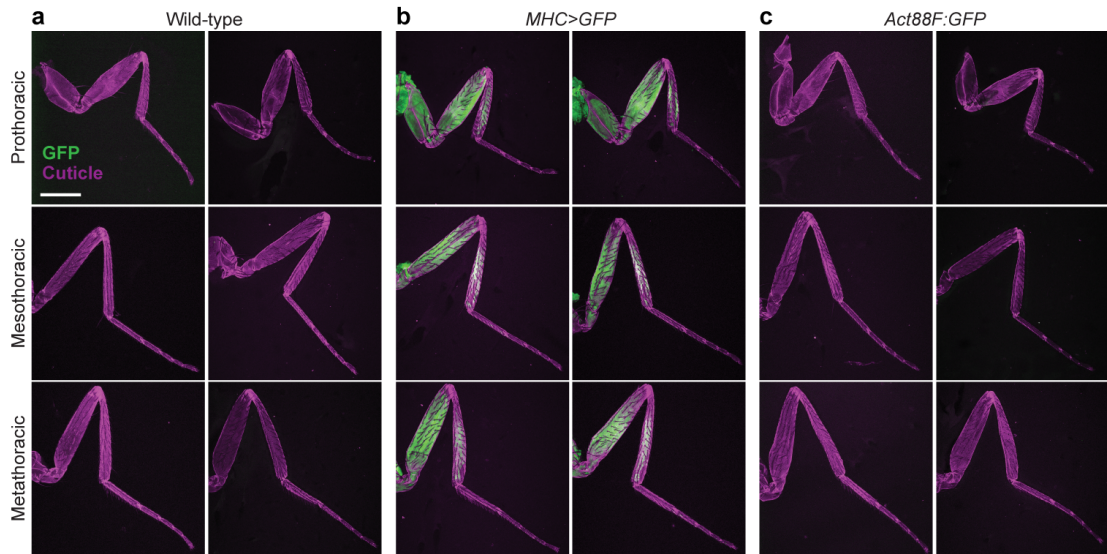


Figure S2.7: **GFP expression in leg muscles.** Representative confocal images of prothoracic, mesothoracic, or metathoracic legs from (a) two wild-type flies: negative controls without GFP expression, (b) two *MHC>GFP* flies: positive controls with leg muscle GFP expression, or (c) two *Act88F:GFP* flies. Shown are endogenous GFP fluorescence (green) and cuticular autofluorescence (magenta). Scale bar is 300 μm .

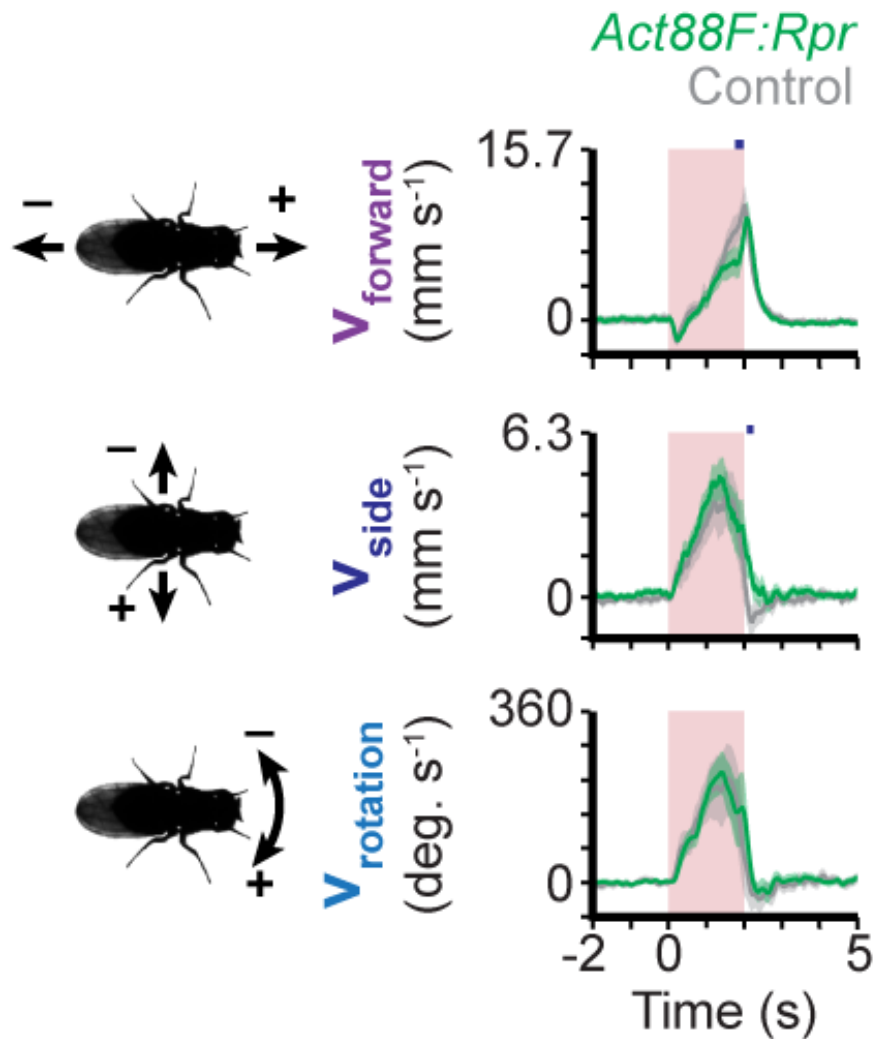


Figure S2.8: **Locomotor behaviors in control and *Act88F:Rpr* animals.** Forward, sideways, and rotational locomotor velocities for *Act88F:Rpr* (green: *Act88F:Rpr*; *R57C10-GAL4/UAS-GCaMP6s-p2A-tdTomato*), or control (grey: +; *R57C10-GAL4/UAS-GCaMP6s-p2A-tdTomato*) animals. Shown are the means (solid lines) and bootstrapped 95% confidence intervals (transparencies). Red transparency indicates period with near-infrared laser stimulation of the right antenna. Blue bars show time points with significant differences between *Act88F:Rpr* and control animals ($P < 0.05$; Mann-Whitney U -test with a Holm-Bonferroni correction).

2.11.2 Supplementary Videos

Video S2.1: **VNC imaging volume.** 2-photon z-stack illustrating horizontal sections across the dorsal-ventral extent of the VNC. GCaMP6s (cyan) and tdTomato (red) are expressed throughout the nervous system (*GMR57C10>GCaMP6s; tdTomato*). Imaging depth indicated on the top-left.

[Download Video S2.1](#)

Video S2.2: **Horizontal VNC imaging.** 2-photon imaging of a single horizontal section of the VNC in a fly that walks and grooms. GCaMP6s (cyan) and tdTomato (red) are expressed throughout the nervous system (*GMR57C10>GCaMP6s; tdTomato*). Shown are synchronized raw fluorescence images (**top-left**), $\% \Delta F/F$ images (**top-right**), behavior video images (**bottom-left**), and forward, sideways, and rotational velocities of the animal (bottom-right). Experimenter-administered air puffs are indicated by the appearance of a red box above the behavior video images. Registration was performed using $\gamma = 0$ and $\lambda = 500$. Movie is 4x faster than real-time.

[Download Video S2.2](#)

Video S2.3: **Coronal VNC imaging.** 2-photon imaging of a single coronal section of the VNC in a fly that walks. GCaMP6s (cyan) and tdTomato (red) are expressed throughout the nervous system (*GMR57C10>GCaMP6s; tdTomato*). Shown are synchronized raw fluorescence images (**top-left**), $\% \Delta F/F$ images (**top-right**), behavior video images (**bottom-left**), and forward, side-ways, and rotational velocities of the animal (**bottom-right**). Registration was performed using $\gamma = 50$ and $\lambda = 10,000$. Movie is 4x faster than real-time.

[Download Video S2.3](#)

Video S2.4: **Coronal cervical connective imaging.** 2-photon imaging of a single coronal section of the cervical connective in a fly that walks. GCaMP6s (cyan) and tdTomato (red) are expressed throughout the nervous system (*GMR57C10>GCaMP6s; tdTomato*). Shown are synchronized raw fluorescence images (**top-left**), $\% \Delta F/F$ images (**top-right**), behavior video images (bottom-left), and forward, sideways, and rotational velocities of the animal (bottom-right). Registration was performed using $\gamma = 50$ and $\lambda = 5,000$. Movie is 4x faster than real-time.

[Download Video S2.4](#)

Chapter 2. Imaging neural activity in the ventral nerve cord of behaving adult *Drosophila*

Video S2.5: **Motion and deformation correction.** 2-photon imaging of a single horizontal section of the VNC in three different animals during behavior. Data are from [Figure 2.4](#) (Fly 1: $\lambda = 500$ and $\gamma = 0$; Fly 2: $\lambda = 1000$ and $\gamma = 4$; Fly 3: $\lambda = 300$ and $\gamma = 4$). Raw, unregistered, fluorescence images (**top**). Spatially down sampled transformation vector field used to register raw images (**middle**). Final, registered fluorescence images (**bottom**). Images for flies 1 and 2 are 512 x 512 pixels. Images for fly 3 are 256 x 256 pixels.

[Download Video S2.5](#)

Video S2.6: **Semi-automated behavioral classification.** Illustration of semi-automated grooming and walking annotations used for [Figure 2](#). Grooming and walking ROIs are shown (white boxes). The current behavioral descriptor is indicated on the top-left.

[Download Video S2.6](#)

Video S2.7: **Coronal cervical connective imaging of dorsal Moonwalker Ascending Neurons.** Moonwalker Ascending Neurons. 2-photon imaging of a single coronal section of the cervical connective in a behaving fly. GCaMP6s (cyan) and tdTomato (red) are expressed in MANs (*MAN>GCaMP6s; tdTomato*). Raw fluorescence images of the left and right dMANs are presented and outlined by ROIs (**top-left**). These images are used to calculate $\% \Delta R/R$ traces for each neuron (**top-right**). Corresponding behavior videography (**bottom-left**) and forward, sideways, and rotational velocities of the animal (**bottom-right**) are shown.

[Download Video S2.7](#)

Video S2.8: **Behavioral responses associated with dorsal Moonwalker Ascending Neuron activity events.** Behavioral responses associated with dorsal Moonwalker Ascending Neuron activity events. Three example behaviors (rows) produced at the onset of dMAN fluorescence events for three flies (columns). Red squares indicate the onset time of each fluorescence event ($t = 0$ s). Movie is 3x slower than real-time.

[Download Video S2.8](#)

Video S2.9: **Coronal cervical connective imaging of Moonwalker Descending Neurons.** 2-photon imaging of a single coronal section of the cervical connective in a behaving fly. GCaMP6s (cyan) and tdTomato (red) are expressed in MDNs (*MDN-1>GCaMP6s; tdTomato*). Raw fluorescence images of the left and right MDNs are presented and outlined by ROIs (top-left). These images are used to calculate $\% \Delta R/R$ traces for each neuron (top-right). Corresponding behavior videography (bottom-left) and forward, sideways, and rotational velocities of the animal (bottom-right) are shown.

[Download Video S2.9](#)

Video S2.10: **Behavioral responses associated with Moonwalker Descending Neuron activity events.** Descending Neuron activity events. Three example behaviors (rows) produced at the onset of MDN fluorescence events for three flies (columns). Red squares indicate the onset time of each fluorescence event ($t = 0$ s). Movie is 3x slower than real-time.

[Download Video S2.10](#)

Video S2.11: **Coronal cervical connective imaging of A1 neurons.** Descending Neuron activity events. 2-photon imaging of a single coronal section of the cervical connective in a behaving fly. GCaMP6s (cyan) and tdTomato (red) are expressed in A1 neurons (*A1>GCaMP6s; tdTomato*). Raw fluorescence images of the left and right A1 neurons are presented and outlined by ROIs (**top-left**). These images are used to calculate $\% \Delta R/R$ traces for each neuron (**top-right**). Corresponding behavior videography (**bottom-left**) and forward, sideways, and rotational velocities of the animal (**bottom-right**) are shown.

[Download Video S2.11](#)

Video S2.12: **Behavioral responses associated with left A1 neuron activity events.** Three example behaviors (rows) produced at the onset of A1 fluorescence events for three flies (columns). Red squares indicate the onset time of each fluorescence event ($t = 0$ s). Movie is 3x slower than real-time.

[Download Video S2.12](#)

Video S2.13: **Behavioral responses associated with right A1 neuron activity events.** Three example behaviors (rows) for each of three flies (columns) generated at the onset of right A1 neuron fluorescence events. Red squares indicate the time of each fluorescence event ($t = 0$ s). Movie is 3x slower than real-time.

[Download Video S2.13](#)

Video S2.14: **Behaviors and neural activity in Act88F:Rpr and control animals.** Horizontal section imaging data from the prothoracic neuromere of Act88F:Rpr animals (**left**, *Act88F:Rpr/elav-GAL4; GCaMP6s/+*), or control animals (**right**, *+elav-GAL4; GCaMP6s/+*). 2-photon imaging data are not registered.

[Download Video S2.14](#)

Video S2.15: **Coronal and horizontal section imaging of A1 neurons in the VNC.** A comparison of coronal (**left**), or horizontal (**right**) section imaging of the cervical connective in the same animal. GCaMP6s (cyan) and tdTomato (red) are expressed in A1 neurons (*A1>GCaMP6s; tdTomato*). Raw fluorescence images (**top**) are presented alongside corresponding behavior video images (**bottom**).

[Download Video S2.15](#)

Video S2.16: **Long-term behavior in animals used to image dMAN activity.** Behavior movies for three flies (*MAN>GCaMP6s; tdTomato*) during the first imaging experiment (0 min) as well as 20 min and 40 min afterwards.

[Download Video S2.16](#)

Video S2.17: **Long-term behavior in animals used to image MDN activity.** Behavior movies for three flies (*MDN>GCaMP6s; tdTomato*) during the first imaging experiment (0 min) as well as 20 min and 40 min afterwards.

[Download Video S2.17](#)

Chapter 2. Imaging neural activity in the ventral nerve cord of behaving adult *Drosophila*

Video S2.18: **Long-term behavior in animals used to image A1 activity.** Behavior movies for three flies (*A1>GCaMP6s; tdTomato*) during the first imaging experiment (0 min) as well as 20 min and 40 min afterwards.

[Download Video S2.18](#)

3 Ascending neurons convey behavioral state to integrative sensory and action selection centers in the brain

Disclaimer: This chapter is reproduced from the following article with permissions of all co-authors and journal.

Chin-Lin Chen, Florian Aymanns, Ryo Minegishi, Denis Fortun, Victor D. V. Matsuda, Nicolas Talabot, Semih Günel, Barry J. Dickson, Pavan Ramdya. "Ascending neurons convey behavioral state to integrative sensory and action selection centers in the brain", *bioRxiv*, 2022.02.09.479566, 2022. The copy is archived to <https://doi.org/10.1101/2022.02.09.479566>

My contribution: In general, I participated in conceptualizing the project and coordinating with co-authors to accomplish data collection, analysis, and manuscript writing with the advice of Professor Pavan Ramdya. I performed main experiments, including (i) a screen of two-photon imaging in ascending neurons of tethered flies behaving on the spherical treadmill to acquire the neural activity, ball rotations, and behavioral videography simultaneously. (ii) Collaborating with Victor Matsuda to examine the labeling pattern and expression intensity of targeted neurons in each driver line. (iii) Labelling single neurons to check the existence of putative axon terminals among representative ascending neurons based on micro-structures and presynaptic marker expression. (iv) Presenting air and CO₂ puff to flies to check if the neural response in puff-responding ascending neurons is odor-dependent. Data analysis: (i) Building a pipeline to label proboscis extension events by integrating the trained DeepLabCut model for proboscis landmark prediction with the homemade semi-auto event classifier. (ii) Coordinating with Nicolas Talabot to use AxoID to segment regions-of-interest in two-photon image stacks semi-automatically. (iii) Evaluating the covariance between joint angles. (iv) Initial attempt to test the feasibility of linear model to quantify the relationship between neural activity and behavior with a smaller dataset. (v) Collaborating with Florian Aymanns to finalize the version of behavior classes and validate the results of the general linear model with the full dataset.

Chapter 3. Ascending neurons convey behavioral state to integrative sensory and action selection centers in the brain

(vi) Building pipeline for synchronizing two-photon data, ball rotations, and behavioral data, and follow-up analysis of behavior epoch-based neural activity, neural activity event-based ball rotations, and the corresponding statistics. (vii) Tracing single neuron projection in MCFO images from collaborator Barry Dickson and Ryo Minegishi, and quantifying the innervation in the central nervous system. (viii) Investigating the relationship between innervation pattern, encoded behavior, the synchronicity of neural activity. Finally, I worked with Pavan Ramdya in drafting and editing figures and the manuscript, preparing the paper submission, and releasing the dataset and codes.

3.1 Abstract

Knowing one's own behavioral state has long been theorized as critical for contextualizing dynamic sensory cues and identifying appropriate future actions. Ascending neurons (ANs) in the motor system that project to the brain are well-positioned to provide such behavioral state signals. However, what ANs encode and where they convey these signals remains largely unknown. Here, through large-scale functional imaging in behaving flies, deep learning-based analyses, and morphological quantification we investigate the encoding, brain targeting, and motor patterning of 247 genetically-identifiable ANs in the adult fly, *Drosophila melanogaster*. We reveal that ANs encode high-level behaviors, specifically conveying self-motion to the AVL, an integrative sensory hub, and discrete actions to the GNG, a locus for action selection. Additionally, AN projection patterns within the motor system are predictive of their encoding. Thus, ascending populations inform distinct brain hubs of self-motion and ongoing actions: crucial substrates for computations that give rise to adaptive behaviors.

3.2 Introduction

To generate adaptive behaviors, animals [25] and robots [48] must not only sense their environment but also be aware of their own behavioral state including low-level movements of their limbs and high-level behaviors such as walking and resting. This self-awareness has long been theorized to overcome at least two major challenges for robust, autonomous control. First, knowing if one is at rest or in motion permits the accurate interpretation of whether sensory cues, like visual motion during feature tracking or odor intensity fluctuations during plume following, result from exafference (the movement of objects in the world), or reafference (self-motion with respect to stationary objects) [25]. Second, being aware of one's current posture enables the selection of appropriate future actions that are not destabilizing, or physically impossible.

In line with these theoretical predictions, neural representations of behaviors have been observed widely across the brains of mice [4–6], and in the fly, *Drosophila melanogaster* [7–10]. Furthermore, studies in *Drosophila* have supported roles for behavioral state signals in sensory contextualization (e.g., flight [7] and walking [8] modulate neurons in the visual system [9, 33]), and action selection (e.g., an animal's walking speed regulates its decision to run or freeze in response to a fear-inducing stimulus [12]).

Despite these advances, the cellular origins of behavioral state signals in the brain remain largely unknown. On one hand, they might arise from efference copies generated by descending neurons (DNs) in the brain that project to and drive downstream motor systems [25]. However, these efference copies would not be expected to provide the most precise readout of one's own behavioral state: the brain's descending commands are sculpted by musculoskeletal interactions with the environment. Instead, a more categorically and temporally precise readout of ongoing behaviors might be obtained from ascending neurons in the motor system that process proprioceptive and tactile signals and then convey a holistic representation of behavioral states to the brain. Although these behavioral signals may come from a subset of primary mechanosensory neurons in the limbs [30], they are more likely to be computed and conveyed by second- and higher-order ascending neurons (ANs) residing in the spinal cord of vertebrates [24, 26, 27, 29], or insect ventral nerve cord (VNC) [35, 121]. In *Drosophila*, ANs have been shown to process limb proprioceptive and tactile signals [16, 30, 122], perhaps to generate a complex readout of ongoing movements and behaviors.

To date only a few genetically-identifiable AN cell types have been studied in behaving animals—primarily in the fly, *Drosophila melanogaster*, which has a relatively small number of neurons that can also be genetically targeted for repeated investigation. These studies support the hypothesis that ANs are a prominent source of behavioral state signals in the brain. First, microscopy recordings of AN terminals in the brain have shown that Lco2N1 and Les2N1D ANs are active during walking [18], and that LAL-PS-ANs convey walking signals to the visual

Chapter 3. Ascending neurons convey behavioral state to integrative sensory and action selection centers in the brain

system [32]. Second, artificial activation of pairs of PER_{in} ANs [34], or Moonwalker ANs [28] regulate action selection and behavioral persistence, respectively.

These first insights urgently motivate a more comprehensive and quantitative analysis of large AN populations to investigate three fundamental questions. First, what information do ANs convey to the brain (**Figure 3.1A**)? They might encode low-level movements of the joints or limbs, or high-level behavioral states like whether an animal is walking, or grooming. Second, where do ANs convey this information to in the brain (**Figure 3.1B**)? They might project widely across brain regions, or narrowly target circuit hubs with specific functions. Third, what can an AN's patterning within the VNC tell us about how it derives its encoding (**Figure 3.1C, red**)? Answering these questions would open the door to a cellular-level understanding of how neurons encode behavioral states by integrating proprioceptive, tactile, and other sensory feedback signals. It would also enable the study of how behavioral state signals are used by brain circuits to contextualize multimodal cues and select appropriate future actions.

To address these questions, we developed and used a number of advanced experimental and analytical tools. First, we screened a library of split-GAL4 *Drosophila* driver lines (R.M. and B.J.D., unpublished). These, along with the published MAN-spGAL4 [28] and 12 sparsely expressing GAL4 lines [65], together allowed us to gain repeated genetic access to 247 ANs (**Figure 3.1D; Table S3.1**). Using these driver lines and a multi-color flip-out (MCFO) approach [70], we then quantified the projections of ANs within the brain and VNC (**Figure 3.1E**). Second, we screened the encoding of these ANs by two-photon microscopy-based functional recordings of neural activity within the VNC of tethered, behaving flies [49]. To overcome noise and movement-related deformations in imaging data, we developed and used 'AxoID', a deep learning-based software to semi-automatically identify and track axonal Regions-of-Interest (ROIs)(see Methods). Third, to precisely quantify joint angles and limb kinematics, we used a multicamera array to record behavior during two-photon imaging. We processed these videos using DeepFly3D, a deep learning-based 3D pose estimation software [56]. By combining these 3D joint positions with measured spherical treadmill rotations, a proxy for locomotor velocities [40], we could then segment and classify behavioral time-series to study the relationship between behavioral states and ongoing neural activity using linear models.

These analyses uncovered a number of fundamental characteristics of ANs. First, as a population, ANs do not project broadly across the brain but principally target two hubs: (i) the anterior ventrolateral protocerebrum (AVLP), a site for higher-order multimodal convergence—vision [123], olfaction [124], audition [125–127], and taste [128]—, and (ii) the gnathal ganglion (GNG), a region important for action selection [34, 38, 129]. Second, ANs encode high-level behavioral states, primarily walking, rather than low-level joint or limb movements. Third, distinct behavioral states are systematically conveyed to different brain targets. The AVLP is informed of self-motion states like resting, walking, and the presence of gust-like stimuli,

perhaps to contextualize sensory cues. By contrast, the GNG receives precise signals about actions—turning, eye grooming, and proboscis extension—likely to guide action selection.

To understand the relationship between AN behavioral state encoding and brain projection patterns, we then performed a more in-depth investigation of seven AN classes. We observed a correspondence between the morphology of ANs in the VNC and their behavioral state encoding: ANs with neurites targeting all three VNC neuromeres (T1-T3) encode global locomotor states (e.g., resting and walking) while those with projections only to the T1 prothoracic neuromere encoded foreleg-dependent behaviors (e.g., eye grooming). Notably, we also observed AN axons within the VNC. This suggests that ANs are not simply passive relays of behavioral state signals to the brain but that they may also help to orchestrate motor actions and/or compute state encodings. This latter possibility is illustrated by a class of ‘PE-ANs’ that seems to encode the number of proboscis extensions generated over tens of seconds, possibly through recurrent interconnectivity within the VNC. In summary, these data provide a first comprehensive view of ascending signals to the brain, opening the door for a cellular-level understanding of how behavioral states are computed, and how ascending motor signals enable the brain to contextualize sensory signals and select appropriate future actions.

3.3 Results

3.3.1 A large-scale screen of ascending neuron movement encoding, brain targeting, and motor system patterning

We performed a functional screen of 108 driver lines that each express fluorescent reporters in a small number of ANs (**Figure 3.1D**). This allowed us to address to what ANs encode low-level joint and limb movements, or high-level behavioral states. To quantify limb movements, we recorded each fly using six synchronized cameras (a seventh camera was used to position the fly on the ball) (**Figure 3.1F**). We processed these videos using DeepFly3D [56], a markerless 3D pose estimation software that outputs joint positions and angles (**Figure 3.1G**). We also measured spherical treadmill rotations using two optic flow sensors [40] and converted these into three fly-centric velocities: forward (mm/s), sideways (mm/s), and yaw (degree/s) (**Figure 3.1H**) that correspond to forward/backward walking, side-slip, and turning, respectively. A separate DeepLabCut [59] deep neural network was used to track proboscis extensions (PEs) from one camera view (**Figure S3.1A-D**). We studied spontaneously generated actions but also used a puff of CO₂ to elicit behaviors from sedentary animals.

Synchronized with movement quantification, we recorded the activity of ANs by performing two-photon imaging of the cervical connective within the thoracic ventral nerve cord (VNC) [49]. The VNC houses motor circuits that are functionally equivalent to those in the vertebrate spinal cord (**Figure 3.1I, left**). Neural activity was read-out as changes in the fluorescence of a genetically-encoded calcium indicator, OpGCaMP6f, expressed in a small number

Chapter 3. Ascending neurons convey behavioral state to integrative sensory and action selection centers in the brain

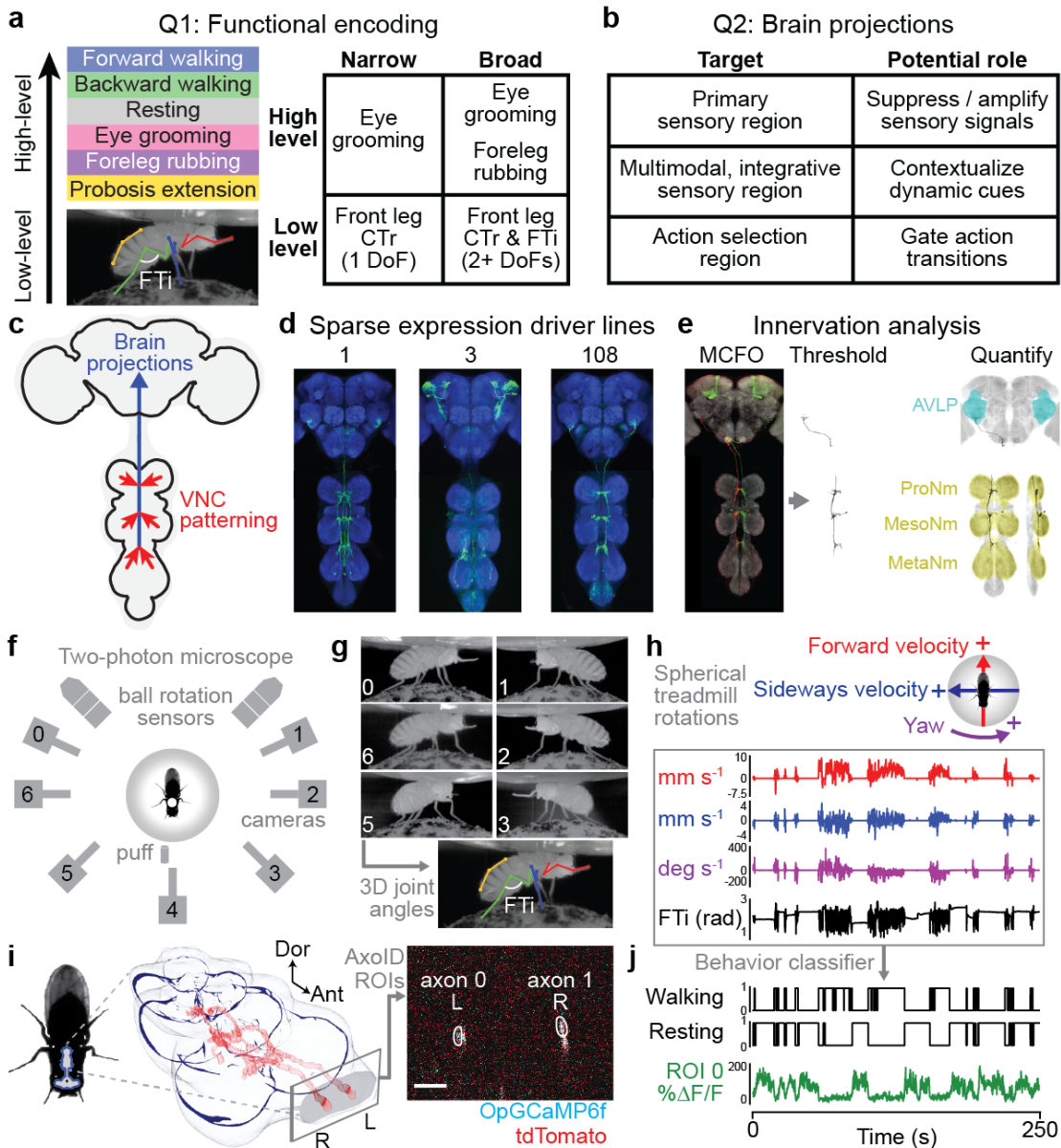


Figure 3.1: Large-scale functional and morphological screen of ascending neuron movement encoding and nervous system targeting. (a-c) Schematics and tables of the main questions addressed. (a) To what extent do ascending neurons (ANs) encode high-level behaviors, or low-level limb movements? This encoding may be either narrow (e.g., one behavior, or joint degree-of-freedom), or broad (e.g., several behaviors, or joint DoFs). (b) Where in the brain do ANs convey behavioral states? ANs might target the brain's (i) primary sensory regions (e.g., optic lobe, or antennal lobe) for sensory gain control, (ii) multimodal and integrative sensory regions (e.g., anterior ventrolateral protocerebrum, or mushroom body) to contextualize dynamic, time-varying sensory cues, and (iii) action selection centers (e.g., gnathal ganglion, or central complex) to gate action transitions. Individual ANs may project broadly to multiple

brain regions, or narrowly to one region. (C) To what extent is an AN's patterning within the VNC predictive of its brain targeting and encoding? (d) We screened 108 sparsely expressing driver lines. The projection patterns of the lines with active ANs and high signal-to-noise ratio (157 ANs) were examined in the brain and VNC. (e) These were quantified by tracing single-cell MCFO confocal images. (f) Overhead schematic of the behavior measurement system used during two-photon microscopy. A camera array captures six views of the animal. Two optic flow sensors measure ball rotations. A puff of CO₂ (or air) is used to elicit behavior from sedentary animals. (g) 2D poses are estimated for six camera views using DeepFly3D. These data are triangulated to quantify 3D poses and joint angles for six legs and the abdomen (color-coded). The Femur-Tibia (FTi) joint angle is indicated (white). (h) Two optic flow sensors measure rotations of the spherical treadmill as a proxy for forward (red), sideways (blue), and yaw (purple) walking velocities. Positive directions of rotation ('+') are indicated. (i, left) A volumetric representation of the ventral nerve cord (VNC) including a reconstruction of ANs targeted by the *SS27485-spGAL4* driver line (red). Indicated are the dorsal-ventral ('Dor') and anterior-posterior ('Ant') axes, as well as the fly's left (L) and right (R) sides. (i, right) Sample two-photon cross-section image of the thoracic neck connective showing ANs that express OpGCaMP6f (cyan) and tdTomato (red). AxoID is used to semi-automatically identify two axonal regions-of-interest (ROIs, white) on the left ('L') and right ('R') sides of the connective. (j) Spherical treadmill rotations and joint angles are used to classify behaviors. Binary classifications are then compared with simultaneously recorded neural activity for 250 s trials of spontaneous and puff-elicited behaviors. Shown is an activity trace from ROI 0 (green) in panel i.

See also [Figure S3.1](#), and [Video S3.1](#), [Video S3.2](#), and [Video S3-52](#).

of ANs. Simultaneously, we recorded tdTomato fluorescence as an anatomical fiduciary. Imaging coronal (x-z) sections of the cervical connective allowed us to keep AN axons within the imaging field-of-view despite behaviorally-induced motion artifacts that would disrupt conventional horizontal (x-y) section imaging [49]. Sparse spGAL4 and GAL4 fluorescent reporter expression facilitated axonal region-of-interest (ROI) detection. To semi-automatically segment and track AN ROIs across thousands of imaging frames, we developed and used AxoID, a deep network-based software ([Figure 3.1I, right](#); [Figure S3.2](#)). AxoID also helped perform ROI detection despite significant movement-related ROI translations and deformations as well as, for some driver lines, relatively low transgene expression levels and suboptimal imaging signal-to-noise ratios (SNR).

To relate AN neural activity with ongoing limb movements, we trained classifiers using 3D joint angles and spherical treadmill rotational velocities to accurately and automatically detect nine behaviors—forward and backward walking, spherical treadmill pushing, resting, eye and antennal grooming, foreleg and hindleg rubbing, and abdominal grooming ([Figure 3.1J](#)). This classification was highly accurate ([Figure S3.1E](#)). Additionally, we classified non-orthogonal, co-occurring behaviors like proboscis extensions (PEs) and recorded the timing of CO₂ puff stimuli ([Video S3-52](#)).

Chapter 3. Ascending neurons convey behavioral state to integrative sensory and action selection centers in the brain

Our final dataset encompassed 247 ANs targeted using 70 sparsely-labelled driver lines (more than 32 h of data). These data included (i) anatomical projection patterns, and temporally synchronized (ii) neural activity, (iii) joint angles, and (iv) spherical treadmill rotations. Here we focus on the results for 157 of the most active ANs taken from 50 driver lines (more than 23 h of data) (**Video S3.2**). The remainder were excluded due to redundancy with other driver lines, a lack of neural activity, or a low SNR (as determined by smFP confocal imaging, or two-photon imaging of tdTomato and OpGCaMP6f). Representative data from each of these selected driver lines illustrate the richness of our dataset (**Video S3-52**).

3.3.2 Ascending neurons encode high-level behaviors

With these data, we first asked to what extent AN activity encode low-level joint angles and leg movements, or high-level behaviors like walking, resting, and grooming (**Figure 3.1A**). We expected that, unlike primary limb mechanosensory neurons, second- and higher-order ANs would more likely integrate and process proprioceptive and tactile sensory signals to encode high-level behavioral states. This remained unknown because previous studies of AN encoding [18,32,34] did not quantify movements at high enough resolution, or study more than a few ANs in total. To address this gap, with the data from our large-scale functional screen, we performed a linear regression analysis to quantify the degree to which the movements of individual joints, legs, pairs of legs, or epochs of high-level behaviors could explain the time-course of AN activity. Specifically, we quantified the unique explained variance (UEV, or ΔR^2) for each movement, or behavioral regressor via cross-validation by subtracting a reduced model R^2 from a full regression model R^2 . Specifically, in the reduced model, the regressor of interest was shuffled while keeping the other regressors intact (see Methods). To compensate for the temporal mismatch between fast leg movements and slower calcium signal decay dynamics, every joint angle and behavioral state regressor was convolved with a calcium indicator decay kernel chosen to maximize the explained variance in neural activity, with the aim of reducing the occurrence of false negatives.

First we examined to what extent individual joint angles could explain the activities of 157 ANs. We confirmed that the vast majority of joint angles do not covary with others—with the exception of the middle and hindleg CTr and FTi pitch angles, which were correlated to one another (**Figure S3.3**). This is important because if two regressors are highly correlated, one regressor can compensate when shuffling the other, resulting in a potential false negative. We did not find any evidence of joint angles explaining AN activity (**Figure 3.2A**). Similarly, individual leg movements (tested by shuffling all of the joint angle regressors for a given leg) could not explain the variance of AN activity (**Figure 3.2B**). Additionally, with the exception of ANs from SS25469 whose activities could be explained by movements of the front legs (**Figure 3.2C**), AN activity largely could not be explained by the movements of pairs of legs. By contrast, the activity of ANs could be explained by high-level behavioral states (**Figure 3.2D**).

Most ANs encoded self-motion—forward walking and resting—but some also encoded specific actions like eye grooming, proboscis extensions, as well as responses to puff stimuli.

Our regression approach is inherently conservative: it avoids false positives. However, because it is thus prone to false negatives for infrequently occurring behaviors like abdominal grooming and hindleg rubbing, as an additional alternative approach, we measured the mean normalized $\Delta F/F$ of each AN for each high-level behavioral state. Using this complementary approach, we confirmed and extended our results (**Figure S3.4A**). We considered results from both our linear regression and mean normalized $\Delta F/F$ analyses when selecting neurons for further in-depth analyses.

3.3.3 Ascending neurons target integrative sensory, or action selection brain regions as a function of their encoding

Having identified high-level behavioral state encoding for a large population of 157 ANs, we next wondered to what extent these distinct state signals are routed to specific and distinct brain targets (**Figure 3.1B**). On one hand, individual ANs might project diffusely to multiple brain regions. Alternatively, they might target one, or only a few regions. For instance, locomotor signals carried by walking and resting encoding ANs might be conveyed to brain regions to contextualize time-varying visual and olfactory cues with respect to an animal's own self-motion. On the other hand, ANs that signal when an animal is grooming might target action selection brain regions to prohibit future actions that might result in unstable postures. To address these possibilities, we quantified the brain projections of all 157 ANs by staining and imaging the expression of spFP and MCFO reporters in these neurons (**Figure 3.1E**).

Strikingly, we found that AN projections to the brain were largely restricted to two regions: the AVLP, a site known for multimodal, integrative sensory processing [123–128] and the GNG, a hub for action selection [34, 38, 129] (**Figure 3.3A**). ANs encoding resting and puff-responses almost exclusively target the AVLP (**Figure S3.4B,C**) providing a means for interpreting whether sensory cues arise from self-motion, or the movement of objects in the external environment (i.e., while resting, an animal might still perceive visual motion due to moving objects, or odor fluctuations due to gust-like puffs of air). By contrast, the GNG is targeted by ANs encoding a wide variety of behavioral states including walking, eye grooming, and proboscis extensions (**Figure S3.4B,C**). These signals may help to ensure that future actions are compatible with ongoing ones.

Because AN dendrites and axons within the VNC might be used to compute behavioral state encodings, we next asked to what extent their projection patterns within the VNC are predictive of an AN's encoding. For example, ANs encoding resting might require sampling each VNC leg neuromere (T1, T2, and T3) to confirm that every leg is inactive. By quantifying AN projections within the VNC (**Figure 3.3B**), we found that, indeed, an AN's VNC projection pattern can

Chapter 3. Ascending neurons convey behavioral state to integrative sensory and action selection centers in the brain

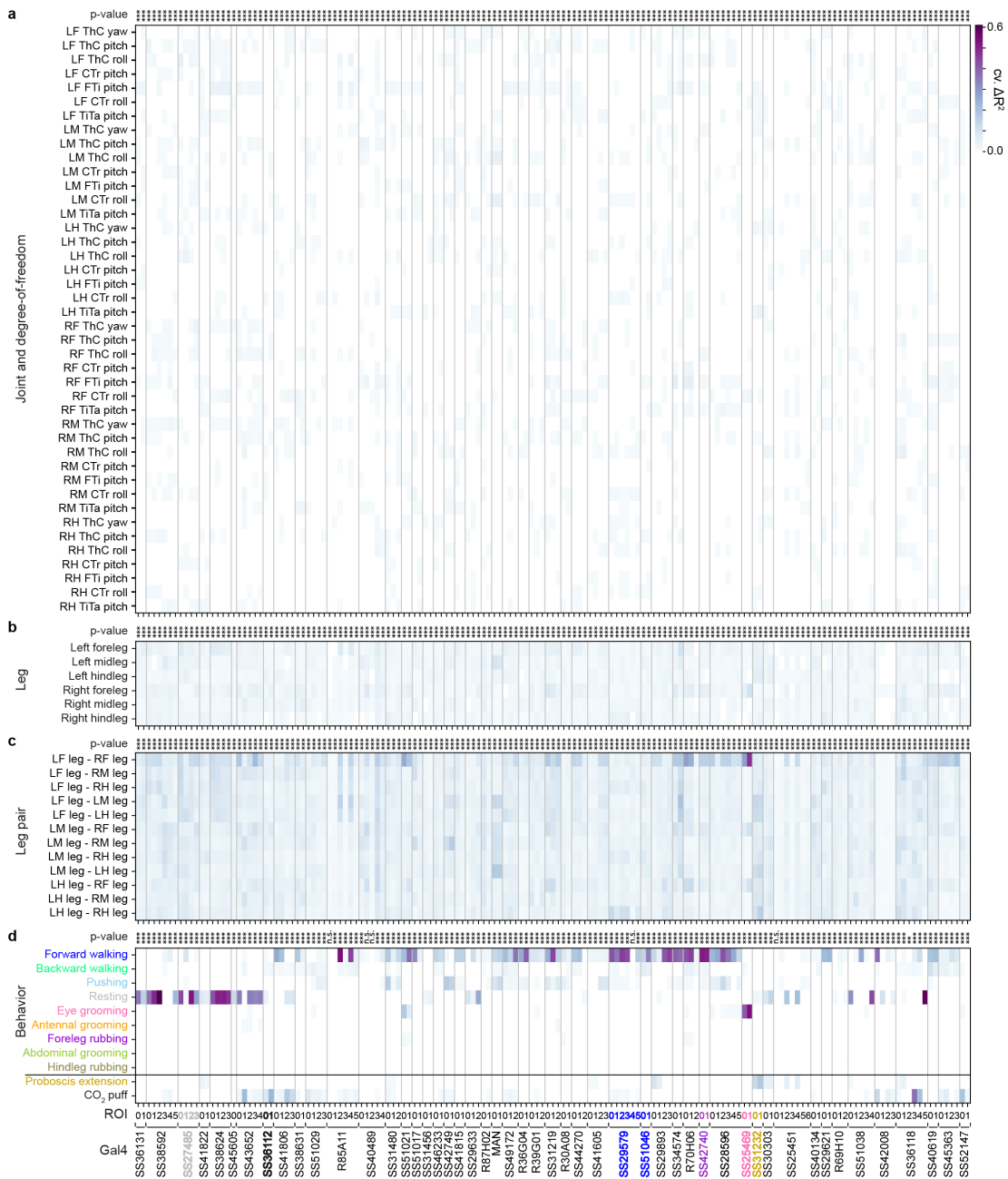


Figure 3.2: Ascending neurons encode high-level behaviors. Proportion of variance in AN activity that is uniquely explained by regressors (cross-validated ΔR^2) based on (a) joint movements, (b) the movements of individual legs, (c) the movements of pairs of legs, (d) high-level behaviors. Regression analyses were performed for 157 ANs recorded from 50 driver lines. Lines selected for more in-depth analysis are color-coded by the behavioral class best explaining their neural activity: SS27485 (resting), SS36112 (puff responses), SS29579 (walking), SS51046 (turning), SS42740 (foreleg movements), SS25469 (eye grooming), and SS31232 (proboscis extensions). Non-orthogonal regressors (PE and CO₂ puffs) are separated

from the others. p -values report the F-statistic of overall significance of the complete regression model with none of the regressors shuffled (* $p < 0.05$, ** $p < 0.01$, and *** $p < 0.001$). See also [Figure S3.3](#) and [Figure S3.4](#).

be predictive of behavioral state encoding. As hypothesized, ANs encoding resting (e.g., SS27485) each project to all VNC leg neuromeres ([Figure S3.4B,D](#)). By contrast, ANs encoding foreleg-dependent eye grooming (SS25469) only project within the T1 VNC neuromere housing motor circuits to control the front legs ([Figure S3.4B,D](#)). To more deeply understand how the morphological features of ANs relate to behavioral state encoding, we next performed a detailed study of a diverse subset of ANs that encode resting, puff-responses, walking, turning, foreleg-dependent behaviors, eye grooming, and proboscis extensions.

3.3.4 Distinct rest- and puff-encoding by morphologically similar ANs

AN classes that encode resting and puff responses exhibit coarsely similar projection patterns: both almost exclusively target the brain's AVLP while also both sampling from all three VNC leg neuromeres (T1-T3) ([Figure S3.4](#)). We therefore next investigated which more detailed morphological features might be predictive of their very distinct encoding.

We addressed this question by closely examining the functional and morphological properties of specific pairs of 'rest-ANs' (SS27485) and 'puff-ANs' (SS36112). Neural activity traces of rest-ANs and puff-ANs could be reliably predicted by regressors for resting ([Figure 3.4A](#)), and puff-stimuli ([Figure 3.4G](#)), respectively. This was statistically confirmed by comparing behavior-triggered averages of AN responses at the onset of resting ([Figure 3.4B](#)), versus puff stimulation ([Figure 3.4H](#)), respectively. Importantly, although CO₂ puffs frequently elicited brief periods of backward walking, close analysis revealed that puff-ANs primarily respond to gust-like puffs and do not encode backward walking ([Figure S3.5A-D](#)). They also did not encode responses to CO₂ specifically: the same neurons responded equally well to puffs of air ([Figure S3.5E-M](#)).

As mentioned, rest- and puff-ANs, despite their very distinct encoding, exhibit similar innervation patterns in the brain and VNC. However, MCFO-based single neuron analysis revealed a few subtle but potentially important differences. First, rest- and puff-AN cell bodies are located in the T2 ([Figure 3.4C](#)) and T3 ([Figure 3.4I](#)) neuromeres, respectively. Second, although both AN classes project medially into all three leg neuromeres (T1-T3), rest-ANs have a simpler morphology ([Figure 3.4D](#)) compared with the more complex arborization of puff-ANs in the VNC ([Figure 3.4J](#)). In the brain, both AN types project to nearly the same ventral region of the AVLP where they exhibit varicose terminals ([Figure 3.4E](#) and [Figure 3.4K](#)). Using *syt:GFP*, a GFP tagged synaptotagmin (presynaptic) marker, we confirmed that these varicosities house

Chapter 3. Ascending neurons convey behavioral state to integrative sensory and action selection centers in the brain

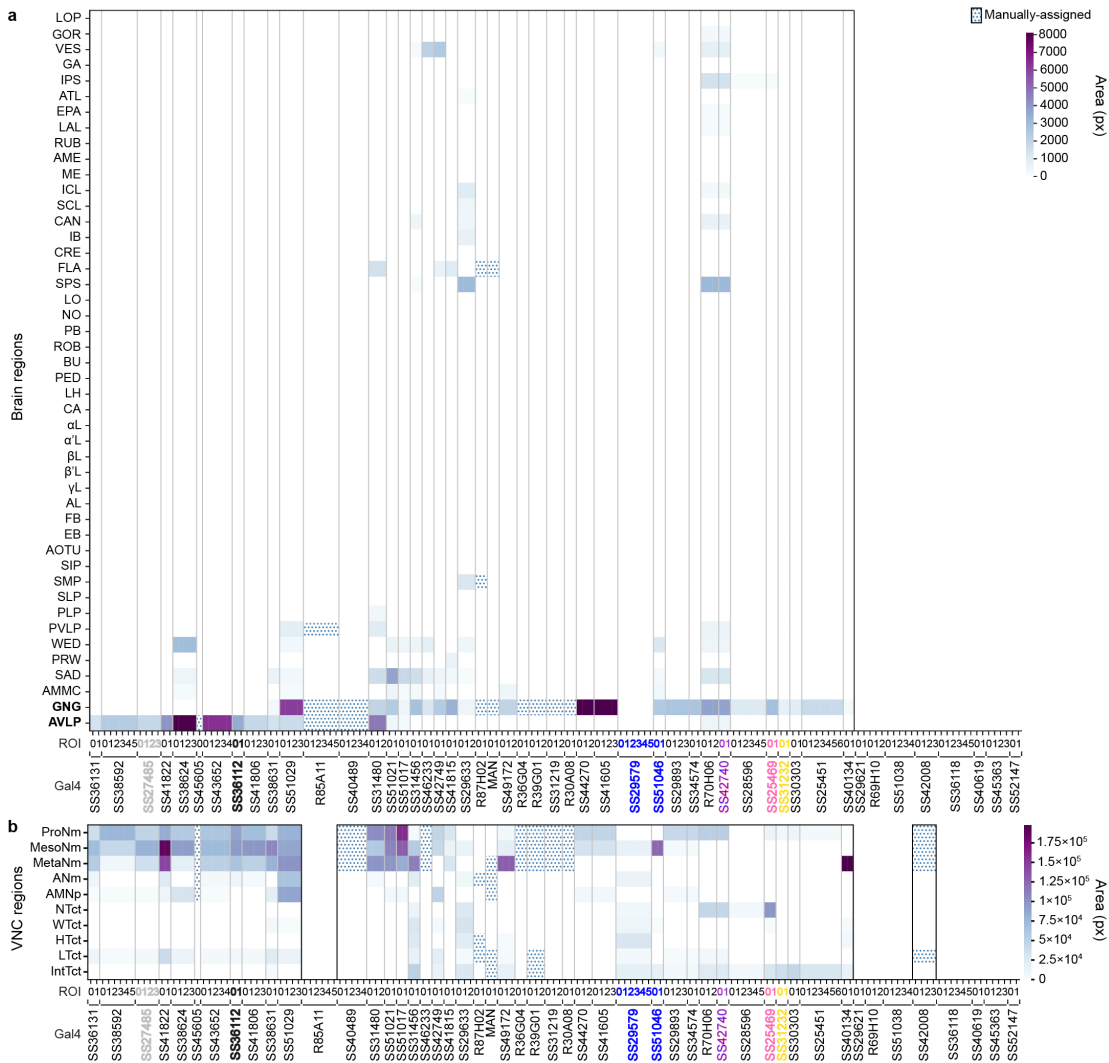


Figure 3.3: Ascending neurons principally project to the brain's AVLP and GNG and the VNC's leg neuromeres. Regional innervation of (a) the brain, or (b) the VNC. Data are for 157 ANs recorded from 50 driver lines and automatically quantified through pixel-based analyses of MCFO labeled confocal images. Other, manually quantified driver lines are indicated (dotted). Lines for which projections could not be unambiguously identified are left blank. Lines selected for more in-depth evaluation are color-coded by the behavioral state that best explains their neural activity: SS27485 (resting), SS36112 (puff responses), SS29579 (walking), SS51046 (turning), SS42740 (foreleg-dependent behaviors), SS25469 (eye grooming), and SS31232 (proboscis extensions).

See also [Figure S3.4](#).

synaptic terminals ([Figure 3.4F, top](#) and [Figure 3.4L, top](#)). Notably, in addition to smooth, likely dendritic arbors, both AN classes have axon terminals within the VNC ([Figure 3.4F, bottom](#) and [Figure 3.4L, bottom](#)).

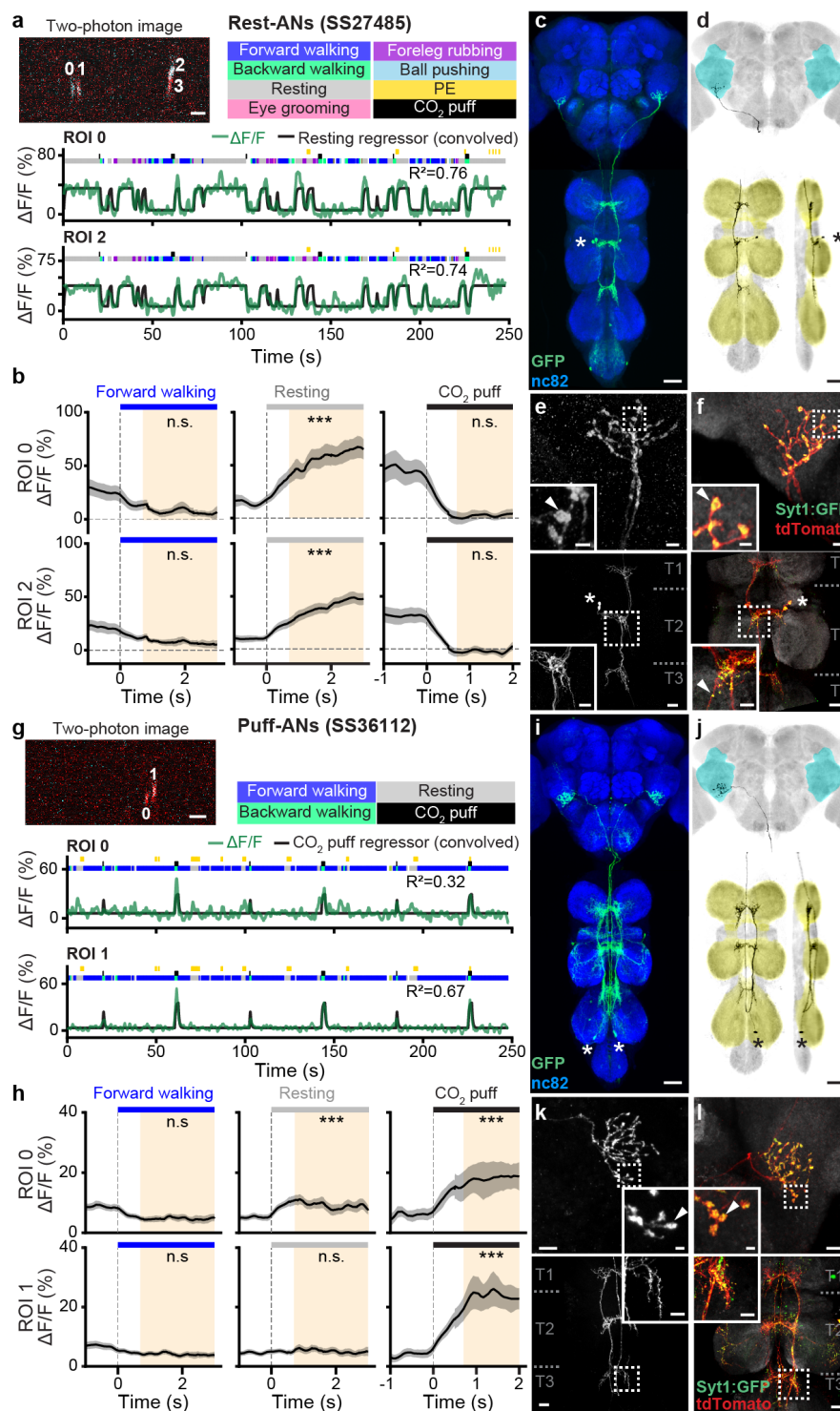


Figure 3.4: Functional and anatomical properties of ascending neurons that encode resting, or responses to puffs. (a,g) (top-left) Two-photon image of axons from an **(a)** *SS27485-GAL4*, or **(g)** *SS36112-GAL4* animal expressing OpGCaMP6f (cyan) and tdTomato (red). ROIs are

Chapter 3. Ascending neurons convey behavioral state to integrative sensory and action selection centers in the brain

numbered. Scale bars are $5\mu\text{m}$. **(bottom)** Behavioral epochs are color-coded. Representative $\Delta F/F$ time-series from two ROIs (green) overlaid with a prediction (black) obtained by convolving **(a)** resting epochs, or **(g)** puff stimuli with Ca^{2+} indicator response functions. Explained variances are indicated (R^2). **(b,h)** Mean (solid line) and 95% confidence interval (gray shading) of $\Delta F/F$ traces for **(b)** rest-ANs, or **(h)** puff-ANs during epochs of forward walking (left), resting (middle), or CO_2 puffs (right). 0 s indicates the start of each epoch. Here and for similar analyses in later figures, data more than 0.7s after onset (yellow region) are compared with an otsu thresholded baseline (ANOVA and Tukey posthoc comparison, *** $p < 0.001$, ** $p < 0.01$, * $p < 0.05$, n.s. not significant). **(c,i)** Standard deviation projection image of an **(c)** *SS27485-GAL4*, or **(i)** *SS36112-GAL4* nervous system expressing smFP and stained for GFP (green) and Nc82 (blue). Cell bodies are indicated (white asterisk). Scale bars are $40\mu\text{m}$. **(d,j)** Projection as in **(c,i)** but for one MCFO-expressing, traced neuron (black asterisk). The brain's AVL (cyan) and VNC's leg neuromeres (yellow) are color-coded. Scale bars are $40\mu\text{m}$. **(e,f,k,l)** Higher magnification projections of **(top)** brains and **(bottom)** VNCs from **(e,f)** *SS27485-GAL4*, or **(k,l)** *SS36112-GAL4* animals expressing **(e,k)** the stochastic label MCFO, or **(f,l)** the synaptic marker, syt:GFP (green), and tdTomato (red). Insets magnify dashed boxes. Indicated are cell bodies (asterisks), bouton-like structures (white arrowheads), and VNC leg neuromeres ('T1, T2, T3'). Scale bars for brain images and insets are **(e)** $5\mu\text{m}$ or **(k)** $10\mu\text{m}$, and $2\mu\text{m}$ for insets. Scale bars for VNC images and insets are $20\mu\text{m}$ and $10\mu\text{m}$, respectively. See also [Figure S3.5](#).

Taken together, these results demonstrate that even very subtle differences in VNC patterning can give rise to dramatically different AN tuning properties. In the case of rest- and puff-ANs, we speculate that this might be due to physically close, but distinct presynaptic partners—possibly leg proprioceptive afferents for rest-ANs, and leg tactile afferents for puff-ANs.

3.3.5 Walk- or turn- encoding correlates with the laterality of VNC projections

Among the ANs we analyzed, most encode walking ([Figure 3.2D](#)). However, this broad category of locomotion includes more subtle dimensions including walking direction and turning. We reasoned that an AN's patterning within the VNC may be predictive of whether it encodes locomotion broadly (e.g., walking), or narrowly (e.g., turning).

Indeed, we observed that while the activity of one pair of ANs (SS29579, 'walk-ANs') was remarkably well explained by the timing and onset of walking epochs ([Figure 3.5A-C](#)), for other ANs a broad walking regressor could account for much less of the variance in neural activity ([Figure 3.2D](#)). We reasoned that these ANs might instead encode narrower locomotor dimensions like turning. For a bilateral pair of DN01 descending neurons, their difference in activity correlates with turning direction [49, 130]. To see if this relationship might also hold for some pairs of walk-encoding ANs, we quantified the degree to which the difference in pairwise activity can be explained by spherical treadmill yaw or roll velocity—a proxy for turning

(**Figure 3.5H**). Indeed, we found several pairs of ANs for which turning explained a relatively large amount of variance. For one pair of ‘turn-ANs’ (SS51046), although a combination of forward and backward walking regressors poorly predicted neural activity (**Figure 3.5I**), a regressor based on spherical treadmill roll velocity strongly predicted the pairwise difference in neural activity (**Figure 3.5J**). When an animal turned right, the right (ipsilateral) turn-AN was more active, and the left turn-AN was more active during left turns (**Figure 3.5K**). During forward walking, both turn-ANs were active (**Figure 3.5L**).

We next asked how VNC patterning might predict this distinction between broad (walk-ANs) versus narrow (turn-ANs) locomotor encoding. Both AN classes have cell bodies in the VNC’s T2 neuromere (**Figure 3.5D,M**). However, walk-ANs bilaterally innervate the T2 neuromere (**Figure 3.5E**), whereas turn-ANs unilaterally innervate T1 and T2 (**Figure 3.5N, black**). Their ipsilateral T2 projections are smooth and likely dendritic (**Figure 3.5O₁,P₁**), while their contralateral T1 projections are varicose and exhibit *syt:GFP* puncta, suggesting that they harbor presynaptic terminals (**Figure 3.5O₂,P₂**). Both walk-ANs (**Figure 3.5D,E**) and turn-ANs (**Figure 3.5M,N**) project to the brain’s GNG. However, only turn-ANs project to the WED (**Figure 3.5N**). Notably, walk-AN terminals in the brain (**Figure 3.5F**) are not labelled by *syt:GFP* (**Figure 3.5G**), suggesting that they may be neuromodulatory in nature, relying on another class of synaptic machinery [131].

These data support the notion that broad versus narrow AN behavioral state encoding may depend on the laterality of VNC patterning. Additionally, we observed that pairs of broadly-tuned walk-ANs that bilaterally innervate the VNC are synchronously active. By contrast, pairs of narrowly-tuned turn-ANs are asynchronously active. This correlation between the bilaterality of an AN pair’s VNC projections and their synchrony appears to be a general principle (**Figure S3.6**).

Chapter 3. Ascending neurons convey behavioral state to integrative sensory and action selection centers in the brain

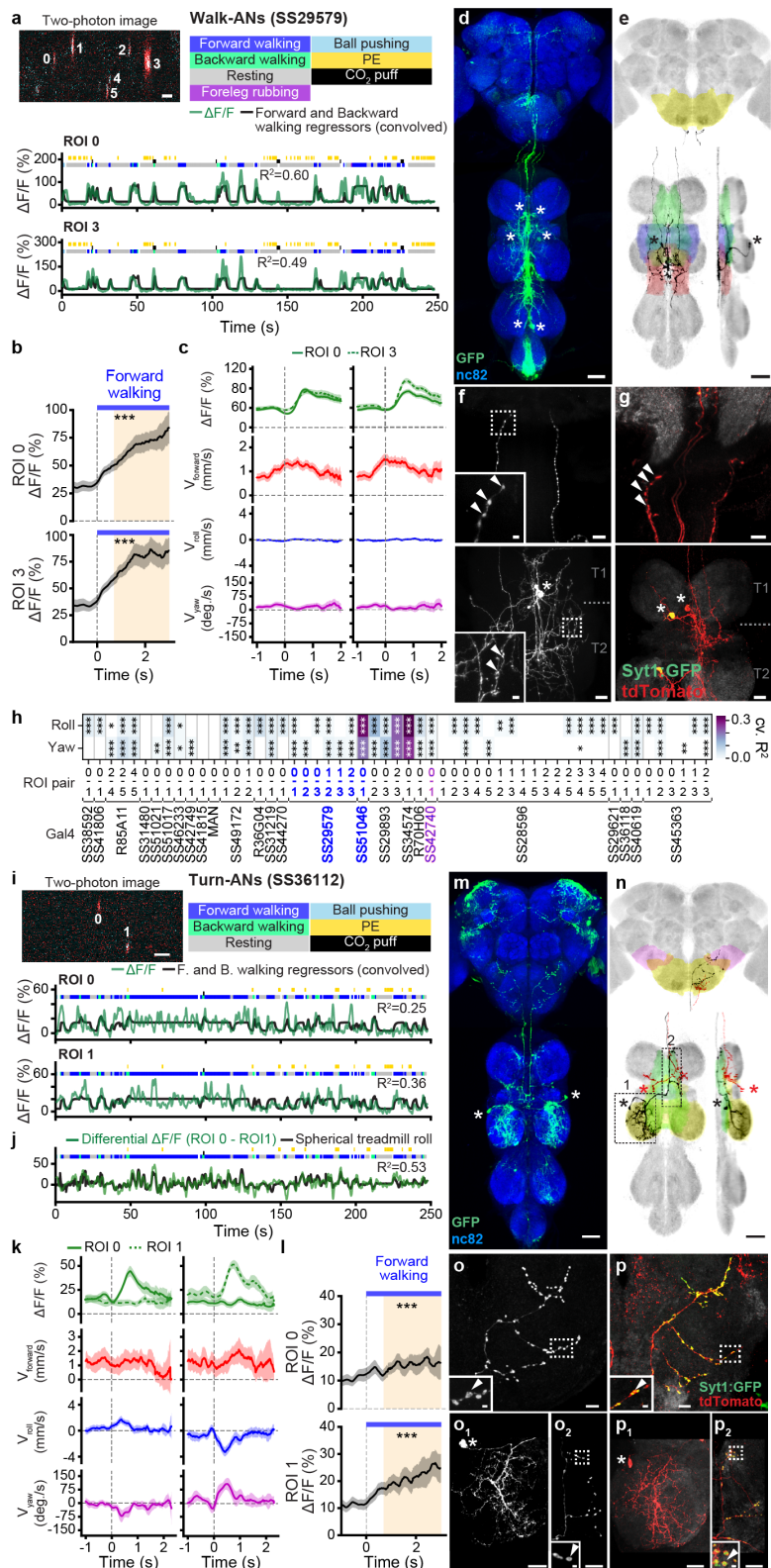


Figure 3.5: **Functional and anatomical properties of ascending neurons that encode walking, or turning.** (a, i) (top-left) Two-photon image of axons from an (a) SS29579-GAL4, or (i) SS51046-GAL4 animal expressing OpGCaMP6f (cyan) and tdTomato (red). ROIs are numbered.

Scale bars are 5 μm . **(bottom)** Behavioral epochs are color-coded. Representative $\Delta\text{F}/\text{F}$ time-series from two ROIs (green) overlaid with a prediction (black) obtained by convolving forward and backward walking epochs with Ca^{2+} indicator response functions. Explained variance is indicated (R^2). **(b,l)** Mean (solid line) and 95% confidence interval (gray shading) of $\Delta\text{F}/\text{F}$ traces during epochs of forward walking. 0 s indicates the start of each epoch. **(c,k)** Fluorescence (OpGCaMP6f) event-triggered average ball rotations for **(left)** ROI 0, or **(right)** ROI 3 of **(c)** an *SS29579-GAL4* animal, or **(left)** ROI 0, or **(right)** ROI 1 of **(k)** an *SS51046-GAL4* animal. Fluorescence events are time-locked to 0 s (green). Shown are mean and 95% confidence intervals for forward (red), roll (blue), and yaw (purple) ball rotational velocities. **(d,m)** Standard deviation projection image for a **(d)** *SS29579-GAL4*, or **(m)** *SS51046* nervous system expressing smFP and stained for GFP (green) and Nc82 (blue). Cell bodies are indicated (white asterisks). Scale bar is 40 μm . **(e,n)** Projection as in **d, m** but for one MCFO-expressing, traced neuron (black asterisks). The brain's GNG (yellow) and WED (pink), and VNC's intermediate (green), wing (blue), haltere (red) tectulum and mesothoracic leg neuromere (yellow) are color-coded. Scale bar is 40 μm . **(f,g,o,p)** Higher magnification projections of **(top)** brains and **(bottom)** VNCs of **(f,g)** *SS29579-GAL4* animals, or **(o,p)** *SS51046-GAL4* animals expressing **(f,o)** the stochastic label MCFO, or **(g,p)** the synaptic marker, *syt:GFP* (green), and tdTomato (red). Insets magnify dashed boxes. Indicated are cell bodies (asterisks), bouton-like structures (white arrowheads), and VNC leg neuromeres ('T1, T2'). **o₁** and **p₁**, or **o₂** and **p₂** correspond to the locations '1' and '2' in **(n)**. Scale bars for brain images and insets are 10 μm and 2 μm , respectively. Scale bars for VNC images and insets are 20 μm and 4 μm , respectively. See also [Figure S3.6](#).

3.3.6 Foreleg-dependent actions are encoded by ANs in the anterior VNC

In addition to locomotion, flies use their forelegs to perform complex movements including reaching, boxing, courtship tapping, and several kinds of grooming—eye grooming, antennal grooming, and foreleg rubbing. An ongoing awareness of these behavioral states is critical to select appropriate future actions that do not lead to unstable postures. For example, before deciding to groom its hindlegs, an animal must first confirm that its forelegs are stably on the ground and not also grooming.

We noted that some ANs project only to the VNC's anterior-most, T1 leg neuromere ([Figure S3.4D](#)). This pattern implies a potential role in encoding actions that only depend on the forelegs. Indeed, close examination revealed two classes of ANs that encode foreleg-related behaviors. We found ANs (SS42740) that were broadly active during multiple foreleg-dependent behaviors including walking, pushing, and grooming ('foreleg-ANs'; overlaps with R70H06) ([Figure S3.4A](#)) ([Figure 3.6A,B](#)). By contrast, another pair of ANs (SS25469) was narrowly tuned and sometimes asynchronously active only during eye grooming ('eye groom-ANs') ([Figure S3.4A,B](#)) ([Figure 3.6G,H](#)). Similar to walking and turning, we hypothesized that this broad (foreleg) versus narrow (eye groom) behavioral encoding might be reflected by a difference in the promiscuity and laterality of AN innervations in the VNC.

Chapter 3. Ascending neurons convey behavioral state to integrative sensory and action selection centers in the brain

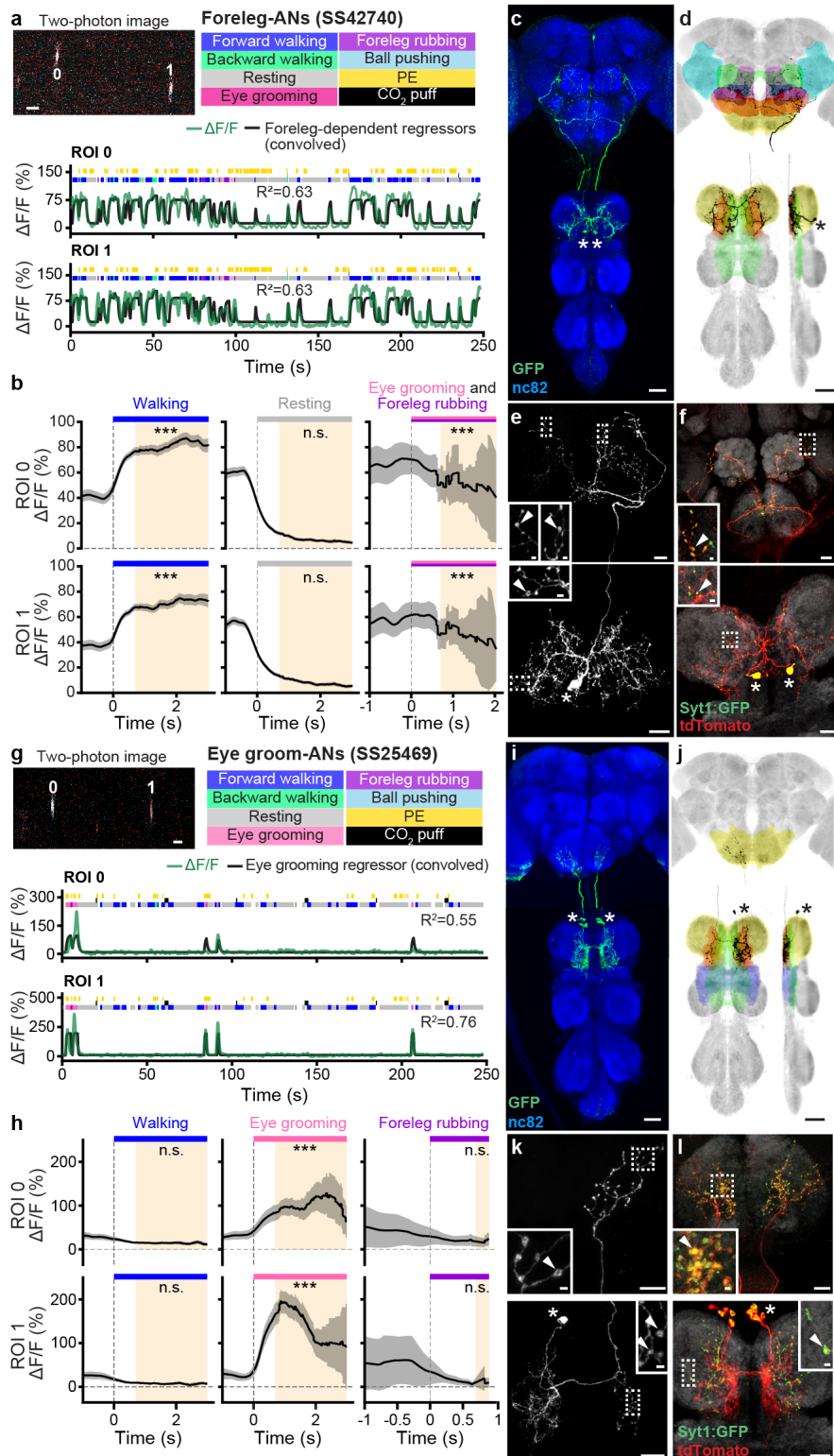


Figure 3.6: **Functional and anatomical properties of ascending neurons that encode multiple foreleg behaviors, or only eye grooming.** (a,g) (top-left) Two-photon image of axons from an (a) *SS42740-GAL4*, or (g) *SS25469-GAL4* animal expressing OpGCaMP6f (cyan) and tdTomato (red). ROIs are numbered. Scale bar is 5 μ m. (bottom) Behavioral epochs are color-coded.

Representative $\Delta F/F$ time-series from two ROIs (green) overlaid with a prediction (black) obtained by convolving all foreleg-dependent behavioral epochs (forward and backward walking as well as eye, antennal, and foreleg grooming) for an **(a)** *SS42740-GAL4* animal, or eye grooming epochs for an **(g)** *SS25469-GAL4* animal with Ca^{2+} indicator response functions. Explained variance is indicated (R^2). **(b,h)** Mean (solid line) and 95% confidence interval (gray shading) of $\Delta F/F$ traces for **(b)** foreleg-ANs during epochs of forward walking (left), resting (middle), or eye grooming and foreleg rubbing (right), or **(h)** eye groom-ANs during forward walking, eye grooming, or foreleg rubbing epochs. 0 s indicates *the start of each epoch*. **(c,i)** Standard deviation projection image for an **(c)** *SS42740-GAL4*, or **(i)** *SS27485-GAL4* nervous system expressing smFP and stained for GFP (green) and Nc82 (blue). Cell bodies are indicated (white asterisks). Scale bars are 40 μm . **(d,j)** Projections as in **c,i** but for one MCFO-expressing, traced neuron (black asterisks). The brain's GNG (yellow), AVLP (cyan), SAD (green), VES (pink), IPS (blue), SPS (orange), and VNC's neck (orange), intermediate tectulum (green), wing tectulum (blue), and prothoracic leg neuromere (yellow) are color-coded. Scale bars are 40 μm . **(e,f,k,l)** Higher magnification projections of **(top)** brains and **(bottom)** VNCs from **(e,f)** *SS42740-GAL4*, or **(k,l)** *SS25469-GAL4* animals expressing **(e,k)** the stochastic label MCFO, or **(f,l)** the synaptic marker, syt:GFP (green), and tdTomato (red). Insets magnify dashed boxes. Indicated are cell bodies (asterisks), and bouton-like structures (white arrowheads). Scale bars for brain images and insets are 20 μm and 2 μm , respectively. Scale bars for VNC images and insets are 20 μm and 2 μm , respectively. See also [Figure S3.4](#).

To test this hypothesis, we compared the morphologies of foreleg- and eye groom-ANs. Both had cell bodies in the T1 neuromere, although foreleg-ANs were posterior ([Figure 3.6C](#)) and eye groom-ANs were anterior ([Figure 3.6I](#)). Foreleg- and eye groom-ANs also both projected to the dorsal T1 neuromere with eye groom-AN neurites restricted to the tectulum ([Figure 3.6D](#) and [Figure 3.6J](#)). Notably, foreleg-AN puncta ([Figure 3.6E, bottom](#)) and syt:GFP expression ([Figure 3.6F, bottom](#)) were bilateral and diffuse while eye groom-AN puncta ([Figure 3.6K, bottom](#)) and syt:GFP expression ([Figure 3.6L, bottom](#)) were largely restricted to the contralateral T1 neuromere. Projections to the brain paralleled this difference in VNC projection promiscuity: foreleg-ANs terminated across multiple brain areas—GNG, AVLP, SAD, VES, IPS, and SPS ([Figure 3.6E,F top](#))— while eye groom-ANs narrowly targeted the GNG ([Figure 3.6K,L top](#)).

These results further illustrate how an AN's encoding relates to its VNC patterning. Here, diffuse, bilateral projections are associated with encoding multiple behaviors that require foreleg movements whereas focal, unilateral projections are related to a narrow encoding of eye grooming.

3.3.7 Temporal integration of proboscis extensions by a cluster of ANs

Flies often generate spontaneous proboscis extensions (PEs) while resting (**Figure 3.7A, yellow ticks**). We observed that ‘PE-ANs’ (SS31232, overlap with SS30303) (**Figure 3.2D**) become active during PE trains—a sequence of PEs that occur within a short period of time (**Figure 3.7A**). Close examination revealed that PE-AN activity slowly ramped up over the course of PE trains. This made them difficult to model using a simple PE regressor: their activity levels were lower than predicted early in PE trains, and higher than predicted late in PE trains. On average, across many PE trains, PE-AN activity reached a plateau by the seventh PE (**Figure 3.7B**).

Thus, PE-AN activity seemed to convey the temporal integration (or counting) of discrete events [132, 133]. Therefore, we next asked if PE-AN activity might be better predicted using a regressor that integrates the number of PEs within a given time window. By testing a range of window sizes, we determined that the most accurate prediction of PE-AN dynamics could be obtained using an integration window of more than 10 s (**Figure 3.7C, red circles**). This additional integration window made it possible to predict both the undershoot and overshoot of PE-AN activity at the start and end of PE trains, respectively (**Figure 3.7D**).

Temporal integration can be implemented using a line attractor model [134, 135] based on recurrently connected circuits. To explore the degree to which PE-AN might support an integration of PE events via recurrent interconnectivity, we examined PE-AN morphologies more closely. PE-AN cell bodies were located in the anterior T1 neuromere (**Figure 3.7E**). From there they projected dense neurites into the midline of the T1 neuromere (**Figure 3.7F**). Among these neurites in the VNC, we observed puncta and syt:GFP expression consistent with presynaptic terminals (**Figure 3.7G,H, bottom**). Their dense and highly overlapping arbors would be consistent with a mutual interconnectivity between PE-ANs. These putative recurrent connections could enable the integration of PE events over tens-of-seconds. This integration might be used to filter out sparse PE events associated with feeding and allow PE-ANs to convey long PE trains observed during deep rest-states [136] to the brain’s GNG (**Figure 3.7G,H, top**).

3.4 Discussion

Animals must be aware of their own behavioral states to accurately interpret sensory cues and select appropriate future actions. Here, we examined how this self-awareness might be conveyed to the brain by studying the activity and targeting of ascending neurons residing within the *Drosophila* motor system. Specifically, we addressed a number of fundamental questions (**Figure 3.1A-C**). First, to what extent do ANs encode the low-level movements of joint and legs, versus high-level behavioral states like walking and grooming? Second, are individual AN encodings narrow (conveying one movement or behavior), or broad (conveying multiple movements or behaviors)? Third, to what extent do ANs target multiple or single

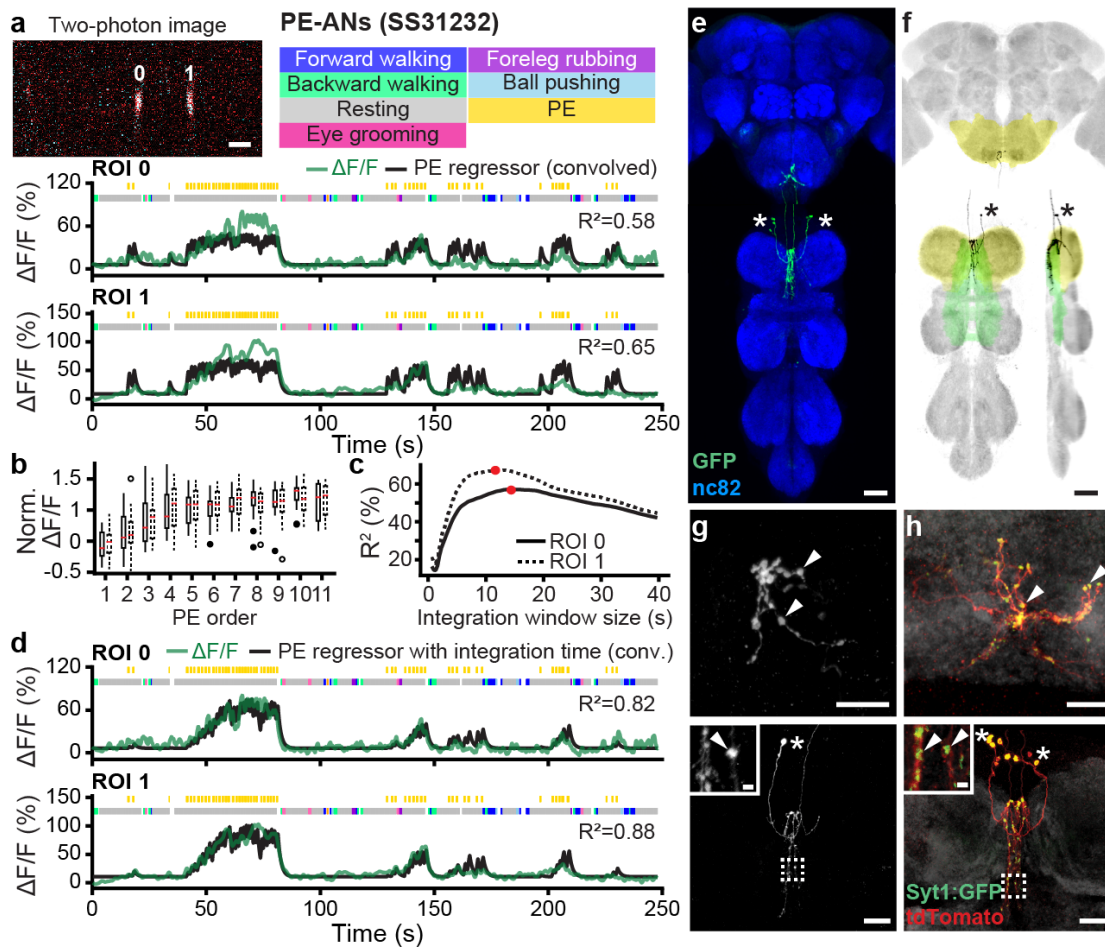


Figure 3.7: Functional and anatomical properties of ascending neurons that integrate the number of proboscis extensions over time. (a) (top-left) Two-photon image of axons from an *SS31232-GAL4* animal expressing OpGCaMP6f (cyan) and tdTomato (red). ROIs are numbered. Scale bar is $5\ \mu\text{m}$. (bottom) Behavioral epochs are color-coded. Representative $\Delta F/F$ time-series from two ROIs (green) overlaid with a prediction (black) obtained by convolving proboscis extension epochs with a Ca^{2+} indicator response function. Explained variance is indicated (R^2). (b) $\Delta F/F$, normalized with respect to the neuron's 90th percentile, as a function of proboscis extension (PE) number within a PE train for ROIs 0 (solid boxes, filled circles), or 1 (dashed boxes, open circles). (c) Explained variance (R^2) between $\Delta F/F$ time-series and a prediction obtained by convolving proboscis extension epochs with a Ca^{2+} indicator response function and a time-window. Time-windows that maximize the correlation for ROIs 0 (solid line) and 1 (dashed line) are indicated (red circles). (d) Behavioral epochs are color-coded. Representative $\Delta F/F$ time-series from two ROIs (green) are overlaid with a prediction (black) obtained by convolving proboscis extension epochs with a Ca^{2+} response function as well as the time windows indicated in panel c (red circles). Explained variance is indicated (R^2). (e) Standard deviation projection image of a *SS31232-GAL4* nervous system expressing smFP and stained for GFP (green) and Nc82 (blue). Cell bodies are indicated (white asterisks). Scale bar is $40\ \mu\text{m}$. (f) Projection as in e but for one MCFO-expressing, traced neuron (black asterisks).

Chapter 3. Ascending neurons convey behavioral state to integrative sensory and action selection centers in the brain

The brain's GNG (yellow) and VNC's intermediate tectulum (green), and prothoracic leg neuromere (yellow) are color-coded. Scale bar is 40 μm . (**g,h**) Higher magnification projections of (**top**) brains and (**bottom**) VNCs for *SS31232-GAL4* animals expressing (**g**) the stochastic label MCFO, or (**h**) the synaptic marker, *syt:GFP* (green), and *tdTomato* (red). Insets magnify dashed boxes. Indicated are cell bodies (asterisks), and bouton-like structures (white arrowheads). Scale bars for brain images are 10 μm . Scale bars for VNC images and insets are 20 μm and 2 μm , respectively.

brain regions? Fourth, do ANs that convey distinct signals also target distinct brain regions? Fifth, which characteristics of an AN's patterning in the VNC are predictive of their encoding? Sixth, are ANs a simple feedforward relay of signals to the brain, or might they also contribute to computations within the VNC? To address these questions, we performed a large-scale functional and anatomical screen that leveraged a library of *Drosophila* driver lines expressing reporters in small sets of ANs, as well as new experimental and computational tools for recording and quantifying neural activity in behaving animals.

3.4.1 Encoding of high-level behavioral states

We discovered that ANs functionally encode high-level behavioral states (**Figure 3.8A**), predominantly those related to self-motion like walking and resting. These encodings could be further distinguished as either broad (e.g., walk-ANs and foreleg-ANs), or narrow (e.g., turn-ANs and eye groom-ANs). Similarly, neurons in the vertebrate dorsal spinocerebellar tract have been shown to be more responsive to whole limb versus individual joint movements [137]. To compensate for the technical hurdle of relating relatively rapid joint movements to slow calcium indicator decay kinetics, we convolved joint angle time-series' with a kernel that would maximize the explanatory power of our regression analyses. Additionally, we confirmed that potential issues related to the non-orthogonality of joint angles and leg movements would not obscure our ability to explain the variance of AN neural activity (**Figure S3.3**). Our observation that eye groom-AN activity could be explained by movements of the forelegs gave us further confidence that, in principle, leg movement encodings could be detected (**Figure 3.2C**). To further confirm the absence of low-level joint and leg movement AN encoding, future work might directly manipulate the legs of animals while recording AN activity [138]. Finally, we sometimes observed that the activity of putative walk-encoding ANs was not fully explained by our walking regressor, nor our turn analysis, (e.g., SS44270, overlaps with SS41605). This suggests that some ANs may encode other features of locomotion.

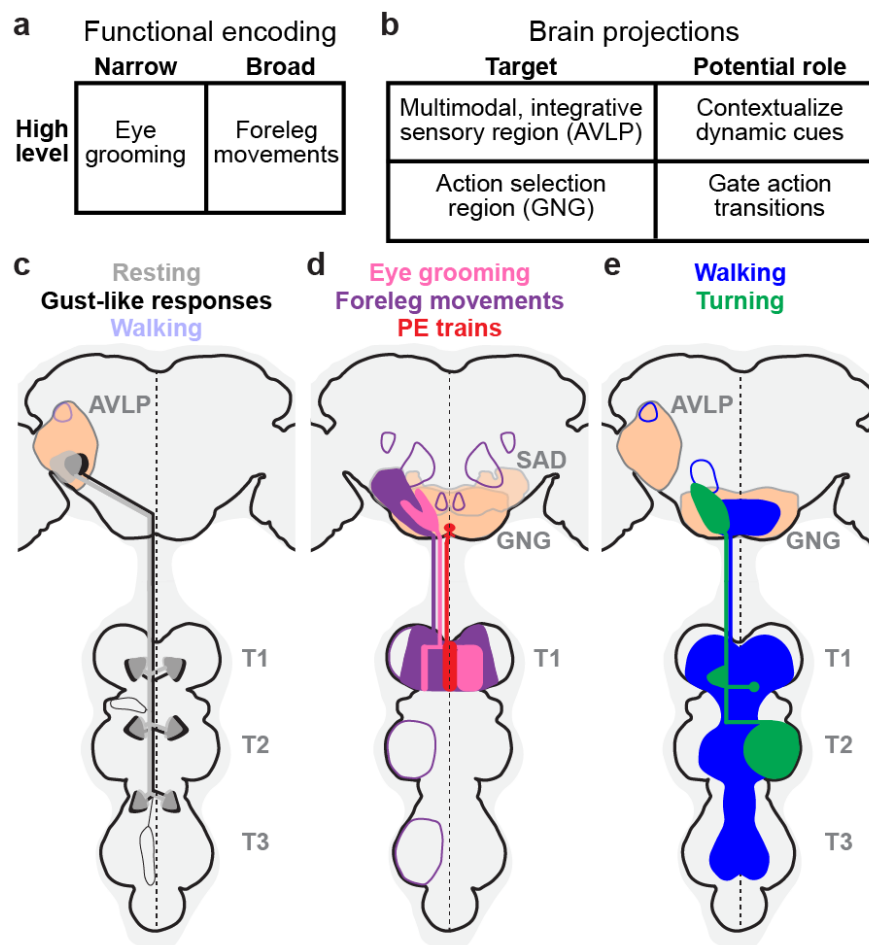


Figure 3.8: **Summary of ascending neuron functional encoding, brain targeting, and VNC patterning.** (a) ANs encode high-level behaviors in a narrow (e.g., eye grooming), or broad (e.g., foreleg movements) manner. (b) Corresponding anatomical analysis shows that ANs primarily target the AVLP, a multimodal, integrative brain region, and the GNG, a region associated with action selection. (c,d) By comparing functional encoding with brain targeting and VNC patterning, we find that (c) signals critical for contextualizing object motion—walking, resting, and gust-like stimuli—are sent to the AVLP, while (d) signals indicating diverse ongoing behaviors are sent to the GNG, potentially to influence future action selection. (e) Broad (e.g., walking), or narrow (e.g., turning) behavioral encoding is associated with diffuse and bilateral, or restricted and unilateral VNC innervations, respectively. (c-e) AN projections are color-coded by behavioral encoding. Axons and dendrites are not distinguished from one another. Brain and VNC regions are labelled. Frequently innervated brain regions—the GNG and AVLP—are highlighted (light orange). Less frequently innervated areas are outlined. The midline of the central nervous system is indicated (dashed line).

3.4.2 Predominant projection to the brain's AVLP and GNG

We found that the majority of ANs do not project diffusely across the brain but rather specifically target either the AVLP and GNG (Figure 3.8B). We hypothesize that this may reflect

Chapter 3. Ascending neurons convey behavioral state to integrative sensory and action selection centers in the brain

the contribution of AN behavioral state signals to two fundamental brain computations. First, the AVLPL is a site known for multimodal, integrative sensory convergence [123–128]. Thus, the projection of ANs encoding resting, walking, and gust-like puffs to the AVLPL (Figure 3.8C) may serve to contextualize time-varying visual and olfactory signals to indicate if they arise from self-motion, or from objects moving and odors fluctuating in the world. A similar role—conveying self-motion—has been proposed for neurons in the vertebrate dorsal spinocerebellar tract [27]. Second, the GNG is thought to be an action selection center [34, 38, 129]. Thus, the projection of ANs encoding diverse behaviors—walking, turning, foreleg movements, eye-grooming, and proboscis extensions (Figure 3.8D,E)—to the GNG may contribute to the computation of whether potential future actions are compatible with ongoing behaviors. This role would be consistent with a hierarchical control approach used in robotics [48]. Notably, walk-ANs that project to the ventral GNG may be neuromodulatory in nature. Thus, they may be particularly well-poised to shift an animal's internal state and the relative values of potential future actions.

Notably, the GNG is also heavily innervated by descending neurons (DNs). Because ANs and DNs both contribute to action selection [28, 34, 38, 139], we speculate that they may connect within the GNG, forming a feedback loop between the brain and motor system. Specifically, ANs that encode specific actions might excite DNs that drive the same actions to generate behavioral persistence, while also suppressing DNs that drive conflicting actions. For example, turn-ANs may excite DNa01 and DNa02 which control turning [49, 130, 140], and foreleg-ANs may excite aDN1 and aDN2 that control grooming [141]. Of course the opposite might also be true: ANs might *inhibit* DNs that encode the same action to ensure that motor actions are terminated once they have been performed. These competing hypotheses may soon be tested using emerging connectomics datasets.

3.4.3 Patterning within the VNC is predictive of behavioral encoding

The morphology of an AN's neurites in the VNC is, to a remarkable degree, predictive of its encoding (Figure 3.8C-E). We observed this in several ways. First, ANs innervating all three leg neuromeres (T1, T2, and T3) encode global self-motion—walking, resting, and gust-like puffs. By contrast, those with more restricted projections to one neuromere (T1 or T2) encode discrete actions—turning, eye grooming, foreleg movements, and PEs. This might reflect the cost of neural wiring, a constraint that may encourage a neuron to sample the minimal sensory and motor information required to compute a particular behavioral state. Second, broadly tuned ANs (encoding walking and foreleg-dependent behaviors) exhibited bilateral projections in the VNC while narrowly tuned ANs (encoding turning and eye grooming) exhibited unilateral and smooth, putatively dendritic projections. This was correlated with the degree of synchrony in the activity of pairs of ANs (Figure S3.6).

Strikingly, for all ANs that we examined in-depth, we found evidence of axon terminals within the VNC. Thus, ANs may not simply relay behavioral state signals to the brain but may also perform other roles. For example, they might contribute to motor control as components of central pattern generators (CPGs) that generate rhythmic movements [1]. Similarly, rest-ANs might control the limb muscle tone needed to maintain a natural resting posture. ANs might also participate in computing behavioral states. For example, here we speculate that recurrent interconnectivity among PE-ANs might give rise to their temporal integration and encoding of PE number [134, 135]. Finally, ANs might contribute to action selection within the VNC. For example, eye groom-ANs might project to the contralateral T1 neuromere to suppress circuits driving other foreleg-dependent behaviors like walking and foreleg rubbing.

3.4.4 Future work

Here we investigated animals that were generating spontaneous and puff-induced behaviors including walking and grooming. However, ANs likely also encode other behavioral states, unmeasured internal forces like posture-maintaining muscle stiffness, or even metabolic states. This is hinted at by the fact that some ANs' neural activities were not well explained by any of our behavioral regressors (e.g., R87H02, R39G01, R69H10, and SS29633). Additionally, nearly one-third of the ANs we examined were unresponsive, possibly due to the absence of appropriate context. For example, we found that some silent ANs could become very active during leg movements *only* when the spherical treadmill was removed (SS51017 and SS38631)([Figure S3.7](#)). Thus, future work may investigate AN encoding in other contexts including tethered flight. Finally, it would also be interesting to test the degree to which AN encoding is genetically hardwired or capable of adapting during motor learning or after injury [142, 143]. Our finding that ANs encode high-level behaviors and convey these states to integrative sensory and action selection centers in the brain may guide the study of ascending neurons in the mammalian spinal cord [27, 29, 137, 144–146], and also accelerate the development of more effective bioinspired algorithms for robotic sensory contextualization and action selection [48].

Chapter 3. Ascending neurons convey behavioral state to integrative sensory and action selection centers in the brain

3.5 Materials and Methods

3.5.1 Key resource table

REAGENT OR RESOURCE	SOURCE	IDENTIFIER
<i>Drosophila melanogaster</i> stocks		
Split-GAL4 (spGAL4) lines	Laboratory of Barry Dickson and FlyLight project (Janelia Research Campus, Ashburn VA USA, see Table S3.2)	SS*****
<i>MAN-spGAL4</i> (; <i>VT50660-AD</i> ; <i>VT14014-DBD</i>)	[28] Laboratory of Michael Dickinson (Caltech, Pasadena CA USA)	N/A
<i>R85A11-GAL4</i>	[65] Bloomington Stock Center	R85A11
<i>R87H02-GAL4</i>	[65] Bloomington Stock Center	R87H02
<i>R36G04-GAL4</i>	[65] Bloomington Stock Center	R36G04
<i>R39G01-GAL4</i>	[65] Bloomington Stock Center	R39G01
<i>R30A08-GAL4</i>	[65] Bloomington Stock Center	R30A08
<i>R70H06-GAL4</i>	[65] Bloomington Stock Center	R70H06
<i>R69H10-GAL4</i>	[65] Bloomington Stock Center	R69H10
<i>R57C10-Flp2::PEST in su(Hw)attP8</i> ; ; <i>HA-V5-FLAG</i>	[70] Bloomington Stock Center	MCFO-5
<i>R57C10-Flp2::PEST in attP18</i> ; ; <i>HA-V5-FLAG-OLLAS</i>	[70] Bloomington Stock Center	MCFO-7
<i>UAS-syt::GFP</i> (<i>Pw[+mC]=UAS-syt.eGFP1, w[*]; ;</i>)	Bloomington Stock Center	N/A
<i>UAS-OpGCaM6f</i> ; <i>UAS-tdTomato</i> (; <i>P20XUAS-IVS-Syn21-OpGCaM6F-p10 su(Hw)attP5</i> ; <i>Pw[+mC]=UAS-tdTom.S3</i>)	Laboratory of Michael Dickinson (Caltech, Pasadena CA USA)	N/A
<i>UAS-smFP</i> (; ; <i>10xUAS-IVS-myr::smGdP-FLAG (attP2)</i>)	Laboratory of Brian McCabe (EPFL, Lausanne CH)	N/A
Antibodies		
rabbit anti-GFP	ThermoFisher	RRID: AB_2536526
mouse anti-Bruchpilot / nc82	Developmental Studies Hybridoma Bank	RRID: AB_2314866
rabbit anti-HA-tag	Cell Signaling Technology	RRID:AB_1549585
rat anti-FLAG-tag (DYKDDDDK)	Novus	RRID:AB_1625981
rabbit polyclonal anti-DsRed	Takara Biomedical Technology	RRID: AB_10013483
rabbit anti-V5-tag (GKIPNPLLGLDST) conjugated with DyLight 550	Cayman Chemical	Cat# 11261
goat anti-rabbit secondary antibody conjugated with Alexa 488	ThermoFisher	RRID: AB_143165
goat anti-mouse secondary antibody conjugated with Alexa 633	ThermoFisher	RRID: AB_2535719
donkey anti-rabbit secondary antibody conjugated with AlexaFluor 594	Jackson ImmunoResearch Labs	RRID:AB_2340621
donkey anti-rat secondary antibody conjugated with AlexaFluor 647	Jackson ImmunoResearch Labs	RRID:AB_2340694

3.5 Materials and Methods

donkey anti-mouse secondary antibody conjugated with AlexaFluor 488	Jackson ImmunoResearch Labs	RRID:AB_2341099
donkey anti-rabbit secondary antibody conjugated with Cy3	Jackson ImmunoResearch Labs	RRID:AB_2307443
Chemicals		
Triton-X	Sigma-Aldrich	
PBS		
Normal goat serum (NGS)		
Slowfade	Thermofisher	Cat#: S36936
Software and digital resources		
Anaconda3	Anaconda	https://www.anaconda.com/products/individual
Python3.6	Python	https://www.python.org/
R 3.6.1	R	https://www.rstudio.com/
DeepLabCut	[59]	https://github.com/DeepLabCut/DeepLabCut
DeepFly3D	[56]	https://github.com/NeLy-EPFL/DeepFly3D
AxoID	This paper	https://github.com/NeLy-EPFL/AxoID
MakeAverageBrain	[147]	https://github.com/NeLy-EPFL/MakeAverageBrain/tree/workstation
Computational Morphometry Toolkit	N/A	https://www.nitrc.org/projects/cmtk
Brain and VNC template	[148]	https://www.janelia.org/open-science/jrc-2018-brain-templates
Fiji	[130]	https://fiji.sc
ThorImage3.1	Thorlabs	https://www.thorlabs.com/newgrouppage9.cfm?objectgroup_id=9072
Thorsync	Thorlabs	https://www.thorlabs.com/newgrouppage9.cfm?objectgroup_id=9072
Adobe Illustrator 2021	Adobe	https://www.adobe.com/
Deposited data and code		
Analysis code	This paper	https://github.com/NeLy-EPFL/Ascending_neuron_screen_analysis_pipeline
Data	This paper	https://dataverse.harvard.edu/dataverse/AN

3.5.2 Fly husbandry

Experimental animals were kept on dextrose cornmeal food at 25°C and 70% humidity on a 12-12 h day-light cycle using standard laboratory tools. All strains used are listed in the Key Resource Table. Female flies were subjected to experiments on 3-6 days post-eclosion. Crosses used for experiments were flipped every 2-3 days.

Chapter 3. Ascending neurons convey behavioral state to integrative sensory and action selection centers in the brain

3.5.3 *In vivo* two-photon calcium imaging experiments

Two-photon imaging was performed as described in [49] with minor changes in the recording configuration. We imaged coronal sections of AN axons in the cervical connective to avoid having neurons move outside the field of view due to behavior-related tissue deformations. Imaging was performed using a Galvo-Galvo scanning system. Image dimensions ranged from 256 x 192 pixels (4.3 fps) to 320 x 320 pixels (3.7 fps), depending on the location of axonal regions-of-interest (ROIs) and the degree of displacement caused by animal behavior. During two-photon imaging, a 7-camera system was used to record fly behaviors as described in [56]. Rotations of the spherical treadmill, and the timing of puff stimuli were also recorded. Air or CO₂ puffs (0.08 L/min) were controlled using either a custom Python script, or manually with an Arduino controller. Puffs were delivered through a syringe needle positioned in front of the animal to stimulate behavior in sedentary animals, or to interrupt ongoing behaviors. To synchronize signals acquired at different sampling rates—optic flow sensors, two-photon images, puff stimuli, and videography—signals were digitized using a BNC 2110 terminal block (National Instrument, USA) and saved using ThorSync software (Thorlabs, USA). Sampling pulses were then used as references to align data based on the onset of each pulse. Then signals were interpolated using custom Python scripts.

3.5.4 Immunofluorescence tissue staining and confocal imaging

Fly brains and VNCs were dissected and fixed as described in [49] with small modifications in staining including antibodies and incubation conditions (see details below). Both primary (rabbit anti-GFP at 1:500; mouse anti-Bruchpilot / nc82 at 1:20) and secondary antibodies (goat anti-rabbit secondary antibody conjugated with Alexa 488 at 1:500; goat anti-mouse secondary antibody conjugated with Alexa 633 at 1:500) for smFP and nc82 staining were performed at room temperature for 24h.

To perform high-magnification imaging of MCFO samples, nervous tissues were incubated with primary antibodies: rabbit anti-HA-tag at 1:300 dilution, rat anti-FLAG-tag (DYKDDDDK) at 1:150 dilution, and mouse anti-Bruchpilot/nc82 at 1:20 dilution. These were diluted in 5% normal goat serum in PBS with 1% Triton-X (PBSTS) for 24 h at room temperature. The samples then were rinsed 2-3 times in PBS with 1% Triton-X (PBST) for 15 min before incubation with secondary antibodies: donkey anti-rabbit secondary antibody conjugated with AlexaFluor 594 at 1:500 dilution, donkey anti-rat secondary antibody conjugated with AlexaFluor 647 at 1:200 dilution, and donkey anti-mouse secondary antibody conjugated with AlexaFluor 488 at 1:500 dilution. These were diluted in PBSTS for 24 h at room temperature. Again, samples were rinsed 2-3 times in PBS with 1% Triton-X (PBST) for 15 min before incubation with the last diluted antibody: rabbit anti-V5-tag (GKPIPPLLGLDST) conjugated with DyLight 550 at 1:300 dilution for another 24 h at room temperature.

To analyze single neuron morphological patterning, we crossed spGAL4 lines with MCFO-7 [70]. Dissection and MCFO staining were performed by Janelia FlyLight according to the FlyLight 'IHC-MCFO' protocol: <https://www.janelia.org/project-team/flylight/protocols>. Samples were imaged on an LSM710 confocal microscope (Zeiss) with a Plan-Apochromat 20x /0.8 M27 objective.

To prepare samples expressing tdTomato and syt:GFP, we chose to only stain tdTomato to minimize false positive signals for the synaptotagmin marker. Samples were incubated with a diluted primary antibody: rabbit polyclonal anti-DsRed at 1:1000 dilution in PBSTs for 24 h at room temperature. After rinsing, samples were then incubated with a secondary antibody: donkey anti-rabbit secondary antibody conjugated with Cy3. Finally, all samples were rinsed 2–3 times for 10 min each in PBST after staining and then mounted onto glass slides with bridge coverslips in Slowfade mounting-media.

Confocal imaging was performed as described in [49]. In addition, high-resolution images for visualizing fine structures were captured using a 40x oil-immersion objective lens with an NA of 1.3 (Plan-Apochromat 40x/1.3 DIC M27, Zeiss) on an LSM700 confocal microscope (Zeiss). The zoom factor was adjusted based on the ROI size of each sample between $84.23 \times 84.23 \mu\text{m}^2$ and $266.74 \times 266.74 \mu\text{m}^2$. For high-resolution imaging, z-steps were fixed at $0.33 \mu\text{m}$. Images were denoised, their contrasts were tuned, and standard deviation z-projections were generated using Fiji [108].

3.5.5 Two-photon image analysis

Raw two-photon imaging data were converted to gray-scale *.tiff image stacks for both green and red channels using custom Python scripts. RGB image stacks were then generated by combining both image stacks in Fiji [108]. We used AxoID to perform ROI segmentation and to quantify fluorescence intensities. Briefly, AxoID was used to register images using cross-correlation and optic flow-based warping [49]. Then, raw and registered image stacks underwent ROI segmentation, allowing $\% \Delta F/F$ values to be computed across time from absolute ROI pixel values. Simultaneously, segmented RGB image stacks overlaid with ROI contours were generated. Each frame of these segmented image stacks was visually examined to confirm AxoID segmentation, or to perform manual corrections using the AxoID GUI. In these cases, manually corrected $\% \Delta F/F$ and segmented image stacks were updated.

3.5.6 Behavioral data analysis

To reduce computational and data storage requirements, we recorded behaviors at 30 fps. This is nearly the Nyquist frequency for rapid walking (up to 16 step cycles/s [21]).

Chapter 3. Ascending neurons convey behavioral state to integrative sensory and action selection centers in the brain

3D joint positions were estimated using DeepFly3D [56]. Due to the amount of data collected, manual curation was not practical. We therefore classified points as outliers when the absolute value of any of their coordinates (x , y , z) was greater than 5 mm (much larger than the fly's body size). Furthermore, we made the assumption that joint locations would only be incorrectly estimated for one of the three cameras used for triangulation. The consistency of the location across cameras could be evaluated using the reprojection error. To identify a camera with a bad prediction, we calculated the reprojection error only using two of the three cameras. The outlier was then replaced with the triangulation result of the pair of cameras with the smallest reprojection error. The output was further processed and converted to angles as described in [149].

We classified behaviors based on a combination of 3D joint angle dynamics and rotations of the spherical treadmill. First, to capture the temporal dynamics of joint angles, we calculated wavelet coefficients for each angle using 15 frequencies between 1 and 15 [51, 150]. We then trained a histogram gradient boosting classifier [151] using joint angles, wavelet coefficients, and ball rotations as features. Because flies perform behaviors in an unbalanced way (some behaviors are more frequently than others), we balanced our annotations using SMOTE [152]. The model was validated using 5-fold, three times repeated, stratified cross-validation. Fly speeds and heading directions were estimated using optical flow sensors [49]. To further improve the accuracy of the onset of walking we applied empirically-determined thresholds (pitch: 0.0038; roll: 0.0038; yaw: 0.014) to the rotational velocities of the spherical treadmill. The rotational velocities were smoothed and denoised using a moving average filter (length 81). All frames that were not previously classified as grooming or pushing, and for which the spherical treadmill was classified as moving, were labeled as 'walking'. These were further subdivided into forward or backward walking depending on the sign of the pitch velocity. Conversely, frames for which the spherical treadmill was not moving were labeled as 'resting'. To reduce the effect of optical flow measurement jitter, walking and resting labels were processed using a hysteresis filter that only changed state if at least 15 consecutive frames are in a new state. Classification in this manner was generally effective but most challenging for kinematically similar behaviors like eye- and antennal-grooming, or hindleg rubbing and abdominal grooming (Figure S3.1E).

Proboscis extension (PE) events were classified based on the length of the proboscis (Figure S3.1A-D). First, we trained a deep network [59] to identify the tip of the proboscis and a static landmark (the ventral part of the eye) from side-view camera images. Then, the distance between the tip of proboscis and this static landmark was calculated to obtain the PE length for each frame. A semi-automated PE event classifier was made by first denoising the traces of PE distances using a median filter with a 0.3 s running average. Traces were then normalized to be between 0 (baseline values) and 1 (maximum values). Next, PE speed was calculated using a data point interval of 0.1 s to detect significant changes in PE length. This way, only peaks larger than a manually set threshold of $0.03 \Delta \text{norm.length} / 0.1 \text{ s}$ were considered. Because the

peak speed usually occurred during the rising phase of a PE, a kink in PE speed was identified by multiplying the peak speed with an empirically-determined factor ranging from 0.4 to 0.6, and finding that speed within 0.5 s prior to the peak speed. The end of a PE was the time-point at which the same speed was observed within 2 s after the peak PE speed. This filtered out occasions where the proboscis remained extended for long periods of time. All quantified PE lengths and durations were then used to build a filter to remove false positives. PEs were then binarized to define PE epochs.

To quantify animal movements when the spherical treadmill was removed, we manually thresholded the variance of pixel values from a side view camera within a region of the image that included the fly. Pixel value changes were calculated using a running window of 0.2 s. Next, the standard deviation of pixel value changes was generated using a running window of 0.25 s. This trace was then smoothed and values lower than the empirically-determined threshold were called 'resting' epochs. The remainder were considered 'movement' periods.

3.5.7 Regression analysis of PE integration time

To investigate the integrative nature of the PE-AN responses, we convolved PE traces with uniform time windows of varying sizes. This convolution was performed such that the fluorescence at each time point would be the sum of fluorescence during the previous 'window_size' frames (i.e., not a *centered* sliding window but one that only uses previous time points), effectively integrating over the number of previous PEs. This integrated signal was then masked such that all time points where the fly was not engaged in PE were set to zero. Then, this trace was convolved with a calcium indicator decay kernel, notably yielding non-zero values in the time intervals between PEs. We then determined the explained variance as described elsewhere and finally chose a window size maximizing the explained variance.

3.5.8 Linear modeling of neural fluorescence traces

Each regression matrix contains elements corresponding to the results of a ridge regression model for predicting the time-varying fluorescence ($\% \Delta F/F$) of ANs using specific regressors (e.g., low-level joint angles, or high-level behaviors). To account for slow calcium indicator decay dynamics, each regressor was convolved with a calcium response function. The half-life of the calcium response function was chosen from a range of 0.2 to 0.95 [49] in 0.05 steps, in order to maximize the variance in fluorescence traces that convolved regressors could explain. The rise time was fixed at 0.1415 [49]. The ridge penalty parameter was chosen using nested 10-fold stratified cross-validation [153]. The intercept and weights of all models were restricted to be positive, limiting our analysis to excitatory neural activity. Values shown in the matrices are the mean of 10-fold stratified cross-validation. We calculated Unique (UEV) and All-Explained Variance (AEV) by temporally shuffling the regressor in question, or all other

Chapter 3. Ascending neurons convey behavioral state to integrative sensory and action selection centers in the brain

regressors, respectively [6]. We tested the overall significance of our models using an F-statistic to reject the null hypothesis that the model does not perform better than an intercept-only model. The prediction of individual traces were performed using a single regressor plus intercept. Therefore they were not regularized.

3.5.9 Behavior-based neural activity analysis

For a given behavior, $\Delta F/F$ traces were compiled, cropped, and aligned with respect to their onset times. Mean and 95% confidence intervals for each time point were then calculated from these data. Because the duration of each behavioral epoch was different, we only computed mean and confidence intervals for epochs that had at least five data points.

To test if each behavior-triggered average $\Delta F/F$ was significantly different from the baseline, first, we aligned and upsampled fluorescence data that were normalized between 0 (baseline mean) and 1 (maximum) for each trial. For each behavioral epoch, the first 0.7 s of data were removed. This avoided contaminating signals with neural activity from preceding behaviors (due to the slow decay dynamics of OpGCaMP6f). Next, to be conservative in judging whether data reflected noisy baseline or real signals, we studied their distributions. Specifically, we tested the normality of twenty resampled groups of 150 bootstrapped datapoints—a size that reportedly maximizes the power of the Shapiro-Wilk test [154]. If a majority of results did not reject the null hypothesis, the entire recording was considered baseline noise and the $\Delta F/F$ for a given behavioral class was not considered significantly different from baseline. On the other hand, if the datapoints were not normally distributed, the baseline was determined using an Otsu filter. For recordings that passed this test of normality, if the majority of six ANOVA tests on the bootstrapped data rejected the null hypothesis and the datapoints of a given behavior were significantly different ($***p < 0.001$, $**p < 0.01$, $*p < 0.05$) from baseline (as indicated by a posthoc Tukey test), these data were considered signal and not noise.

To analyze PE-AN responses to each PE during PE trains, putative trains of PEs were manually identified to exclude discrete PE events. PE trains included at least 3 consecutive PEs in which each PE lasted at least 1 s and there was less than 3 s between each PE. Then, the mean fluorescence of each PE was computed for 25 PE trains ($n=11$ animals). The median, IQR, and 1.5 IQR were then computed for PEs depending on their ordered position within their PE trains. We focused our analysis on the first 11 PEs because they had a sufficiently large amount of data.

3.5.10 Neural fluorescence-triggered averages of spherical treadmill rotational velocities

A semi-automated neural fluorescence event classifier was constructed by first denoising $\Delta F/F$ traces by averaging them using a 0.6 s running window. Traces were then normalized to

be between 0 (their baseline values) and 1 (their maximum values). To detect large deviations, the derivative of the normalized $\Delta F/F$ time-series was calculated at an interval of 0.1 s. Only peaks greater than an empirically determined threshold of $0.03 \frac{d\text{norm } \Delta F/F}{0.1 \text{ s}}$ were considered events. Because peak fluorescence derivatives occurred during the rising phase of neural fluorescence events, the onset of a fluorescence event was identified as the time where the $\Delta F/F$ derivative was 0.4-0.6x the peak within the preceding 0.5 s time window. The end of the event was defined as the time that the $\Delta F/F$ signal returned to the amplitude at event onset before the next event. False positives were removed by filtering out events with amplitudes and durations that were lower than the empirically determined threshold. Neural activity event analysis for turn-ANs was performed by testing if the mean normalized fluorescence event for one ROI was larger than the other ROI by an empirically determined factor of 0.2x. Corresponding ball rotations for events that pass this criteria were then collected. Fluorescence events onsets were then set to 0 s and aligned with spherical treadmill rotations. Using these rotational velocity data, we calculated the mean and 95% confidence intervals for each time point with at least five data points. A 1 s period before each fluorescence event was also analyzed as a baseline for comparison.

3.5.11 Brain and VNC confocal image registration

All confocal images, except for MCFO image stacks, were registered based on nc82 neuropil staining. We built a template and registered images using the CMTK munger extension [147]. Code for this registration process can be found at: <https://github.com/NeLy-EPFL/MakeAverageBrain/tree/workstation>. Brain and VNC of MCFO images were registered to JRC 2018 templates [148] using the Computational Morphometry Toolkit: <https://www.nitrc.org/projects/cmtk>. The template brain and VNC can be downloaded here: <https://www.janelia.org/open-science/jrc-2018-brain-templates>.

3.5.12 Analysis of individual AN innervation patterns

Single AN morphologies were traced by masking MCFO confocal images using either active tracing, or manual background removal in Fiji [108]. Axons in the brain were manually traced using the Fiji plugin 'SNT'. Most neurites in the VNC were isolated by (i) thresholding to remove background noise and outliers, and (ii) manually masking debris in images. In the case of ANs from SS29579, a band-pass color filter was applied to isolate an ROI that spanned across two color channels. The boundary of the color filter was manually tuned to acquire the stack for a single neuron mask. After segmentation, the masks of individual neurons were applied across frames to calculate the intersectional pixel-wise sum with another mask containing either (i) neuropil regions of the brain and VNC, (ii) VNC segments, or (iii) left and right halves of the VNC. Brain and VNC neuropil regions and their corresponding abbreviations were according to established nomenclature [86]. Neuropil region masks can be downloaded here:

Chapter 3. Ascending neurons convey behavioral state to integrative sensory and action selection centers in the brain

<https://v2.virtualflybrain.org>. These were also registered to the JRC 2018 template. Masks for T1, T2, and T3 VNC segments were based on previously delimited boundaries [38]. The laterality of a neuron's VNC innervation was calculated as the ratio of the absolute difference between its left and right VNC innervations divided by its total innervation. Masks for the left and right VNC were generated by dividing the VNC mask across its midline.

3.5.13 AxoID: a deep learning-based software for tracking axons in imaging data

AxoID aims to extract the GCaMP fluorescence values for axons present on coronal section two-photon microscopy imaging data. In this manuscript, it is used to record activity from ascending neurons (ANs) passing through the *Drosophila melanogaster* cervical connective. Fluorescence extraction works by performing the following three main steps (Figure S3.2A). First, during a *detection* stage, ROIs corresponding to axons are segmented from images. Second, during a *tracking* stage, these ROIs are tracked across frames. Third, *fluorescence* is computed for each axon over time.

To track axons, we used a two-stage approach: detection and then tracking. This allowed us to improve each problem separately without the added complexity of developing a detector that must also do tracking. Additionally, this allowed us to detect axons without having to know how many there are in advance. Lastly, significant movement artifacts between consecutive frames pose additional challenges for robustness in temporal approaches while, in our case, we can apply the detection on a frame-by-frame basis. However, we note that we do not leverage temporal information.

Detection

Axon detection consists of finding potential axons by segmenting the background and foreground of each image. An ROI or putative axon is defined as a group of connected pixels segmented as foreground. Pixels are considered connected if they are next to one another.

By posing detection as a segmentation problem, we have the advantage of using standard computer vision methods like thresholding, or artificial neural networks that have been developed for medical image segmentation. Nevertheless, this simplicity has a drawback: if axons appear very close to one another and their pixels are connected, they may be segmented as one ROI rather than two. We try to address this issue using an ROI separation approach described later.

Image segmentation is performed using deep learning on a frame-by-frame basis, whereby a network generates a binary segmentation of a single image. As a post-processing step, all ROIs smaller than a minimum size are discarded. Here, we empirically chose 11 pixels as the

minimum size as a trade-off between removing small spurious regions while still detecting small axons.

We chose to use a U-Net model [155] with slight modifications because of its, or its derivatives', performance on recent biomedical image segmentation problems [156–158]. We add zero-padding to the convolutions to ensure that the output segmentation has the same size as the input image, thus fully segmenting it in a single pass, and modify the last convolution to output a single channel rather than two. Batch normalization [159] is used after each convolution and its non-linearity function. Finally, we reduce the width of the network by a factor of 4: each feature map has 4 times fewer channels than the original U-Net, not counting the input or output. The input pixel values are normalized to the range $[-1, 1]$, and the images are sufficiently zero-padded to ensure that the size can be correctly reduced by half at each max-pooling layer.

To train the deep learning network, we use the Adam optimizer [160] on the binary cross-entropy loss with weighting. Each background pixel is weighted based on its distance to the closest ROI, given by $1 + \exp(-\frac{d^2}{3})$ with d the Euclidean distance, plus a term that increases if the pixel is a border between two axons, given by $\exp(-\frac{d_1+d_2}{6})$ with d_1 and d_2 as the distances to the two closest ROIs, as in [155]. These weights aim to encourage the network to correctly segment the border of the ROI and to keep a clear separation between two neighboring regions. At training time, the background and foreground weights are scaled by $\frac{b+f}{2b}$ and $\frac{b+f}{2f}$, respectively, to take into account the imbalance in the number of pixels, where b and f are the quantity of background and foreground (i.e., ROI) pixels in the entire training dataset. To evaluate the resulting deep network, we use the Sørensen-Dice coefficient [161, 162] at the pixel level, which is equivalent to the F1-score. The training is stopped when the validation performance does not increase anymore.

The network was trained on a mix of experimental and synthetic data. We also apply random gamma corrections to the training input images, with γ sampled in $[0.7, 1.3]$ to keep reasonable values, and to encourage robustness against intensity variations between experiments. The target segmentation of the axons on the experimental data was generated with conventional computer vision methods. First, the images were denoised with the non-local means algorithm [163] using the Python implementation of OpenCV [164]. We used a temporal window size of 5, and performed the denoising separately for the red and green channels, with a filter strength $h = 11$. The grayscale result was then taken as the per-pixel maximum over the channels. Following this, the images were smoothed with a Gaussian kernel of standard deviation 2 pixels, and thresholded using Otsu's method [165]. A final erosion was applied and small regions below 11 pixels were removed. All parameter values were set empirically to generate good qualitative results. In the end, the results were manually filtered to keep only data with satisfactory segmentation.

Chapter 3. Ascending neurons convey behavioral state to integrative sensory and action selection centers in the brain

Because the experimental data have a fairly simply visual structure, we constructed a pipeline in Python to generate synthetic images visually similar to real ones. This was achieved by first sampling an image size for a given synthetic experiment, then by sampling 2D Gaussians over it to simulate the position and shape of axon cross-sections. After this, synthetic tdTomato levels were uniformly sampled and GCaMP dynamics were created for each axons by convolving a GCaMP response kernel with Poisson noise to simulate spikes. Then, the image with the Gaussian axons was deformed multiple times to make different frames with artificial movement artifacts. Eventually, we sampled from the 2D Gaussians to make the axons appear pixelated, and added synthetic noise to the images.

In the end, we chose a deep learning-based approach because our computer vision pipeline alone was not be robust enough. Our pipeline is used to generate a target segmentation dataset from which we manually select a subset of acceptable results. These results are then used to train the deep learning model.

Fine-tuning At the beginning of the detection stage, an optional fine-tuning of the network can be applied to try to improve the segmentation of axons. The goal is to have a temporary network adapted to the current data for better performance. To do this, we train the network on a subset of experimental frames using automatically generated target segmentations.

The subset of images is selected by finding a cluster of frames with high cross-correlation-based similarity. For this, we only consider the tdTomato channel to avoid the effects of GCaMP dynamics. Each image is first normalized by its own mean pixel intensity μ and standard deviation σ : $p(i, j) \leftarrow \frac{p(i, j) - \mu}{\sigma}$, where $p(i, j)$ is the pixel intensity p at the pixel location i, j . The cross-correlation is then computed between each pair of normalized images p_m and p_n as $\sum_{i, j} p_m(i, j) \cdot p_n(i, j)$. Afterwards, we take the opposite of the cross-correlation as a distance measure and use it to cluster the frames with the OPTICS algorithm [166]. We set the minimal number of sample for a cluster to 20, in order to maintain at least 20 frames for fine-tuning, and a maximum neighborhood distance of half the largest distance between frames. Finally, we select the cluster of images with the highest average cross-correlation (i.e., the smallest average distance between its elements).

Then, to generate a target segmentation image for these frames, we take their temporal average and optionally smooth it, if there are less than 50 images, to help remove the noise. The smoothing is done by filtering with a Gaussian kernel of standard deviation 1 pixel, then median filtering over each channel separately. The result is then thresholded through a local adaptive method, computed by taking the weighted mean of the local neighborhood of the pixel, subtracted by an offset. We apply Gaussian weighting over windows of 25×25 pixels, with an offset of -0.05 , determined empirically. Finally, we remove regions smaller than 11 pixels. The result serves as a target segmentation image for all of the fine-tuning images.

The model is then trained on 60% of these frames with some data augmentation, while the other 40% are used for validation. The fine-tuning stops automatically if the performance on the validation frames drops. This avoids bad generalization for the rest of the images. The binary cross-entropy loss is used, with weights computed as discussed previously. For the data augmentation, we use random translation ($\pm 20\%$), rotation ($\pm 10^\circ$), scaling ($\pm 10\%$), and shearing ($\pm 5^\circ$).

Tracking

Once the regions of interest are segmented, the next step of the pipeline consists of tracking the axons through time. This means defining which axons exist, and then finding the ROI they correspond to in each frame.

Tracking template To accomplish this, the tracker records the number of axons, their locations with respect to one another, and their areas. It stores this information into what we call the ‘tracker template’. Then, for each frame, the tracker matches its template axons to the ROIs to determine which regions correspond to which axons.

The tracker template is built iteratively. It is first initialized and then updated by matching with all experimental data. The initialization depends on the optional fine-tuning in the detection step. If there is fine-tuning, then the smoothed average of the similar frames and its generated segmentation are used. Otherwise, one frame of the experiment is automatically selected. For this, AxoID considers only the frames with a number of ROIs equal to the most frequent number of ROIs, and then selects the image with the highest cross-correlation with the temporal average of these frames. It is then smoothed and taken with the segmentation produced by the detection network as initialization. The cross-correlation and smoothing are computed identically as in the fine-tuning. Each ROI in the initialization segmentation defines an axon in the tracker template, with its area and position recorded as initial properties.

Afterwards, we update them by matching each experimental frame to the tracker template. It consists of assigning the ROI to the tracker axons, and then using these regions’ areas and positions to update the tracker. The images are matched sequentially, and the axons properties are taken as running averages of their matched regions. For example, considering the n^{th} match, the area of an axon is updated as:

$$area \leftarrow \frac{area * n + area_{ROI}}{n + 1}$$

Because of this, the last frames are matched to a tracker template that is different from the one used for the first frames. Therefore, we fix the axons properties after the updates and match each frame again to obtain the final identities of the ROIs.

Chapter 3. Ascending neurons convey behavioral state to integrative sensory and action selection centers in the brain

Matching To assign axon identities to the ROIs of a frame, we perform a matching between them as discussed above. To solve it, we define a cost function for matching a template axon to a region which represents how dissimilar they are. Then, using the Hungarian assignment algorithm [167], we find the optimal matching with the minimum total cost (**Figure S3.2B**).

Because some ROIs in the frame may be wrong detections, or some axons may not be correctly detected, the matching has to allow for the regions and axons to end up unmatched for some frames. Practically, we implement this by adding "dummy" axons to the matching problem with a flat cost. To guarantee at least one real match, the flat cost is set to the maximum between a fixed value and the minimum of the costs between regions and template axons with a margin of 10%: $dummy = \max(v, 1.1 \cdot \min(\text{costs}))$ with $v = 0.3$ the fixed value. Then, we can use the Hungarian method to solve the assignment, and all ROIs linked to these dummy axons can be considered unmatched.

We define the cost of assigning a frame's ROI i to a tracker template axon k by their absolute difference in area plus the mean cost of an optimal inner matching of the other ROI to the other axons assuming i and k are already matched:

$$\text{cost}(i, k) = w_{area} |area_i - area_k| + \frac{1}{N_{ROI} - 1} \sum_{i' \neq i} \text{cost}'(i', k_{i'}^*)$$

where $w_{area} = 0.1$ is a weight for balancing the importance of the area, N_{ROI} is the number of ROI in the frame, and $\text{cost}'(i', k_{i'}^*)$ is the inner cost of assigning region $i' \neq i$ to axon $k_{i'}^* \neq k$ selected in an "inner" assignment problem, see below. In other words, the cost is relative to how well the rest of the regions and axons match if we assume that i and k are already matched.

The optimal inner matching is computed through another Hungarian assignment, for which we define another cost function. For this "inner" assignment problem, the cost of matching an ROI $i' \neq i$ and a template axon $k' \neq k$ is defined by how far they are and their radial difference with respect to the matched i and k , plus their difference in area:

$$\text{cost}'(i', k') = \left(\frac{w_{dist}}{\eta_{dist}} \|(x_{i'} - x_i) - (x_{k'} - x_k)\| + \frac{w_{\theta}}{\eta_{\theta}} |\theta_{i'} - \theta_{k'}| \right) \frac{H}{H + x_{k'}^y} + w_{area} |area_{i'} - area_{k'}|$$

$$\text{with } \eta_{\theta} = \arctan \left(\alpha_{\theta} \frac{\eta_{dist}}{\|x_{k'} - x_k\|} \right)$$

where $w_{dist} = 1.0$, $w_{\theta} = 0.1$, and $w_{area} = 0.1$ are weighting parameters, $\eta_{dist} = \min(H, W)$ and η_{θ} are normalization factors with H and W the height and width of the frame and $\alpha_{\theta} = 0.1$ a secondary normalization factor. The \cdot^y operation returns the height component of a vector, and the $\frac{H}{H + x_{k'}^y}$ term is useful to reduce the importance of the first terms if the axon k' is far from axon k in the height direction. This is needed as the scanning of the animal's cervical connective is done from top to bottom, thus we need to allow for some movement artifacts

between the top and bottom of the image. Note that the dummy axons for unmatched regions are also added to this inner problem.

This inner assignment is solved for each possible pair of axon-ROI to get all final costs. The overall matching is then performed with them. Because we are embedding assignments, the computational cost of the tracker increases exponentially with the number of ROIs and axons. It stays tractable in our case as we generally deal with few axons at a time. All parameter values used in the matching were found empirically by trial and error.

Identities post-processing: ROI separation In the case of fine-tuning at the detection stage, AxoID will also automatically try to divide ROIs that are potentially two or more separate axons. We implement this to address the limitation introduced by detecting axons as a segmentation: close or touching axons may get segmented together.

To do this, it first searches for potential ROIs to be separated by reusing the temporal average of the similar frames used for the fine-tuning. This image is initially segmented as described before. Then local intensity maxima are detected on a grayscale version of this image. To avoid small maxima due to noise, we only keep those with an intensity ≥ 0.05 , assuming normalized grayscale values in $[0, 1]$. Following this, we use the watershed algorithm, with the scikit-image [168] implementation, to segment the ROI based on the gray level and detected maxima. In the previous stages, we discarded ROIs under 11 pixels to avoid small spurious detections. Similarly, here we fuse together adjacent regions that are under 11 pixels to only output results after the watershedding above or equal to that size. Finally, a border of 1 pixel width is inserted between regions created from the separation of an ROI.

These borders are the divisions separating the ROI, referred to as "cuts". We parameterize each of these as a line, defined as its normal vector \mathbf{n} and distance d to the origin of the image (top-left). To report them on each frame, we first normalize this line to the current ROI, and then reverse that process with respect to the corresponding regions on the other frames. To normalize the line to an ROI, we fit an ellipse on the ROI contour in a least-square sense. Then the line parameters are transformed into this ellipse's local coordinates following Algorithm 1. It is essentially like transforming the ellipse into a unit circle, centered and axis-aligned, and applying a similar transformation to the cutting line (Figure S3.2C, middle). The choice of fitting an ellipse is motivated by the visual aspect of the axons in the experimental data as they are fairly similar to elongated ellipses. Considering this, a separation between two close ellipses could be simplified to a linear border, motivating the linear representation of the ROI separation.

Because this is done as a post-processing step following tracking, we can apply that division on all frames. To do this, we again fit an ellipse to their ROI contours in the least-squares sense. Then, we take the normalized cutting line and fit it back to each of them according to

Chapter 3. Ascending neurons convey behavioral state to integrative sensory and action selection centers in the brain

Algorithm 1: Normalize a line with an ellipse	Algorithm 2: Fit a line to an ellipse
Input: $line, ellipse$ Output: normalized line $line'$ /* Initialization */ $\mathbf{n} \leftarrow line.normal;$ $d \leftarrow line.distance;$ $\mathbf{c} \leftarrow ellipse.center;$ $w \leftarrow ellipse.width/2;$ $h \leftarrow ellipse.height/2;$ $\theta \leftarrow ellipse.rotation;$ $\mathbf{R}_{-\theta} :=$ rotation matrix of angle $-\theta$; /* Normalization */ $d' \leftarrow d - \mathbf{c} \cdot \mathbf{n};$ $\mathbf{n}' \leftarrow \mathbf{R}_{-\theta} \mathbf{n};$ $\mathbf{n}' \cdot x \leftarrow \mathbf{n}' \cdot x / \mathbf{c} \cdot y;$ $\mathbf{n}' \cdot y \leftarrow \mathbf{n}' \cdot y / \mathbf{c} \cdot x;$ $d' \leftarrow d' / (w * h);$ $line'.distance \leftarrow d' / \ \mathbf{n}'\ ;$ $line'.normal \leftarrow \mathbf{n}' / \ \mathbf{n}'\ ;$	Input: $line, ellipse$ Output: fitted line $line'$ /* Initialization */ $\mathbf{n} \leftarrow line.normal;$ $d \leftarrow line.distance;$ $\mathbf{c} \leftarrow ellipse.center;$ $w \leftarrow ellipse.width/2;$ $h \leftarrow ellipse.height/2;$ $\theta \leftarrow ellipse.rotation;$ $\mathbf{R}_{\theta} :=$ rotation matrix of angle θ ; /* Fitting */ $\mathbf{n}' \leftarrow \mathbf{n};$ $\mathbf{n}' \cdot x \leftarrow \mathbf{n}' \cdot x * \mathbf{c} \cdot y;$ $\mathbf{n}' \cdot y \leftarrow \mathbf{n}' \cdot y * \mathbf{c} \cdot x;$ $d' \leftarrow d * (w * h);$ $d' \leftarrow d' / \ \mathbf{n}'\ ;$ $\mathbf{n}' \leftarrow \mathbf{n}' / \ \mathbf{n}'\ ;$ $line'.normal \leftarrow \mathbf{R}_{\theta} \mathbf{n}';$ $line'.distance \leftarrow d' + \mathbf{c} \cdot \mathbf{n}';$

Algorithm 2. This is similar to transforming the normalized unit circle to the region ellipse and applying the same transform to the line (Figure S3.2C, right).

Finally, a new axon is defined for each cut. In each frame, the pixels of the divided region on the furthest side of the linear separation (with respect to the fitting ellipse center) are taken as the new ROI of that axon for that given frame.

In case there are multiple cuts of the same ROI (e.g., because three axons were close), the linear separations are ordered by distance to the center of the fitting ellipse and are then applied in succession. This is simple and efficient, but assumes there is little to no crossing between linear cuts.

Fluorescence extraction

With the detection and tracking results, we know where each axon is in the experimental data. Therefore, to compute tdTomato and GCaMP fluorophore time-series we take the average of non-zero pixel intensities of the corresponding regions in each frame. We report the GCaMP fluorescence at time t as F_t , and the ratio of GCaMP to tdTomato fluorescence at time t as R_t to gain robustness against image intensity variations.

The final GCaMP fluorescence is reported as in [49]:

$$\Delta F/F = \frac{F_t - F}{F}$$

where F is a baseline fluorescence. Similarly, we report the ratio of GCaMP over tdTomato as in [49, 109]:

$$\Delta R/R = \frac{R_t - R}{R}$$

where R is the baseline. The baseline fluorescences F and R are computed as the minimal temporal average over windows of 10 s of the fluorophore time series F_t and R_t , respectively. Note that axons can be missing in some frames. For instance, if they were not detected or leave the image during movement artifacts. In this case, the fluorescence of that axon will have missing values at the time index t in which it was absent.

3.5.14 Overall workflow

To improve the performance of AxoID, the fluorescence extraction pipeline is applied three times: once over the raw data, once over the data registered using cross-correlation, and once over the data registered using optic-flow warping. Note that the fine-tuning in the detection stage is not used with the raw experimental data as it is based on the cross-correlation between the frames and would therefore lead to worse or redundant results with the data registered using cross-correlation. Eventually, the three fluorescence results can be visualized, chosen from, and corrected by a user through a GUI (**Figure S3.2D**).

Data registration

Registration of the experimental frames consists in transforming each image to make them similar to a reference image. The goal is to reduce the artifacts introduced by animal movements and to align axons across frames. This should help to improve the results of the detection and tracking.

Cross-correlation Cross-correlation registration consists of translating an image so that its correlation to a reference is maximized. Note that the translated image wraps-around (e.g., pixels disappearing to the left reappear on the right). This aims to align frames against translations, but is unable to counter rotations or local deformations. We used the single step Discrete Fourier Transform (DFT) algorithm [118] to find the optimal translation of the frame. It first transforms the images into the Fourier domain, computes an initial estimate of the optimal translation, and then refines this result using a DFT. We based our Python implementation on previous work [169].

Chapter 3. Ascending neurons convey behavioral state to integrative sensory and action selection centers in the brain

For each experiment, the second frame is taken as the reference frame to avoid recording artifacts that sometimes appear on the first recorded image.

Optic-flow registration Optic flow-based registration was previously published [49]. Briefly, this approach computes an optic flow from the frame to a reference image, then deforms it by moving the pixels along that flow. The reference image is taken as the first frame of the experiment. This method has the advantage of being able to compute local deformations, but at a high computational cost.

AxoID GUI

Finally, AxoID contains a GUI where a user can visualize the results, select the best one, and manually correct it.

First, the user is presented with three outputs of the fluorescence extraction pipeline from the raw and registered data with the option of visualizing different information to select the one to keep and correct. Here, the detection and tracking outputs are shown, as well as other information like the fluorescence traces in $\Delta F/F$ or $\Delta R/R$. One of the results is then selected and used throughout the rest of the pipeline.

Following this, the user can edit the tracker template, which will then automatically update the ROI identities across frames. The template and the identities for each frame are shown, with additional information like the image used to initialize the template. The user has access to different tools: axons can be fused, for example, if they actually correspond to a single real axon that was incorrectly detected as two, and, conversely, one axon can be manually separated in two if two close ones are detected together. Moreover, useless axons or wrong detections can be discarded.

Once the user is satisfied with the overall tracker, they can correct individual frames. At this stage, it is possible to edit the detection results by discarding, modifying, or adding ROIs onto the selected image. Then, the user may change the tracking results by manually correcting the identities of these ROIs. In the end, the final fluorescence traces are computed on the selected outputs including user corrections.

3.6 Code availability

Analysis code is available at:

https://github.com/NeLy-EPFL/Ascending_neuron_screen_analysis_pipeline

AxoID code is available at:

<https://github.com/NeLy-EPFL/AxoID>

3.7 Data availability

Data are available at:

<https://dataverse.harvard.edu/dataverse/AN>

3.8 Acknowledgments

We thank the Janelia Research Campus FlyLight project for generating Ascending Neuron split-GAL4 driver lines. PR acknowledges support from an SNSF Project grant (175667) and an SNSF Eccellenza grant (181239). FA acknowledges support from a Boehringer Ingelheim Fonds PhD stipend.

3.9 Author contributions

C-L.C. - Conceptualization, Methodology, Software, Validation, Formal Analysis, Investigation, Data Curation, Validation, Writing – Original Draft Preparation, Writing – Review & Editing, Visualization.

F.A. - Methodology, Software, Formal Analysis, Investigation, Data Curation, Validation, Data Curation, Writing – Original Draft Preparation, Writing - Review & Editing.

R.M. - Methodology, Investigation, Data Curation, Validation. Writing - Review & Editing

V.M. - Investigation, Data Curation, Visualization. Writing - Review & Editing

N.T. - Methodology, Software, Formal Analysis, Data Curation Visualization. Writing - Review & Editing

S.G. - Methodology, Software, Formal Analysis, Data Curation, Visualization. Writing - Review & Editing

B.D. - Resources, Writing - Review & Editing, Supervision, Project Administration, Funding Acquisition. Writing - Review & Editing

P.R. - Conceptualization, Methodology, Resources, Writing – Original Draft Preparation, Writing - Review & Editing, Supervision, Project Administration, Funding Acquisition.

3.10 Declaration of Interests

The authors declare no competing interests.

3.11 Supplementary Information

3.11.1 Supplementary Figures

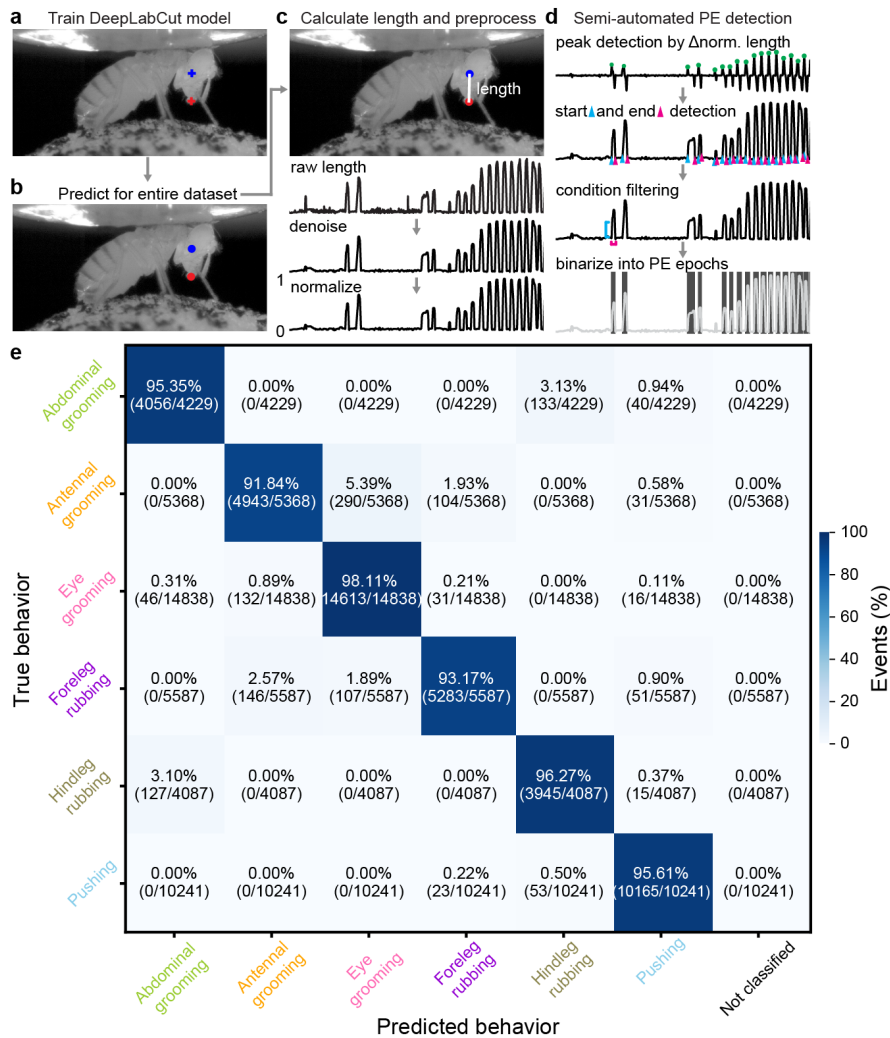


Figure S3.1: **Semi-automated tracking of proboscis extensions, and the accuracy of the behavioral classifier. Related to Figure 3.1.** We detected proboscis extensions using side-view camera images. **(a)** First, we trained a deep neural network model with manual annotations of landmarks on the ventral eye (blue cross) and distal proboscis tip (red cross). **(b)** Then we applied the trained model to estimate these locations throughout the entire dataset. **(c)** Proboscis extension length was calculated as the denoised and normalized distance between landmarks. **(d)** Using these data, we performed semi-automated detection of PE epochs by first identifying peaks from normalized proboscis extension lengths. Then we detected the start (cyan triangle) and end (magenta triangle) of these events. We removed false-positive detections by thresholding the amplitude (cyan line) and duration (magenta line) of events. Finally, we generated a binary trace of PE epochs (shaded regions). **(e)** A confusion matrix quantifies the accuracy of behavioral state classification using 10-fold, stratified cross-validation of a

histogram gradient boosting classifier. Walking and resting are not included in this evaluation because they are predicted using spherical treadmill rotation data. The percentage of events in each category ('predicted' behavior versus ground-truth, manually-labelled 'true' behavior) is color-coded.

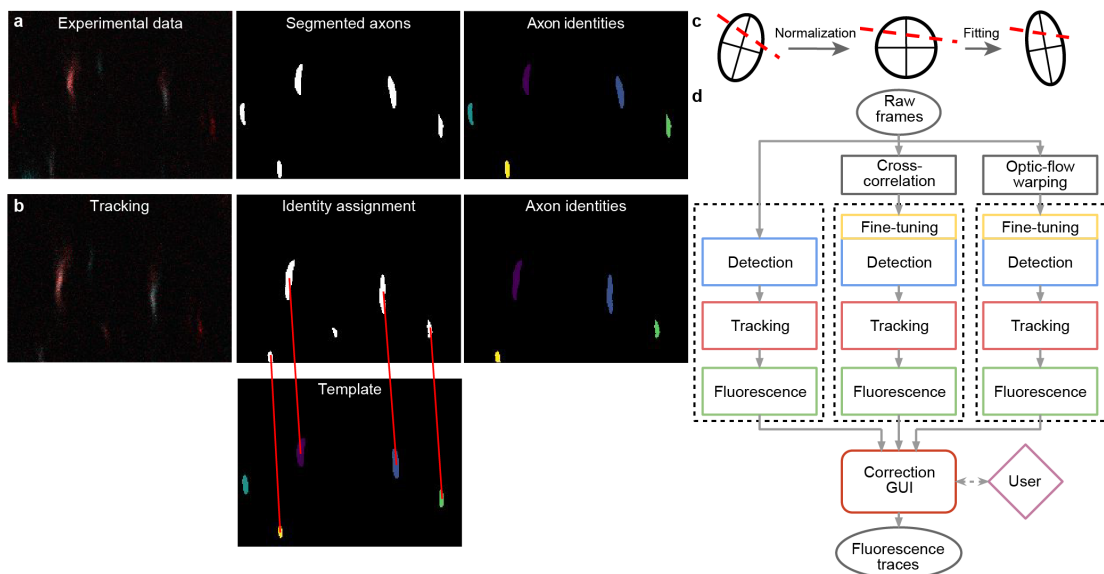


Figure S3.2: **AxoID, a deep learning-based algorithm that detects and tracks axon cross-sections in two-photon microscopy images. Related to Figure 3.1.** (a) Pipeline overview: a single image frame (left) is segmented (middle) during the detection stage with potential axons shown (white). Tracking identities (right) are then assigned to these ROIs. (b) To track ROIs across time, ROIs in a tracker template (bottom-middle) are matched (red lines) to ROIs in the current segmented frame (top-middle). An undetected axon in the tracker template (cyan) is left unmatched. (c) ROI separation is performed for fused axons. An ellipse is first fit to the ROI's contour and a line is fit to the separation (dashed red line). For normalization, the ellipse is transformed into an axis-aligned circle and the linear separation is transformed accordingly. For another frame, a transformation of the circle into a newly fit ellipse is computed and applied to the line. The ellipse's main axes are shown for clarity. (d) The AxoID workflow. Raw experimental data is first registered via cross-correlation and optic flow warping. Then, raw and registered data are separately processed by the fluorescence extraction pipeline (dashed rectangles). Finally, a GUI is used to select and correct the results.

Chapter 3. Ascending neurons convey behavioral state to integrative sensory and action selection centers in the brain

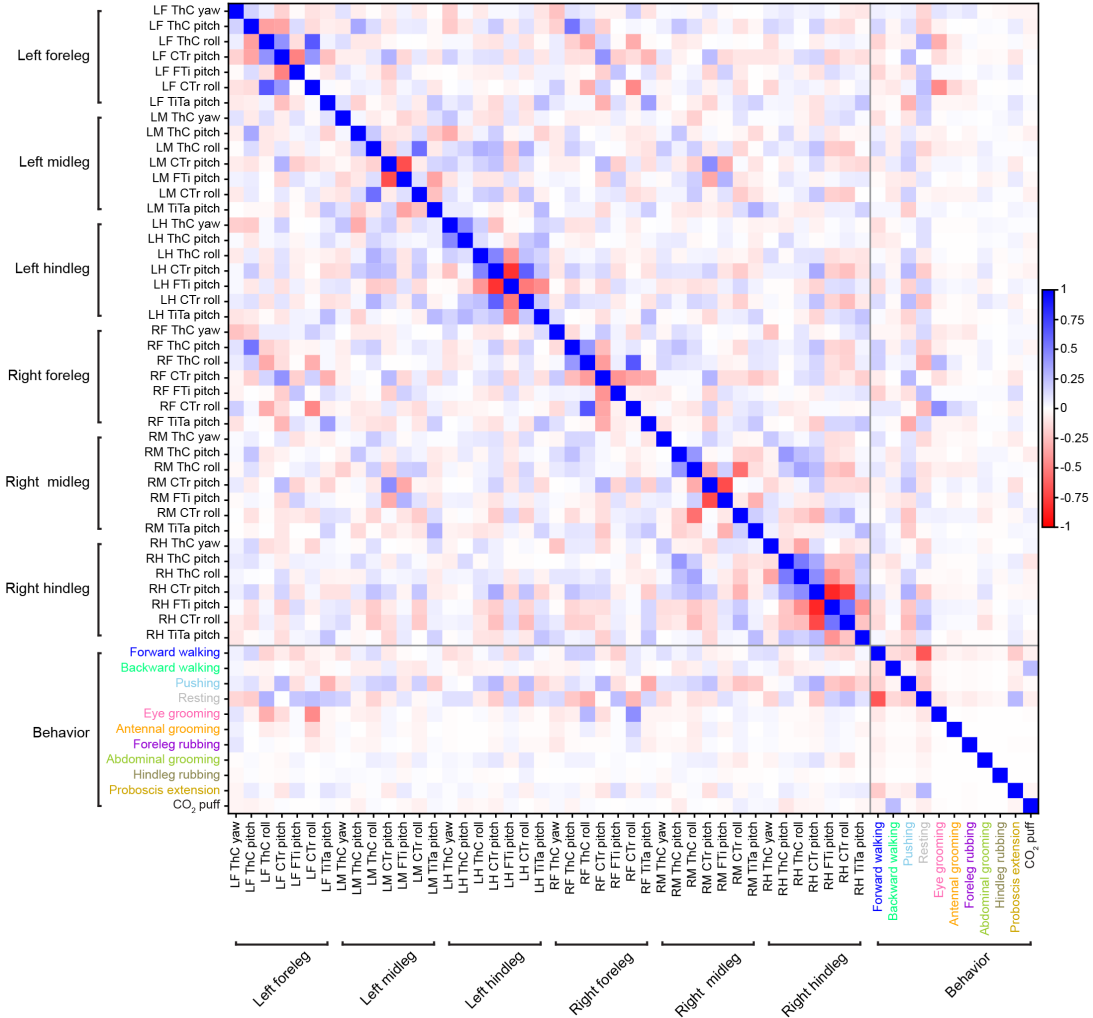


Figure S3.3: Correlations among and between low-level joint angles and high-level behavioral states. Related to Figure 3.2. Pearson correlation coefficients (color-coded) for joint angles, high-level behavioral states, proboscis extensions, and puffs.

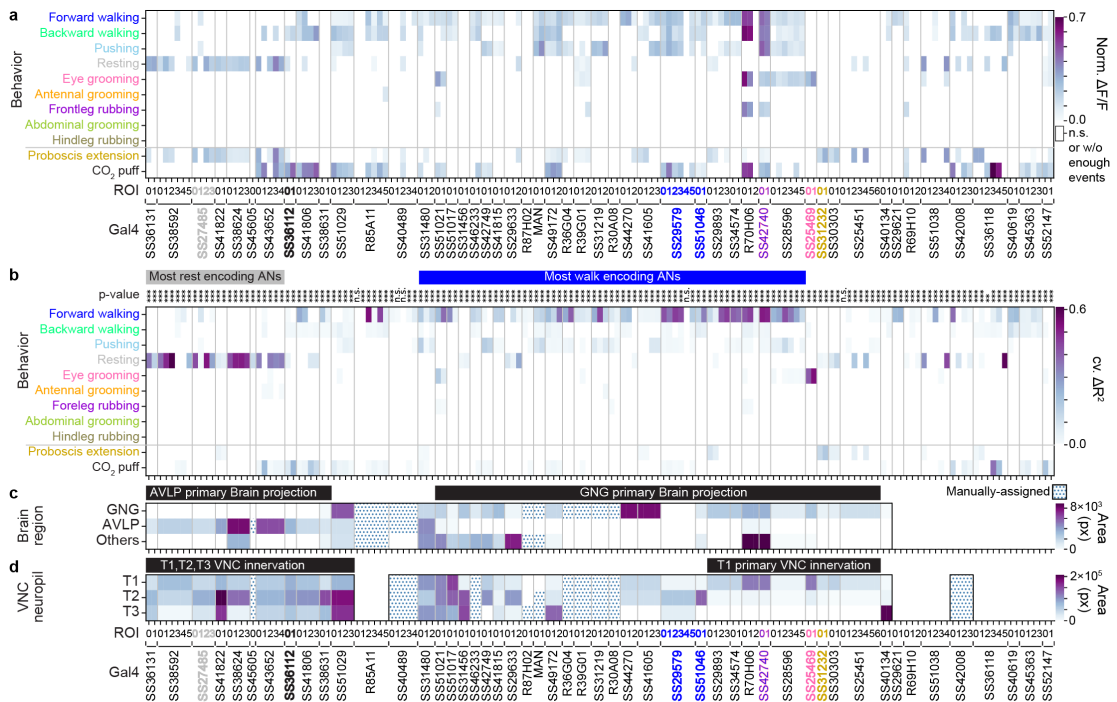


Figure S3.4: **Normalized mean activity ($\Delta F/F$) of ascending neurons during high-level behaviors, and a summary of their behavioral encoding, brain targeting, and VNC patterning. Related to Figure 3.2 and Figure 3.6.** (a) Normalized mean $\Delta F/F$, normalized between 0 and 1, for a given AN across all epochs of a specific high-level behavior. Analyses were performed for 157 ANs recorded from 50 driver lines. Note that fluorescence for non-orthogonal behaviors/events may overlap (e.g., for backward walking and puff, or resting and proboscis extensions). Conditions with less than ten epochs longer than 0.7 s are masked (white). ANOVA and posthoc Tukey tests to correct for multiple comparisons were performed to test if values are significantly different from baseline. Non-significant samples are also masked (white). (b) Variance in AN activity that can be uniquely explained by a regressor (cross-validated ΔR^2) for high-level behaviors. Non-orthogonal regressors (PE and CO₂ puffs) are separated from the others. *P*-values report the F-statistic of overall significance of the complete regression model with no regressors shuffled ($*p < 0.05$, $**p < 0.01$, and $***p < 0.001$). (c,d) The most substantial AN (c) targeting of brain regions, or (d) patterning of VNC regions, as quantified by pixel-based analysis of MCFO labelling. Driver lines that were manually quantified are indicated (dotted cells). Projections that could not be unambiguously identified are left blank. Notable encoding and innervation patterns are indicated by bars above each matrix. Lines (and their corresponding ANs) selected for more in-depth analysis are color-coded by the behavioral class that best explains their neural activity: SS27485 (resting), SS36112 (puff responses), SS29579 (walking), SS51046 (turning), SS42740 (foreleg-dependent behaviors), SS25469 (eye grooming), and SS31232 (proboscis extensions).

Chapter 3. Ascending neurons convey behavioral state to integrative sensory and action selection centers in the brain

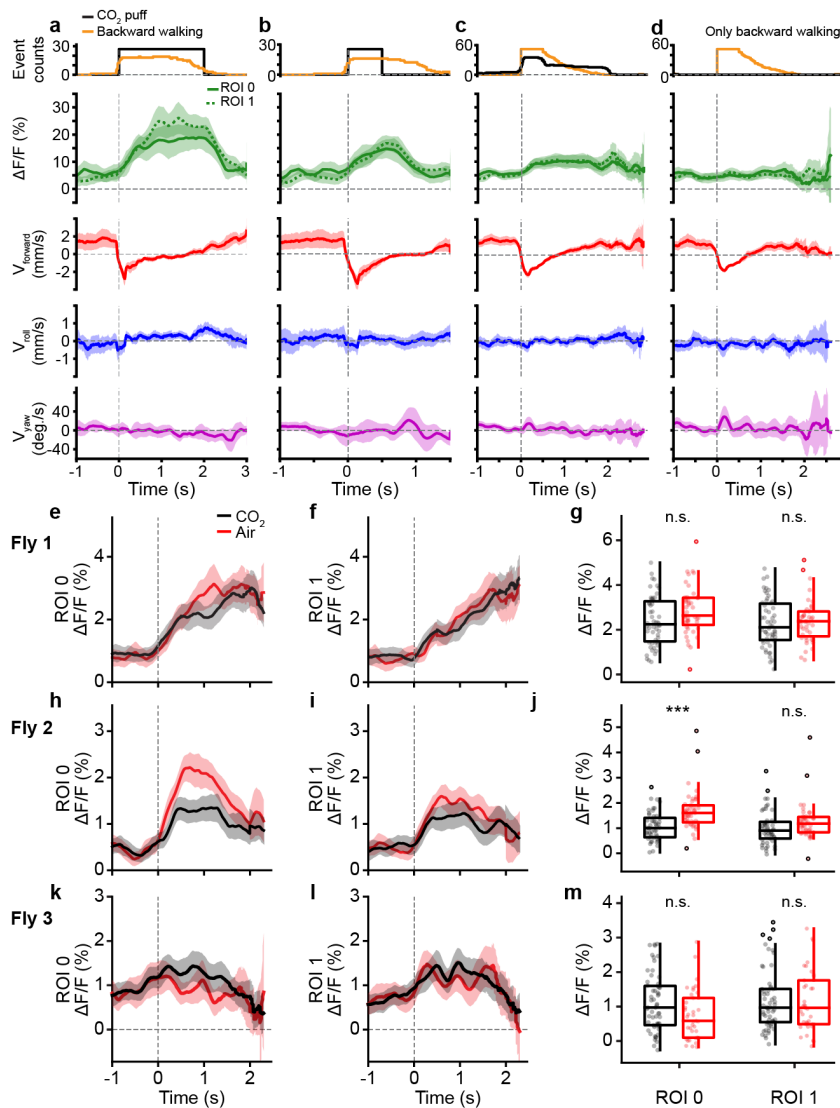


Figure S3.5: **Puff-ANs do not encode backward walking and respond similarly to puffs of air, or CO₂.** Related to **Figure 3.4**. (a-d) Puff-ANs (SS36112) activity (green) and corresponding spherical treadmill rotational velocities (red, blue, and purple) during (a) long, 2 s CO₂-puff stimulation (black) and associated backward walking (orange), (b) short, 0.5 s CO₂-puff stimulation, (c) periods with backward walking, and (d) the same backward walking events as in c but only during periods without coincident puff stimulation. Shown are the mean (solid and dashed lines) and 95% confidence interval (shaded areas) of multiple $\Delta F/F$ and ball rotation time-series. (e-m) Activity of puff-ANs (SS36112) from three flies (e-g, h-j, and k-m, respectively) in response to puffs of air (red), or CO₂ (black). (e-f, h-i, k-l) Shown are mean (solid and dashed lines) and 95% confidence interval (shaded areas) $\Delta F/F$ for ROIs (e,h,k) 0 and (f,i,l) 1. (g,j,m) Mean fluorescence (circles) of traces for ROIs 0 (left) or 1 (right) from 0.7 s after puff onset until the end of stimulation. Overlaid are box plots representing the median, interquartile range (IQR), and 1.5 IQR. Outliers beyond 1.5 IQR are indicated (opaque circles). A Mann-Whitney test (***) $p < 0.001$, ** $p < 0.01$, * $p < 0.05$) was used to compare responses to puffs of CO₂ (red), or air (black).

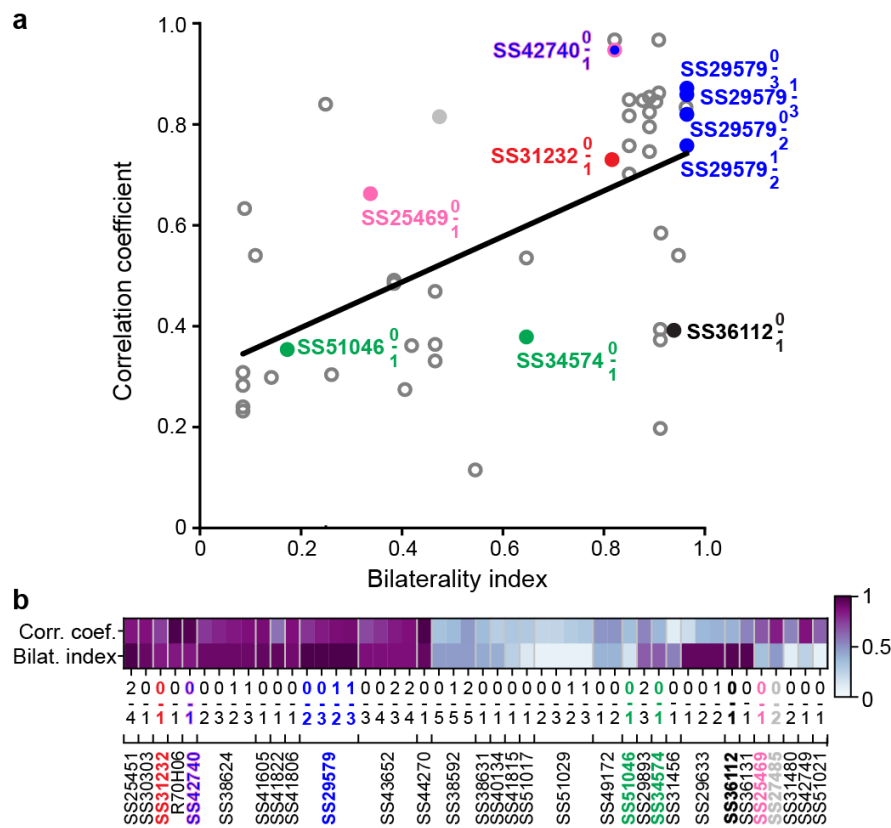


Figure S3.6: **The bilaterality of an ascending neuron pair's VNC patterning correlates with the synchrony of their activity.** Related to Figure 3.5. (a) A bilaterality index, quantifying the differential innervation of the left and right VNC (without distinguishing between axons and dendrites) is compared with the Pearson correlation coefficient computed for the activity of left and right ANs for a driver line pair ($R^2 = 0.31$ and $p < 0.001$ using an F-test). (b) Bilaterality index and Pearson correlation coefficient values for each AN pair.

Chapter 3. Ascending neurons convey behavioral state to integrative sensory and action selection centers in the brain

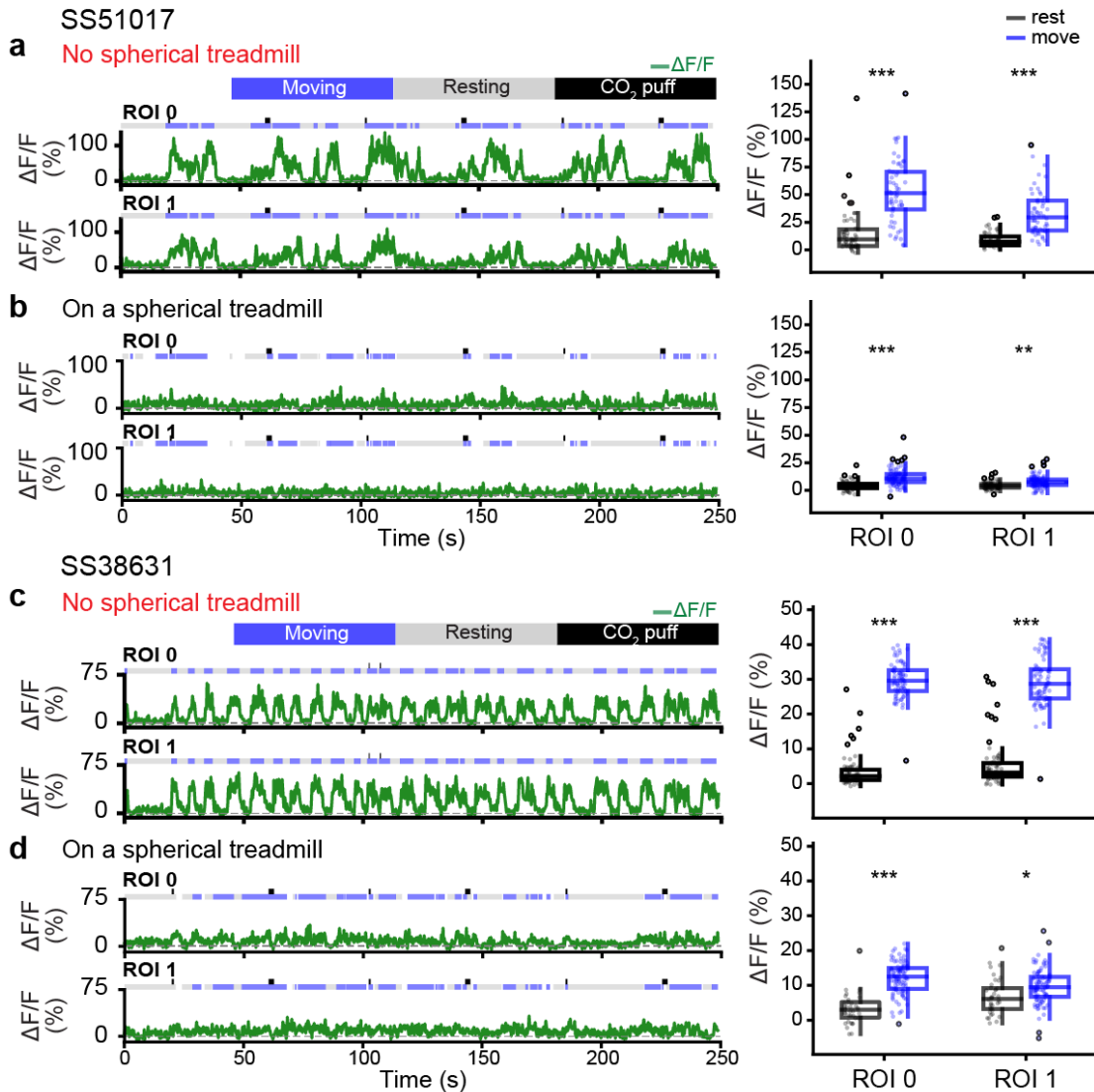


Figure S3.7: Ascending neurons that become active only when the spherical treadmill is removed. Representative AN recordings from ROIs 0 and 1 for an (a,b) SS51017-spGAL4, or (c,d) SS38631-spGAL4 animal measured when it is (a,c) suspended without a spherical treadmill, or (b,d) in contact with the spherical treadmill. Moving, resting, and puff stimulation epochs are indicated. Shown are (left) representative neural activity traces and (right) summary data including the median, interquartile range (IQR), and 1.5 IQR of AN $\Delta F/F$ values when the animals are resting (black), or moving (blue). Outliers (values beyond 1.5 IQR) are indicated (opaque circles). Statistical comparisons were performed using a Mann-Whitney test (***) $p < 0.001$, ** $p < 0.01$, * $p < 0.05$).

3.11.2 Supplementary Tables

Table S3.1: Sparse AN driver lines and associated properties.

No.	Gal4	Confocal SNR of smFP	2P SNR of OpGCaMP6f and tdTomato	Number ROIs	ROI#	Encoding	Level synchronous activity (ROI# vs ROI#: Corr. coef.)	Redundant Gal4	Supp. Video#
1	SS36131	strong	strong	2	0 1	rest rest	0 vs 1: 0.7	SS36132 SS36133	3
2	SS38592	strong	strong	6	0 1 2 3 4 5	rest rest rest unclear unclear rest	0 vs 5: 0.4 1 vs 5: 0.36 2 vs 5: 0.49	SS38598	4
3	SS27485	strong	strong	4	0 1 2 3	rest unclearrest rest	0 vs 2: 0.85	-	5
4	SS41822	strong	strong	2	0 1	rest rest	0 vs 1: 0.71	SS41808 SS41809 SS41820 SS41821	6
5	SS38624	strong	strong	4	0 1 2 3	rest rest rest rest	0 vs 2: 0.84 0 vs 3: 0.7 1 vs 2: 0.9 1 vs 3: 0.87	-	7
6	SS45605	strong	strong	1	0	unclear	-	-	8
7	SS43652	strong	medium	5	0 1 2 3 4	rest puff rest rest rest	0 vs 3: 0.91 0 vs 4: 0.84 2 vs 3: 0.77 2 vs 4: 0.89	-	9
8	SS36112	strong	strong	2	0 1	puff puff	0 vs 1: 0.51	-	10
9	SS41806	strong	strong	4	0 1 2 3	unclear unclear puff puff	2 vs 3: 0.67	-	11
10	SS38631	strong	strong	2	0 1	off ball movement off ball movement	0 vs 1: 0.88	-	12
11	SS51029	strong	medium	4	0 1 2 3	puff puffpuff puff	0 vs 2: 0.32 0 vs 3: 0.33 1 vs 2: 0.37 1 vs 3: 0.4	SS51024	13
12	R85A11	strong	strong	6	0 1 2 3 4 5	unresponsive unresponsive walk unclear walk unclear	2 vs 4: 0.87	-	15
13	SS40489	-	strong	5	0 1 2 3 4	unclear unclear unclear unclear unclear	0 vs 3: 0.38 0 vs 4: 0.43 1 vs 3: 0.53 1 vs 4: 0.53	-	16

Chapter 3. Ascending neurons convey behavioral state to integrative sensory and action selection centers in the brain

Table S3.1 continued from previous page

No.	GAL4	Confocal SNR of smFP	2P SNR of OpGCaMP6f and tdTomato	Number ROIs	ROI#	Encoding	Level synchronous activity (ROI# vs ROI#: Corr. coef.)	Redundant GAL4	Supp. Video#
14	SS31480	strong	strong	3	0 1 2	walk unclear walk	0 vs 2: 0.61	-	17
15	SS51021	strong	strong	2	0 1	foreleg movement foreleg movement	0 vs 1: 0.69	-	18
16	SS51017	strong	strong	2	0 1	off ball movement off ball movement	0 vs 1: 0.67	-	19
17	SS31456	strong	strong	2	0 1	off ball movement off ball movement	0 vs 1: 0.20	-	20
18	SS46233	strong	medium	2	0 1	walk walk	0 vs 1: 0.63	-	21
19	SS42749	strong	strong	2	0 1	push push	0 vs 1: 0.89	-	22
20	SS41815	strong	medium	2	0 1	unclear unclear	0 vs 1: 0.42	-	23
21	SS29633	strong	strong	3	0 1 2	unclear unclear unclear	0 vs 1: 0.11 0 vs 2: 0.41 1 vs 2: 0.42	-	24
22	R87H02	strong	strong	2	0 1	unclear unclear	0 vs 1: 0.48	-	25
23	MAN	strong	strong	2	0 1	push push	0 vs 1: 0.82	-	26
24	SS49172	strong	strong	3	0 1 2	walk walk walk	0 vs 1: 0.54 0 vs 2: 0.53	-	27
25	R36G04	strong	strong	2	0 1	walk walk	0 vs 1: 0.55	-	28
26	R39G01	strong	strong	3	0 1 2	unclear unclear unclear	0 vs 1: 0.09 0 vs 2: 0.82 1 vs 2: 0.19	-	29
27	SS31219	strong	strong	3	0 1 2	walk walk walk	0 vs 1: 0.67 0 vs 2: 0.74	-	30
28	R30A08	strong	medium	2	0 1	unclear unclear	0 vs 1: 0.22	-	31
29	SS44270	strong	strong	3	0 1 2	walk walk walk	0 vs 1: 0.98	SS41605	32
30	SS41605	strong	strong	4	0 1 2 3	unclear unclear push push	2 vs 3: 0.94	SS44270	33
31	SS29579	strong	strong	6	0 1 2 3 4 5	walk walk walk walk unresponsive walk	0 vs 2: 0.84 0 vs 3: 0.89 0 vs 3: 0.89 1 vs 2: 0.78 1 vs 3: 0.87	-	34
32	SS51046	medium	strong	2	0 1	turn turn	0 vs 1: 0.48	-	35

3.11 Supplementary Information

Table S3.1 continued from previous page

No.	GAL4	Confocal SNR of smFP	2P SNR of OpGCaMP6f and tdTomato	Number ROIs	ROI#	Encoding	Level synchronous activity (ROI# vs ROI#: Corr. coef.)	Redundant GAL4	Supp. Video#
33	SS29893	strong	strong	4	0 1 2 3	unclear unclear turn turn	2 vs 3: 0.62	SS34574	36
34	SS34574	strong	strong	2	0 1	turn turn	0 vs 1: 0.44	SS29893	37
35	R70H06	strong	strong	3	0 1 2	foreleg movement foreleg movement unresponsive	0 vs 1: 0.98	SS42740 SS42707	38
36	SS42740	strong	strong	2	0 1	foreleg movement foreleg movement	0 vs 1: 0.97	R70H06 SS42707	39
37	SS25469	strong	strong	2	0 1	eye groom eye groom	0 vs 1: 0.75	SS52106 SS52107 SS52108	40
38	SS31232	strong	strong	2	0 1	proboscis extension proboscis extension	0 vs 1: 0.81	SS30303 SS25451	41
39	SS30303		strong	2	0 1	proboscis extension proboscis extension	0 vs 1: 0.89	SS31232 SS25451	42
40	SS25451	strong	strong	7	0 1 2 3 4 5 6	unresponsive unresponsive proboscis extension unresponsive proboscis extension unresponsive unresponsive	2 vs 4: 0.93	SS31232 SS30303	43
41	SS28596	strong	strong	6	0 1 2 3 4 5	foreleg movement foreleg movement foreleg movement foreleg movement foreleg movement foreleg movement	0 vs 2: 0.4 0 vs 3: 0.65 0 vs 4: 0.61 0 vs 5: 0.21 1 vs 2: 0.52 1 vs 3: 0.5 1 vs 4: 0.46 1 vs 5: 0.28	R86H08	44
42	SS40134	strong	medium	2	0 1	unclear unclear	0 vs 1: 0.34	-	45
43	SS29621	strong	strong	2	0 1	walk walk	0 vs 1: 0.74	-	46
44	R69H10	strong	strong	3	0 1 2	unclear unclear unclear	0 vs 1: 0.21 0 vs 2: 0.07 1 vs 2: 0.02	-	47
45	SS51038	strong	strong	5	0 1 2 3 4	rest unclear unclear unresponsive rest	0 vs 2: -0.41 0 vs 4: 0.86 2 vs 4: -0.43	-	48
46	SS42008	strong	strong	4	0 1 2 3	walk unclear walk unclear	0 vs 2: 0.53	SS42007	49

Chapter 3. Ascending neurons convey behavioral state to integrative sensory and action selection centers in the brain

Table S3.1 continued from previous page

No.	GAL4	Confocal SNR of smFP	2P SNR of OpGCaMP6f and tdTomato	Number ROIs	ROI#	Encoding	Level synchronous activity (ROI# vs ROI#: Corr. coef.)	Redundant GAL4	Supp. Video#
47	SS36118	strong	strong	6	0	unclear		-	50
					1	unclear	2 vs 4: 0.25		
					2	unresponsive	2 vs 5: 0.12		
					3	puff	3 vs 4: 0.75		
					4	puff	3 vs 5: 0.27		
5	rest								
48	SS40619	medium	strong	2	0	walk	0 vs 1: 0.74	-	51
49	SS45363	strong	strong	4	0	puff	0 vs 3: 0.83	-	52
					1	puff	1 vs 3: 0.85		
					2	unclear	2 vs 3: 0.71		
3	puff								
50	SS52147	medium	medium	2	0	puff	0 vs 1: 0.32	-	53
1	1	puff							
51	R38F09	-	strong	10	-	unresponsive	-	-	-
52	SS46269	strong	strong	12	-	unresponsive	-	-	-
53	SS25470	strong	strong	5	-	unresponsive	-	SS48406	-
54	SS25478	strong	strong	5	-	unresponsive	-	-	-
55	SS28382	strong	strong	6	-	unresponsive	-	-	-
56	SS29574	strong	strong	2	-	unresponsive	-	-	-
57	SS31899	strong	strong	8	-	unresponsive	-	-	-
58	SS33380	strong	strong	7	-	unresponsive	-	-	-
59	SS33433	strong	strong	2	-	unresponsive	-	-	-
60	SS38012	strong	strong	6	-	unresponsive	-	SS43528	-
61	SS38386	medium	strong	3	-	unresponsive	-	-	-
62	SS38687	strong	strong	3	-	unresponsive	-	-	-
63	SS46290	medium	medium	2	-	unresponsive	-	-	-
64	SS46300	strong	medium	2	-	unresponsive	-	-	-
65	SS48406	strong	strong	5	-	unresponsive	-	SS25470	-
66	SS48409	strong	strong	2	-	unresponsive	-	SS48632	-
67	SS49982	strong	medium	4	-	unresponsive	-	-	-
68	SS50004	strong	strong	2	-	unresponsive	-	-	-
69	SS50013	medium	medium	1	-	unresponsive	-	-	-
70	SS50652	strong	medium	3	-	unresponsive	-	-	-
71	SS36132	strong	-	-	-	not imaged	-	SS36131	-
						(redundant)		SS36133	
72	SS36133	strong	-	-	-	not imaged	-	SS36131	-
						(redundant)		SS36132	
73	SS38598	strong	-	-	-	not imaged	-	SS38592	-
						(redundant)			
74	SS41808	strong	-	-	-	not imaged	-	SS41822	-
						(redundant)		SS41809	
								SS41820	
								SS41821	
75	SS41809	strong	-	-	-	not imaged	-	SS41822	-
						(redundant)		SS41808	
								SS41820	
								SS41821	
76	SS41820	strong	-	-	-	not imaged	-	SS41822	-
						(redundant)		SS41808	
								SS41809	
								SS41821	

3.11 Supplementary Information

Table S3.1 continued from previous page

No.	GAL4	Confocal SNR of smFP	2P SNR of OpGCaMP6f and tdTomato	Number ROIs	ROI#	Encoding	Level synchronous activity (ROI# vs ROI#: Corr. coef.)	Redundant GAL4	Supp. Video#
77	SS41821	strong	-	-	-	not imaged (redundant)	-	SS41822 SS41808 SS41809 SS41820	-
78	SS42007	strong	-	-	-	not imaged (redundant)	-	SS42008	-
79	SS42707	medium	-	-	-	not imaged (redundant)	-	SS42740 R70H06	-
80	SS43528	strong	weak	-	-	(undetectable in 2P; redundant)	-	SS38012	-
81	SS48632	medium	-	-	-	not imaged (redundant)	-	SS48409	-
82	SS51024	strong	-	-	-	not imaged (redundant)	-	SS51029	-
83	SS52108	strong	weak	-	-	not imaged (redundant)	-	SS25469 SS52106 SS52107	-
84	SS52106	medium	-	-	-	not imaged (redundant)	-	SS25469 SS52107 SS52108	-
85	SS52107	medium	-	-	-	not imaged (redundant)	-	SS25469 SS52106 SS52108	-
86	R86H08	medium	weak	-	-	not imaged (redundant)	-	SS28596	-
87	SS29889	strong (indistinguishable brain neurons)	-	-	-	not imaged (redundant)	-	SS29890	-
88	SS29890	strong (indistinguishable brain neurons)	-	-	-	not imaged (redundant)	-	SS29889	-
89	SS29605	-	unreliable expression	-	-	not imaged (unreliable expression)	-	-	-
90	SS31246	unreliable expression	unreliable expression	-	-	not imaged (unreliable expression)	-	-	-
91	SS46696	unreliable expression	unreliable expression	-	-	not imaged (unreliable expression)	-	-	-
92	R75E01	strong but with glia	-	-	-	not imaged (glia included)	-	-	-
93	SS37652	medium	weak	-	-	not imaged (undetectable)	-	-	-
94	SS41602	strong	weak	-	-	not imaged (undetectable)	-	-	-
95	SS43651	strong	weak	-	-	not imaged (undetectable)	-	-	-
96	SS44305	strong	weak	-	-	not imaged (undetectable)	-	-	-
97	SS46255	strong	weak	-	-	not imaged (undetectable)	-	-	-

Chapter 3. Ascending neurons convey behavioral state to integrative sensory and action selection centers in the brain

Table S3.1 continued from previous page

No.	GAL4	Confocal SNR of smFP	2P SNR of OpGCaMP6f and tdTomato	Number ROIs	ROI#	Encoding	Level synchronous activity (ROI# vs ROI#: Corr. coef.)	Redundant GAL4	Supp. Video#
98	SS41824	strong	weak	-	-	not imaged (undetectable)	-	-	-
99	SS25488	-	weak	-	-	not imaged (undetectable)	-	-	-
100	R81G07	weak	weak	-	-	not imaged (undetectable)	-	-	-
101	SS45635	weak	weak	-	-	not imaged (undetectable)	-	-	-
102	SS45648	weak	weak	-	-	not imaged (undetectable)	-	-	-
103	SS46290	weak	weak	-	-	not imaged (undetectable)	-	-	-
104	SS46847	weak	weak	-	-	not imaged (undetectable)	-	-	-
105	SS47868	weak	weak	-	-	not imaged (undetectable)	-	-	-
106	SS50282	weak	weak	-	-	not imaged (undetectable)	-	-	-
107	SS50829	weak	weak	-	-	not imaged (undetectable)	-	-	-
108	R88C08	weak	weak	-	-	not imaged (undetectable)	-	-	-

3.11 Supplementary Information

Table S3.2: Activation (AD) and DNA-binding Domains (DBD) of split-GAL4 lines used in this study.

	Driver line	AD	DBD
1	SS36131	R70D06	VT033054
2	SS38592	VT016458	VT012410
3	SS27485	R75E01	R18B05
4	SS41822	VT033054	VT026646
5	SS38624	VT002081	R85H01
6	SS45605	R15E01	R41E03
7	SS43652	VT026477	R38E07
8	SS36112	VT026646	VT028606
9	SS41806	VT060737	VT028606
10	SS38631	R72A10	VT038208
11	SS51029	VT034810	VT004985
12	R85A11	-	-
13	SS40489	R36B06	VT007767
14	SS31480	R68C10	VT008150
15	SS51021	VT027767	VT027005
16	SS51017	VT005404	VT027767
17	SS31456	VT013500	VT012768
18	SS46233	VT029814	VT028464
19	SS42749	R66A06	VT056770
20	SS41815	VT043377	VT014669
21	SS29633	R33F06	R76E11
22	R87H02	-	-
23	MAN	VT50660	VT14014
24	SS49172	VT049120	VT008188
25	R36G04	-	-
26	R39G01	-	-
27	SS31219	VT045153	VT019074
28	R30A08	-	-
29	SS44270	VT058560	VT033054
30	SS41605	R80A11	VT038205
31	SS29579	VT023828	VT059224
32	SS51046	VT007177	VT057280
33	SS29893	R67F03	VT050658
34	SS34574	VT008537	VT050658
35	R70H06	-	-
36	SS42740	VT037865	VT061717
37	SS25469	VT027704	VT044958
38	SS31232	VT063643	VT059781
39	SS30303	VT063643	VT018278
40	SS25451	VT063643	VT059224
41	SS28596	R94B04	R86H08
42	SS40134	VT028320	R49A01
43	SS29621	R22E07	R30E10
44	R69H10	-	-
45	SS51038	VT030558	VT001497
46	SS42008	VT033469	VT043682
47	SS36118	VT060737	VT026477
48	SS40619	VT021853	VT050234
49	SS45363	VT062587	VT043920
50	SS52147	VT044164	VT040034
51	R38F09	-	-
52	SS46269	VT023490	VT016254
53	SS25470	VT063643	VT048352

Chapter 3. Ascending neurons convey behavioral state to integrative sensory and action selection centers in the brain

Table S3.2 continued from the previous page

	split-GAL4 line	AD	DBD
54	SS25478	VT025966	VT013121
55	SS28382	R18G02	R49C03
56	SS29574	VT008660	VT043400
57	SS31899	R26H04	R46A10
58	SS33380	R19F01	R60A06
59	SS33433	R94D12	VT060731
60	SS38012	R48E02	R93B07
61	SS38386	VT016966	VT046334
62	SS38687	R30A02	VT015159
63	SS46290	VT029750	VT043288
64	SS46300	VT043146	VT000254
65	SS48406	VT048352	VT039769
66	SS48409	VT036302	VT049125
67	SS49982	R77D08	VT029514
68	SS50004	VT017645	VT049348
69	SS50013	VT008992	VT039485
70	SS50652	R60C01	R80B01
71	SS36132	R70D06	VT025996
72	SS36133	R70D06	VT026646
73	SS38598	VT024634	VT016458
74	SS41808	VT060737	VT033054
75	SS41809	R20E05	VT033054
76	SS41820	VT060737	VT025996
77	SS41821	R20E05	VT025996
78	SS42007	VT033469	VT026646
79	SS42707	VT061717	VT045101
80	SS43528	VT025966	R93B07
81	SS48632	VT036302	R93B07
82	SS51024	VT004985	VT034810
83	SS52108	VT063231	R69H06
84	SS52106	VT063231	VT063626
85	SS52107	VT063231	VT021731
86	R86H08	-	-
87	SS29889	R64G04	VT008537
88	SS29890	R64G04	VT050658
89	SS29605	VT019902	VT048942
90	SS31246	VT038171	VT021780
91	SS46696	VT046782	VT008483
92	SS22675	R44G08	R81A04
93	SS22721	R92D09	R92A07
94	R75E01	-	-
95	SS37652	VT040698	VT023490
96	SS41602	R75E01	R74C01
97	SS43651	VT026477	VT039361
98	SS44305	R21E09	VT016966
99	SS46255	R24H02	VT037862
100	SS41824	R20E05	VT026646
101	SS25488	VT029593	VT020527
102	R81G07	-	-
103	SS45635	VT008882	VT014208
104	SS45648	VT008808	VT029814
105	SS46290	VT029750	VT043288
106	SS46847	VT023490	VT039485
107	SS47868	R24H02	VT002064
108	SS50282	VT037554	VT012768
109	SS50829	VT033290	VT027767

Table S3.2 continued from the previous page

	split-GAL4 line	AD	DBD
110	R88C08	-	-
111	SS22647	R94B04	R66B12
112	SS22377	R12H12	R92A07

Chapter 3. Ascending neurons convey behavioral state to integrative sensory and action selection centers in the brain

3.11.3 Supplement Videos

Video S3.1: **High-level behaviors, their associated 3D poses, and spherical treadmill rotational velocities.** Behaviors were captured from six camera views. Illuminated text (top) indicates the behavioral class being illustrated. Also shown are corresponding 3D poses (bottom-left) and spherical treadmill rotational velocities, proboscis extension (PE) lengths, and puff stimulation periods (bottom-right).

[Download Video S3.1](#)

Video S3.2: **Representative data for 50 comprehensively analyzed, AN-targeting sparse driver lines.** Shown are: **(a)** spFP staining, **(b)** a representative two-photon microscope image, **(c)** outline of the associated cervical connective after filling the surrounding bath with fluorescent dye, **(d)** and PE length, puff stimuli, spherical treadmill rotational velocities, and AN (ROI) $\Delta F/F$ traces. Indicated above are regressors for forward walking ('F.W.'), backward walking ('B.W.'), resting ('Rest'), eye grooming ('Eye groom'), antennal grooming ('Ant. groom'), foreleg rubbing ('Fl. rub'), abdominal grooming ('Abd. groom'), hindleg rubbing ('Hl. rub'), and proboscis extension ('PE'). For each driver line, the title indicates 'date-Gal4-reporters-fly#-trial#'.

[Download Video S3.2](#)

Videos S3.3 - S3.52: **Representative behavioral videos and AN two-photon imaging data for 50 comprehensively analyzed, AN-targeting sparse driver lines.**

[Download Video S3.3 - S3.52](#)

4 Serotonergic Modulation of Walking in *Drosophila*

Disclaimer: This chapter is adapted from the following article in preparation with permissions of all co-authors and journal.

Clare E. Howard, **Chin-Lin Chen**, Tanya Tabachnik, Rick Hormigo, Pavan Ramdya, Richard S.Mann. "Serotonergic Modulation of Walking in *Drosophila*", *Current Biology*, vol.29, pp.4218-4230.e8, 2019. <https://doi.org/10.1016/j.cub.2019.10.042>

My contribution: To examine the behavioral encoding of serotonergic neurons in the VNC (5-HT^{VNC}), I performed simultaneous recordings of neural activity and behavior of tethered flies mounted in the setup of a two-photon microscope, a spherical treadmill with optic-flow sensors, and behavioral cameras via the preparation introduced in [chapter 2](#). The VNCs of experimental flies were also isolated and subjected to immunostaining against the morphological reporter of 5-HT^{VNC} neurons to confirm the consistent expression. To quantify the data, I performed analysis to (i) extract the mean fluorescence values among regions-of-interest in each frame of two-photon image stacks, (ii) classify moving and resting epochs based on the ball rotation, and (iii) synchronize datapoint of fluorescence values, ball rotations, and behavioral videography to visualize the average response during different types of behavior. In sum, my contribution confirmed that 5-HT^{VNC} neurons encode walking.

4.1 Abstract

To navigate complex environments, animals must generate highly robust, yet flexible, locomotor behaviors. For example, walking speed must be tailored to the needs of a particular environment. Not only must animals choose the correct speed and gait, they must also adapt to changing conditions and quickly respond to sudden and surprising new stimuli. Neuromodulators, particularly the small biogenic amine neurotransmitters, have the ability to rapidly alter the functional outputs of motor circuits. Here, we show that the serotonergic system in the vinegar fly, *Drosophila melanogaster*, can modulate walking speed in a variety of contexts and also change how flies respond to sudden changes in the environment. These multifaceted roles of serotonin in locomotion are differentially mediated by a family of serotonergic receptors with distinct activities and expression patterns.

4.2 Introduction

Insects have a remarkable capacity to adapt their locomotor behaviors across a wide range of environmental contexts and to confront numerous challenges. They can walk forward, backward, and upside down, navigate complex terrains, and rapidly recover after injury [28, 142, 170–173]. To achieve this wide range of behaviors, insects regulate their walking speed and kinematic parameters, allowing them to modify stereotyped gaits as needed [87, 172, 174–176]. Because overlapping sets of motor neurons and muscles are recruited for all of these behaviors, animals must be able to rapidly modulate the circuit dynamics that control locomotor parameters [177, 178].

As with limbed vertebrates, most insects use multi-jointed legs to walk [177, 178]. In the vinegar fly, *Drosophila melanogaster*, the neural circuits that orchestrate complex walking gaits are located in the ventral nerve cord (VNC), a functional analog of the vertebrate spinal cord that includes three pairs of thoracic neuromeres (T1, T2, and T3) that coordinate the movements of three corresponding pairs of legs [38, 86, 179, 180]. The VNC receives descending commands from the brain and sends motor output instructions via motor neurons to peripheral musculature [38, 181, 182]. Sensory neurons, which convey proprioceptive and tactile information, project axons from the appendages to the VNC by these same fiber tracts, where they arborize in the leg neuropils [17, 23, 183–185] (Figure 4.1A). Notably, the VNC is capable of executing coordinated leg motor behaviors, such as walking and grooming, even in decapitated animals [186]. Thus, as has been described in other insects, the VNC likely harbors neural networks that can drive the coordinated flexion and extension of each leg joint and also coordinated walking gaits [177, 187].

Numerous studies have established that sensory input from the legs is required for robust and stereotyped locomotor patterns, regulating the timing, magnitude, and coordination of locomotor activity [17, 21, 87, 142, 184, 188–190]. However, sensory feedback cannot be the

only means for tuning locomotion: mutation of proprioceptive receptors or even deafferenting limbs does not block coordinated walking [1, 21, 191–194]. Beyond sensory feedback-driven tuning of gait patterns, larger behavioral changes must be accomplished by other circuits. These likely include neuromodulatory systems, including the monoamines dopamine, norepinephrine, and serotonin, which are highly conserved throughout the animal kingdom [195–197].

Monoamines have been shown to modulate, and even induce, the activities of central pattern generating (CPG) motor circuits. In crustaceans, neuromodulation causes the gastric CPG to generate distinct rhythmic activity patterns from the same neural network to address distinct behavioral demands [195, 198]. Remarkably, the same neuromodulatory systems appear to play similar roles across species. Serotonin has been shown to slow locomotor rhythms in animals as diverse as the lamprey, cat, and locust [199–201]. In *Drosophila*, monoamine neurotransmitters have also been shown to modulate a wide range of behaviors. In addition to slowing walking speed, serotonin modulates sleep, aggression, and anxiety-related motor behaviors [202–208]. Dopamine, in contrast, has been linked to hyperactivity [186, 209–211]. Octopamine has been shown to mediate starvation-induced hyperactivity, and in its absence animals walk more slowly [87, 212, 213]. As each of these neuromodulatory systems plays a variety of roles in regulating complex behaviors, it has thus far been challenging to tease apart which of the effects on walking behavior are due to direct modulation of motor circuitry or are a secondary consequence of modulating higher-order circuits in the brain.

In this work, we show that the serotonergic neurons within the VNC have the ability to modulate walking speed in multiple internal states and many environmental contexts, as well as in response to startling stimuli. Additionally, we demonstrate that these modulatory effects are enacted through serotonin's action on specific receptors that are expressed in different parts of the locomotor circuit. Together, these findings reveal that neuromodulatory systems regulate multiple aspects of walking behavior, helping animals to effectively respond to rapidly changing environments.

4.3 Results

4.3.1 VNC Serotonergic Neurons Arborize within the Leg Neuropils

To identify neuromodulatory neurons that might play a role in modulating walking behavior, we drove expression of a fluorescent reporter with Gal4 under the control of promoters encoding key synthetic enzymes for each neuromodulatory system—*Tryptophan hydroxylase* (*Trh* for serotonin (5-HT) [207]); *tyrosine hydroxylase* (*TH* or *ple* (*pale*) for dopamine [214]); and *Tyrosine decarboxylase 2* (*Tdc2* for octopamine and tyramine [215]). All of these drivers show extensive expression in cells both within the VNC and the brain, with processes that densely innervate VNC leg neuromeres (Figure 4.1).

To determine whether local neuromodulatory VNC neurons or descending neurons originating in the brain innervate the leg neuropils, we used genetic intersectional tools to limit the expression of these Gal4 lines to either the brain or VNC (**Figure 4.1A**) (see **Materials and Method**). These experiments show that neuromodulatory innervation of the leg neuropils arises almost entirely from VNC interneurons and not from descending neurons in the brain (**Figure 4.1B-G**). Moreover, these VNC neurons extensively innervate the leg neuropils. Thus, VNC neuromodulatory neurons are well positioned to directly modulate VNC locomotor circuits.

4.3.2 Activation of VNC Serotonergic Neurons Slows Walking Speed

Previous studies showed that neuromodulatory systems can regulate walking but have not addressed the role of VNC neuromodulatory subpopulations. Using the intersectional genetic tools described above, we addressed whether neuromodulatory neurons in the VNC alone are sufficient to modulate walking behavior. We optogenetically activated these neurons and measured walking speed using the Flywalker behavioral assay [21]. We found that activation of serotonergic VNC populations, but not dopaminergic or octopaminergic/tyraminerpic VNC subpopulations, significantly reduced the average speed at which animals walk (**Figure 4.1H**).

Based on these results, we focused the remainder of our analysis on VNC serotonergic neurons (5-HT^{VNC}). To validate the fidelity of our serotonergic Gal4 driver line and to rule out co-secretion of other neurotransmitters, we performed immunostaining for markers of serotonergic (5-HT), dopaminergic (TH), octopaminergic/tyraminerpic (Tdc2), glutamaterpic (VGlut), cholinergic (ChAT), and GABAergic (GABA) neurons (**Figure S4.1**). These experiments demonstrate that the *Trh-Gal4* line drives expression in 5-HT-expressing neurons and that these neurons do not express any of the other neurotransmitters we surveyed, suggesting that they are primarily serotonergic.

We next characterized the effects on locomotor behavior of activating 5-HT^{VNC} neurons by studying animals freely walking within an arena [216, 217]. This approach allowed us to measure not only an animal's speed but also its walking frequency, angular velocity, and preferred position within the arena (**Figure S4.2A-C**). As with our initial experiments, activation of 5-HT^{VNC} neurons is sufficient to dramatically slow average walking speed in this paradigm (**Figure 4.2A**). Interestingly, activation of 5-HT^{VNC} neurons does not change the overall amount of time animals spend walking, suggesting that speed changes are not simply due to a decrease in overall activity but instead reveal a bias toward slower walking speeds (**Figure S4.2D** and **Figure S4.2F**). Unlike a previous study showing that overexpressing the serotonin transporter in all neurons caused flies to move away from the edge of the arena [204], we see no effect on the distribution of animals within the arena when we limit activation to 5-HT^{VNC} neurons (**Figure S4.2D**). We also find that activation of 5-HT^{VNC} neurons decreases the absolute angular velocity of walking flies (**Figure S4.2D**). Thus, although these flies walk slower, they also

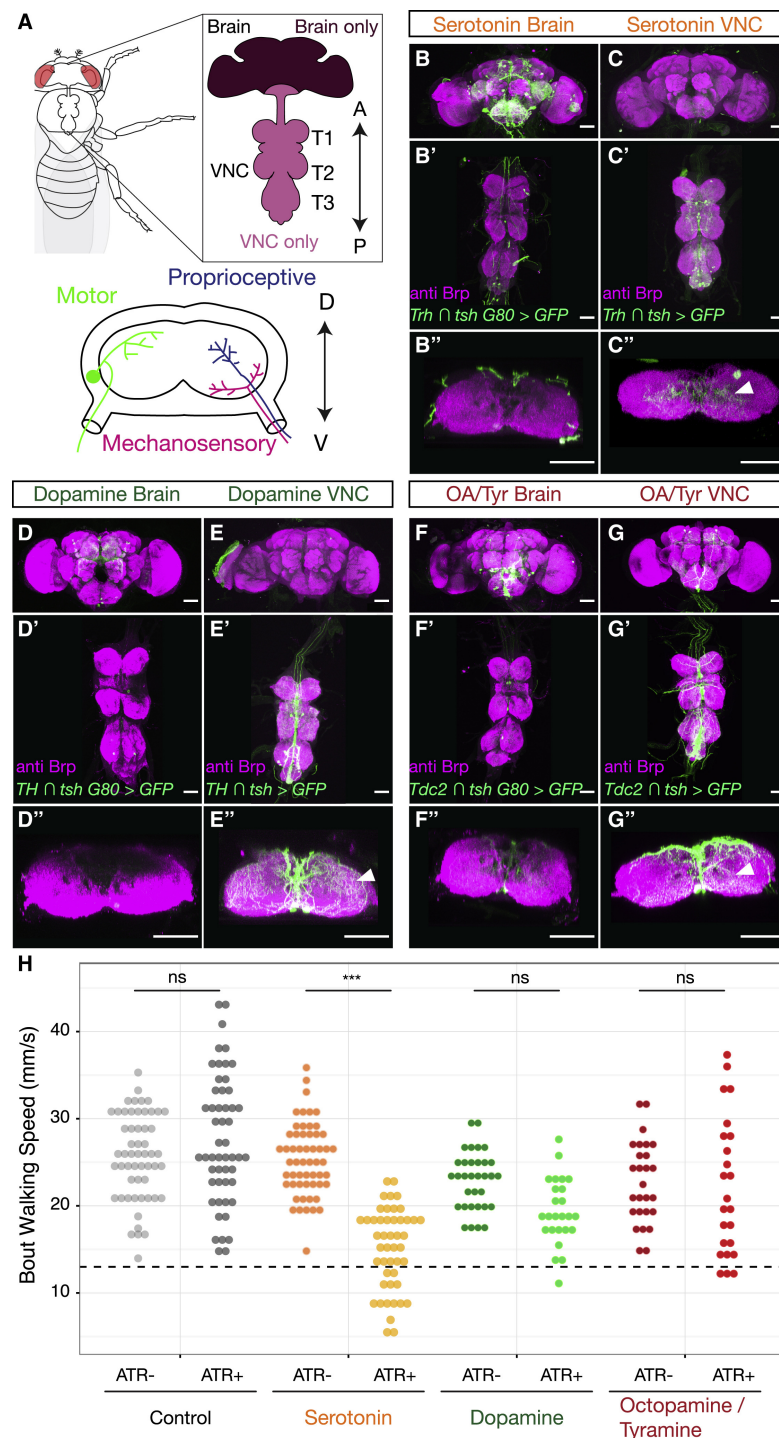


Figure 4.1: **Neuromodulators in the *Drosophila* CNS.** (A) The adult *Drosophila* CNS is composed of the brain and the VNC, which consists of three pairs of thoracic neuropils (T1, T2, and T3), each of which corresponds to a pair of adult legs, and an abdominal ganglion. The anterior (A)-posterior (P) axis is specified. Lower panel: cross-section of a thoracic neuropil

illustrating projections of locomotor circuit components, including motor neurons, and sensory neurons that convey mechanosensory and proprioceptive information from the legs. The dorsal (D)-ventral (V) axis is specified. (**B-G**) Maximum intensity projections show the expression patterns driven by Gal4 lines labeling either brain-derived (**B, D, F**, *Gal4* intersected with *tsh Gal80*) or VNC-derived (**C, E, G**, *Gal4* intersected with *tsh*) serotonergic (**B** and **C**, *Trh Gal4*), dopaminergic (**D** and **E**, *TH Gal4*), or octopaminergic/tyraminerbic (OA/Tyr) (**F** and **G**, *Tdc2 Gal4*) neurons. (**B"-G"**) Projection of a subset of cross sections of the VNC shows innervation of the T1 neuropil. Arrowheads point to innervation in the leg neuropils. All scale bars are 50 μm . (**H**) Optogenetic activation of serotonergic (*Trh* \cap *tsh* $>$ *csChrimson*) neurons in the *Drosophila* VNC but not dopaminergic (*TH* \cap *tsh* $>$ *csChrimson*) or octopaminergic/tyraminerbic (*Tdc2* \cap *tsh* $>$ *csChrimson*) neurons slows walking speed compared to all-trans-retinal (ATR) negative and non-Gal4 (*w¹¹¹⁸* \cap *tsh* $>$ *csChrimson*) controls. These experiments were carried out using the Flywalker assay ([21]); see Figure S4.3A for a schematic). * $p < 0.05$ ** $p < 0.01$ *** $p < 0.001$ by Kruskal-Wallis test with Dunn-Sidak correction for multiple comparisons. n = walking bouts (recorded from N animals) *w¹¹¹⁸* ATR⁻ 55 (14–31); *w¹¹¹⁸* ATR⁺ 52 (14–36); *Trh* ATR⁻ 56 (12–30); *Trh* ATR⁺ 47 (10–23); *TH* ATR⁻ 33 (10–24); *TH* ATR⁺ 25 (10–26); *Tdc2* ATR⁻ 27 (10–27); *Tdc2* ATR⁺ 24 (10–25).

See also Figure S4.1

walk straighter than control flies. This latter observation is unexpected, because straighter trajectories are usually correlated with faster walking speeds (Figure S4.2F).

4.3.3 Inhibition of 5-HT^{VNC} Neurons Increases Walking Speed

Although activation of 5-HT^{VNC} neurons causes flies to walk more slowly, gain-of-function experiments such as these cannot determine whether and in what situations these neurons are normally used to modulate walking speed. To begin to address this question, we expressed the inward rectifying potassium channel Kir2.1 to constitutively inactivate 5-HT^{VNC} neurons. Although neurons were inactivated throughout development and adulthood, we did not observe a change in the number or anatomy of 5-HT^{VNC} neurons, suggesting that their development is not significantly affected (Figure S4.2H and Figure S4.2I).

Consistent with the activation phenotype, inhibition of 5-HT^{VNC} neurons causes animals to walk faster (Figure 4.2B). In fact, the shifts in velocity produced by either optogenetic activation or constitutive inhibition of 5-HT^{VNC} neurons mirror each other (Figure 4.2C). In addition, 5-HT^{VNC} inactivation causes animals to increase their angular velocity (Figure S4.2E and Figure S4.2G) and increases the percentage of time that animals spend walking (Figure S4.2E). The reciprocal effects on speed from either activating or silencing 5-HT^{VNC} neurons suggest that serotonin release in the VNC has the capacity to modulate baseline walking speed.

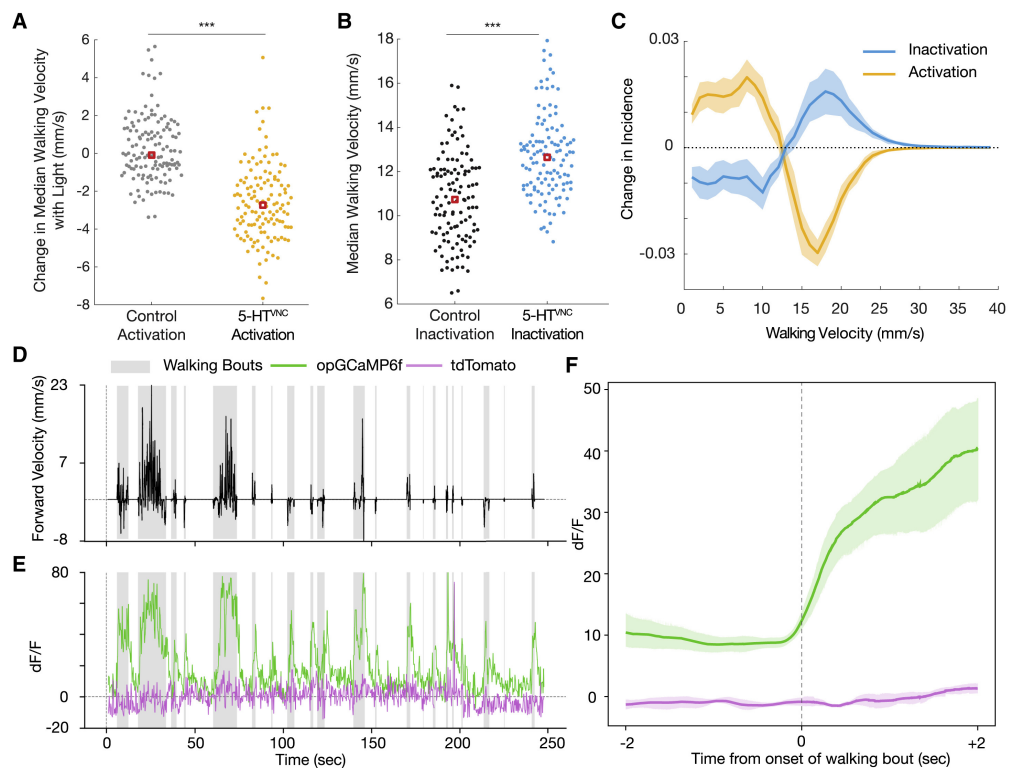


Figure 4.2: 5-HT^{VNC} Neurons Modulate Walking Speed. (A) Activation of 5-HT^{VNC} neurons (*Trh* \cap *tsh* > *csChrimson* fed with ATR) causes animals to walk slower than background-matched non-Gal4 controls (*w¹¹¹⁸* \cap *tsh* > *csChrimson* fed with ATR). *** p < 0.001 by Kruskal-Wallis test. Red box indicates median. N = 130 animals for each genotype. (B) Inactivation of 5-HT^{VNC} neurons (*Trh* \cap *tsh* > *Kir2.1*) causes animals to walk faster than background-matched non-Gal4 controls (*w¹¹¹⁸* \cap *tsh* > *Kir2.1*). *** p < 0.001 by Kruskal-Wallis test. Red box indicates median. N = 119 animals per genotype. (C) The distribution of velocity shifts caused by activation and inhibition of 5-HT^{VNC} neurons are symmetrical. Differences in population average histograms were calculated between control and experimental genotypes and were fit with 95% confidence intervals via bootstrapping. For activation experiments, behavior of *w¹¹¹⁸* \cap *tsh* > *csChrimson* flies fed with ATR was compared to that of *Trh* \cap *tsh* > *csChrimson* flies also fed with ATR for the light on period only. (D and E) Serotonergic processes passing through the cervical connective (labeled using *Trh* \cap *tsh*) are active during walking. (D) A single animal's forward velocity with overlaid boxes showing defined walking bouts. (E) While tdTomato baseline signal (purple line) is not affected by walking bouts, the calcium signal (green line) in these serotonergic processes rises during walking bouts (gray boxes). (F) Calcium signal but not tdTomato signal in these processes rises with the onset of walking bouts. For each animal, all walking bouts were synchronized around their onset, and an average was taken (between 80 and 130 walking bouts per animal). Plotted is the average of all animals (N = 5) with a 95% confidence interval representing the spread between animals.

See also [Figure S4.2](#) and [Figure S4.3](#).

4.3.4 5-HT^{VNC} Neurons Are Active in Walking Flies Neurons Increases Walking Speed

The opposing effects on speed when 5-HT^{VNC} neurons are activated or inhibited suggest that the activity of these neurons will co-vary with walk-stop transitions and velocity changes during baseline walking. To test this prediction, we performed functional calcium imaging of 5-HT^{VNC} processes while flies walked on a spherical treadmill (Figure S4.3A) [49]. To obtain the most robust signal, we focused on fibers in the neck connective, which are likely derived from a subset of ascending 5-HT^{VNC} neurons that target the brain (Figure S4.3B-D).

Activity in these fibers is highly correlated with walking (Figure 4.2D and Figure 4.2E). Fluorescent calcium signals from these cells rise dramatically at the onset of each walking bout (Figure 4.2F). These signals are much weaker when animals perform other motor behaviors, like proboscis extension or grooming (Figure S4.3E). These results suggest that at least a subset of 5-HT^{VNC} neurons are specifically active when flies walk and are not generically active during all legged motor behaviors. We also find that the activity of these serotonergic processes positively correlates with the average speed of the walking bout, suggesting that these neurons may become more active when animals walk faster (Figure S4.3F).

The observation that the activity of some 5-HT^{VNC} neurons is positively correlated with velocity is interesting in light of our behavioral data, which show that flies walk more slowly when 5-HT^{VNC} neurons are optogenetically activated. There are several explanations for these apparently opposing observations. First, because the calcium imaging experiments only focus on a subset of 5-HT^{VNC} processes, while the behavior experiments manipulate the entire set of 5-HT^{VNC} neurons, it may be that the neurons being imaged have a unique function and that their activity is not representative of the entire set. Alternatively, if their activity is representative of the broader population of 5-HT^{VNC} neurons, it would suggest that as flies walk faster more serotonin release is needed to slow animals down. Regardless, the fact that activity in these neurons correlates with velocity supports a role for them in modulating walking speed and raises the possibility that some of them may function in a negative feedback loop.

4.3.5 5-HT^{VNC} Activation Does Not Disrupt Walking Coordination

The slower walking speeds that result when 5-HT^{VNC} neurons are activated could be the result of poor coordination or, alternatively, controlled adjustments of kinematic parameters, which naturally occur when flies walk more slowly [21, 87]. To distinguish between these two possibilities, we returned to the Flywalker assay, which measures kinematic parameters at high temporal and spatial resolution [21] (Figure S4.4A).

Using this assay, we find that optogenetic activation of 5-HT^{VNC} neurons results in highly coordinated walking patterns. Representative traces of an individual's footprints during a

slow walking bout show that activation of these neurons does not perturb stereotyped foot placement or interfere with the straightness of the walking bout (Figure 4.3A and Figure 4.3C). Step and stance traces show that these animals also use highly coordinated gaits, suggesting that interleg coordination is intact (Figure 4.3B and Figure 4.3D). In fact, compared to control flies, 5-HT^{VNC} neuron activation results in more precise foot placement at the onset and offset of each stance phase, suggesting that the walking behavior of these animals is more constrained compared to control animals (Figure S4.4B).

In wild-type flies, most walking parameters are highly correlated with speed, shifting as animals walk faster or slower [21, 87]. For example, as animals walk slower, their step-cycle frequency decreases, they take longer steps, and they slow the velocity of their swinging legs. These shifts are accompanied by a shift in the step duty cycle, as stance duration increases while swing duration remains largely unchanged [21, 87]. When 5-HT^{VNC} neurons are activated, these relationships are maintained and extended into the slower speed range (Figure 4.3E-I). Similarly, as animals walk more slowly, their preferred gait shifts from the three-legged tripod gait to more stable tetrapod and wave gaits [21, 87]. Upon activation of 5-HT^{VNC} neurons, animals continue the trend to preferentially use these slower walking gaits (Figure 4.3J-L). In some cases, such as step length (Figure 4.3G) and stance duration (Figure 4.3I), the parameter-speed relationship when 5-HT^{VNC} neurons are activated is an extrapolation of the wild-type relationship, while, in other cases, such as the choice of tripod gait (Figure 4.3J), the relationship with speed is altered when these neurons are activated. Most of the other parameters fall in between these two extremes.

4.3.6 5-HT^{VNC} Neuron Inactivation Slows Walking in Multiple Contexts

Results from our behavioral experiments suggest a model whereby the VNC serotonergic system is used to regulate walking speed: when the system is activated, flies walk more slowly and when the system is silenced, flies walk faster. Based on these observations, we next tested whether this system is required for flies to naturally adjust their baseline walking speeds. To test this hypothesis, we silenced 5-HT^{VNC} neurons under conditions when flies normally walk at different speeds, including multiple temperatures, body orientations, nutritional states, and in response to mechanosensory stimulation [172, 212, 218–220]. Counter to our expectation, animals in which 5-HT^{VNC} neurons were silenced are still able to adjust their speed in the same direction as wild-type flies in all of these contexts (Figure 4.4A). For example, compared to 25°, flies walk slower at 18°C and faster at 30°C even when 5-HT^{VNC} neurons are silenced, arguing that this system is not required for flies to modulate their speed in response to this difference. In addition, these data reveal that, for all of the contexts tested here, animals in which 5-HT^{VNC} neurons are silenced walk faster than their matched controls. For example, 5-HT^{VNC}-silenced flies walk faster at 18°C compared to control flies at 18°C. Thus, we further conclude that serotonin release in the VNC slows walking speed across a wide spectrum of environmental

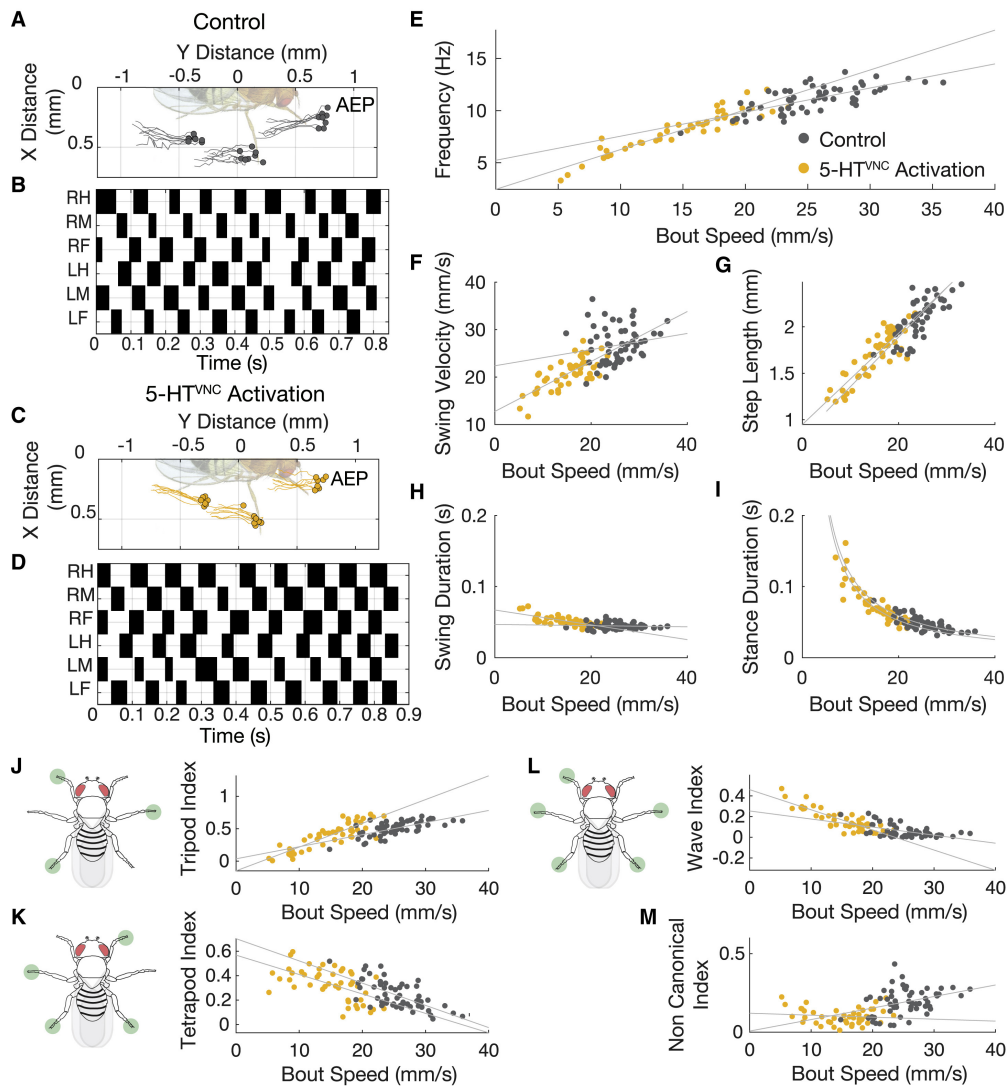


Figure 4.3: **5-HT^{VNC} Neurons Modulate Walking Speed.** (A-D) Representative data from speed-matched slow (19 mm/s) walking bouts show that activation of 5-HT^{VNC} neurons does not disrupt locomotor coordination. Footfalls (filled circles) and stance traces (lines) for all steps taken by the left front, middle, and hind legs show foot touchdown placement is consistent over time and stance traces are relatively straight in both control animals (*Trh* \cap *tsh* > *csChrimson* grown on food lacking ATR) (A) and animals where 5-HT^{VNC} neurons have been activated (*Trh* \cap *tsh* > *csChrimson* fed with ATR) (C). Step trace for each leg during a walking bout for control (B) and experimental (D) animals. Stance phase is indicated in white and swing phase in black. The checkerboard pattern is consistent with a highly coordinated walking gait. (E-I) Quantification of step parameters upon activation of 5-HT^{VNC} neurons. The relationships between speed and frequency (E), swing velocity (F), step length (G), swing duration (H), and stance duration (I) extend the trends observed with control flies. $n = 47$ bouts from $N = 10-23$ animals for *Trh* \cap *tsh* > *csChrimson* ATR⁺ (yellow circles). $n = 56$ bouts from $N = 12-30$ animals for *Trh* \cap *tsh* > *csChrimson* ATR⁻ (gray circles). Speed by ATR interaction effect

in multivariable model: frequency ($p < 0.001$), swing velocity ($p = 0.02$), step length ($p = 0.53$), swing duration ($p < 0.001$), and stance duration ($p = 0.71$). (C) The distribution of velocity shifts caused by activation and inhibition of 5-HT^{VNC} neurons are symmetrical. Differences in population average histograms were calculated between control and experimental genotypes and were fit with 95% confidence intervals via bootstrapping. For activation experiments, behavior of $w^{118} \cap tsh > csChrimson$ flies fed with ATR was compared to that of $Trh \cap tsh > csChrimson$ flies also fed with ATR for the light on period only. (J-M) Quantification of gait selection upon activation of 5-HT^{VNC} neurons. Activation of 5-HT^{VNC} neurons increases wave (L) and tetrapod (K) gait utilization while decreasing time spent using tripod (J) gait. There is a low frequency of non-canonical gait conformations upon activation (M). $n = 47$ bouts from $N = 10-23$ animals for $Trh \cap tsh > csChrimson$ ATR⁺ (yellow circles). $n = 56$ bouts from $N = 12-30$ animals for $Trh \cap tsh > csChrimson$ ATR⁻ (gray circles). Speed by ATR interaction effect in multivariable model: tripod index ($p < 0.001$), tetrapod index ($p = 0.60$), wave index ($p < 0.001$), and non-canonical ($p = 0.006$).

See also [Figure S4.4](#).

contexts. These findings are consistent with a model where the VNC serotonergic system acts as a mild and constitutive break on walking speed, independently of how fast or slow this speed is set by other mechanisms. However, we note that because we are using constitutive inactivation tools, we cannot currently rule out that the observed phenotypes are in part the result of compensation within the network when 5-HT^{VNC} neurons are silenced.

4.3.7 Silencing 5-HT^{VNC} Neurons Alters the Response to Sudden Changes in the Environment

Although the above results suggest the VNC serotonergic system is not needed for flies to adjust their baseline walking speed in many situations, another potentially valuable role for slowing walking speed might be as a response to when animals are startled. In mammals, stereotyped startle behaviors occur in response to a wide variety of sensory stimuli—acoustic, tactile, and vestibular. These responses take place on sub-second timescales, involve simultaneous contraction of muscles throughout the body, and are similar irrespective of the initiating stimulus [221, 222]. Like mammals, *Drosophila* display stereotyped responses to threatening looming stimuli, beginning with an initial freezing period lasting less than a second before escape behaviors are initiated [12, 89, 223]. Because these startle responses are contextually independent and have been shown to be mediated in part by serotonin in mammals [224], we asked whether 5-HT^{VNC} neurons are required for these responses in *Drosophila*.

We tested this idea using two different startle-inducing paradigms: (1) one in which flies abruptly experience total darkness (“blackout paradigm”) and (2) one in which flies suddenly experience strong mechanical stimulation, such as an intense vibration (“earthquake paradigm”) [219]. In both scenarios, control animals on average show a two-tiered response

Chapter 4. Serotonergic Modulation of Walking in *Drosophila*

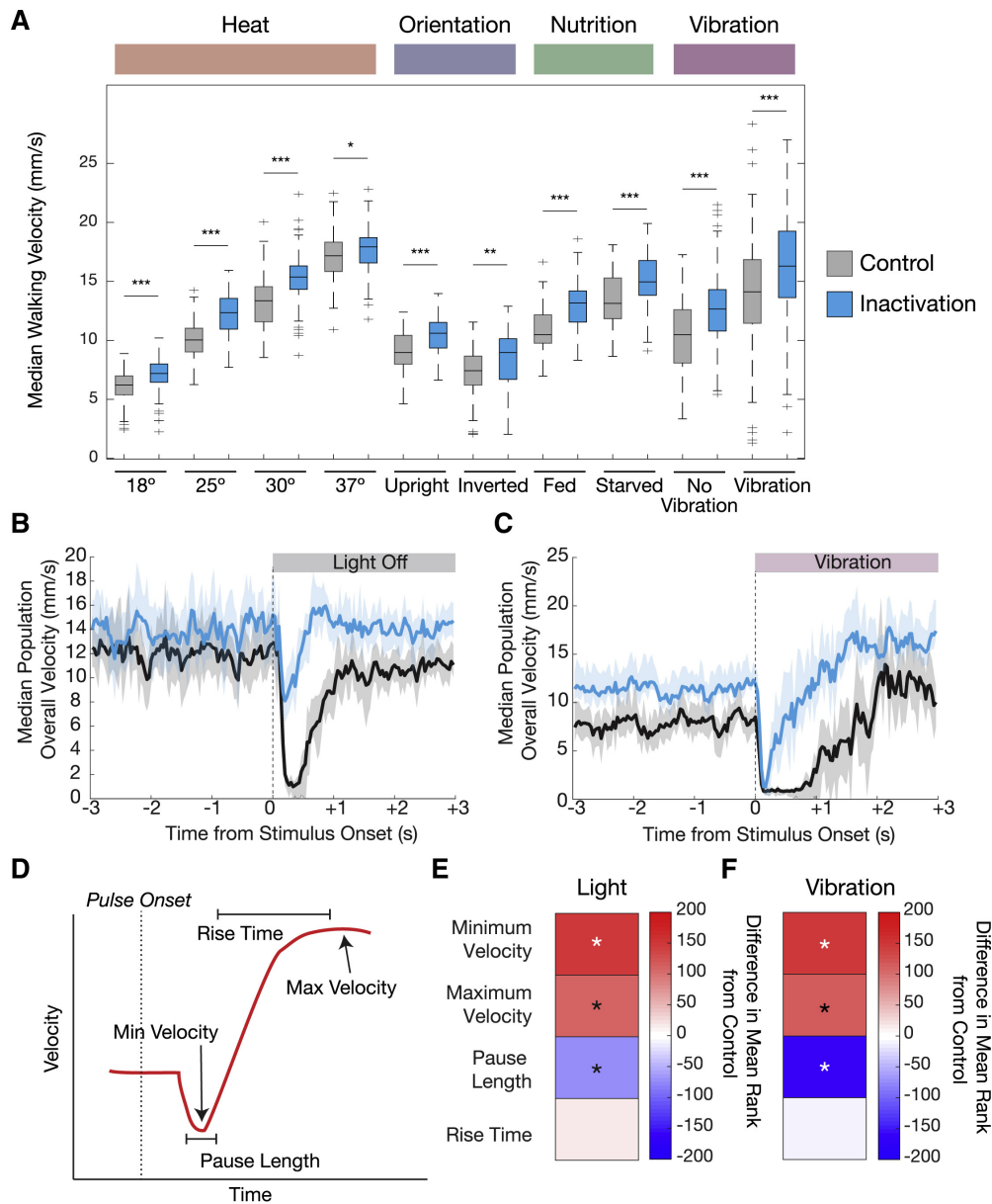


Figure 4.4: Changes in Walking Behavior When 5-HT^{VNC} Neurons Are Silenced. (A) Silencing 5-HT^{VNC} neurons (*Trh* \cap *tsh* > *Kir2.1*) causes an increase in walking speed compared to genetically background-matched non-Gal4 controls (*w¹¹¹⁸* \cap *tsh* > *Kir2.1*) across a diversity of behavioral contexts including different temperatures, orientations, nutritional states, and vibration stimuli. For each condition, genotypes were compared using a Kruskal-Wallis test, *** p < 0.001, ** p < 0.01, * p < 0.05 by Kruskal-Wallis test. For all conditions, p < 0.001 for context effects for both control and experimental genotypes; 18°C, N = 130 per genotype; 25°C, N = 120 per genotype; 30°C, N = 120 per genotype; 37°C, N = *w¹¹¹⁸* (120) *Trh* (119); upright, N = 90 per genotype; inverted *w¹¹¹⁸* (74) *Trh* (70); fed, N = 86 per genotype; starved, N = *w¹¹¹⁸* (86) *Trh* (85); vibration, N = *w¹¹¹⁸* (165) *Trh* (164). (B) and (C) Silencing 5-HT^{VNC} neurons changes

the immediate behavioral responses to sudden contextual changes. When lights switch from on to off (**B**), control animals ($w^{1118} \cap tsh > Kir2.1$, shown in black) show a brief behavioral pause and then resume activity. When 5-HT^{VNC} neurons are silenced ($Trh \cap tsh > Kir2.1$, shown in blue), animals still slow their speed but do not fully pause. In response to the onset of vibration (**C**) control animals stop, pause, and then accelerate speed. When 5-HT^{VNC} neurons are silenced ($Trh \cap tsh > Kir2.1$, shown in blue), animals pause but re-accelerate more quickly than controls. Shaded areas show 95% confidence intervals. For light experiments, N = w^{1118} (150) Trh (140); for vibration experiments N = w^{1118} (167) Trh (166). (**D**) Schematic of behaviors in response to a sudden stimulus. This response is divided into four key parameters that describe different phases of the response, indicated with arrows and bounded lines. (**E** and **I**) Heatmaps quantifying the parameters schematized in (**D**) when 5-HT^{VNC} neurons are inactivated in response to the blackout (**E**) and earthquake (**F**) scenarios. Plotted for every genotype is the difference in mean ranks (Kruskal-Wallis test statistics) for each parameter compared to $w^{1118} \cap tsh > Kir2.1$ control flies. Starred parameters are those where differences between control and experimental animals consistently reached significance ($p < 0.05$; see [Materials and Methods](#)).

See also [Figure S4.5](#).

to these abrupt changes ([Figure 4.4B](#) and [Figure 4.4C](#)): first, many animals rapidly come to a nearly complete stop and then they pause before resuming a behavior that is appropriate for the new context (schematized in [Figure 4.4D](#)). For both the blackout and earthquake paradigms, on average control animals stop within the first 0.25 s, pause for about a second, and then resume walking ([Figure 4.4B](#) and [Figure 4.4C](#)). Animals lacking the ability to release serotonin in the VNC are deficient in these initial responses ([Figure 4.4B](#), [Figure 4.4C](#), [Figure 4.4E](#) and [Figure 4.4F](#)) but still eventually achieve context-appropriate walking speeds ([Figure 4.4A](#)). Moreover, consistent with our earlier analyses, flies with silenced 5-HT^{VNC} neurons walk faster compared to control flies, both before and after the startle-inducing stimulus ([Figure 4.4B](#) and [Figure 4.4C](#)).

Thus, in addition to serving as a constitutive break on locomotor speed, these results suggest that the serotonergic system helps to facilitate an immediate and stimulus-independent pause response when flies are startled.

4.3.8 Different Serotonin Receptor Mutants Alter the Startle Response in Different Ways

All five serotonergic receptors in *Drosophila*—5-HT1A, 5-HT1B, 5-HT2A, 5-HT2B, and 5-HT7—are G-protein-coupled receptors (GPCRs) [225, 226]. Like their mammalian orthologs, members of each serotonin receptor family (1, 2, and 7) have distinct effects upon activation. Receptors in the 1 family, 5-HT1A and 5-HT1B, act through the G_i pathway to inhibit the generation of cAMP, whereas 5-HT7, the only member of the 7 family in *Drosophila*, stimulates the

Chapter 4. Serotonergic Modulation of Walking in *Drosophila*

production of cAMP [227, 228]. Receptors of the 2 family, 5-HT2A and 5-HT2B in *Drosophila*, act through the PLC-IP3 signaling pathway to increase intracellular calcium [226, 229, 230]. Together, this diversity of receptors is thought to allow serotonin to produce complex physiological responses that depend on both synaptic connectivity and receptor expression patterns.

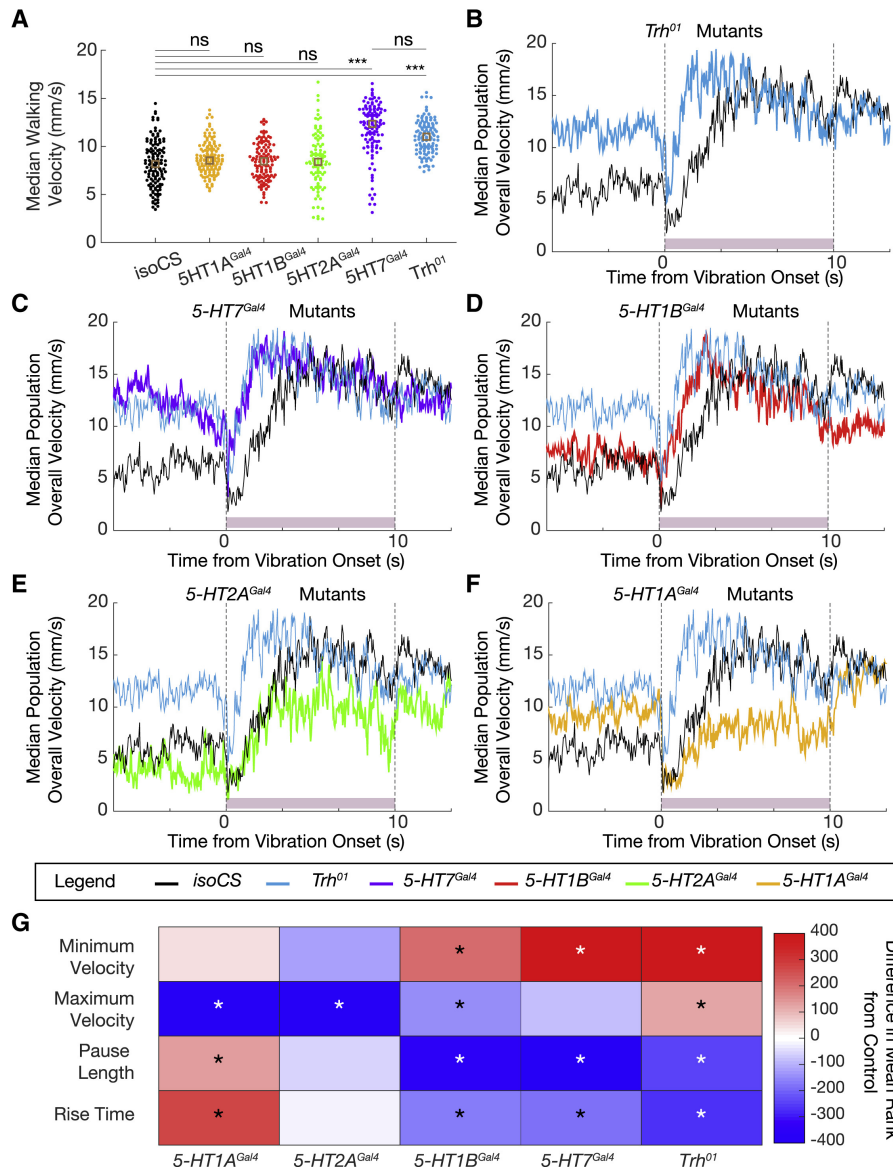


Figure 4.5: Phenotype of the Startle Response of *Trh* and Serotonin Receptor Mutants. (A) Dot plot showing median population walking speed during a 5-min recording session for *Trh*⁰¹ mutants (blue), which walk faster than background-matched isoCS controls (black), consistent with the 5-HT^{VNC} inactivation experiments. 5-HT7^{Gal4} mutants (purple) also walk faster than controls, but the other receptor mutants do not. *** $p < 0.001$, ** $p < 0.01$, * $p < 0.05$ ns $p > 0.05$ by Kruskal-Wallis analysis with Dunn-Sidak correction for multiple comparisons. Brown box indicates median. N = isoCS (130) 5-HT1A^{Gal4} (130) 5-HT1B^{Gal4} (120) 5-HT2A^{Gal4} (100) 5-HT7^{Gal4} (120) *Trh*⁰¹ (120). (B-F) Median population walking speed sampled at 30 Hz

in response to vibration stimulus. Trh^{01} mutants (**B**, blue line) show a blunted and shortened pause in response to the novel stimulus. 5-HT7^{Gal4} mutants (**C**, purple line) and 5-HT1B^{Gal4} mutants (**D**, red line) show a similar phenotype to Trh^{01} mutants. 5-HT2A^{Gal4} mutants (**E**, green line) and 5-HT1A^{Gal4} mutants (**F**, yellow line) have a pause phase comparable to controls, but do not accelerate as much in response to the vibration stimulus. N = isoCS (140) 5-HT1A^{Gal4} (115) 5-HT1B^{Gal4} (124) 5-HT2A^{Gal4} (88) 5-HT7^{Gal4} (120) Trh^{01} (139). (**G**) Heatmap showing how lack of Trh or serotonergic receptors affects the response to vibration stimulus. Plotted for every genotype is the difference in mean ranks (Kruskal-Wallis test with Dunn-Sidak correction for multiple comparisons statistics) for each parameter compared to isoCS control flies. Starred parameters are those where differences between control and experimental consistently reached significance ($p < 0.05$, see STAR Methods (section 4.5)).

See also [Figure S4.5](#).

Before characterizing the phenotypes of these receptor mutants, we analyzed a mutant of the *Trh* gene (Trh^{01}), which is globally unable to produce serotonin [206]. Reassuringly, Trh^{01} animals show a similar phenotype to animals in which 5-HT^{VNC} neurons were silenced: flies walk significantly faster and more frequently than controls and exhibit a similar startle response in the earthquake paradigm ([Figure 4.5A](#), [Figure 4.5B](#), and [Figure 4.5G](#)). In addition, Trh^{01} mutant animals walk closer to the edge of the arena compared to control animals, consistent with previous observations [204] ([Figure S4.5A](#)).

Null receptor mutants 5-HT1A^{Gal4}, 1B^{Gal4}, 2A^{Gal4}, and 7^{Gal4} all increase the percentage of time animals spend walking ([Figure S4.5A](#)) [206]. However, an increase in walking speed is only observed in 5-HT7^{Gal4} mutants ([Figure 4.5A](#)), suggesting that 5-HT7 is the primary receptor responsible for mediating the effects of serotonin on walking speed.

We next tested the receptor mutants in the earthquake paradigm. Interestingly, 5-HT7^{Gal4} and 5-HT1B^{Gal4} mutants closely phenocopy the startle response seen in Trh^{01} mutants and also in the 5-HT^{VNC} inactivation experiments ([Figure 4.5C](#), [Figure 4.5D](#), and [Figure 4.5G](#); [Figure S4.5C-E](#)). By contrast, although 5-HT1A^{Gal4} and 5-HT2A^{Gal4} mutants do not show a dramatic change in pause length, they exhibit a sustained decrease in their final target speed in response to this stimulus ([Figure 4.5E-G](#); [Figure S4.5D](#) and [Figure S4.5G](#)).

These data are consistent with the idea that different receptors influence distinct aspects of the startle response. Notably, mutation of receptors that are predicted to have opposing effects on cAMP production, such as 5-HT1B and 5-HT7, can result in similar phenotypes. Further, some receptor mutants exhibit phenotypes that are not seen in Trh^{01} mutant animals. These complex changes in locomotor behavior might be explained by the differential expression of serotonin receptors in key components of the locomotor circuit.

4.3.9 Serotonin Receptors Are Expressed in Distinct Cell Types

The different effects on walking observed in flies mutant for different serotonin receptors suggest that, in addition to distinct biochemical properties, they may also have different expression patterns within the locomotor circuit. To identify neurons that express these receptors, we used gene and protein trap Gal4 lines from the MiMIC library to drive expression of a GFP reporter in the pattern of each receptor subtype [231] (Figure S4.6G). Each receptor line drives expression in many neurons both within the brain and the VNC (Figure 4.6A-E). Many of these are uncharacterized interneurons that cannot yet be functionally studied. However, each serotonin receptor is also expressed in distinct subsets of leg motor and sensory neurons. In particular, while members of the 5-HT1 family are predominantly expressed in mechanosensory neurons throughout the legs, 5-HT2 and 5-HT7 receptors are expressed in proximal-targeting flexor and extensor motor neurons (Figure S4.6A-F), proprioceptive, and distal sensory neuron populations (Figure 4.6F-K). Thus, serotonin release in the VNC is likely to differentially affect these components of the locomotor circuit, which we hypothesize ultimately contributes to the observed changes in behavior.

4.4 Discussion

Walking is a highly stereotyped behavior, consisting of a small number of well-defined gaits, each with its own set of characteristic kinematic parameters. However, walking must also be flexible, to adapt to a wide variety of environments, complex terrains, and novel situations. How nervous systems manage to orchestrate behaviors that are simultaneously stereotyped and flexible is not well understood. Here, we show in the fly that (1) serotonergic VNC neural activity can modulate walking speed in a wide variety of contexts and (2) these neurons play a role in a fly's response to the sudden onset of a startling stimulus. Below, we discuss these findings and present a preliminary model that summarizes serotonin's role in modulating walking behavior.

4.4.1 A Common Role for Serotonin in Modulating Walking Speed across Species

A central finding of our study is that serotonergic neuron activity in the VNC modulates baseline walking speed in *Drosophila*. This finding parallels previous observations in the motor systems of other organisms. For example, consistent with our calcium imaging experiments, activity of serotonergic neurons in the cat brainstem is correlated with motor behavior and walking speed [232, 233]. Additionally, in vertebrates as diverse as the lamprey and cat, serotonin induces an increase in oscillatory and step-cycle period, respectively, slowing locomotion [199, 200]. One recent study in mice showed that activation of the dorsal raphe nucleus—a key serotonergic brain region—produces rapid suppression of spontaneous locomotion and locomotor speed, while showing minimal effect on kinematic parameters,

such as gait, or on non-locomotor behaviors such as grooming [234]. Although this study focused on a subset of serotonergic neurons targeting the forebrain, the parallels to our results suggest that the modulatory role of the serotonergic system in regulating locomotor speed is remarkably conserved across the animal kingdom.

4.4.2 Serotonergic Modulation of the Startle Response

In our experiments, we observed that the onset of a startling stimulus (be it visual or mechanosensory) induces a brief period of pausing behavior in wild-type flies. We hypothesize that these behavioral pauses are similar to startle responses seen in both mammalian systems and some species of insects, which also have a pause phase before animals embark on an appropriate behavioral action [12, 89, 221, 222, 224, 235, 236]. In *Drosophila* and the locust, these pauses are thought to optimally prepare animals for maximally effective escape behaviors. For example, prior to initiating flight in response to a looming threat, *Drosophila* pause for about 200 ms to execute a series of postural adjustments that help orient the direction of takeoff [89]. It may also be that pauses allow animals to collect additional sensory information before they select an appropriate response to the startling stimulus. Interestingly, however, not all insects appear to exhibit a pause phase; for example, studies of the American cockroach, *Periplaneta americana*, suggest that the escape behavior in response to a predator is immediate [237].

Although our 5HTVNC silencing experiments were done using constitutive inactivation tools, which makes it difficult to rule out a developmental defect, the similar phenotype exhibited by the Trh mutant argues that the inability to release serotonin from these neurons is the cause of the startle response defect. In mammals, the absence of serotonin, due to the lesion of key serotonergic brain regions or pharmacological blockade, is generally associated with an increase in the intensity of startle responses [238, 239]. Although this may seem counter to our results, other studies have shown that serotonin increases startle responses when injected directly into the lumbar spinal cord [240, 241]. Thus, serotonin may play distinct roles in the forebrain and in the spinal cord. Together with our results, we suggest that the role of spinal cord/VNC serotonin release is to extend the duration of and/or amplify the startle response.

4.4.3 A Model for Serotonin-Mediated Modulation of Walking in Flies

Putting the various lines of evidence presented here together, we can formulate a preliminary model for serotonin's role in modulating *Drosophila* walking behavior. First, we suggest that one function of serotonin release in the VNC is to act as a mild constitutive brake. In non-startle contexts, the system would oppose forward acceleration that is driven by other inputs, such as descending commands from the brain [28, 38, 139]. Consistent with this idea, when the brake is removed (5-HT^{VNC} neurons are silenced), flies walk slightly faster, and, when the brake is stronger (5-HT^{VNC} neurons are activated), flies slow down. The calcium imaging

Chapter 4. Serotonergic Modulation of Walking in *Drosophila*

results showing that the activity of a subset of 5-HT^{VNC} neurons increases as flies walk faster suggest that the brake may be stronger at higher speeds. A caveat to this latter idea is that the calcium imaging experiments monitored only a subset of the 5-HT^{VNC} neurons, raising the possibility that the activity of other 5-HT^{VNC} neurons have a different relationship with speed.

When flies are startled, our data are consistent with the idea that serotonin release in the VNC serves to put a strong brake on walking speed, presumably to allow flies to prepare for an appropriate behavioral response. When the 5-HT^{VNC} neurons are silenced, flies are unable to apply this brake and consequently have a compromised response. Notably, however, even when these neurons are silenced flies are still able to respond, albeit more weakly, to being startled, suggesting that part of the response is still intact. One possibility is that, in addition to triggering a serotonin-mediated brake, the response to being startled may also independently dampen the accelerator, reducing walking drive.

The observation that serotonin release in the VNC similarly affects the response to both the earthquake and blackout paradigms, which are perceived by two very different sensory systems, suggests that this neuromodulator is affecting locomotor components that are shared by both systems. Although the expression of 5-HT receptors in sensory and motor neurons is consistent with this notion, we note that this model is likely incomplete as we cannot as of now incorporate the role of local interneurons that also express 5-HT receptors.

Nevertheless, because the primary receptors expressed in motor neurons are 5-HT7 and 5-HT2B, which have been shown to upregulate the production of cAMP and facilitate calcium entry [226], we hypothesize that serotonin amplifies activity in these motor neurons. There is ample evidence in the literature to support this role for serotonin both in rodent models as well as in human studies [242, 243]. Further, the motor neurons expressing these serotonergic receptors target both flexor and extensor muscles in the coxa and femur, two proximal leg segments. These observations suggest that serotonin acting on these motor neurons may facilitate co-contraction, a mechanism that would partially stiffen these leg joints, potentially resulting in slower walking speeds. Consistent with this notion, co-contraction has been shown to enable joint stability in the face of a complex environment and also during the preparatory phase for certain escape behaviors [?, 89, 236, 244, 245]. Co-contraction of tibia flexor and extensor muscles is also part of the initial pause phase of the startle response in the locust, suggesting that this mechanism may be shared [236].

In addition to motor neurons, serotonin receptors are expressed in distinct classes of leg sensory neurons that target the leg neuropils of the VNC. Considering the broad expression of serotonergic receptors in sensory organs, it is interesting that one of the behavioral roles of serotonin we identified is its ability to mediate the response to vibration. Vibration is sensed by the chordotonal organ, and our expression analysis reveals that serotonin receptors are expressed to different extents in chordotonal neurons [138, 185, 246]. Together, these

observations suggest that modulation of sensory information as it is entering the VNC could play a key role in how serotonin modulates the response to a vibration stimulus.

Finally, the observed distribution of serotonergic receptor subtypes in sensory processes may serve to shift the balance of sensory information as a consequence of serotonergic input. Based on the known downstream signaling properties of these receptors, we predict that increased levels of serotonin in the VNC would amplify proprioceptive and distal sensory inputs at the expense of more proximal sensory information. These shifts in sensory processing may also contribute to increased stability and might be useful in other contexts where slow walking is preferred, such as navigating complex terrains where improved sensory information might be beneficial. It may also be that these shifts in sensory input are important during the pause phase of the startle response, as they may allow animals to gather valuable information in order to compute the next phase of escape behaviors.

4.5 Materials and Methods

4.5.1 Key Resources Table

REAGENT OR RESOURCE	SOURCE	IDENTIFIER
Fly lines		
Rabbit anti VGlut; 1:10,000	Aaron DiAntonio [247]	N/A
Rabbit anti 5-HT; 1:1000	Millipore Sigma	RRID:AB_477522
Mouse anti TH; 1:1000	Immunostar	RRID:AB_572268
Mouse anti ChAT4B1; 1:500	Developmental Studies Hybridoma Bank (DSHB)	RRID:AB_528122
Mouse anti nc82 c; 1:20 – 1:100	DSHB	RRID:AB_2314866
Rabbit anti GABA; 1:1000	Millipore Sigma	RRID:AB_477652
Rabbit anti Tdc2; 1:200	Cova Labs	pab0822-P
Rabbit anti dsRed; 1:1000	Takara Bio	RRID:AB_10013483
Experimental Models: Strains of <i>D. melanogaster</i>		
; <i>Trh Gal4</i>	Bloomington <i>Drosophila</i> Stock Center (BDSC) [207]	RRID:BDSC_38389
; <i>TH Gal4</i>	BDSC [214]	RRID:BDSC_8848
; <i>Tdc2 Gal4</i> ;	BDSC [215]	RRID:BDSC_9313
<i>w1118</i> ; <i>Iliso</i> ; <i>Illiso</i>	BDSC [248]	RRID:BDSC_5905
<i>w1118</i> ; <i>Iliso</i> ; <i>Trh-Gal4</i>	This study	N/A
<i>w1118</i> ; <i>Iliso</i> ; <i>TH-Gal4</i>	This study	N/A
<i>w1118</i> ; <i>Tdc2 Gal4</i> ; <i>Illiso</i>	This study	N/A
<i>w1118</i> ; <i>Iliso</i> ; <i>Trh iso Gal4</i> ; outcrossed 10 x to <i>w1118</i> ; <i>Iliso</i> ;	This study	N/A
<i>Illiso</i>		
; <i>UAS-mCD8::GFP</i> ;	[97]	N/A
<i>tub > gal80 ></i> ; <i>tsh-LexA</i> , <i>LexAop-Flp</i> ;; <i>Tsh LexA</i> made by Julie Simpson. Combined tool provided by Wes Grueber	[249]	N/A
; <i>tsh-Gal80</i> ;	Julie Simpson	N/A
; <i>UAS-csChrimson::mVenus</i>	BDSC [250]	RRID:BDSC_55136

Chapter 4. Serotonergic Modulation of Walking in *Drosophila*

REAGENT OR RESOURCE	SOURCE	IDENTIFIER
; UAS-Kir2.1	BDSC [251]	RRID:BDSC_6595
; 20XUAS-hexameric-GFP	BDSC / Steve Stowers [252]	RRID:BDSC_52262
; UAS-OpGCamp6f; UAS-tdTomato	Pavan Ramdya [49]	N/A
IsoCS	Yi Rao [206]	N/A
w+ 5-HT1A ^{Gal4} ;	Yi Rao [206]	N/A
w+ 5-HT1BGal4 ;	Yi Rao [206]	N/A
w+; 5-HT2A ^{Gal4}	Yi Rao [206]	N/A
w+; 5-HT7 ^{Gal4}	Yi Rao [206]	N/A
w+; Trh ⁰¹	Yi Rao [206]	N/A
; 5-HT1A-Gal4 (MI04464);	Herman A. Dierick [231]	N/A
; 5-HT1B-Gal4 (MI05213);	Herman A. Dierick [231]	N/A
; 5-HT2A-Gal4 (MI00459)	Herman A. Dierick [231]	N/A
; 5-HT2A-Gal4 (MI03299)	Herman A. Dierick [231]	N/A
; 5-HT2B-Gal4 (MI05208)	Herman A. Dierick [231]	N/A
; 5-HT2B-Gal4 (MI06500)	Herman A. Dierick [231]	N/A
; 5-HT2B-Gal4 (MI07403)	Herman A. Dierick [231]	N/A
; 5-HT7-Gal4 (MI00215)	Herman A. Dierick [231]	N/A
VGlut ⁺ LexAVP16, LexO-CD8GFP /FM7; VGlut ⁺ LexAVP16, UASFlp, LexO-CD8GFP /CyO; LexO-CD8GFP; LexO-CD8GFP; VGlut ⁺ LexAVP16 /TM2	Myungin Baek	N/A
; Mhc-RFP ;	BDSC	RRID:BDSC_38464
Software and Algorithms		
Fiji	[108]	https://fiji.sc
Caltech FlyTracker	[217]	http://www.vision.caltech.edu/Tools/FlyTracker/index.html
Flywalker	[21]	N/A
Flycapture		https://www.flir.com/products/flycapture-sdk
Fview2	Andrew Straw, modified from [253]	N/A
MATLAB 2018a	Mathworks	https://www.mathworks.com/products/matlab.html
R Studio 3.3.2		https://www.rstudio.com
Python 2.7 Anaconda		https://www.anaconda.com/distribution/
NIS Elements AR	Nikon	https://www.microscope.healthcare.nikon.com/products/software/nis-elements
PuTTY		https://www.chiark.greenend.org.uk/sgtatham/putty/
Arduino IDE 1.8.5	Arduino	https://www.arduino.cc/en/Main/Software
Deposited Data and Code		
Code_data.zip	Zenodo	https://doi.org/10.5281/zenodo.3497587

4.5.2 Fly Husbandry

Experimental model for this study was the vinegar fly *Drosophila melanogaster*. A full list of strains used in the paper is included in the Key Resource Table. Unless otherwise described, flies were maintained at 25°C on dextrose cornmeal food using standard laboratory techniques.

4.5.3 Animal Rearing for Behavioral Experiments

For Flywalker experiments, flies were maintained on dextrose cornmeal food at 25°C. For arena experiments, flies were maintained on Nutrifly German Sick food (Genessee Scientific 66-115) in an incubator humidified at 60% with a 12h:12h light:dark cycle. Crosses used for behavioral experiments were flipped every 2-3 days to prevent overcrowding. As animals eclosed, females of the appropriate genotype were collected under CO₂ anesthesia every 2-3 days. Females were used for all experiments due to their larger size which facilitated accurate tracking. For non-optogenetic experiments, flies were collected onto Nutrifly Food without any additive. For optogenetic experiments, flies were collected onto Nutrifly food supplemented with 0.4 mM ATR dissolved in EtOH or an equal concentration of solvent alone (for arena experiments), or corn food supplemented with 0.4mM ATR dissolved in DMSO or an equal concentration of solvent alone for Flywalker experiments. Animals were aged in the dark (for optogenetic experiments) or on the same light:dark cycle for 2-3 more days at 25°C before being assayed. Gal4 driver lines used for arena experiments had been outcrossed ten times to an isogenized w¹¹¹⁸ control population. Gal4 driver lines used for Flywalker experiments had been isogenized on two chromosomes, but not on the chromosome containing the Gal4 transgene. For a complete list of lines used in this paper please refer to the Key Resources Table.

4.5.4 Immunostaining Brain and VNC

Brains and VNCs were dissected in phosphate buffered saline with 0.3% Triton (PBST) and fixed in 4% Paraformaldehyde (PFA) for 20 minutes. Samples were washed five times for 20 minutes in PBST with 0.1% Bovine serum albumin (BSA), and then blocked in PBST-BSA for one hour at room temperature, or overnight at 4°C. Samples were incubated with primary antibody diluted in PBST-BSA overnight at 4°C, and washed five times 20 minutes with PBST-BSA the next day. Primary antibodies used were: anti-VGlut (gift from Aaron DiAntonio, described in [247]); anti-5HT (1:1000 Sigma); anti-TH (1:1000 Immunostar); anti-ChAT (1:500 DSHB); anti-Brp (1:50-1:100 DSHB); anti-GABA (1:1000 Sigma); anti-Tdc2 (1:200 Cova Labs). Samples were then incubated in secondary antibody diluted in PBST-BSA overnight at 4°C. Secondary antibodies used Goat Anti-Rabbit Alexa 555 (1:500 Invitrogen); Donkey Anti-Mouse 647 (1:500 Jackson Immunolabs); Goat Anti-Mouse 555 (1:500 Life Technologies). The next day, samples were washed five times for 20 minutes in PBST, and then the liquid was replaced with Vectashield and samples were incubated overnight prior to mounting. Brains and VNCs from the same animals were mounted together, with the ventral surface of the VNC and the anterior surface of the brain facing up.

Validation of expression patterns during two photon experiments were performed as described in [49]. Briefly, brains and VNCs were dissected out of the animal, and fixed in 4% PFA for 20 min at room temperature. Samples were washed 2-3 × 10-15 min in 1% PBST and blocked for

Chapter 4. Serotonergic Modulation of Walking in *Drosophila*

one hour at room temperature in 1% PBST with 5% NGS. Samples were stained overnight at room temperature with primary antibody diluted in blocking solution. Primary antibodies used included anti-Brp (1:20 DSHB anti-dsRed (1:1000 Takara Bio). The next day, samples were washed 2-3 × 10-15 min in 1% PBST. Samples were incubated with secondary antibody overnight at room temperature in the dark. Secondaries included Goat Anti-Rabbit Cy3 (1:400 Jackson); Goat Anti-Mouse 633 (ThermoFisher). The next day, samples were washed 2-3 × 10-15 min 1% PBST and mounted dorsal side up in Slow Fade Gold mounting medium (ThermoFisher).

4.5.5 Immunostaining Brain and VNC

Mounted brains and VNCs were imaged on a Leica TCS SP5 confocal at 20X magnification with a resolution of 1024 × 512 pixels, and at a scanning rate of 200 Hz and 3x averaging. Sections were taken at 1 μm increments. Laser power and detector gain were maintained constant for the brain and VNC of the same animals, but were adjusted for optimal signal between animals.

Imaging of fixed samples following two photon live imaging experiments was performed as described in [49] on a Zeiss LSM 700 Laser Scanning Confocal Microscope at 20X magnification and 2X averaging, with a 0.52 X 0.52 μm pixel size. Z sections were taken at 1 μm intervals.

4.5.6 Cell Counting and Quantification

Images were analyzed in Fiji [101]. For quantification of the number of cells driven by *Tth*-Gal4 in the brain and VNC, mVenus or GFP positive and 5-HT positive cell bodies were counted from five or more individual animals.

4.5.7 Leg Dissection, Imaging, and Image Processing

To prepare legs for imaging, fly heads and abdomens were removed, and thoraces with legs attached were fixed overnight in 4% PFA at 4°C. Carcasses were washed 5x with 0.03% PBST, and then placed in Vectashield overnight before legs were mounted. Imaging was performed on a Leica SP5 confocal at 20X magnification and 1024 × 1024 pixel resolution with 3x averaging, and Z sections were taken at 1 μm. Two PMT detectors were set to capture green fluorescent signal and the green autofluorescence of the cuticle. Laser power was adjusted independently for each line to achieve optimal visualization of structures. Images were processed in Fiji [108]. Autofluorescence was subtracted from the green channel to allow for clearer visualization of leg structures.

4.5.8 Arena Experiments

Hardware

The skeleton of the system was built of 80-20 bars and acrylic plates and the arena itself was machined out of polycarbonate to the specifications published in [?]. The polycarbonate plastic arena was embedded in an aluminum plate to maintain a level surface. During experiments, the arena was covered with an acrylic disc with a small hole for mouth pipetting in flies. The inside of the lid was coated in a thin layer of Fluon (Amazon, B00UJLH12A) to prevent flies from walking on the ceiling.

A Point Grey Blackfly Mono USB3 camera fitted with a Tamron 1/2" F/1.2 IR C-mount lens (B&H photo) was mounted above the arena and connected by USB 3 cable to a System 76 Leopard WS computer running Ubuntu 14.04 LTS. A Kodax 3x3" 89B Opaque IR filter (B&H photo) was placed in front of the camera detector to allow for detection of IR but not visible light.

Backlighting and optogenetic stimulation was provided by a plate of LEDs sitting under the arena. An acrylic diffuser was placed between the lighting plate and the arena. Each plate was designed with two sets of LEDs – one for IR backlighting (ledlightsworld.com SMD3528-300) and one for optogenetic or white light stimulation (superbrightLEDS.com NFLS-x-LC2 in Red or Natural White). These plates were swapped out when experiments required different color LEDs. To allow for detection of the on state of non-IR lights, an additional IR light was wired in series with each visible light array, and placed within the field of view of the camera.

Each set of lights was powered separately by an Arduino Uno driver, allowing for modulation of light intensity via Pulse Width Modulation (PWM). Commands to set LED brightness and start and end experiments were sent to this driver using a PuTTY terminal and USB serial interface. For all the experiments described here, both IR and visible spectrum LEDs were set at 100% brightness. At the center of the arena this corresponded roughly to intensities of:

Light ON	Percent	Intensity	Wavelength Measured
		.13 mW	1050 nm
Infrared	100	.08 mW	635 nm
		.08mW	535 nm
Infrared +Red	100	.6 mW	635 nm
Infrared White	100	.62 mW	635 nm
		.68 mW	535 nm

Data Acquisition

All behavioral recordings were done during the three-hour morning activity peak. Prior to the experiment, the arena was leveled, the lid cleaned, and a new layer of Fluon applied. For each

Chapter 4. Serotonergic Modulation of Walking in *Drosophila*

experiment, videos were recorded of cohorts of 10 flies. For each recording session, flies were mouthpipetted into the arena through a small hole and then the arena lid was slid to move the hole out of the field of view. A blackout curtain cover (Thor Labs, BK5) was used to surround the arena, protecting it from any contaminating light.

Experimental protocols were programmed into the Arduino through serial communication via a PuTTY terminal. Videos were recorded at a rate of 30 frames per second and stored in a compressed “fly movie format” using custom software written by Andrew Straw at the University of Freiberg based on work previously described [253].

Orientation

For inverted experiments, animals were introduced into the arena set-up when it was upright, and the lid of the arena was taped in place. The entire arena was manually inverted and propped up on two overturned ice buckets. Flies were either recorded upright and then inverted, for five minutes each, or in the opposite order.

Orientation

For inverted experiments, animals were introduced into the arena set-up when it was upright, and the lid of the arena was taped in place. The entire arena was manually inverted and propped up on two overturned ice buckets. Flies were either recorded upright and then inverted, for five minutes each, or in the opposite order.

Starvation

24 hours prior to behavioral assay, half of the flies were transferred to an empty tube with a wet Kim Wipe. Behavioral recordings were collected as described above and lasted for five minutes.

Heat

Heated experiments were carried out inside a walk-in temperature-controlled incubator, which was set at either 18, 25, 30, or 37°C and 40% humidity. Flies were introduced to the arena immediately after entering the temperature-controlled room, recording began immediately thereafter and lasted for five minutes.

Light

For experiments examining responses to light stimuli, flies were first exposed to five minutes of white light, and then a one minute period of darkness.

Vibration

To provide a vibration stimulus, four 3V haptic motors (1670-1023-ND, Digikey) were attached to the aluminum plate in which the arena sat using 3D printed holders. The motors were wired in series and driven by the same Arduino system driving the arena's LED lighting array. For all experiments described, vibration was set at 10% power. The protocol for vibration experiments consisted of a brief habituation period (five minutes for inactivation experiments, 30 s for mutant experiments) followed by a 10 s vibration pulse and a 110 s recovery period.

4.5.9 Flywalker Experiments

Hardware

The Flywalker was constructed as described in [21] with modifications. The rig consisted of a frame of 80/20 supporting a sheet of 6 mm Borofloat optical glass with polished edges placed over an Andor Zyla 4.2 Magapixel sCMOS camera with an AF Nikkor 24-85mm 1:2.8-4 D lens (Nikon). On each edge of the glass were placed four Luxeon Neutral White (4100K) Rebel LED on a SinkPAD-II 10mm Square Base (230 lm @ 700mA) wired in series. Each set of lights was driven by a dedicated 700mA, Externally Dimmable, BuckPuck DC Driver (Luxeon), and all four of these drivers were connected to a single power supply. Each driver was independently adjustable.

Chambers were 3D printed by Protolabs (schematics available upon request). The ceiling and walls of the chamber were painted with Fluon mixed with india ink, to prevent flies from walking on the ceiling while maintaining an effective dark background. Small far-red LEDs were embedded in the walls of the chamber for Chrimson optogenetic experiments (LXM3-PD01 LUXEON). These lights were controlled by an Arduino driver that used pulsewidth modulation to adjust light brightness. Commands were sent to this driver using a PuTTY terminal and USB serial interface. For all the experiments described here, LEDs were set at 20% brightness.

Data Acquisition

The Flywalker was calibrated using a calibration reticle prior to use on each day. On the day of the experiment, animals were mouthpipetted into a clean glass tube and allowed to equilibrate

for five minutes to get rid of as much dirt and food as possible, to prevent contamination of the glass surface. 2-3 flies were added to the chamber by mouth pipette.

Videos were recorded using the NIS Elements AR software. A constant region of interest was defined such that the rate of recording was 226 fps. Each group of animals was recorded for one minute. Videos were cut to select traces where flies walked straight without touching the wall for > 6 steps without other flies in the frame.

4.5.10 Functional Imaging Experiments

Functional imaging experiments on *Trh* \cap *tsh* > *OpGCaMP6f*, *tdTomato* animals were performed as described in [49].

4.5.11 Quantification and Statistical Analysis

4.5.12 Arena Experiments

Tracking

Videos were tracked using the FlyTracker software from the Caltech vision lab [58]. Prior to tracking, pixel to mm conversion was calibrated using an inbuilt GUI. One calibration file was generated for all videos taken on the same day. Background model and thresholds were adjusted to provide optimal recognition of animals and were not standardized between recording sessions. If present, the state of an indicator light was annotated by custom-written MATLAB software.

Behavioral classifiers

Each frame of an individual's walking bout was assigned a behavioral classifier based on the definitions below:

- *Jump*: Jumps were classified as frames where the velocity of the animal exceeded 50 mm/s.
- *Walk*: Walking frames were defined using a dual threshold Schmitt trigger filter. Speed thresholds were set at 1 and 2.5 mm/s, and time thresholds were 0.1 s. Walking frames were also specified to be those in which the fly was not already engaged in a jump.
- *Stop*: Stop frames were classified as any frames where animals were not performing walking or jumping behaviors.

Parameters

Baseline walking parameters:

- *Walk Frequency*: the percent of frames classified as walking during the recording period.
- *Overall Velocity*: the median of all velocities over the recording period.
- *Walking Velocity*: the median of velocities during all frames when the animal is classified as walking.
- *Maximum Walking Velocity*: the maximum velocity an animal reaches during walking.
- *Angular velocity*: the median value of angular velocity. This parameter takes into account directionality of turning.
- *Absolute Angular Velocity*: the median of the absolute value of angular velocities. This parameter does not take into account directionality of turning.
- *Distance from Wall*: the median distance from the closest point on the arena wall during the recording period.
- *Walking bout number*: bouts were defined as contiguous frames of walking (longer than 0.1 s as specified in the walking classifier). The number of bouts was calculated for the entire recording period.
- *Walking bout duration*: the length of each bout was calculated, and the median of all bout lengths was taken for each animal.
- *Stop bout number and duration*: calculated as for walking bouts.
- *Jump Frequency*: the percent of time that an animal spends in the jump state as defined above.

Startle parameters:

- Startle responses were highly variable between individuals. To generate smoother average traces and model fitting, the data was serially resampled, with the median velocity of 20 animals selected for each frame, generating an average trace of random animals each run. The number of resampling runs for each genotype matched the actual number of animals studied.

Parameters calculated for each averaged trace included:

Chapter 4. Serotonergic Modulation of Walking in *Drosophila*

- *Minimum Velocity*: defined as the minimum velocity reached within the first three seconds of the walking bout. This time threshold was selected based on aggregate traces that show the initial pause phase is well below this threshold.
- *Maximum Velocity*: defined as the maximum velocity reached during the vibration stimulus period.
- *Pause Length*: a Schmitt trigger classifier was used to define pause bouts. For inactivation light data and mutant vibration data, speed thresholds were defined as 2 mm/s faster than the minimum speed, and 5 mm/s faster than the minimum speed. For inactivation vibration data thresholds were 2 mm/s faster than the minimum speed and 3 mm/s faster than the minimum speed. Time thresholds were defined as 0.17 s for the “not paused” classification. No constraints were set on the length of the pause phase. The length of the first pause bout after the onset of the stimulus was recorded as “pause length.” The thresholds of the classifier were tested with ten average traces per genotype and classifier fit was validated by eye.
- *Rise Time*: defined as the time from the end of the pause phase to the maximum speed during the vibration pulse.

Statistics

For optogenetic arena experiments, behavior parameters described above were calculated for the five-minute light on period and compared to the same metric calculated during the light off period for each individual. For each activation experiment, we recorded behavior from both experimental ($Trh \cap tsh > csChrimson$) and control ($w^{1118} \cap tsh > csChrimson$) flies. For each genotype, we analyzed data from flies that had been fed with ATR, the required co-factor for optogenetic activation, and flies from the same cross that had been fed on food depleted of ATR. Figures show comparisons between ATR+ control and experimental animal behavior, as we found these populations had the most similar light off behavior pattern. However, significant differences in parameters are consistent even when all controls are included in the analysis.

For constitutive inhibition arena experiments, behavior during the five-minute light off period was analyzed for experimental ($Trh \cap tsh > Kir2.1$) and control ($w^{1118} \cap tsh > Kir2.1$) flies fed on the same ATR negative food we used for optogenetic experiments.

All analysis on data from arena experiments was performed in MATLAB using custom-written scripts. For each individual and parameter, a Z score was calculated comparing that individual's behavior to the mean and standard deviation of the control group. Z scores of different genotypes were compared using Kruskal-wallis analysis with Dunn-sidak multiple correction testing when multiple groups were being compared. To compare changes in velocity distribu-

tion, bootstrapping (1000 replicates) was used to estimate the median difference between two genotypes and fit a 95% confidence interval around this difference.

For experiments under different conditions (heat, orientation, starvation, vibration), median walking speed was compared between control and experimental animals under each condition using Kruskal-wallis analysis. For all conditions except vibration, animals who spent less than 30 s of the five minute recording period walking were excluded from the analysis. The response of each genotype to contextual shifts was independently assessed by Kruskal-wallis analysis with Dunn-sidak correction for multiple comparisons.

As described above, for vibration and light experiments, parameters were defined for each average trace, with the number of traces per genotype corresponding to the actual number of animals in the experimental group. For a particular parameter, genotypes were compared using Kruskal Wallis test with subsequent Dunn-sidak correction for multiple comparisons. The model and statistical analysis was run ten times for each dataset to identify parameters that consistently were found to be significant.

The statistical tests performed for specific experiments are described in the figure legend for each experiment.

4.5.13 Flywalker Experiments

Tracking Flywalker videos were automatically tracked using custom software written by Imre Bartos as described in [21]. Tracking was then validated by eye and incorrect footprint calls were corrected. Summary plots were then screened by eye for gross errors and for linear traces. If traces were short (< 3 traces per foot) or excessively turning, they were excluded.

Parameters

Behavioral parameters were calculated as described in [21]. Gait parameters were defined as follows. Leg order in combination: LF RF LM RM LH RH. 1 indicates the leg is in stance phase, 0 indicates the leg is in swing phase.

Tripod	Tetrapod	Wave	Non-Canonical
100110	011011	011111	All Other
011001	011110	101111	
	100111	110111	
	110110	111011	
	101101	111101	
	111001	111110	

Statistics

For Flywalker experiments, behavior was recorded for a one minute walking bout with red light illumination. Light off conditions were not possible as the white light LEDs required to generate fTIR signal contained the red wavelength used to activate our optogenetic tool. For each activation experiment, we recorded behavior from both experimental (*Trh* – or other neuromodulatory *Gal4 driver* – \cap *tsh* > *csChrimson*) and control (*w¹¹¹⁸* \cap *tsh* > *csChrimson*) flies. For each genotype, we analyzed data from flies that had been fed with ATR, the required co-factor for optogenetic activation, and flies from the same cross that had been fed on food depleted of ATR. Figures show comparisons between ATR+ and ATR- controls, as these populations provide the best genetic control and had the most similar behavioral pattern. However, significant differences in parameters are consistent even when all controls are included in our multivariate model (described below).

Statistical analysis of Flywalker data was performed using custom scripts written in MATLAB and R. For each walking bout, an average was calculated for every parameter across three to five footprints per leg. For parameters that exponentially related to speed, the natural logarithm was taken of both the bout speed and parameter values. A multivariable regression model was then run on the data for every kinematic parameter. The formula for this model was as follows:

$$y \sim speed * ATR$$

This model was designed to analyze the effects of activation while controlling for speed, which is the largest contributor to behavioral shifts.

We also ran a version of this model that contained all control data, to validate our results:

$$y \sim speed * Genotype * ATR$$

To prevent model overfitting, we selected our model based on Akaike information criterion using the R `step()` package.

4.5.14 Functional Imaging Experiments

Analysis

- *Initial image Processing:* TIFF videos from two-photon microscopy were processed in Fiji to merge green (opGCaMP6f) and red (tdTomato) channels [108]. No brightness or contrast adjustments were performed, in order to standardize region-of-interest (ROI) selection.

- *ROI Selection:* The tdTomato channel was used to select ROIs containing neuronal processes, using custom Python software relying on OpenCV and Numpy libraries. Images were converted into 8-bits, color ranges were extended, and contrast was augmented to better detect ROIs. Baseline signals were subtracted and then brightness was scaled to a maximum value of 255. A blur filter was applied to the image (blur value = 10), and then an Otsu Threshold was applied to binarize the grayscale image. After the image was thus thresholded, an erosion function (kernel size 5) was used to avoid the detection of overly large or small ROIs. The contours of all ROIs were detected on the eroded image and a copy of the contrast-augmented image was returned with ROI contours drawn super-imposed. A minimum threshold of 150 pixels was set on the ROI size to avoid overly small detections.
- *Fluorescence extraction:* Mean fluorescence values for the tdTomato, or opGCaMP6f channels were calculated over all ROIs combined. Baseline signals for $\Delta F/F$ calculations were defined as mean raw fluorescence binned over 2.5 s.
- *Synchronization:* Fluorescence measurements, behavior videography, and optic flow of spherical treadmill rotations were all recorded at different frame rates. Thus, we used interpolation to upsample fluorescence signals and behavioral videography acquisition rates to that of optic flow. Optic flow and fluorescence data were then smoothed (window size 200 ms). Optic flow data was then translated into mm/s in the anterior-posterior and medial-lateral directions and into degrees/s for yaw.
- *Automatic Walking Classifier:* An automatic walking classifier was used to define walking bouts. A velocity of 0.31 mm/s was empirically determined as a threshold for distinguishing between walking and standing. The minimum threshold for bout length was empirically set to 2 s.
- *Manual behavioral annotation:* Videos showing a side view of the fly on the spherical treadmill were manually annotated to capture four behaviors: (1) walk, (2) stop, (3) proboscis extension reflex, and (4) groom. All frames that could not neatly be classified as one of these four behaviors were defined as (5) other.

Statistics

- *Manually Annotated Behaviors:* For each animal, the average $\Delta F/F$ for frames labeled a particular behavior classification was calculated. Comparisons between behaviors were made using Kruskal-Wallis testing with Dunn's correction for multiple comparisons.
- *Time Courses:* For each behavioral classification, an average time course was determined for each animal by averaging $\Delta F/F$ for all behavioral bouts (between 80 and 130 bouts per animal), centering them on bout onset. Averages across all animals were then calculated, and 95% confidence intervals fit by bootstrapping.

- *Correlation Analysis*: A Pearson R correlation coefficient was calculated between walking velocity and $\Delta F/F$.

4.6 Data and Code Availability

Tracking of flies in Flywalker and arena experiments was done using published tracking code [21, 217]. Analysis performed on Flywalker data was completed in R. Analysis performed on arena datasets was completed in MATLAB. Analysis of functional imaging data was completed in Python. Custom scripts written for these analyses and associated data are available for download at [Zenodo.org](https://zenodo.org/https://doi.org/10.5281/zenodo.3497586): <https://doi.org/10.5281/zenodo.3497586>.

4.7 Acknowledgments

We thank Cesar Mendes for helping to optimize the Flywalker system; Imre Bartos for help in updating the Flywalker analysis code; Andrew Straw for editing software; Meredith Peterson, Floris van Bruegel, Irene Kim, and Michael Dickinson for assistance with hardware and data analysis; Randy Bruno for assistance with analysis; and Laura Hermans for assistance with data analysis. We thank Daniel Wolpert and the anonymous referees for helpful comments on the manuscript. This work was supported by NIH grants to R.S.M. (1U01NS090514 and 1U19NS104655), the Columbia MD/PhD Training program (GM007367), and the Columbia Neuroscience Program (5T32NS064928). P.R. acknowledges support from the Swiss National Science Foundation (31003A_175667).

4.8 Author contributions

C.E.H. and R.S.M. conceived of the project and designed the experiments; T.T. and R.H. designed and built the behavior rigs; C.E.H. conducted all of the experiments and performed all data analysis, with the exception of calcium imaging experiments, which were carried out by C.-L.C. and analyzed by C.E.H., C.-L.C., and P.R.; C.E.H. and R.S.M. wrote the paper, and P.R. edited it.

4.9 Declaration of Interests

The authors declare no competing interests.

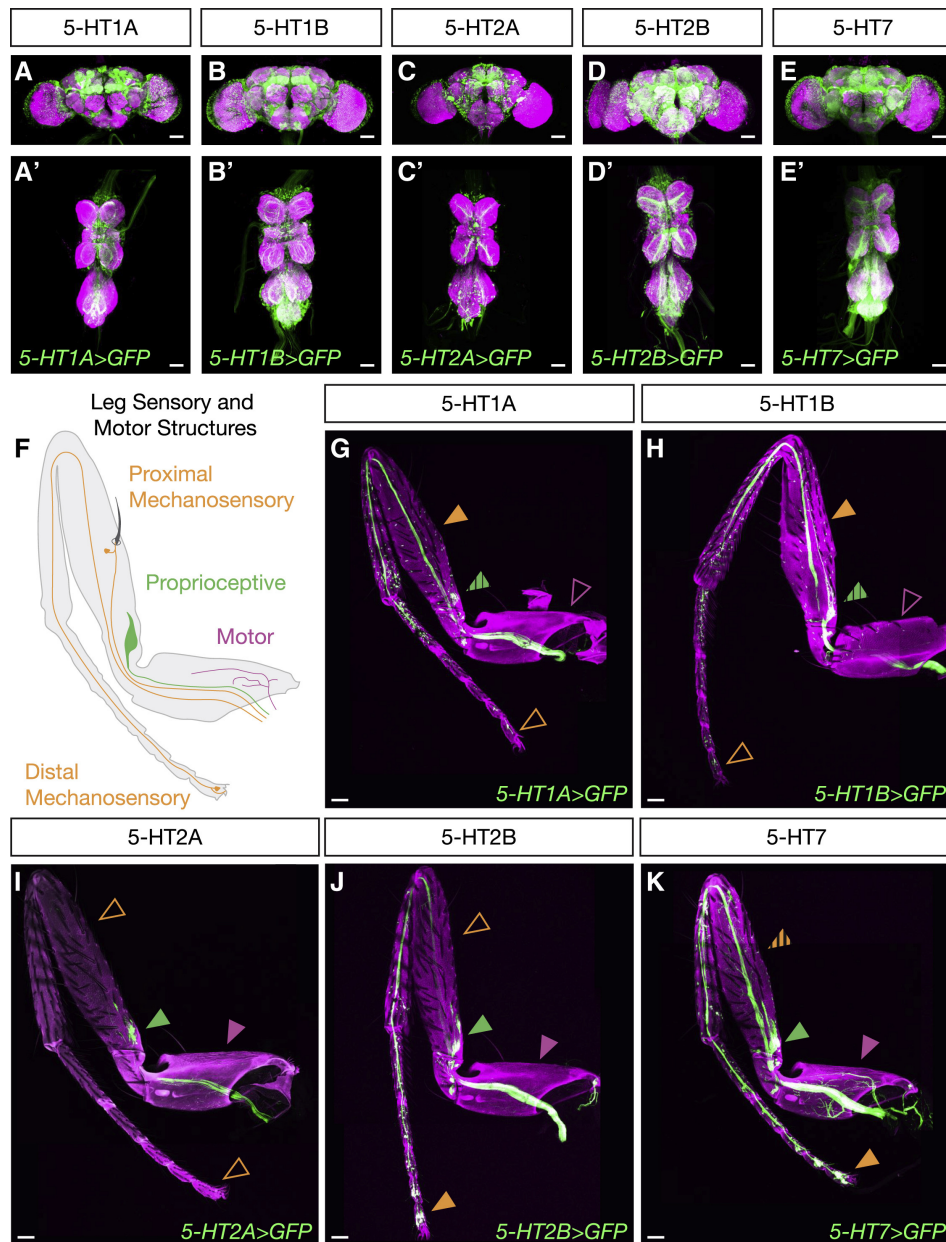


Figure 4.6: **Differential Expression of Serotonin Receptors in Locomotor Circuit Components.** (A) Maximum intensity projections show Gal4-driven expression of serotonin receptors in both the brain (A–E) and VNC (A'–E'). All scale bars are 50 μm. (F) Schematic of sensory and motor neuron populations in an adult leg. (G–K) Maximum intensity projections show Gal4-driven expression of serotonin receptors in neuronal processes in the adult leg. Each receptor is expressed in a distinct pattern in sensory-motor components. While some are expressed in motor neurons (purple arrows, hatched arrows indicate limited or weak expression) and proprioceptive neurons (green arrows), others are not. All receptors are expressed in a subset of mechanosensory neurons (orange arrows), but some are preferentially expressed in proximal or distal leg segments. All scale bars are 50 μm. See also [Figure S4.6](#)

4.10 Supplementary Information

4.10.1 Supplementary Figures

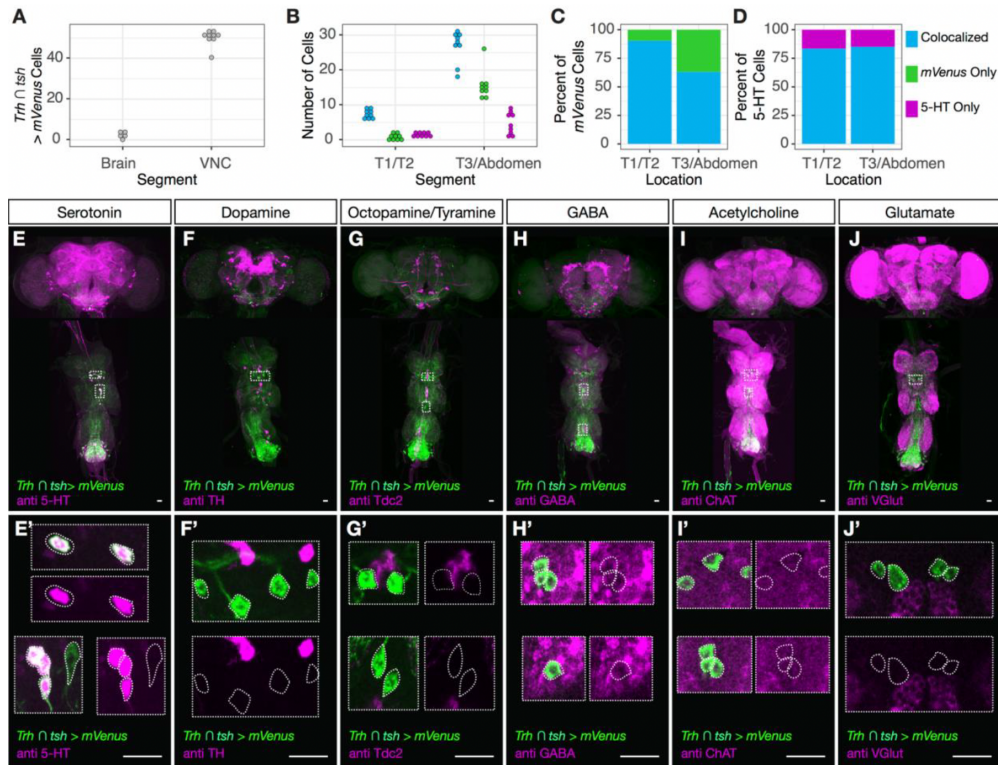


Figure S4.1: *Trh*-Gal4 accurately drives expression in serotonergic VNC neurons. Related to **Figure 4.1**. **(A)** Intersection with *tsh* reliably limits *Trh*-Gal4 expression to the VNC. The number of *Trh* ∩ *tsh* positive cells was quantified in the brain and the VNC (N>5). The reporter was mVenus fused to csChrimson (*UAS-csChrimson::mVenus*). **(B)** Quantification of the overlap between *Trh* ∩ *tsh* > *csChrimson::mVenus* and anti-serotonin (5-HT) immunostain. The number of co-localized, mVenus only, and 5-HT only cells was quantified separately for T1/T2 and T3/Abdomen (N=9). **(C-D)** *Trh* ∩ *tsh* has limited ectopic expression and effectively labels the majority of serotonergic neurons in the VNC. The average percent of *Trh* ∩ *tsh* > *csChrimson::mVenus* cells that colocalize with 5-HT **(C)**, and 5-HT positive cells that also express mVenus **(D)** is shown for the T1/T2 and T3/Abdominal regions (N=9). **(E-J)** Thoracic neurons labeled by *Trh* ∩ *tsh* > *csChrimson::mVenus* do not co-express other neurotransmitters. Maximum intensity projections of brain and VNCs of animals where the expression of *Trh*-Gal4 was restricted to the VNC and co-stained for 5-HT **(E)**, tyrosine hydroxylase **(F, TH)**, Tyrosine decarboxylase 2 **(G, Tdc2)**, GABA textbfH), Cholineacetyl transferase **(I, ChAT)**, and the vesicular glutamate transporter **(J, VGlut)**. White dotted boxes indicate regions that are shown in E'-J'. E'-J') Examples of *Trh* ∩ *tsh* > *csChrimson::mVenus* labeled thoracic neurons and neurotransmitter immunostains. Projections of 10-20 image sections show *Trh* ∩ *tsh* labeled neurons – dotted white outline – do express 5-HT **(E')**, but do not express TH **(F')**, Tdc2 **(G')**, GABA **(H')**, ChAT **(I')**, and VGlut **(J')**. All scale bars are 20 μm.

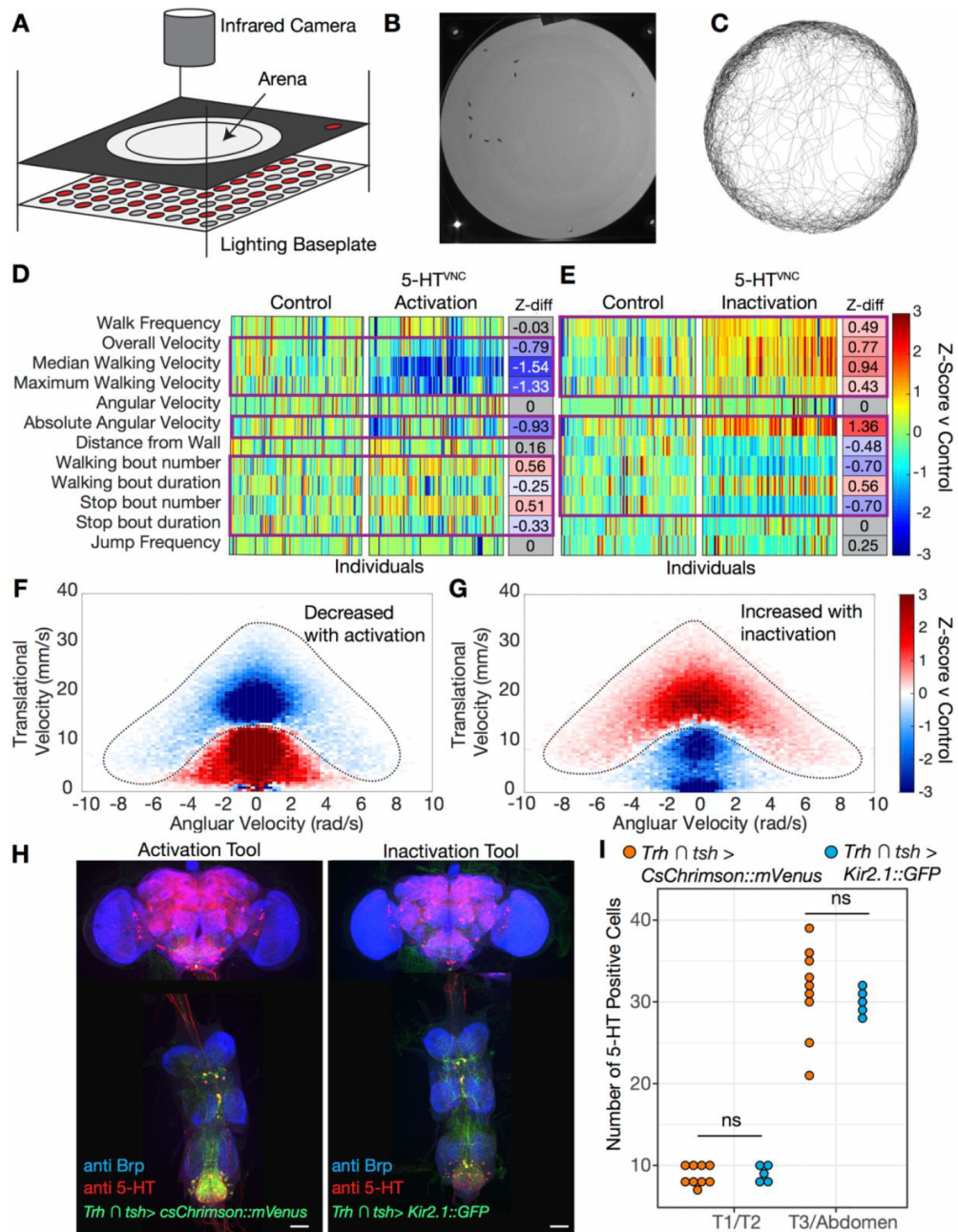


Figure S4.2: Activation and inactivation of 5-HT^{VNC} neurons shifts locomotor behavior. Related to **Figure 4.2**. (A) Schematic of the arena system used to record fly walking behavior. The system consisted of an overhead IR camera, an arena set in an aluminum plate, and a baseplate with IR backlighting and either red (for optogenetic experiments) or white LEDs. (B) Image of flies in the arena during a behavioral experiment. (C) Traces of ten animals from one five-minute recording period. (D-E) Heatmaps of behavioral changes induced by 5-HT^{VNC} neuron activation (D) and inactivation (E). Each column represents one animal, and each row one parameter. The color shows the Z-score (mean difference divided by control standard deviation) of genotype comparisons. For optogenetic experiments, behavioral change with light is compared between *Trh* ∩ *tsh* > *CsChrimson* and background matched non-Gal4 controls

Chapter 4. Serotonergic Modulation of Walking in *Drosophila*

($w^{1118} \cap tsh > csChrimson$), both fed with all-trans-retinal (ATR). For inactivation experiments, $Trh \cap tsh > Kir2.1$ and $w^{1118} \cap tsh > Kir2.1$ were directly compared. N=130 per condition for activation experiments and N=119 for inactivation experiments. Boxed are parameters where experimental animals behave significantly differently than controls $p < .05$ calculated by Kruskal-Wallis. Shown to the right of each heatmap is the median difference in Z-score between the control and experimental population, color coded by significance level and effect direction. Non significant parameters ($p > .05$) are colored gray. **(F-G)** Heatmaps showing the difference in incidence for particular velocity/angular velocity combinations with either activation **(F)** or inhibition **(G)** of 5-HT^{VNC} neurons. For activation experiments, change in incidence with light was calculated for each animal and average and standard deviation was generated for each genotype ($w^{1118} \cap tsh > csChrimson$ ATR+, $Trh \cap tsh > csChrimson$ ATR+). Color represents the Z-score (mean difference divided by control standard deviation) of genotype comparisons. For inactivation, experimental animals ($Trh \cap tsh > Kir2.1$) and control ($w^{1118} \cap tsh > Kir2.1$) populations were directly compared. N=130 per condition for activation experiments and N=119 for inactivation experiments. **(H)** Max projections of *Trh-Gal4* driving expression of fluorescent tagged activation (*UAS-csChrimson::mVenus*) and inhibition (*UAS-Kir2.1::GFP*) tools selectively in the VNC. Anti 5-HT immunostain is shown in red. **(I)** Quantification of the number of anti 5-HT immunostain positive cells in the T1/T2 and T3/Abdominal regions of the VNC in control ($Trh \cap tsh > csChrimson::mVenus$ ATR-, N=9) and constitutive inhibition ($Trh \cap tsh > Kir2.1::GFP$, N=5) conditions. Genotypes were compared using a Welch two sample t-test. T1/T2 region $p = .72$, T3/Abdominal region $p = .52$.

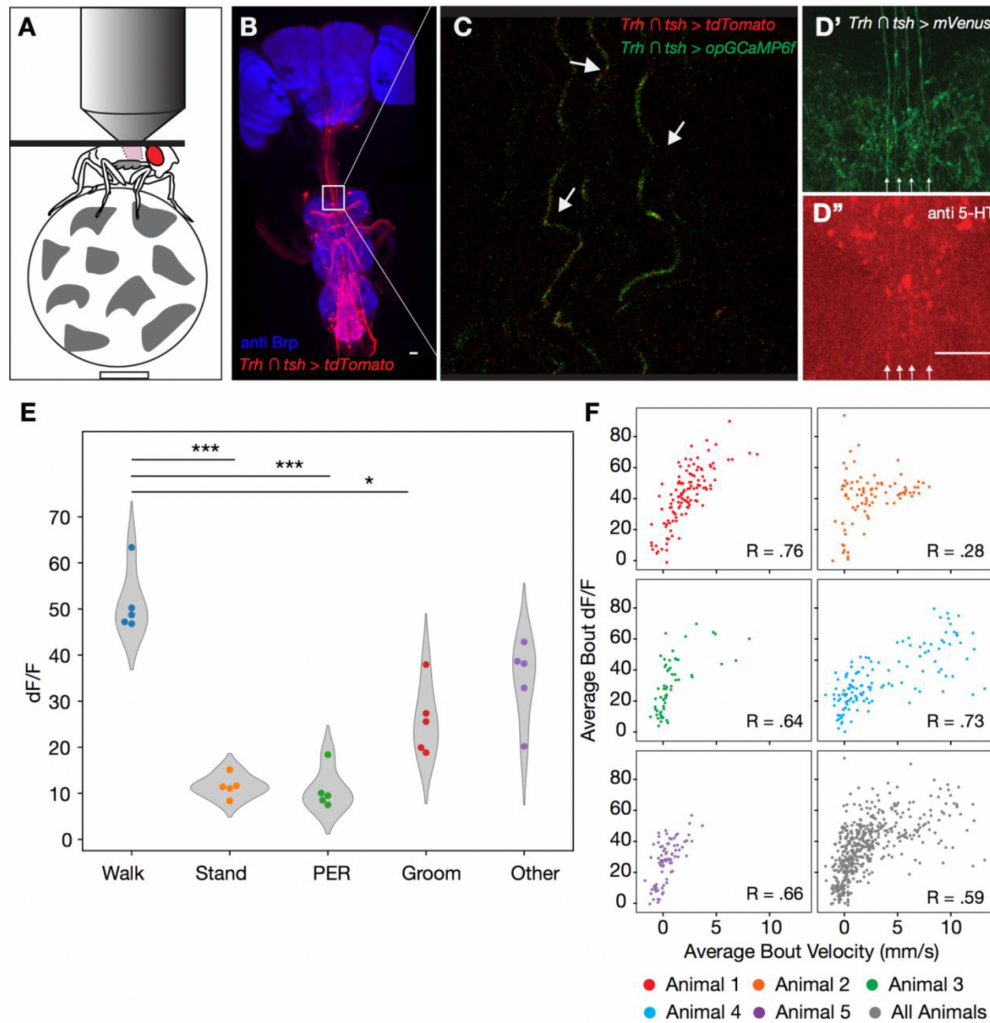


Figure S4.3: **Imaging 5-HT^{VNC} neurons in actively behaving flies.** Related to [Figure 4.2](#). (A) Schematic showing the set-up for VNC calcium imaging in a behaving animal. The dorsal aspect of the fly is dissected, and the fly is secured to a stage. The fly is able to freely walk on a ball suspended on an airpuff, while a two-photon microscope images fluorescence of a calcium indicator. (B) Expression pattern of tdTomato reporter driven by *Trh* \cap *tsh*. This marker is expressed in the expected pattern, but has some ectopic expression in the chordotonal organ, a structure that does not express *Trh*. White box indicates the approximate window that was visualized during calcium imaging. Scale bar is 25 μ m. (C) Single two photon image of view through recording window. Fibers - indicated by white arrows - running anterior to posterior express tdTomato (red) and codon optimized GCaMP6f (green) driven by *Trh* \cap *tsh*. (D', D'') Image of *Trh* \cap *tsh* > *csChrimson::mVenus* in the VNC shows the same fibers that we are recording from. A co-immunostain with anti 5-HT in this tissue shows that these fibers express serotonin. Scale bar = 25 μ m. (E) The distribution of the average $\Delta F/F$ for each manually scored behavioral category for each animal (N=5). Significance between groups was determined by Kruskal-Wallis test with follow up Dunn's correction for multiple hypothesis testing. * $p < .05$, *** $p < .001$ (F) Correlation between average bout velocity and $\Delta F/F$ for each animal, and all animals in the study (N=5). Corresponding Pearson R correlation coefficient is shown at the bottom right of each graph.

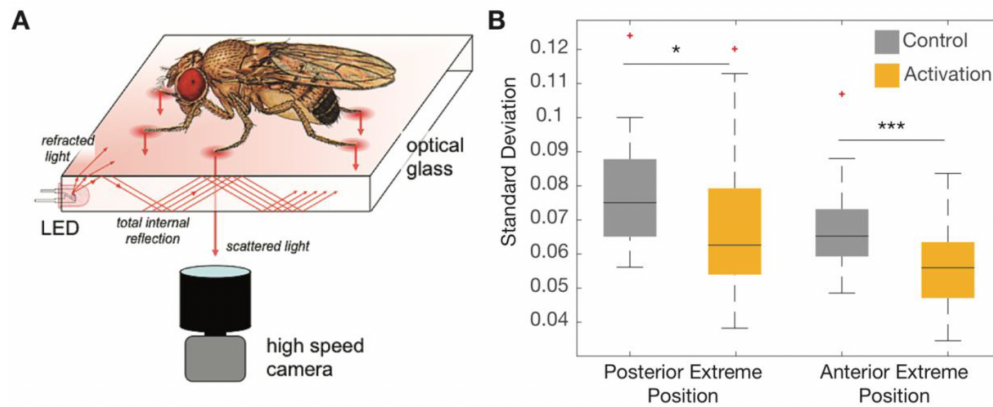


Figure S4.4: **5-HT^{VNC} activation reduces variance in foot placement.** Related to [Figure 4.3](#). (A) Schematic of the Flywalker apparatus, reproduced from [Figure S4.1](#). (B) Boxplots showing the standard deviation of footprint position for individuals during one walking bout, either at touchdown (AEP) or lift off (PEP). N = 47 bouts from 10-23 animals for *Trh* \cap *tsh* > *csChrimson* ATR⁺. N=56 bouts from 12-30 animals for *Trh* \cap *tsh* > *csChrimson* ATR⁻. Genotypes were compared using a two-sample t-test. * p <.05, *** p <.001

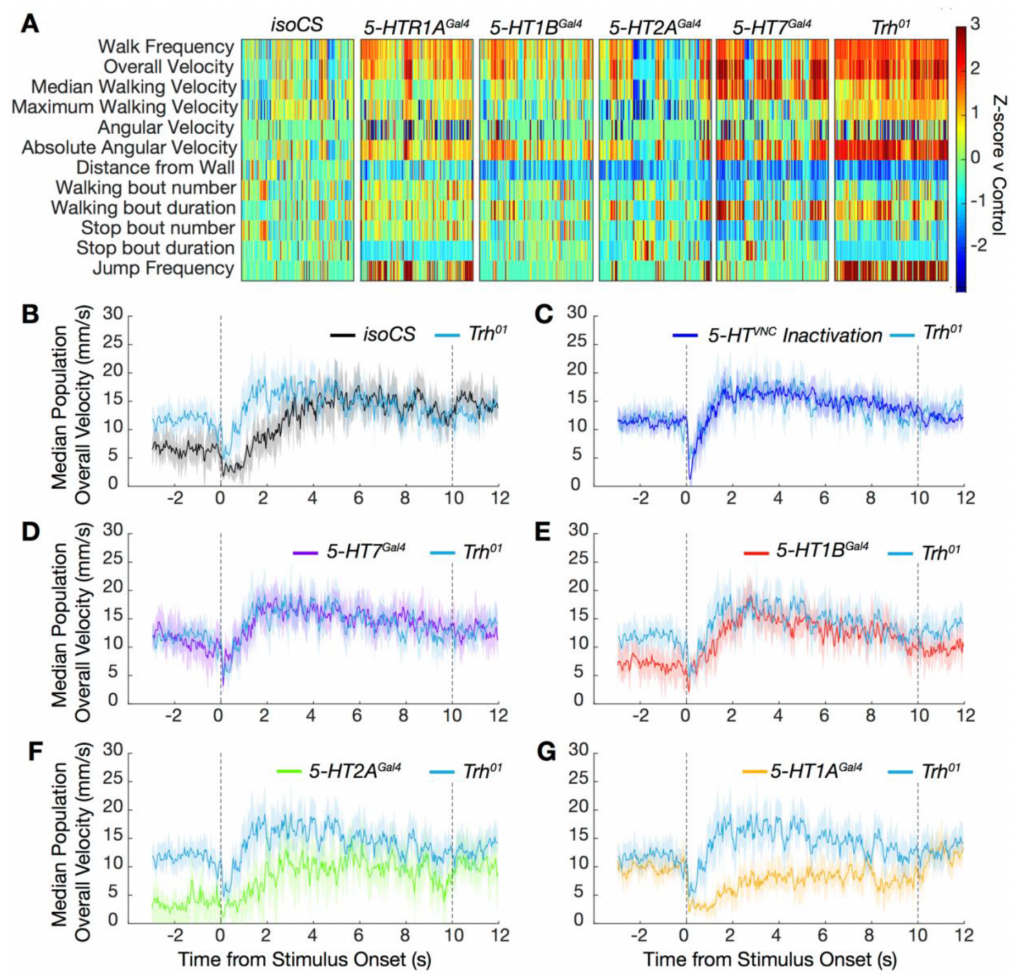


Figure S4.5: 5-HT^{VNC} inactivation, mutation of *Trh*, and mutation of 5-HT receptors shifts behavioral responses to startling stimuli. Related to [Figure 4.4](#) and [Figure 4.5](#) (A) Heatmap of behavioral differences between control animals (*isoCS*) and flies mutant for 5-HT receptors or *Trh* itself. Z-score for each individual was calculated using the *isoCS* group mean and sd as a control. Genotype (N): *isoCS* (130), *5-HT1A^{Gal4}* (130), *5-HT1B^{Gal4}* (120), *5-HT2A^{Gal4}* (100), *5-HT7^{Gal4}* (120), *Trh⁰¹* (120). (B-G) Median population walking speed sampled at 30 Hz in response to vibration stimulus with 95% confidence intervals shaded. (B) *Trh⁰¹* mutants show a blunted and shortened pause in response to novel stimulus compared to *isoCS* controls. (C) The behavior of *Trh⁰¹* mutants replicates that caused by inactivation of 5-HT^{VNC} neurons. *5-HT7^{Gal4}* mutants (D), purple line) and *5-HT1B^{Gal4}* mutants (E, red line) show a similar phenotype to *Trh* mutants (blue line). *5-HT2A^{Gal4}* mutants (F, green line) and *5-HT1A^{Gal4}* mutants (G, yellow line) have a distinct behavioral profile from *Trh⁰¹* mutants (blue lines). N= *isoCS* (140) *5-HT1A^{Gal4}* (115) *5-HT1B^{Gal4}* (124) *5-HT2A^{Gal4}* (88) *5-HT7^{Gal4}* (120) *Trh⁰¹* (139).

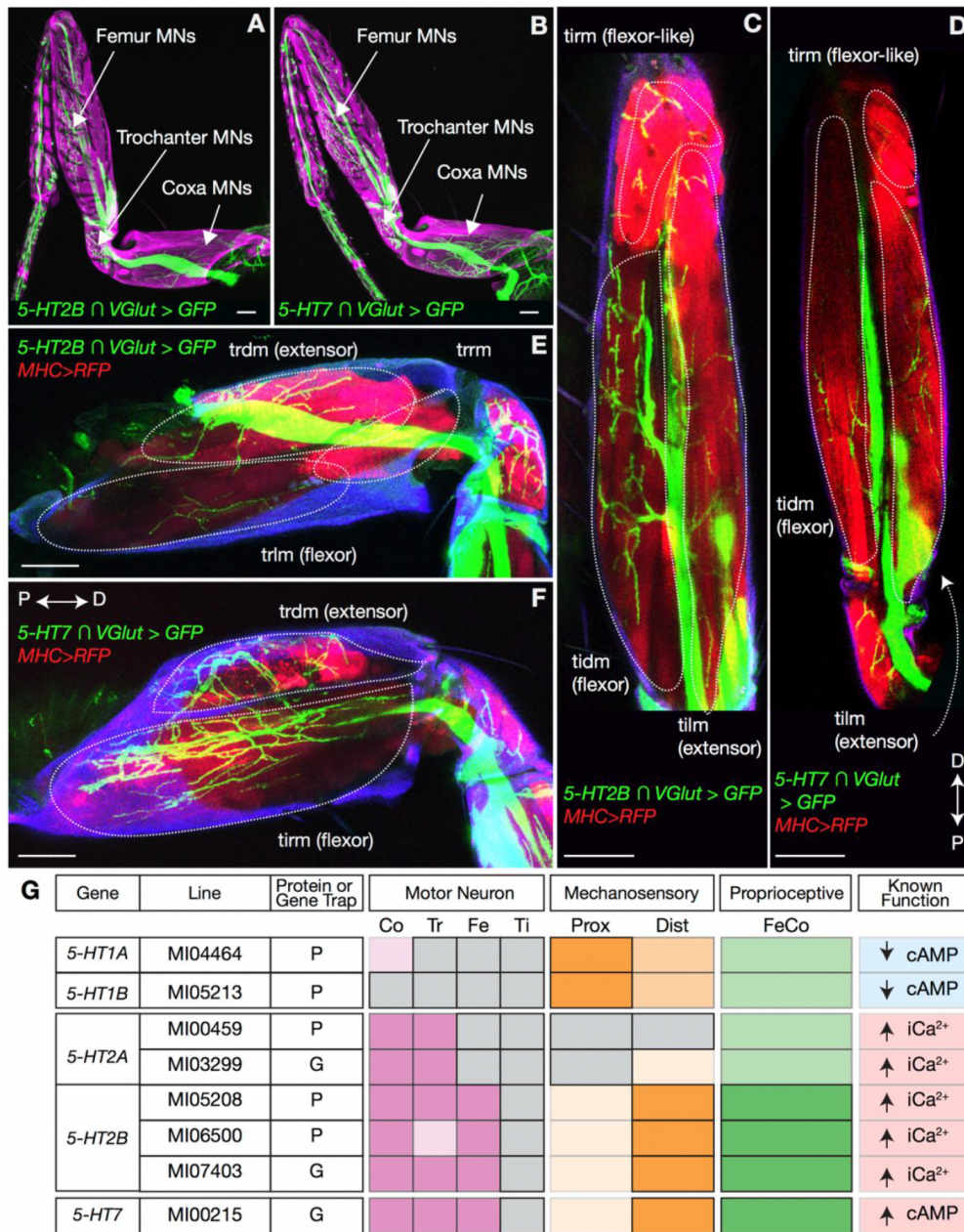


Figure S4.6: **5-HT receptors are expressed in both flexor- and extensor-like muscles in the leg.** Related to **Figure 4.6**. (A) and (B) Expression driven by (A) *5-HT2B-Gal4* or (B) *5-HT7-Gal4* after intersection with *VGlut*. Maximum Z-projection images show that both lines drive expression in motor neurons in the coxa, trochanter, and femur, but do not show expression in motor neurons of the tibia. Expression in the tarsal segments is due to ectopic driver expression in some sensory populations. Scale bars represent 50 μm . (C-F) Motor neurons expressing 5-HT receptors innervate complementary flexor-extensor muscle pairs in the femur (C and D) and coxa (E) and (F). Leg muscles are labeled in red using *MHC::RFP* and are reliably identified by position and insertion points. (C and D) Max projections of multiple imaging sections through the femur shows labeled motor neuron innervation of the tibial levator muscle (tilm) – an extensor-like muscle, the tibial depressor muscle (tidm) – a flexor-like

muscle, and the tibial reductor muscle (tirm) – also a flexor-like muscle. (E and F) Max projections of multiple imaging sections through the coxa shows labeled motor neuron innervation of the trochanter levator muscle (trlm) – a flexor-like muscle, the trochanter depressor muscle (trdm) – an extensor-like muscle, and the trochanter redactor muscle (trrm). Scale bars represent 50 μm . The proximal (P) – distal (D) axis is indicated. (G) Expression in leg motor, sensory, and proprioceptive structures is annotated for all Gal4 lines tested. Strong expression is indicated as darkly colored blocks, and weaker/more selective expression is indicated by progressively lighter color. Also annotated is whether these lines were gene (G) or protein (P) traps. Different insertion points for the same gene have highly replicable expression patterns. As described in [Figure 4.6](#), receptors families with different mechanisms of action also show distinct expression profiles.

5 Extensive and Diverse Patterns of Cell Death Sculpt Neural Networks in Insects

Disclaimer: This chapter is adapted from the following article in preparation with permissions of all co-authors:

Sinziana Pop, **Chin-Lin Chen**, Connor J Sproston, Shu Kondo, Pavan Ramdya, Darren W Williams. "Extensive and Diverse Patterns of Cell Death Sculpt Neural Networks in Insects", *eLife*, vol.9, pp.e59566, 2020. <https://doi.org/10.7554/eLife.59566>

My contribution: To know if artificially preserved octopaminergic neuron in the VNC is functional, I performed two-photon imaging to compare the calcium response of the octopaminergic neurons between control and programmed cell death-prevented groups in tethered flies behaving on the spherical treadmill. To quantify the encoding of octopaminergic neurons in control and undead groups, the average response during walking and resting was compared. First, I synchronized the datapoints of fluorescence values extracted from the segmented fluorescence stacks and the behavior labels derived from the classification via thresholding ball rotations. Then, both groups' mean calcium signals during walking and resting were computed across trials. Moreover, I further strengthened the conclusion by analyzing the calcium signal in sub-ROIs across the bundle of undead octopaminergic neurons and visualizing them along with behavioral labels. Overall, my contribution proved that the undead octopaminergic neurons in the VNC are functionally integrated into the local network.

5.1 Abstract

Changes to the structure and function of neural networks are thought to underlie the evolutionary adaptation of animal behaviours. Among the many developmental phenomena that generate change programmed cell death (PCD) appears to play a key role. We show that cell death occurs continuously throughout insect neurogenesis and happens soon after neurons are born. Mimicking an evolutionary role for increasing cell numbers, we artificially block PCD in the medial neuroblast lineage in *Drosophila melanogaster*, which results in the production of ‘undead’ neurons with complex arborisations and distinct neurotransmitter identities. Activation of these ‘undead’ neurons and recordings of neural activity in behaving animals demonstrate that they are functional. Focusing on two dipterans which have lost flight during evolution we reveal that reductions in populations of flight interneurons are likely caused by increased cell death during development. Our findings suggest that the evolutionary modulation of death-based patterning could generate novel network configurations.

5.2 Introduction

Nervous systems are exquisitely adapted to the biomechanical and ecological environments in which they operate. How they evolve to be this way is largely unknown. Such changes can occur through modifications in receptor tuning, transmitter/receptor repertoires, neuronal excitability, neuromodulation, structural connectivity, or in the number of neurons within specific regions of the central nervous system (CNS). The differences seen in networks, over an evolutionary timescale, ultimately result from heritable changes in developmental processes [254]. Advancing our knowledge of the mechanisms of neural development using comparative approaches will help us understand how specific elements can be modified, how new ‘circuits’ and behaviours evolve, and will ultimately lead to a better understanding of how nervous systems function [255]. Studies comparing the nervous systems of mammalian species that occupy diverse ecological niches reveal clear differences in the number of cells within homologous brain regions [256]. Such differences have occurred either through expansion or reduction of specific cell populations, through changes in proliferation or apoptotic programmed cell death (PCD) during development [257]. Most studies of nervous system evolution have focused on stem cell identity and the role of differential proliferation dynamics [258, 259, 259, 260]. While one recent study has elegantly shown a role for PCD in the evolution of peripheral olfactory sensory neurons in drosophilids and mosquitoes [261], how changes in cell death can modify central circuits still remains an open question.

In insects, the number and arrangement of neural progenitor cells that generate central neurons (termed neuroblasts, NBs) are highly conserved despite the remarkable diversity of insect body plans and behaviours [258, 262–270, 270, 271]. In the ventral nerve cord (VNC – functionally equivalent to the vertebrate spinal cord) all but one NBs are arranged in a

bilaterally symmetric array across the midline, while an unpaired, single medial neuroblast (MNB) stands out in the posterior end of each segment (**Figure 5.1A,B**).

In the *Drosophila* embryo a first wave of neurogenesis generates the larval nervous system after which the majority of NBs become quiescent. Following reactivation from quiescence NBs produce neurons throughout larval life until the early pupal stages [263, 270]. These postembryonic neurons – which make up most of the adult CNS – extend simple neuritic processes into the neuropil and stall until the pupal-adult transition when they grow complex arborisations, synapsing with their target cells [274]. In the VNC, NBs bud off a ganglion mother cell (GMC) which undergoes a terminal division to generate two neurons with distinctly different cell fates (an A cell and a B cell). As the A and B cells result from a single division, one cannot be produced without the other. After several rounds of GMC divisions, a lineage produced by a single NB is composed of two half-lineages: ‘hemilineage A’ made up of all the A cells and ‘hemilineage B’ made up of B cells (**Figure 5.1C**). Hemilineages act as functional units in adult flies [104, 180, 275–278]. For example, in the MNB lineage, hemilineage A cells mature into GABAergic local interneurons while hemilineage B cells become efferent octopaminergic neurons. Our previous work showed that a common fate of postembryonic neurons is PCD affecting approximately 40% of VNC hemilineages (**Figure 5.1D,E**; [278]), this is also seen in the brain [276, 279, 280]. The pattern of PCD is stereotypical and targets the same hemilineages across individuals. Taken together, the breadth of PCD suggests it plays a major role in shaping the final makeup of the adult nervous system, while its stereotypy points towards a heritable genetic basis. We therefore propose that changes in neural circuits may result from heritable alterations in the extent and pattern of PCD in hemilineages.

To mimic such an evolutionary role for PCD, we use the powerful genetic tools available in *Drosophila* to block death in one doomed hemilineage. We chose to target the MNB lineage for the following reasons; Its easy-to-locate position made the MNB identifiable in all developing insects described from as early as 1891 by Wheeler, 1891 [271], and spanning all insect orders from wingless silverfish to locusts, beetles, moths and flies [258, 260, 262–265, 267, 268, 270, 281]. The MNB gives rise to two distinct populations of neurons, one GABAergic and one octopaminergic, which are also homologous across insects [275, 282–291]. There appears to be a relationship between cell number and function in these populations. Flying insects have greater numbers of octopaminergic neurons within segments that control wings [289], while grasshoppers have more GABAergic neurons in the fused metathoracic/abdominal ganglia, where they receive auditory input from the abdomen [290, 291]. Alongside differences in numbers of the same cell type between segments and species, numbers of GABAergic and octopaminergic neurons found in one segment are never equal. This is especially intriguing as during development each GABAergic neuron is a sister cell to an octopaminergic neuron, arising from one cell division and are produced in equal number (**Figure 5.1C**). The greater number of GABAergic cells in each segment results from PCD targeting octopaminergic neurons in both grasshoppers [283] and fruit flies [278] (see **Figure 5.1D**). Pieced together,

Chapter 5. Extensive and Diverse Patterns of Cell Death Sculpt Neural Networks in Insects

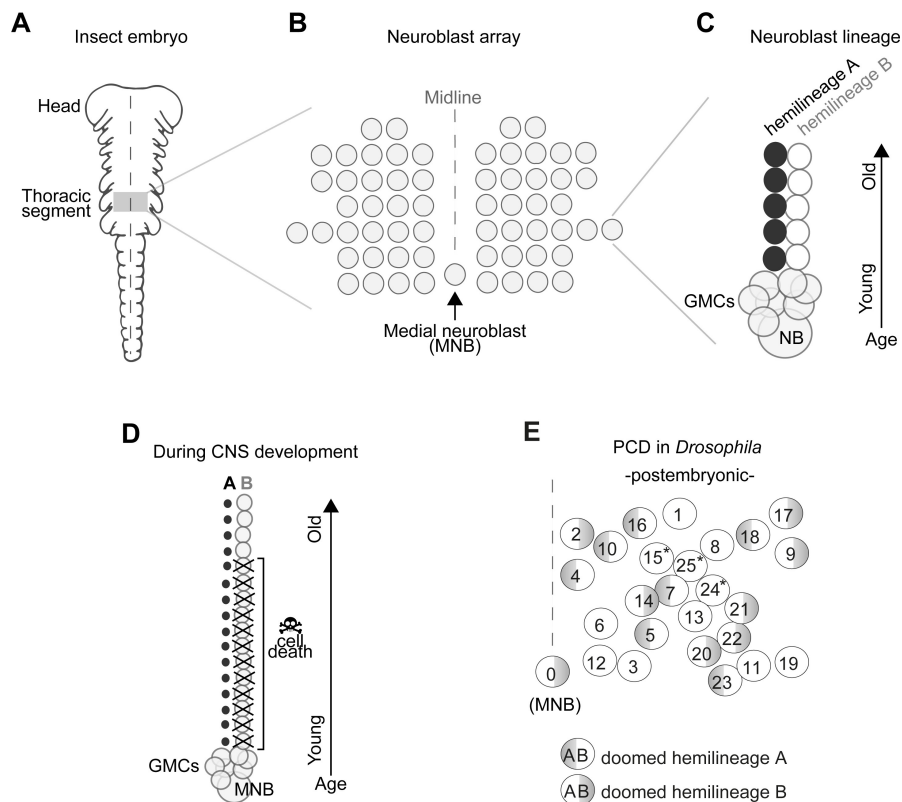


Figure 5.1: Early neurogenesis in insects. (A) Cartoon of a young grasshopper embryo, here used as a depiction of a generic insect embryo (modified from Truman, 1996 [269]). Thoracic territory where one segment-worth of neuroectoderm generates an array of neuroblasts (NB) (grey box). (B) Schematic of NB array showing bilaterally symmetric NBs organised in seven rows and six columns and a single median neuroblast (MNB) (modified from Truman, 1996). (C) Schematic of a lineage derived from an NB. Every NB buds off a ganglion mother cell (GMC) which undergoes a terminal division to generate two neurons with distinct cell fates, an A cell (black) and a B cell (grey). As the A and B cells result from a single division, one cannot be produced without the other. After several rounds of GMC divisions, a lineage produced by a single NB is composed of two half-lineages: ‘hemilineage A’ made up of all the A cells and ‘hemilineage B’ made up of B cells. Arrow indicates relative age, with newly born cells located close to the NB. (D) Schematic of MNB during development with ‘hemilineage A’ cells (black) and ‘hemilineage B’ (grey). The first neurons in hemilineage B cells survive (they are the oldest). After this point, all hemilineage B cells are removed by PCD whereas ‘hemilineage A’ cells from the same GMC division are left intact. (E) Schematic representation of the pattern of hemilineage-specific cell death in one hemisegment in the mesothorax. Each circle represents one lineage produced by one NB. Numbers represent postembryonic lineage nomenclature established by Truman et al., 2004. Shaded half circle refers to doomed hemilineage. Lineage 0 is the postembryonic name given to the MNB lineage. Asterisks mark lineages in which one hemilineage produces motor neurons and the other hemilineage generates glia [272, 273].

these data suggest that, at least in part, the evolution of some behaviours can be explained by variation in the number of octopaminergic neurons caused by PCD during MNB development.

Octopamine release in the thoracic ganglion has been reported to induce and maintain rhythmic behaviours such as stepping movements and flight muscle contractions in locusts [292] and walking, wing flicking and hindleg grooming in decapitated fruit flies [186]. All octopaminergic neurons produce tyramine as well, the precursor of octopamine, and tyramine has also been shown to induce fictive walking and flight in a thoracic preparation in locusts [293]. Throughout our work, we do not discriminate between the role of tyramine and octopamine release from hemilineage 0B and collectively refer to these neurons as octopaminergic. Consistent with its role in both (1) walking and (2) flight, we show that (1) blocking PCD in the octopaminergic hemilineage produced by the MNB in *Drosophila melanogaster* results in mature differentiated ‘undead’ neurons that survive into adulthood, elaborate complex arborisations and induce walking when activated; and (2) PCD may be responsible for reducing hemilineage 0B in the mesothorax of the flightless swift louse *Crataerina pallida*. Alongside, we propose that PCD may have caused reductions in flight hemilineages within thoracic networks in another true fly, *Braula coeca* (the bee louse), during the evolution of flightlessness. Additionally, using new tools in *D. melanogaster*, we demonstrate that PCD takes place in these neurons early, very soon after they are born. We find evidence of this early PCD in primitively wingless firebrats and hippoboscid louseflies suggesting that it is deployed widely. This ‘early’ death is categorically different to the neuronal death described in the majority of studies in insects, that focus on hormonally gated PCDs occurring at moults [294].

Our work highlights the importance of viewing hemilineages as functional units of neurodevelopment in all insects and shows that their alteration through an early mode of PCD can lead to adaptive changes in central circuits during evolution.

5.3 Results

5.3.1 An early and rapid mode of developmental cell death eliminates significant numbers of newly born neurons throughout postembryonic development in *Drosophila*

First, we wondered what specific type of PCD is responsible for sculpting VNC lineages in *D. melanogaster*, reasoning that only by gaining insight into the exact developmental process involved can we understand its role in nervous system evolution. The majority of studies on neuronal PCD in insects have focused on its role at metamorphic transitions, where death eliminates fully differentiated neurons either at puparium formation [274] or in adults post-eclosion [295, 296]. Both of these remodelling events are gated by ecdysteroids. However, our previous observations in *Drosophila* [278], together with studies in the fly brain [276, 280, 297, 298], made us consider that hemilineage-specific PCD takes place early, in newly born

Chapter 5. Extensive and Diverse Patterns of Cell Death Sculpt Neural Networks in Insects

neurons. So far, the dynamics of cell death has been difficult to evaluate on a cell-by-cell basis within a complex nervous system.

To interrogate postembryonic neuronal death, we have built a novel genetically encoded effector caspase probe called SR4VH (**Figure 5.2A,B**). SR4VH consists of a membrane-bound red fluorescent protein (Src::RFP) and a yellow fluorescent protein with a strong nuclear localisation signal from histone H2B (Venus::H2B) separated by four tandem repeats of the amino acid sequence DEVD. When effector caspases cleave the DEVD site, Venus accumulates in the nucleus while RFP remains bound to the cell membrane (**Figure 5.2B**). This reporter is similar in design to Apoliner [299], but has different subcellular localisation signals as well as four tandem caspase cleavage sites instead of one. We also found that tethering the probe to the membrane with the myristoylation signal from Src means that there is no excess signal accumulation in the Golgi apparatus (Mukherjee et al., in preparation). The nuclear localisation signal from H2B allows for highly efficient sequestration of cleaved Venus in the nucleus even in late stages of apoptosis, when the nuclear membrane is likely compromised.

Using the GAL4/UAS system and the NB driver *Worniu-GAL4*, we found we could visualise postembryonic neurogenesis and label up to 20 of the most recently born progeny from a single NB (this is due to GAL4 and reporter perdurance). The number of progeny we can detect at any one time using *Worniu-GAL4* varies from 10 to 20, most likely as a result of differential proliferation rates across lineages. We confirmed that SR4VH is reliable as a reporter for cell death in larvae by analysing its expression pattern in all lineages of postembryonic neurons in the thoracic VNC and comparing it to our previous work on MARCM homozygous mutant clones of the initiator caspase *Dronc* ([278]; **Figure 5.2C-F** and **Figure S5.1**). We found dying cells associated with lineages in the brain and VNC throughout the whole of postembryonic neurogenesis (**Figure 5.2C-F**), which lasts for 3.5 days, from mid-2nd instar (L2) to 12 hr after pupariation. As previously suggested [278], the time course of PCD indicates that cells die early – very soon after they are born – often before they have even extended a neuritic process. This death appears to be unlike the ‘trophic’ PCD found in vertebrates, where a neuron extends a process, interacts with its target cell and dies in the absence of appropriate survival signals. In support of an early onset of PCD, we were able to see sequential stages of cell death, dependent on the distance from the NB (**Figure 5.2G-I** and **Figure S5.1B**). Older cells located further away from the NB appear to be at a more advanced stage of PCD indicated by the complete translocation of Venus from the membrane to the nucleus (Cell three in **Figure 5.2G,H**) and by the accumulation of RFP-positive dead cell membranes close to the lineage bundle (arrowheads in **Figure 5.2E,F**).

The number of dying cells within a doomed lineage varied from 1 to 8, with most lineages containing 1–2 dying cells from a total of 10–20 cells labelled with *Worniu-GAL4* (dying cells/lineage: 1.3 ± 1.5 given as average \pm standard deviation; $n = 444$ doomed lineages from 5 VNCs). From a total of 444 doomed lineages, 243 harboured more than one dying cell, of

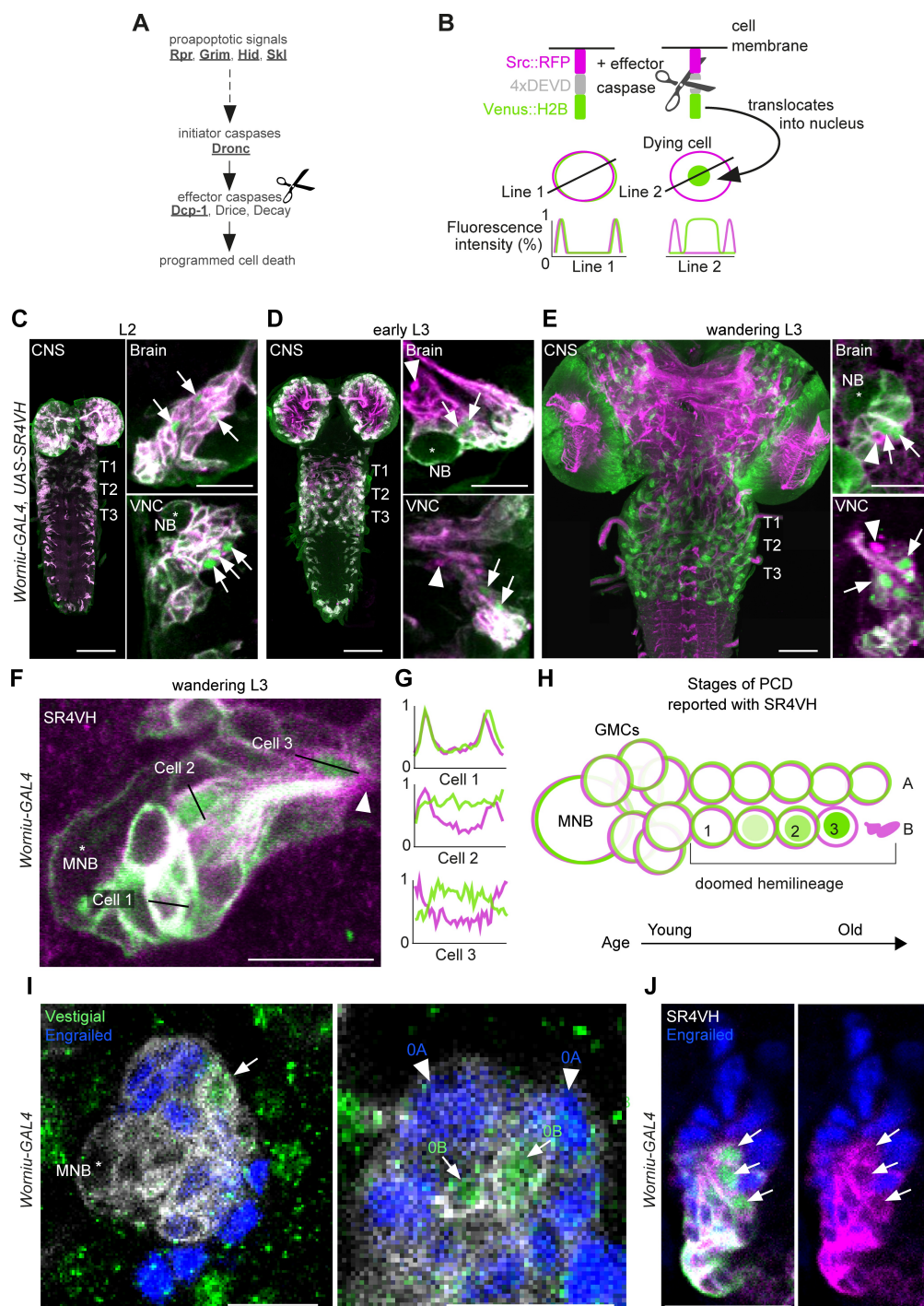


Figure 5.2: Early neuronal cell death occurs throughout postembryonic development. (A) Simple schematic of programmed cell death (PCD) in *Drosophila*. Elements disrupted in this study, or used as a PCD readout are underlined. (B) Schematic of effector caspase reporter SR4VH (top) and idealised fluorescence patterns in two cells with distinct caspase activity (bottom): RFP (magenta) and Venus (green) present in the cell membrane (Line 1) versus RFP

Chapter 5. Extensive and Diverse Patterns of Cell Death Sculpt Neural Networks in Insects

at the cell membrane and Venus accumulation in the nucleus of a cell undergoing PCD (Line 2). (C–E) SR4VH driven by *Worniu-GAL4* reveals dying cells in the central nervous system (CNS) throughout postembryonic neurogenesis in a 2nd instar (C, n = 9), early 3rd instar (D, n = 8) and wandering 3rd instar (E, n = 18) larva. Right panels show examples of lineages with dying cells located close to the NB (*) in the brain (top) and ventral nerve cord (VNC, bottom). Arrows indicate dying cell, arrowheads indicate RFP-positive dead cell membranes. Scale bars, 50 μm (left panels), 10 μm (right panels). (F) SR4VH driven by *Worniu-GAL4* reveals younger cells at earlier stages of cell death (Cell 2) are located closer to the MNB than older cells at later stages of cell death (Cell 3), which are closer to the lineage bundle (arrowhead). Image represents a single optical section. Scale bar, 10 μm . (G) Fluorescence intensity profiles (normalised to the maximum value along the line for each channel) plotted along the lines indicated in (F). (H) Schematic representing successive stages of cell death correlated with distance from NB and cell age in doomed lineages as reported with SR4VH. (I) Revealing markers for lineage 0. Immature hemilineage A progeny revealed with anti-Engrailed (blue – arrowheads) and immature hemilineage B progeny labelled with anti-Vestigial (green – arrows) in a third instar *Worniu-GAL4; UAS-CD8::GFP* larva (white). Expression of markers is mutually exclusive. Scale bars, 10 μm . (J) SR4VH driven by *Worniu-GAL4* together with antibodies for Engrailed (blue) reveal that only Engrailed-negative cells from hemilineage 0B undergo PCD (white arrowheads) during postembryonic development in the thoracic VNC. Scale bar, 10 μm . n = 6.

which 148 displayed a progression of cell death (Figure 5.2G,H). Truman and Bate [270] approximated the cell cycle of an NB to 55 min and that of a GMC to 6.5 hr, with 7 GMCs present in a proliferating lineage at all times. Therefore, after subtracting the NB and GMCs from clusters of 10–20 *Worniu-GAL4*-labelled cells, 2–12 will be neurons which resulted from 1 to 6 divisions, each separated in time by 55 min. This means that PCD was initiated early, at some time between 0 and 5.5 hr after neurons were born.

To look at death specifically during the development of the MNB lineage (lineage 0) we imaged SR4VH in wandering L3 larvae and used molecular markers to identify members of hemilineage 0A and 0B. The transcription factors Engrailed/Invected (En/Inv) are known to be expressed in immature and fully differentiated interneurons of hemilineage A [180, 275, 300, 301]. As previously reported, the mature differentiated octopaminergic neurons found in hemilineage B express the transcription factor Vestigial (Vg) [302]. Here, we find that a small number of immature postembryonic neurons (about 3–5) in close proximity to the MNB also express Vg (Figure 5.2J). Within these immature neurons the expression of Vg and En are mutually exclusive. Using *Worniu-GAL4* to drive SR4VH we found that only the engrailed-negative cells are undergoing apoptosis (Figure 5.2K), i.e. the same small number of cells that express Vg. Their proximity to the MNB suggests that Vg-positive B cells (i.e. immature octopaminergic neurons) undergo an early death, very soon after they are born.

5.3.2 Blocking PCD in *Drosophila* generates identifiable, differentiated populations of undead neurons

After observing the extent of early PCD during development, we wondered if, by reducing PCD, we could generate novel functional expansions of a hemilineage. To explore this, we made use of the powerful genetic tools available in *Drosophila* to block PCD in the MNB lineage to determine if ‘undead’ cells survive into adulthood, elaborate their neurites and acquire a distinctive neurotransmitter identity.

From our previous work [278], we know that during postembryonic neurogenesis MNB hemilineage A survives, expresses Engrailed [180] and differentiates into GABAergic interneurons [275]. Because during embryonic development the MNB hemilineage B produces a small number of octopaminergic neurons, we hypothesised that preventing PCD would generate additional octopaminergic neurons in the later postembryonic phase of neurogenesis. In postembryonic nomenclature, all the neurons generated by the MNB are collectively called lineage 0 and therefore we will refer to octopaminergic neurons generated by the MNB as hemilineage 0B.

Using the octopaminergic neuron driver, *TDC2-GAL4*, we observed a 4- to 9-fold increase in the number of octopaminergic neurons in the thoracic VNC of *H99/XR38* adult flies deficient for proapoptotic genes (*hid*^{+/-}, *grim*^{+/-}, *rpr*^{-/-} and *skl*^{+/-}) [99, 303] compared with wild-type control animals (Figure 5.3A-D), (T1: 20.9 ± 2.3, Mann-Whitney U = 0, p = 0.0002; T2: 26.3 ± 4.4, Mann-Whitney U = 0, p=0.0004; T3: 27.5 ± 3.5, Mann-Whitney U = 0, p = 0.0004; n = 11 each). These ‘undead’ neurons also express the vesicular glutamate transporter VGlut (Figure 5.2E,F), just like wild-type octopaminergic neurons [304].

Ideally, to label and manipulate dying neurons from hemilineage 0B, we require a specific driver line expressed only in the newly born doomed neurons. To test if we could use *TDC2-GAL4* to label and manipulate dying neurons from hemilineage 0B during their development, we performed a timeline of expression in wild-type and *H99/XR38* flies (Figure S5.2). Unfortunately, even though undead neurons are generated from L2 onwards in *H99/XR38* flies, the *TDC2-GAL4* is only active in the undead cells days later. Gradually, in pupae, *TDC2-GAL4* expression reveals the remaining undead B cells (Figure S5.2C,D). We concluded that the *TDC2* driver line cannot be used to visualise and manipulate newly born postembryonic ‘doomed cells’. Instead, *TDC2-GAL4* allowed us to accurately reveal ‘undead’ hemilineage 0B neurons but only in the adult (see cartoon Figure 5.3G).

To ensure sparse labelling and the precise manipulation of only doomed cells from hemilineage 0B, we generated postembryonic *TDC2-GAL4*-expressing MARCM clones homozygous for the loss-of-function allele *Dronc*^{ΔA8} (in which PCD is inhibited) [278, 305]. This strategy guarantees that, even though cell death can be rescued in other lineages, it is only within the *TDC2*-positive postembryonic neurons that UAS-based tools are expressed.

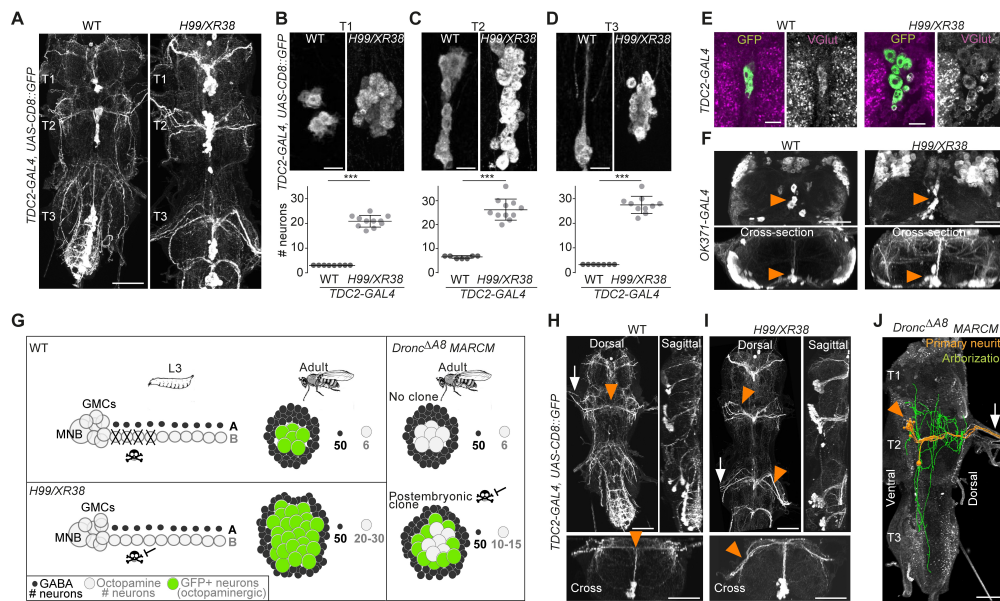


Figure 5.3: Blocking death results in differentiated undead neurons in the medial neuroblast (NB) lineage. (A) CD8::GFP expression driven by *TDC2-GAL4* in octopaminergic neurons from hemilineage 0B in the VNC of wild-type (WT, left) and PCD-blocked adult flies (*H99/XR38* deficient for *hid*^{+/-}, *grim*^{+/-}, *rpr*^{-/-} and *skt*^{+/-}, right). Scale bar, 50 μ m. (B–D) Quantifications of the number of *TDC2-GAL4*-positive octopaminergic neurons in the VNC of WT and *H99/XR38* adult flies. Bars represent mean \pm standard deviation. (B) ****p* = 0.0002 in T1, (C) ****p* = 0.0004 in T2, (D) ****p* = 0.0004 in T3, Mann-Whitney. Scale bar, 10 μ m. n = 11 each. Mann-Whitney. Scale bar, 10 μ m. n = 11 each. (E) Antibodies for the vesicular glutamate transporter VGLut and (F) GFP expression driven by the glutamatergic driver line *OK371-GAL4* label both WT and undead (*H99/XR38*) octopaminergic neurons. Orange arrowheads indicate cell bodies. Scale bars, 10 μ m (VGLut), 50 μ m (*OK371*). (G) Schematic of *TDC2-GAL4* expression in postembryonic lineage 0 in wild-type and *H99/XR38* third instar larvae and adults (**left panels**). Postembryonic hemilineage B populations only start expressing *TDC2-GAL4* in early pupal development and maintain it throughout adult life. MARCM mosaics clones that are homozygous for a null *Dronc* allele lack GAL80. These show robust expression of GAL4 in small numbers of surviving postembryonic hemilineage B cells (**right panel**). In adult WT and *H99/XR38* flies, GFP is expressed in both embryonically born and postembryonic *TDC2*-positive neurons, while in MARCM flies GFP is only present in postembryonic cells. (H–I) CD8::GFP expression driven by *TDC2-GAL4* in WT (G) and *H99/XR38* (H). WT and undead primary neurites project dorsally and branch extensively in the dorsal neuropil. In WT neurons the primary neurite bifurcates at the dorsal midline, while undead neurons are unable to bifurcate and turn to one side (orange arrowheads). In *H99/XR38* flies which contain both WT and undead neurons, the primary neurite to one side is thicker (orange arrowhead). Both WT and undead neurons join thoracic nerves (white arrows). Scale bars, 50 μ m. (J) Reconstructed arborisations of undead neurons expressing CD8::GFP driven by *TDC2-GAL4* in flies bearing MARCM clones homozygous for the loss-of-function allele *Dronc* ^{Δ A8} (in which PCD is blocked). The 3D-rendered image is tilted at a 45° angle. Undead neurons have somata that are located

at the ventral midline (orange arrowhead), branch extensively in the neuropil (green), have a turning primary neurite (orange) and project to the periphery through a thoracic nerve (arrow). Scale bar, 50 μm .

Analysis of the projection patterns of undead neurons revealed that they display both common and distinct features compared to their wild-type embryonically born counterparts. Similar to wild-type octopaminergic cells [306], the undead neurons have cell bodies located ventrally at the midline, at the posterior border of the thoracic segment (Figure 5.3H,I,J), project a primary neurite in the dorsal-most region of the neuropil, the tectulum [86] and join thoracic nerves ([307]; Figure 5.3H,I,J, Figure S5.3 and Figure S5.4). Unlike wild-type cells which bifurcate and branch extensively in the tectulum, the primary neurite of undead neurons fails to bifurcate, branches in both dorsal and ventral regions of the neuropil and sends projections to neighbouring segments (Figure 5.3J and Figure S5.4). As we describe in Figure S5.2 and Figure S5.3, a few wild-type octopaminergic neurons are produced in all thoracic segments during postembryonic neurogenesis in lineage 0. We propose that the very few bilateral projecting neurons we encounter in our clones are wild-type cells (Figure S5.2E-G). To avoid any uncertainty when performing our behavioural experiments (below), we excluded flies which contained a bifurcating neuron in undead MARCM clones. Thus, using MARCM clonal approaches we show that undead neurons in hemilineage 0B become octopaminergic, elaborate complex neurites and join thoracic nerves.

5.3.3 Undead neurons are functional and integrate into motor networks

We next asked if these differentiated undead neurons are functional. To address this, we tested if activating undead neurons with the warm temperature-gated ion channel TrpA1 in headless adult *Drosophila* could elicit behaviours (Figure 5.4 and Video S5.1). For this purpose, we deployed the same MARCM-based technique detailed above which ensured that only postembryonic octopaminergic neurons expressed CD8::GFP and TrpA1. The stochastic nature of MARCM allowed for generating both controls and flies with undead neurons in one mating cross using the same genotype, rearing and heat-shock conditions, i.e. there would be animals that would have experienced the heat-shock but have no octopaminergic neurons labelled. This further meant that behavioural experiments were performed blindly and each fly was matched to its control or undead neuron group only following dissection and imaging of the VNC. As mentioned above, we excluded flies with MARCM clones containing bilaterally symmetric neurons from our analysis, as these may be wild-type (see Figure S5.2 and Figure S5.3E-G). Additionally, we examined the effects of heat exposure in negative control flies with the genotype UAS-TrpA1 and the effects of heat-activation of wild-type octopaminergic neurons in positive controls expressing UAS-TrpA1 driven by *TDC2-GAL4*.

Chapter 5. Extensive and Diverse Patterns of Cell Death Sculpt Neural Networks in Insects

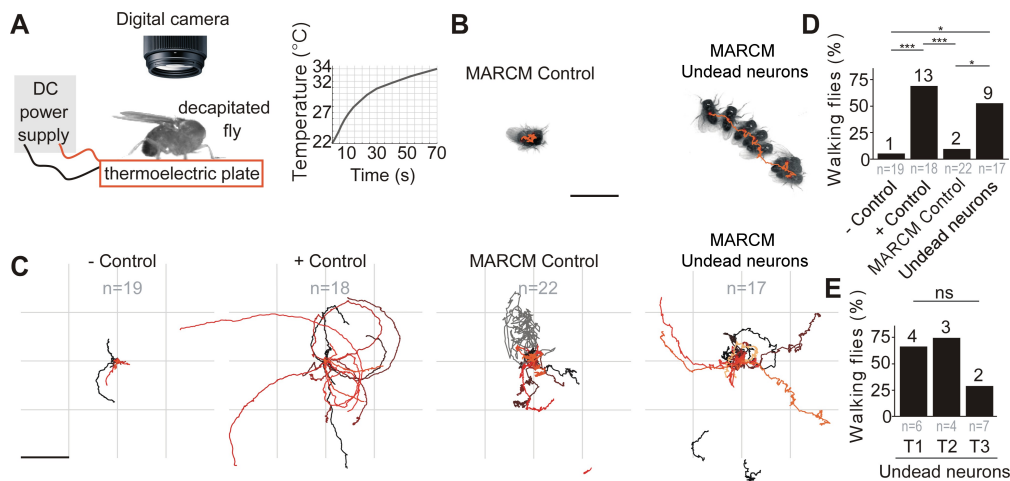


Figure 5.4: Undead neurons are functional: thermogenetic activation of undead neurons induces walking in decapitated *Drosophila*. (A) Schematic of behavioural assay with *TrpA1* activation. Decapitated flies are placed on a thermoelectric plate connected to a DC power supply, exposed to a temperature ramp (right panel) and filmed from above using a digital camera. (B) Examples of a stationary MARCM Control fly and a walking fly with undead neurons. Images represent maximum intensity projections of 13 frames at 0.3 fps tracing the centroid over time (orange line). Scale bar, 5 mm. (C) Fly body tracks generated by identifying the geometric centre of the fly body in each frame and storing the centre coordinates, plotted as a continuous line, one for each fly (walking or stationary) for negative controls (*UAS-TrpA1*), positive controls (*TDC2 > TrpA1*), MARCM control flies and flies with MARCM clones of undead neurons. Each trace represents one individual fly. Scale bar, 5 mm. (D) Quantification of the percentage of flies that walked per experimental group. *** $p = 0.0002$ for negative versus positive control, *** $p = 0.0002$ for positive controls versus MARCM Control, * $p = 0.0242$ for MARCM control versus undead neurons, * $p = 0.0135$ for negative control versus undead neurons, Pearson's chi-squared corrected for multiple comparisons using a Bonferroni correction. $n = 19$ for negative controls, $n = 18$ for positive controls, $n = 22$ for MARCM control, $n = 17$ for undead neurons. n numbers for each group are given below and the number of flies which walked is shown above each bar. (E) Quantification of the number of walking undead neuron flies split into three anatomical subgroups according to the location of MARCM clones in T1, T2, or T3. $ns p = 0.2628$, Pearson's chi-squared. $n = 6$ for T1, $n = 4$ for T2, $n = 7$ for T3. Numbers at the base are the number of walking flies. The percentage is shown above each bar.

In *TDC2-GAL4* positive controls (expressing *TrpA1* in wild-type embryonic-born octopaminergic neurons), thermogenetic stimulation induced long bouts of locomotion (Figure 5.4C,D and Video S5.1) in 13/18 flies. Importantly, we found *UAS-TrpA1* negative controls (i.e. an absence of a *GAL4*) and MARCM control flies (containing no *GAL4*-positive clones; see Figure S5.3A) did not walk in response to temperature elevation (Figure 5.4B-D and Video S5.1) (1/19 negative control, 2/22 MARCM control). We found that the activation of undead neurons expressing *TrpA1* caused decapitated males to walk in 9/17 samples (Figure 5.4B-E and Video

S5.1; also see **Figure S5.3B-D** for examples of MARCM clones of undead neurons) (negative control versus positive control, $\chi^2 = 17.6$, $p = 0.0002$; negative control versus MARCM control, $\chi^2 = 0.2$, $p = 6$; negative control versus MARCM undead neurons, $\chi^2 = 10.2$, $p = 0.0135$; MARCM control versus positive control, $\chi^2 = 16.8$, $p = 0.0002$; MARCM control versus MARCM undead neurons, $\chi^2 = 9.1$, $p = 0.0242$; MARCM undead neurons versus positive control, $\chi^2 = 1.4$, $p = 1.4283$; All comparisons were performed using Pearson's chi-squared and p values were adjusted using a Bonferroni correction). A further analysis of the occurrence of walking after splitting the MARCM undead neuron group into the three anatomical subgroups T1, T2 and T3 according to the location of undead neurons in the pro-, meso- or metathoracic segment, yielded no significant differences: 4/6 T1, 3/4 T2 and 2/7 T3 ($\chi^2 = 2.9$, $p = 0.262855$, Pearson's chi-squared) (**Figure 5.4E**).

As previously reported, decapitated flies walked slowly by moving their limbs in a seemingly erratic manner, without having a tripod gait [104, 186]. Flies were considered to be walking if they covered a distance of at least one body length during recordings and if they moved their legs in the order T3-T2-T1 at least once on each side, as evidence of intersegmental coordination [175] (Strauss and Heisenberg, 1990). The direction of walking was either forward, sideways or backwards and most flies turned or walked in circles (**Figure 5.4C**), probably caused by variation in step size [104, 186].

Our data are consistent with the observation that octopamine applied to the exposed anterior notum of decapitated flies causes walking [186] and suggests that undead neurons are functional and capable of releasing neurotransmitters in the CNS. The extent of walking was greater in positive control flies than in the undead MARCM condition (compare panels in **Figure 5.4C** and **Video S5.1**). This is likely because, alongside activating thoracic octopaminergic neurons in the VNC, in the positive controls we also stimulate the severed axons of octopaminergic cells in the brain which send descending projections to the VNC. These are not present in our *TDC2-GAL4* MARCM flies.

To determine if undead neurons are integrated into thoracic motor circuits, we recorded the activity of mixed undead and wild-type octopaminergic neuron populations expressing GCaMP6s (an activity reporter) and tdTomato (an anatomical fiduciary) in intact *H99/XR38* flies during tethered behaviour on a spherical treadmill ([49]; **Figure 5.5A,B**). The complexity of our calcium imaging experiment (see **Figure 5.5A**), together with a rate of success for obtaining MARCM clones with undead neurons of 15%, prompted us to approach our question whether undead neurons are functional during natural walking by using *H99/XR38* flies. Keeping in mind that, instead of bifurcating, undead neurons collectively take a turn (see **Figure 5.3I,J** and **Figure S5.3B-D**), we interpret activity from the thickest bundle in the bifurcation as belonging to both undead and wild-type neurons. In these animals we observed conspicuous increases in neural activity during air-puff-induced walking in both wild-type controls (**Figure S5.5**) and in *H99/XR38* flies (**Figure 5.5C-E** and **Video S5.2**, **Video S5.3**, **Video**

S5.4). Because undead neurons outnumber their wild-type counterparts by a ratio of 6.5 to 1 (see **Figure 5.3A-D**), these results imply that both neuronal types are active in *H99/XR38* flies. Supporting this, we observed an increase in GCaMP6s fluorescence across all subregions along the width of the thickest primary neurite bundle in the bifurcation, which contains all undead neurons together with three wild-type cells (**Figure S5.6** and **Video S5.4**). Taken together, these data reveal that ‘undead’ neurons in the adult fly are functional and can integrate into motor networks.

5.3.4 Hemilineage-specific cell death in the MNB lineage correlates with loss of flight in the swift lousefly *Crataerina pallida*

Our observation that undead neurons functionally integrate into the CNS of adult flies strongly supports the possibility that PCD could be leveraged to modify neural circuits over the course of evolution. Alongside walking, octopaminergic neurons in the MNB lineage have a well-known function in flight [308], and differences in neuron numbers correlate well with varying degrees of flight performance (**Figure 5.6**). Proficient fliers such as locusts and most flies have more octopaminergic neurons in winged thoracic segments (highlighted in yellow in **Figure 5.6**), while clumsy fliers such as cockroaches and crickets have similar numbers of neurons across thoracic segments. **Figure 5.6** reviews our current knowledge of the number of GABAergic (hemilineage A) and octopaminergic (hemilineage B) neurons in the MNB of insects compiled from multiple studies spanning decades of research (see references in **Figure 5.6**). The lack of data for one population or the other is indicated with a question mark. Alongside our own data from swift louseflies (see **Figure 5.7**), here we also include our unpublished observations in the horse lousefly (for 0B) and the bee lousefly (for 0A). Having limited samples and antibody, we successfully labelled one preparation each and therefore resort to depicting these as a cartoon in **Figure 5.6**.

Because octopaminergic population size reflects flight ability across insects, and dipterans generally display larger populations in the mesothorax, we wondered if flies which have lost flight during evolution show reduced numbers of octopaminergic neurons in this segment. To this end, we described the MNB lineage in the flightless dipteran *Crataerina pallida*, the swift lousefly (**Figure 5.7A**), a viviparous haematophagous ectoparasite of the swift *Apus apus* [309–313]. We labelled lousefly octopaminergic neurons from hemilineage 0B using antibodies for tyramine β -hydroxylase [314] and by comparing the ratio of octopaminergic cells in the mesothorax (winged segment) and the prothorax (lacks wings), we found that, unlike flying dipterans, the swift lousefly has lost segment-specific variability of cell numbers (fruit fly [2.2 ± 0.2 , $n = 7$] versus swift lousefly [1.1 ± 0.2 , $n = 3$], $p=0.012$, Mann-Whitney $U = 0$, Mann-Whitney t -test) (**Figure 5.7B-F**). In the sister hemilineage 0A we found a considerably larger number of GABAergic neurons (**Figure 5.7F**), suggesting that PCD may be responsible for the selective elimination of the octopaminergic hemilineage.

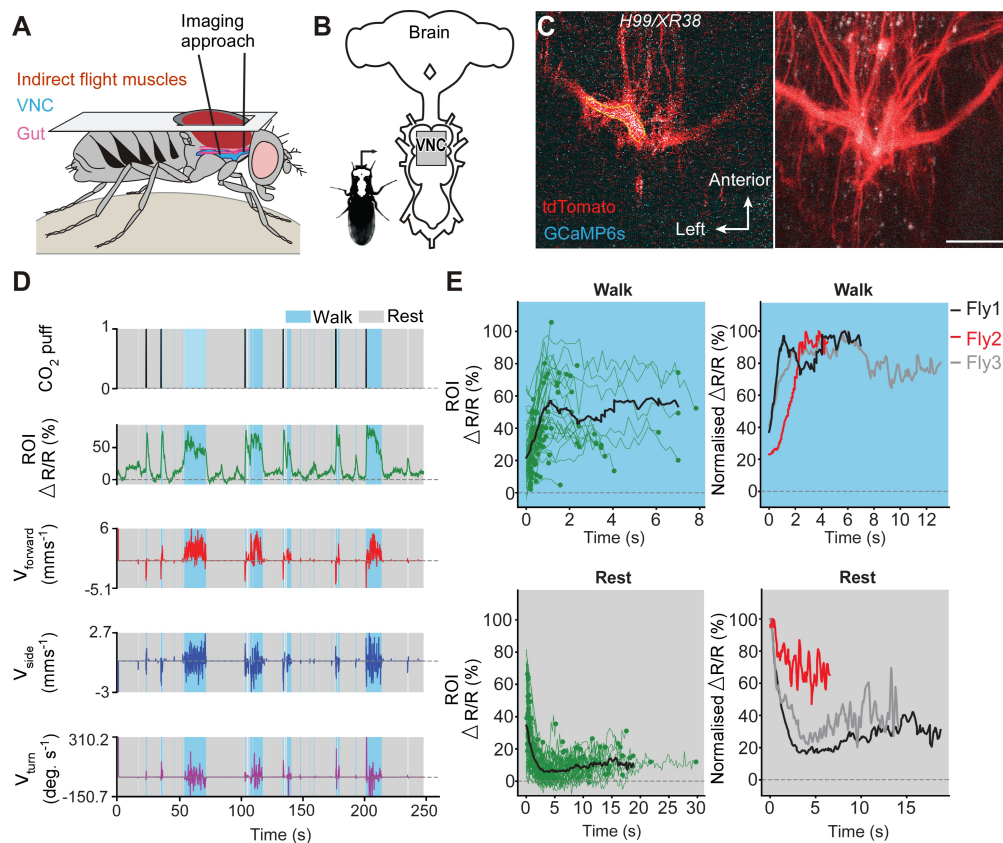


Figure 5.5: Undead neurons integrate into VNC networks: undead neurons are active during naturalistic behaviours in intact adult *Drosophila*. (A) Schematic of the dorsal thoracic dissection and approach for ventral nerve cord functional imaging in tethered, adult flies. (B) Location of the imaging region-of-interest (grey box) with respect to a schematic of the adult CNS. (C) Raw 2-photon image of *TDC2-GAL4*-positive neurons co-expressing tdTomato (red) and GCaMP6s (cyan) in *H99/XR38* flies (left). Region-of-interest used to calculate $\% \Delta R/R$ is outlined (yellow). Standard deviation z-projection of a dorsal-ventral image stack of the functional imaging region-of-interest in (B) (right). Scale bar, $50 \mu\text{m}$. (D) Representative behavioural and functional imaging data in *H99/XR38* flies. Shown are: CO_2 stimulation (black), $\% \Delta R/R$ (ratio of GCaMP6s/tdTomato) signal (green) and ball rotations indicating forward walking (red), sideways walking (blue), and turning (purple). The behaviour of the fly was classified as either walking (light blue), or resting (grey) by applying a threshold on ball rotation speed. (E) (left) Individual (green) and average (black) $\% \Delta R/R$ traces within each behavioural epoch for walking ($n = 82$) and resting ($n = 86$) events processed from 750 s of imaging data. Solid green circles indicate the end of a behavioural epoch. The average trace (black line) was calculated for only periods with four or more traces. (right) Normalised average $\% \Delta R/R$ traces for three different flies during walking and resting. The average (black) trace is the same as in the left panel.

Chapter 5. Extensive and Diverse Patterns of Cell Death Sculpt Neural Networks in Insects

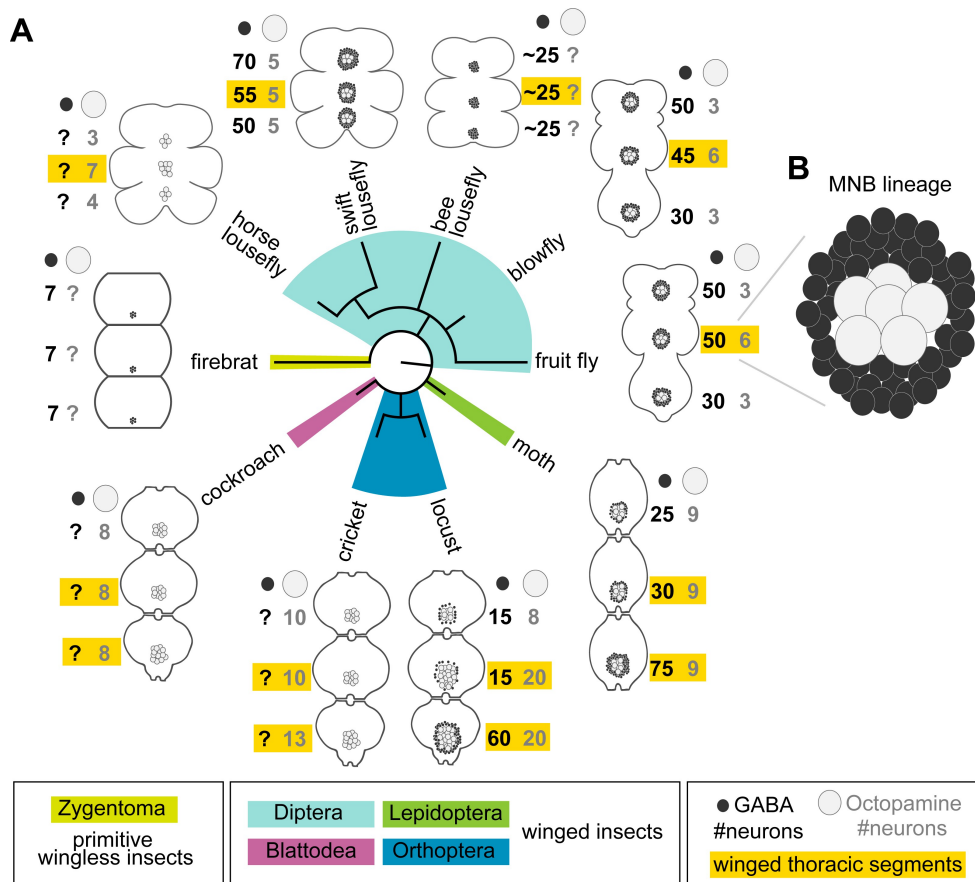


Figure 5.6: Median neuron numbers vary between insect species. (A) Schematic showing summary of thoracic midline neuron population data from 5 orders of insects (colour-coded in the phylogenetic tree and in the figure key below) including the primitive wingless firebrat *Thermobia domestica*, the cockroach *Periplaneta americana*, the cricket *Gryllus bimaculatus*, the locust *Schistocerca gregaria*, the moth *Manduca sexta*, the fruit fly *Drosophila melanogaster*, the blowfly *Calliphora vicina*, the horse lousefly *Hippobosca equina* and the flightless bee lousefly *Braula coeca* and swift lousefly *Crataerina pallida*. The numbers of GABAergic neurons (black cells) and octopaminergic neurons (grey cells) produced by the MNB is given for each thoracic segment. Except for the moth, a higher number of octopaminergic neurons can be found in winged segments in flying insects (yellow boxes). Cell numbers in this homologous lineage vary both between segments and species. Data on firebrats, cockroaches, crickets, locusts, moths, fruit flies and blowflies are compiled from Monastirioti et al., 1995; Stevenson and Spörhase-Eichmann, 1995; Witten and Truman, 1998; Schlurmann and Hausen, 2003; Lacin et al., 2019; and unpublished data from Dacks, Pflüger and Hildebrand (AM Dacks, personal communication, May 2020), while data on horse, swift and bee louseflies are from our own work. (B) Cartoon of *Drosophila* mesothoracic midline lineage populations with ‘hemilineage A’ cells revealed by GABA immunoreactivity (black) and ‘hemilineage B’ revealed by octopamine immunoreactivity (grey).

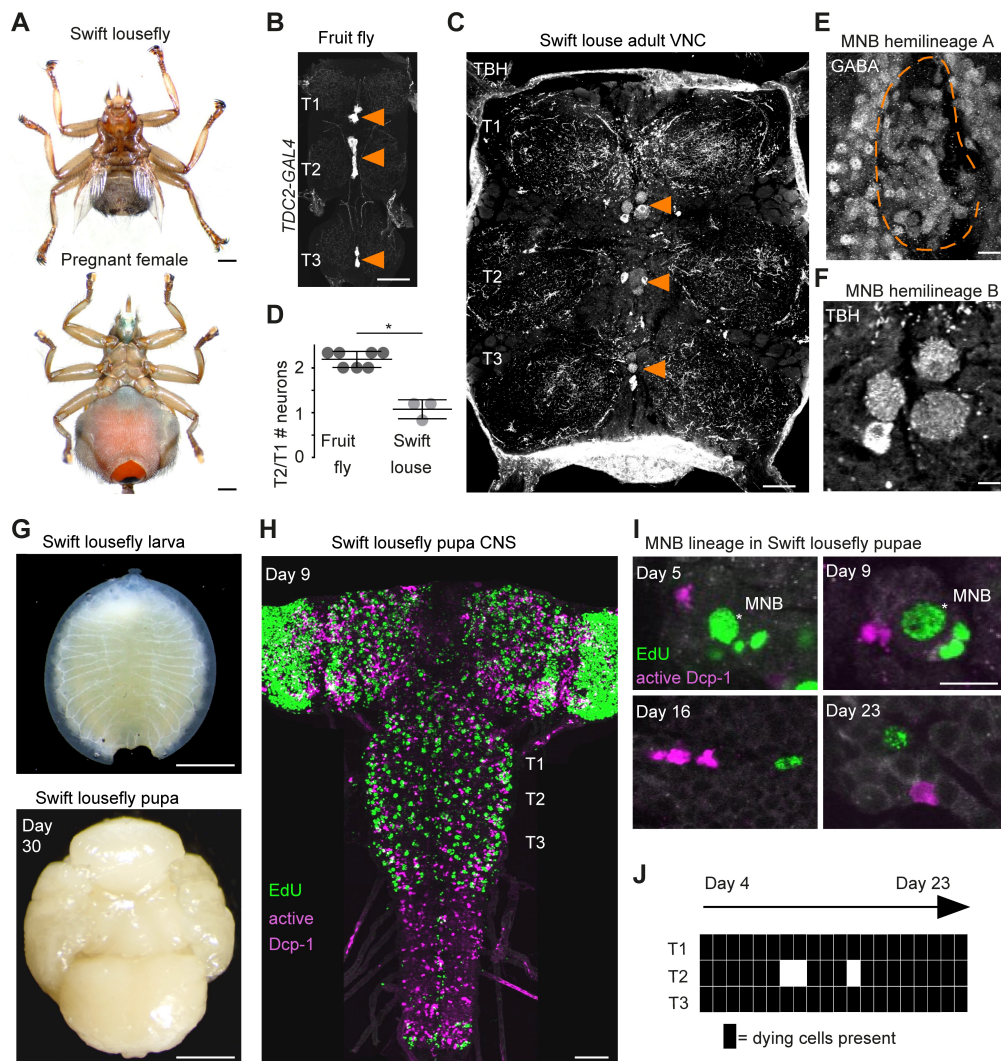


Figure 5.7: Hemilineage-specific cell death may be responsible for reduced octopaminergic neurons in the swift lousefly. (A) Dorsal view of an adult swift lousefly with vestigial wings (top). Ventral view of a female pregnant with a prepupa (bottom). Scale bars, 1 mm. (B) Wild-type octopaminergic neurons in hemilineage 0B in a *Drosophila melanogaster* VNC labelled with CD8::GFP driven by *TDC2-GAL4* (orange arrowheads). Scale bar, 50 μ m. (C) Octopaminergic neurons in hemilineage 0B in a swift lousefly VNC labelled with antibodies for tyramine β -hydroxylase (TBH, orange arrowheads). Fluorescence in the neuropil is derived from secondary antibodies trapped in the tracheal system and does not mark the true presence of TBH protein. Scale bar, 50 μ m. (D) Quantification of T2/T1 number of octopaminergic neurons in fruit flies and swift louseflies shows that swift louseflies have lost the T2-specific higher numbers typical of flying dipterans (* $p = 0.012$, Mann-Whitney. $n = 7$ fruit flies, $n = 3$ swift louseflies). Bars represent mean \pm standard deviation. (E) Cluster of cell bodies belonging to hemilineage 0A (dashed outline) labelled with antibodies for GABA and (F) cell bodies belonging to hemilineage 0B labelled with TBH antibodies in the prothorax (T1) of a swift lousefly. (G) Swift lousefly larva (top) and Day 30 swift lousefly pupa removed from its

Chapter 5. Extensive and Diverse Patterns of Cell Death Sculpt Neural Networks in Insects

puparial case (bottom). Scale bars, 1 mm (H) EdU labels proliferating cells and antibody-labelling for active Dcp-1 reveals dying cells in the CNS of a swift lousefly pupa 9 days after pupariation. Scale bar, 50 μm . (I) Dying cells in lineage 0 labelled with antibodies for active Dcp-1 are located close to proliferating cells (e.g., NB*) throughout neurogenesis at Day 5 (top left), Day 9 (top right), Day 16 (bottom left) and Day 23 (bottom right) after pupariation. Scale bar, 10 μm . n = 1 each. (J) The occurrence of active Dcp-1-positive cells in lineage 0 in T1, T2 and T3 from Day 4 to Day 23 after pupariation in swift lousefly pupae (n = 1 each). Each black box indicates one occurrence.

We next wondered if we can find evidence of early PCD in hemilineages in the swift lousefly. Swift louseflies are viviparous, with only one progeny being produced and carried by the female at any one time (see [Figure 5.7A](#), lower panel). Larvae hatch and remain inside the uterus for their entire larval life, feeding on lipid-rich secretions from milk glands until pupariation, when they are deposited in the swift nests and pupate. Adults only emerge the following spring, when swifts return from North Africa [309, 310]. To capture postembryonic development, we dissected both larvae from inside female abdomens and pupae staged from Day 0 onwards, indicating days passed since laying ([Figure 5.7G](#)). Similar to the tsetse fly [274], neurodevelopment is significantly delayed compared to ‘typical’ dipteran flies - the nervous system only acquires dipteran larval-like features many days after pupariation ([Figure 5.7H](#)). Using EdU to label proliferating cells and immunostaining for active Dcp-1 ([Figure 5.7H-J](#)), we found dying cells located close to NBs throughout the 24 days of pupal neurogenesis (**Pop et al., in preparation**). In the MNB lineage, which is easily identified by its medial position and projection pattern in the neuropil, we found cell death in thoracic segments at all time points examined, from Day 4 after pupariation to Day 23 ([Figure 5.7I,J](#)).

Because cell death is present during neurogenesis in winged insects: selectively eliminating hemilineages in the fruit fly [278], killing off immature octopaminergic neurons produced by the MNB in the grasshopper [283], appearing to sculpt neural networks in swift louseflies (see [Figure 5.7H-J](#)); we wondered if PCD also occurs during CNS development in a ‘primitive’ wingless insect. Using TUNEL labelling in the firebrat *Thermobia domestica* ([Figure 5.8A,B](#)), we found dying cells close to many NBs in all thoracic neuromeres at 50–55% of embryonic development ([Figure 5.8C-E](#)).

Similar to what we see in *Drosophila* (see [Figure 5.2](#)Figure 2 and [Figure S5.1](#)), our observation that dying cells are found close to NBs in firebrats and louseflies suggests that this early PCD may be a universal and ancestral feature that sculpts the nervous system of all insects. To further explore if changes in PCD may have been deployed during evolution to accommodate adaptive modifications to behaviour, we next searched for evidence of increased PCD in other flight hemilineages of flightless dipterans.

5.3.5 Increased hemilineage-specific PCD in flightless dipterans may be responsible for adaptive modifications to neural circuits

To explore the possibility that changes in the pattern and/or extent of PCD are adaptive, we looked for evidence of evolutionary modifications in the VNC of yet another species, the bee lousefly *Braula coeca* (Figure 5.9A-D). *Braula*, a close relative of drosophilids, is wingless, lacks halteres and has an extremely reduced thorax (Figure 5.9A). Bee louseflies spend their entire adult life as kleptoparasites on the honeybee *Apis mellifera* (Imms, 1942; McAlister, 2018). We specifically asked whether lineages known to function in flight circuitry might be modified in flightless insects. In *Drosophila*, a thorough anatomical study recently described the pattern of innervation for each lineage into known functional domains of the adult neuropil and categorised them accordingly as being involved in leg, wing and both leg and wing control [277]. In addition, the functional role of most hemilineages was previously assessed by thermogenetic activation in headless flies and those involved in flight-associated behaviours, such as wing wave, wing buzz or take-off, were identified [104]. Together, these studies provide an excellent starting point for anatomical comparisons of homologous hemilineages which may have served an ancestral role in flight.

Using antibodies for Neuroglian, we compared homologous hemilineages involved in the flight circuits of the two flightless dipterans, the swift lousefly *Crataerina pallida* and the bee lousefly *Braula coeca*. Comparing the Neuroglian-labelled axon bundle width of homologous

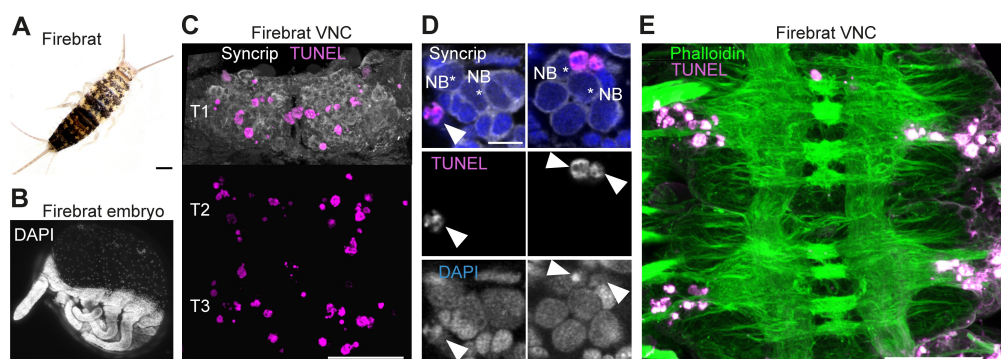


Figure 5.8: **Cell death during neurogenesis in the ‘primitive’ wingless firebrat.** (A) Adult firebrat. Scale bar, 1 mm. (B) Maximum intensity projection of DAPI staining in a wholemount firebrat embryo (*Thermobia domestica*) at 50–55% of embryonic development. Scale bar, 100 μm . (C) Dying cells in the thoracic VNC of a firebrat embryo labelled using TUNEL (magenta) and Syncrip (white) antibodies. Syncrip was used here as a proxy for Neuroglian staining to reveal lineages. Scale bar, 50 μm . (D) Dying cells (arrowheads) are located close to NBs (*). Scale bar, 10 μm . (E) Dying cells (magenta, TUNEL) are located in the cortex of the VNC, where neurogenesis takes place, and not in the neuropil (green, Phalloidin) in a firebrat embryo. Scale bar, 50 μm .

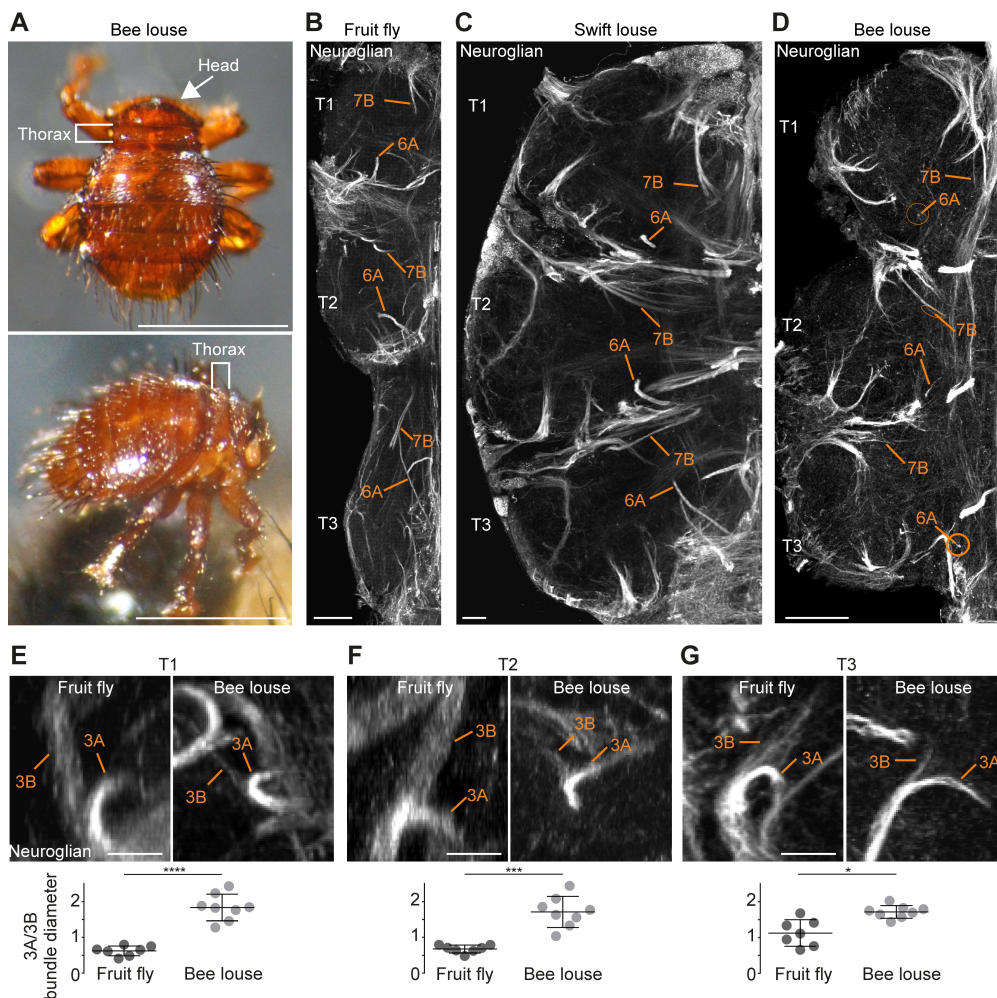


Figure 5.9: **Neuronal cell death sculpts the wing circuitry of wingless dipterans.** (A) Dorsal (top) and side view (bottom) of an adult bee lousefly with a reduced thorax lacking wings and halteres. Scale bar, 1 mm. (B–D) Hemilineage VNC fibre tracts labelled with Neuroglial in a fruit fly (B), a swift lousefly (C) and a bee lousefly (D). Shown are hemilineages 6A and 7B which are reduced in the bee lousefly in all three thoracic segments (T1, T2, T3). Scale bars, 50 μm . (E–G) 3A and 3B hemilineage fibre tracts labelled with Neuroglial in a fruit fly (top left) and a bee lousefly (top right). Shown are maximum intensity projections, chosen to best display hemilineages, from cross-section T1 (E), T2 (F) and frontal perspectives T3 (G). Quantifications of 3A/3B hemilineage bundle diameter ratios in fruit flies and bee louseflies are given below (**** $p < 0.0001$ in T1, independent samples t-test, *** $p = 0.0001$ for T2, Welch's t-test, * $p = 0.0044$, Welch's t-test. $n = 7$ fruit flies each, $n = 8$ bee louseflies each). Bars represent mean \pm standard deviation.

hemilineages between flightless and flying species, we found that hemilineages 3B, 7B, 11B and 12A, which produce wing waving, wing buzzing or take-off in the fruit fly [104], hemilineages 6A and 19B, which innervate the wing neuropil, and 5B, which innervates both leg and

wing neuropils [277], are reduced in bee louseflies, but not in swift louseflies (**Figure 5.9B-D**). Among the latter, hemilineages 5B and 6A are known to contribute to leg movements and changes in posture, while the role for 19B is yet to be determined [104]. Importantly, 3B, 6A, 11B, 12A and 19B belong to lineages in which both hemilineages survive in fruit flies (see schematic in **Figure 5.1E**). A difference in axon bundle diameter between sister hemilineages could indicate a difference in cell number, possibly established by PCD during development. We chose to quantify the ratio of axon bundle diameters in lineage three because we expected a reduction in hemilineage 3B, which innervates the wing neuropil, but no change in hemilineage 3A, which projects into the leg neuropil [277]. The fibre tracts of 3A and 3B originate as a common bundle and split only in the intermediate neuropil. After they split, the sister fibre tracts sit in the same plane before they defasciculate, making them easy to trace and compare (**Figure 5.9E-G**). We found that the ratio between sister hemilineages A and B is significantly higher in bee louseflies compared to fruit flies, indicating that hemilineage 3B, which controls flight-related behaviours, is severely reduced in these flightless flies (T1: fruit fly [0.6 ± 0.1 , $n = 7$] versus bee louse [1.8 ± 0.4 , $n = 8$], $p < 0.0001$, $t = 8.084$, independent samples t-test; T2: fruit fly [0.7 ± 0.1 , $n = 7$] versus bee louse [1.7 ± 0.4 , $n = 8$], $p = 0.0001$, $F = 42.22$, Welch's t-test; T3: fruit fly [1.1 ± 0.4 , $n = 7$] versus bee louse [1.7 ± 0.2 , $n = 8$], $p = 0.0044$, $F = 14.84$, Welch's t-test). Even though we cannot make a precise inference of cell numbers in each hemilineage, as the fibre tract of hemilineage 3B appears frayed while 3A is more compact in both species, our results clearly show that 3B is greatly reduced, associated with the loss of flight machinery.

5.4 Discussion

5.4.1 Hemilineage-specific cell death occurs in newly born neurons

To help us understand more about the patterning of PCD, we designed and used a new effector caspase probe SR4VH, which allowed us to interrogate the extent and dynamics of hemilineage-specific cell death. It shows us that an early onset PCD is responsible for the elimination of postembryonic neurons in the fly VNC, that this happens throughout the entire 3.5 days of postembryonic neurogenesis, and is hemilineage-specific. Although PCD has been reported as a fate within lineages in the embryo [315,316], the impact of this 'early' and hemilineage-specific PCD on the construction of the adult network has yet to be fully appreciated. This type of PCD is responsible for removing almost half of all postembryonic neurons that are born in the fly (Truman et al., 2010). Until now, the most frequently reported type of neuronal death described in insects has been the hormonally regulated PCD that removes mature neurons during the narrow developmental windows at the beginning of metamorphosis and within the first day after adult eclosion [295,317]. We now know from our data that these make up only a small fraction, compared to the total number of neuronal deaths in the fly.

Chapter 5. Extensive and Diverse Patterns of Cell Death Sculpt Neural Networks in Insects

Our SR4VH probe allows us to see that newly born neurons initiate cell death within the first 5.5 hr after birth. We can capture different stages of cell death: with young cells at very initial stages of PCD located closer to the NB, while older cells at more advanced stages of PCD with RFP labelled cell membranes found close to the lineage bundle. Importantly, death happens before neurites have extended, strongly suggesting that this PCD is not an analogue of neurotrophic death, found in vertebrates - where neuron-target interactions play a major role in the decisions of cell survival [318]. In *Thermobia domestica* and *Crataerina pallida*, where the use of sophisticated genetic reporters such as SR4VH was not yet possible, EdU incorporation to mark dividing cells and immunolabelling for the active effector caspase Dcp-1 as a proxy for cell death revealed dying cells close to sites of division. Dying cells were found in the proximity of NBs (identifiable in all insects by their large size and position in the outermost layer of the CNS cortex) and far removed from mature neurons which congregate in the innermost layer of the cortex, adjacent to the neuropil. Therefore, we speculate that these cells are immature neurons and propose that they too undergo a death with rapid onset following division, similar to the early hemilineage-specific cell death we see with SR4VH in fruit flies.

The critical question that these data bring into focus is how early onset PCD is orchestrated, especially that an early intrinsically determined mode of cell death seems to be widespread across animals, from *C. elegans* to mice [319, 320]. Early PCD likely involves a combination of intrinsic patterning and cell-cell interactions between sibling neurons which ultimately deploy the activity of proapoptotic genes *rpr*, *hid*, *grim* and/or *skl*. Previously, patterning genes such as *Ubx* have been shown to contribute to the survival of hemilineages in the thoracic VNC in a parasegment-specific manner [321], while the transcription factor *Unc-4* has been recently demonstrated to provide neural identity to hemilineages involved in flight [322]. Such spatial patterning is also required to establish NB identity which, in turn, can determine which hemilineage is maintained and which dies. In the developing optic lobe Bertet et al., 2014 [279] have shown that the temporal sequence of transcription factors expressed in NBs (inherited by the GMC and newly born neurons) produces a switch in the selective survival of one hemilineage over the other. In this manner, the changes to NB identity which have been documented in other insects [258], despite a conserved NB array and progeny, could in turn influence the pattern of PCD. Alongside, cell-cell interactions between newly born neurons could influence fate choices. The requirement of interactions between newly born siblings in determining asymmetric fates has been shown in the grasshopper VNC [323, 324], although this exact same mechanism has not been demonstrated in *Drosophila*.

The spatio-temporal pattern of death revealed with SR4VH shows us that understanding the molecular control of hemilineage-based death is the key question going forward and is likely to provide insight into how networks evolve.

5.4.2 Blocking death results in functional neurons that integrate into adult networks

Here we blocked PCD within the MNB lineage (called lineage 0 in the postembryonic literature) and found that ‘doomed’ neurons become octopaminergic, generate arborisations and target the tectulum neuropil [86]. Previous work has shown that octopamine can induce and maintain walking in locusts (Sombati and Hoyle, 1984) and decapitated fruit flies [186]. Consistently, we find that our ‘undead’ hemilineage 0B cells can induce walking when activated thermogenetically in headless flies and show calcium activity during naturalistic bouts of locomotion. Thus, by blocking death, we have ‘resurrected’ functional neurons that are able to integrate into thoracic motor networks. Although this ‘dialling up’ of cell numbers, in our system, is artificial, it reveals how doomed neurons possess cryptic cellular phenotypes that can emerge when death is blocked, advocating for the evolvability of such a hemilineage-based system.

While these undead hemilineage 0B octopaminergic neurons share many conserved features with wild-type cells, the variations we see in their morphology could act as a substrate for evolutionary change. A recent study has linked structural changes in the VNC with changes in behaviour between strains of *Drosophila melanogaster* [325]. Mellert et al. [325] show that hemilineage 12A in the mesothorax has variable bundle morphologies and that these correlate well with the time of flight initiation. Flight is used as an escape response and can be instrumental for predator evasion, one of the major evolutionary forces which have selected for flight in insects in the first place [326]. With this in mind, it seems plausible that changes in either neuron number and/or innovations in ‘undead’ neuron structure could affect adult behaviour and be ultimately adaptive. Recently it has been shown that undead sensory neurons that are functional, integrate and appear to be tuned to specific odours [261]. Importantly, Prieto-Godino et al. [261] also show that there is cell number variation in this neuronal population across drosophilids and that blocking PCD in *melanogaster* results in the survival of mosquito-like CO₂-sensing neurons in the maxillary palps. This suggests that both the central and peripheral nervous system may use similar modes of early PCD to sculpt circuits during the evolution of true flies.

5.4.3 Cell death during neurogenesis is widespread across insects

Our data show that PCD is extensive and widespread during neurogenesis in the CNS of insects, from the primitive firebrats *Thermobia domestica*, to true flies *Drosophila melanogaster* and the swift lousefly *Crataerina pallida*.

We wondered whether alterations in cell death may have contributed to adaptations in the VNC of flightless dipterans and found that a greater extent of PCD in the MNB lineage may be responsible for abolishing the segment-specific difference in octopaminergic cell numbers

Chapter 5. Extensive and Diverse Patterns of Cell Death Sculpt Neural Networks in Insects

in the swift lousefly *Crataerina pallida* – which has lost flight and gained adaptations to a parasitic lifestyle [309–311, 313, 327, 328]. As octopaminergic neurons are involved in flight-related behaviours [213, 308, 329], we suggest that PCD has been co-opted in this lineage during the evolution of flightlessness in the swift louse. We believe that this PCD takes place early, in newly born neurons, as we have seen dying cells close to the MNB in all of our 20 pupae, from Day 4 to Day 23. Therefore, the decrease in octopaminergic cell number in the mesothoracic segment of swift louseflies is likely the result of increased hemilineage-specific PCD during evolution. Alternatively, an increase in the number of neurons in the non-flying prothorax and metathorax could lead to a uniform population size across thoracic segments in swift louseflies. This could be achieved either by additional MNB divisions, or by reduced PCD. If changes in MNB proliferation play a role remains to be determined.

5.4.4 Midline neurons show hemilineage-based variations in different species

The midline neurons within the VNC of insects have long been a source of interest because they are homologous across species, yet show a diversity in cell numbers correlated with body form and function [275, 289, 291]. For example, flying insects have greater numbers of midline octopaminergic neurons within segments that control wings [282, 283, 286–288, 306, 330–335], while grasshoppers have more GABAergic neurons in the metathoracic/abdominal ganglia, which receives auditory input [290, 291]. These two midline neuronal populations are derived from the same NB, the MNB, which buds off multiple GMCs, each dividing once to generate a GABAergic (A cell) and an octopaminergic (B cell) neuron. Both A and B neurons are generated in equal numbers but, in all cases, the numbers of GABAergic ('hemilineage A') and octopaminergic ('hemilineage B') neurons within one segment are never the same. The greater numbers of GABAergic cells within each segment has been shown in grasshoppers [283] and fruit flies [278] to be the result of removal by PCD of large numbers of cells from hemilineage B.

As suggested by our previous work, the 'hemilineage' emerges as a discrete developmental unit that shows common features of gene expression and function [104, 273, 275, 277, 278]. Therefore, we refer here to the PCD found in the MNB lineage of grasshoppers as 'hemilineage-specific PCD'. Following our observations of PCD during development in other insects, together with a vast body of knowledge on homology in insect nervous systems [336, 337], we suggest that variations in neural circuits between species is very likely set up by modifying hemilineages, with PCD playing a major role.

5.4.5 Hemilineage-specific reductions in fibre diameter in the bee lousefly

In the wingless bee lousefly *Braula coeca*, we found clear reductions in the thickness of fibre tracts in several hemilineage bundles which in *Drosophila* are associated with flight-related

behaviours [104]. It remains for us to determine if early PCD takes place in these specific bee lice lineages during development and causes the reduction in bundle diameter that we see in flight hemilineages. As with most parasitic insects, bee and swift louseflies are impossible to maintain in the laboratory in the absence of their hosts and procuring them is a challenge (e.g. bee louseflies are now only found on two islands in the UK, while collecting swift louseflies is restricted to the summer months due to *Apus apus* migrations). Nonetheless, our observations that PCD is widespread across insects complements our findings in bee louseflies, strongly suggesting that an extensive PCD in flight hemilineages may have accompanied the loss of flight during evolution. Interestingly, the reduction in fibre diameter we see in bee louseflies was not evident in swift louseflies. This difference is likely due to the more significant changes to body plan in bee louseflies, i.e. a complete loss of the flight apparatus during evolution. Swift louseflies however still maintain vestigial wings and halteres [313], whereas bee louseflies have a severely reduced thorax, completely lacking wings, halteres and flight muscles [338].

5.4.6 Conclusions

Here we have shown that undead neurons elaborate complex arborisations, express distinct transmitter identities and function. We find that ‘early’ PCD is widespread during the development of the CNS of insects from the primitive firebrats, to most derived true flies. Early cell death appears to be a specific subtype of PCD present across animals. Understanding how early PCD is specified across species should help us elucidate how nervous systems are built and evolve. Our exploration of homologous lineages in flightless dipterans shows that changes in body plan may accompany changes in the extent and pattern of PCD. As the evolutionary changes seen in neural networks ultimately result from heritable differences in developmental processes, our future endeavours will be directed towards elucidating how genetic programs are deployed to establish the pattern of PCD. The cellular leitmotif of hemilineage-based cell death, we present here, provides us with something tangible that we can search for. Thus, we suggest that viewing the evolution of insect nervous systems through the lens of the ‘hemilineage’ will be critical for understanding how development brings about adaptive changes in neural network motifs.

5.5 Materials and Methods

5.5.1 Key resources table

Reagent type (species) or resource	Designation	Source or reference	Identifiers	Additional information
Gene (<i>Drosophila melanogaster</i>)	worniu	FlyBase	FLYB: FBgn0001983	
Gene (<i>Drosophila melanogaster</i>)	TDC2	FlyBase	FLYB: FBgn0050446	
Gene (<i>Drosophila melanogaster</i>)	VGlut	FlyBase	FLYB: FBgn0031424	
Gene reagent (<i>Drosophila melanogaster</i>)	hid	FlyBase	FLYB: FBgn0003997	
Gene reagent (<i>Drosophila melanogaster</i>)	grim	FlyBase	FLYB: FBgn0015946	
Gene reagent (<i>Drosophila melanogaster</i>)	rpr	FlyBase	FLYB: FBgn0011706	
Gene reagent (<i>Drosophila melanogaster</i>)	skl	FlyBase	FLYB: FBgn0036786	
Gene reagent (<i>Drosophila melanogaster</i>)	Dronc	FlyBase	FLYB: FBgn0026404	
Gene reagent (<i>Drosophila melanogaster</i>)	Worniu-GAL4	Bloomington <i>Drosophila</i> Stock Center	BDSC:56553; FLYB:FBtp0021524; RRID:BDSC_56553	FlyBase symbol: Pwor.GAL4.A
Gene reagent (<i>Drosophila melanogaster</i>)	Tdc2-GAL4	Bloomington <i>Drosophila</i> Stock Center	BDSC:9313; FLYB:FBtp0127561; RRID:BDSC_9313	FlyBase symbol: PTdc2-GAL4.C
Gene reagent (<i>Drosophila melanogaster</i>)	OK371-GAL4	Bloomington <i>Drosophila</i> Stock Center	BDSC: 26160; FLYB:FBti0076967; RRID:BDSC_26160	FlyBase symbol: Dmel\PGawB VGlut ^{OK371}
Gene reagent (<i>Drosophila melanogaster</i>)	UAS-SR4VH	This paper		Fly line maintained in DW Williams lab; See Materials and methods, section 'Contstruction of UAS-SR4VH'
Gene reagent (<i>Drosophila melanogaster</i>)	UAS-CD8::GFP	Bloomington <i>Drosophila</i> Stock Center	BDSC:5137; FLYB:FBtp0002652; RRID:BDSC_5137	FlyBase symbol: PUAS-mCD8::GFPL
Gene reagent (<i>Drosophila melanogaster</i>)	UAS-tdTomato- p2A-GCaMP6s	[49]		Gift from MH Dickinson
Gene reagent (<i>Drosophila melanogaster</i>)	H99	Bloomington <i>Drosophila</i> Stock Center	BDSC:1576; FLYB:FBab0022359; RRID:BDSC_1576	FlyBase symbol: Df(3L)H99
Gene reagent (<i>Drosophila melanogaster</i>)	XR38	[303]	FLYB:FBab0027961	FlyBase symbol: Df(3L)XR38

5.5 Materials and Methods

Reagent type (species) or resource	Designation	Source or reference	Identifiers	Additional information
Gene reagent (<i>Drosophila melanogaster</i>)	dronc ^{ΔA8}	[305]	FLYB:FBal0244156	FlyBase symbol: Dronc ^{ΔA8}
Biological sample (<i>Crataerina pallida</i>)	Swift lousefly	Collected from Cambridgeshire and Suffolk, UK		Whole CNS or just VNC freshly dissected from <i>Crataerina pallida</i>
Biological sample (<i>Braula coeca</i>)	Bee lousefly	A. Abrahams, Isle of Colonsay, UK		VNC freshly dissected from <i>Braula coeca</i>
Biological sample (<i>Thermobia domestica</i>)	Firebrat	Buzzard Reptile and Aquatics (buzzardreptile.co.uk)		VNC freshly dissected from <i>Thermobia domestica</i>
Antibody	anti-GFP (Chicken polyclonal)	Abcam	Cat# ab13970, RRID:AB_300798	IF(1:500)
Antibody	anti-Neuroglian (Mouse monoclonal)	DSHB	Cat# BP 104, RRID:AB_528402	IF(1:50)
Antibody	anti-Cleaved <i>Drosophila</i> Dcp-1 (Rabbit polyclonal)	Cell Signaling Technology	Cat# 9578, RRID:AB_2721060	IF(1:100)
Antibody	anti-Syncrip (Guinea pig polyclonal)	Gift from I. Davis		IF(1:100)
Antibody	anti-Engrailed/Invected (Mouse monoclonal)	DSHB	Cat# 4D9, RRID:AB_528224	IF(1:2)
Antibody	anti-DVGLUT C-terminus (Rabbit polyclonal)	Gift from H. Aberle	Cat# AB-DVGLUT-C, RRID:AB_2490071	IF(1:5000)
Antibody	anti-tyramine β-hydroxylase (Rat monoclonal)	Gift from M. Monastirioti	Cat# Tyramine β-hydroxylase (TBH), RRID:AB_2315520	IF(1:50)
Antibody	anti-vestigial (Rabbit polyclonal)	Gift from S. Carroll and K. Gruss		IF(1:400)
Antibody	anti-GABA (Rabbit polyclonal)	ImmunoStar	Cat# 20094, RRID:AB_572234	IF(1:100)
Recombinant DNA reagent	pUAST (plasmid)	Brand and Perrimon, 1993		Insect expression, <i>Drosophila</i> ; See Materials and methods, section 'Construction of UAS-SR4VH'
Commercial assay or kit	Click-iT Edu Cell Proliferation Kit for Imaging	<i>life technologies</i>	Cat# C10337	
Commercial assay or kit	Click-iT Plus TUNEL Assay for In Situ Apoptosis Detection	<i>life technologies</i>	Cat# C10618	
Software, algorithm	Python Programming Language	Python Programming Language	RRID:SCR_008394	
Software, algorithm	MATLAB	MathWorks	RRID:SCR_001622	
Software, algorithm	SPSS	IBM	RRID:SCR_002865	
Software, algorithm	Fiji	Fiji	RRID:SCR_002285	
Other	DAPI	Sigma-Aldrich	Cat# D9542	(1 μg/mL)
Other	Phalloidin-488	<i>life technologies</i>	Cat# A12379	(1:100)

Chapter 5. Extensive and Diverse Patterns of Cell Death Sculpt Neural Networks in Insects

5.5.2 Animals

We used the following *Drosophila melanogaster* stocks: *Worniu-GAL4; Dr/TM3, Ubx-LacZ, Sb* (BDSC_56553), *TDC2-GAL4* (BDSC_9313), *OK371-GAL4* (BDSC_26160), *UAS-SR4VH* (described here), *UAS-CD8::GFP* (BDSC_5137), *UAS-tdTomato-p2A-GCaMP6s* [49] (kind gift from M. Dickinson), *H99/TM3, Sb* (BDSC_1576), *XR38/TM3* (Peterson et al., 2002), *Sb, If/CyO; dronc^{ΔA8}, FRT2A/TM6^β, Tb, Hu* [305] and *hs-flp;; TubP-GAL80, FRT2A/TM3, Sb* [278].

Firebrat adults of *Thermobia domestica* were obtained from Buzzard Reptile and Aquatics (<https://buzzardreptile.co.uk/buzzardreptile.co.uk>) and reared on a diet of fish flakes and wholemeal bran at 40°C in darkness inside a humid plastic container. A staging series was calculated by time to hatching.

Crataerina pallida swift lousefly adults were collected from swift (*Apus apus*) nesting boxes fitted behind the louvres of belfry windows from churches in Cambridgeshire and Suffolk (UK) with the help of local conservationists Simon Evans, Richard Newell and Bill Murrells. Swift louseflies were kept at 20°C on a 12 hr dark:12 hr light cycle until dissected. Pregnant females, recognised by their enlarged and translucent abdomen through which larvae or prepupae could be detected, were kept separately and checked daily for pupa ejection. The day in which a pupa was laid was defined as ‘Day 0’ of external development (outside the mother’s abdomen).

Braula coeca bee lousefly adults were obtained from a black bee (*Apis mellifera mellifera*) colony on the Isle of Colonsay, UK (kind gift from A. Abrahams). Bee louseflies were shipped by post in small cages containing worker bees feeding on bee fondant. The black bees and bee louseflies were anaesthetised by placing the cage on a CO₂ pad and the bee louseflies were removed for dissection.

5.5.3 Construction of UAS-SR4VH

SR4VH was constructed by standard molecular biology procedures. It comprises the myristylation signal of *Drosophila* Src64B (amino acids 1–95), a monomeric red fluorescent protein mRFP1 [339], a linker that contains four DEVD sites, a yellow fluorescent protein Venus [?], and a nuclear localisation signal of *Drosophila* histone H2B (amino acids 1–51). While the design is similar to the previously reported caspase probe Apoliner [299], the Src64B myristylation signal and the H2B NLS offers better membrane and nuclear localisation, respectively, and four DEVD sites are expected to provide higher sensitivity. The probe was cloned in pUAST [64] and introduced into the *Drosophila* genome by P element-mediated transformation.

5.5.4 Immunohistochemistry and chemical staining

Drosophila larvae were dissected in PBS without anaesthesia. Firebrat embryos were removed from their chorion and dissected using minuten pins. *Drosophila*, swift lousefly and bee lousefly adults were anaesthetised on ice, briefly submerged in absolute ethanol and dissected in PBS. Swift lousefly pupae were immobilised on double sided sticky tape, removed from their pupal case using forceps and dissected in PBS without anaesthesia. Samples were fixed in 3.6% paraformaldehyde in PBS for 30 min (larvae and pupae) or 1 hr (adults), washed 3 times in 0.3% PBST (0.3% Triton-X100 in PBS, Sigma-Aldrich), blocked in 5% goat serum (Sigma-Aldrich) in PBST for 1 hr and incubated with primary antibodies in block for 1–3 days at 4°C (*Drosophila*, bee louseflies, swift lousefly pupae), room temperature (firebrats) or 37°C to increase antibody penetration (swift lousefly adults; block supplemented with 0.02% NaN₃ to prevent microbial growth). Samples were then washed four times throughout the day in PBST and incubated with secondary antibodies in block for a further 1–3 days, followed by final washes in PBST and PBS. Brains and VNCs were mounted on poly-L-lysine-coated coverslip, dehydrated in increasing serial concentrations of ethanol (15%, 30%, 70%, 80%, 90% and twice in 100%) for 5 min each, dipped once in xylene, then incubated twice for 5 min in fresh xylene. A droplet of DePeX (EMS) was added on top of the mounted sample and the coverslip was placed face-down on a glass slide.

We used the following primary antibodies: chicken anti-GFP (1:500; ab13970, Abcam), mouse anti-Neuroglian (1:50; BP 104, Developmental Studies Hybridoma Bank), rabbit anti-cleaved *Drosophila* Dcp1 (1:100; 9578, Cell Signaling), guinea pig anti-Syncrip (1:100; kind gift from I. Davis; to label NBs and early progeny in lineages - JW Truman, personal communication, January 2019), mouse anti-Engrailed/Invected (1:2; 4D9, Developmental Studies Hybridoma Bank), rabbit anti-DVGLUT C-terminus [340] (1:5000; AB_2490071, kind gift from H. Aberle), rat anti-tyramine β -hydroxylase [314] (1:50; AB_2315520, kind gift from M. Monastirioti), rabbit anti-vestigial (1:400; kind gift from Sean Carroll and Kirsten Gruss) and rabbit anti-GABA (1:100; 20094, ImunoStar).

Secondary antibodies were Alexa Fluor 488-conjugated goat anti-chicken (1:500; A11039, Invitrogen, Thermo Fisher Scientific), Alexa Fluor 488-conjugated goat anti-rabbit (1:500; A11070, Invitrogen, Thermo Fisher Scientific), Cy3-conjugated donkey anti-rabbit (1:500; 711-006-152, Jackson ImmunoResearch), Cy5-conjugated donkey anti-mouse (1:500; 715-006-151, Jackson ImmunoResearch), Alexa Fluor 488-conjugated donkey anti-rat cross-adsorbed against mouse (1:100; 712-545-153, Jackson ImmunoResearch), Alexa Fluor 488-conjugated donkey anti-guinea pig (1:500; A11073, Invitrogen, Thermo Fisher Scientific).

In firebrat embryos we detected dying cells using the Click-iT Plus TUNEL assay kit (C10618, life technologies). To stain cell nuclei and neuropil, firebrat samples were incubated with DAPI (1 μ g/mL; D9542, Sigma-Aldrich) and Phalloidin-488 (1:100, A12379, life technologies)

Chapter 5. Extensive and Diverse Patterns of Cell Death Sculpt Neural Networks in Insects

in PBST for 30 min at room temperature. Incubations were carried out following secondary antibody treatment. Samples were then washed in PBST and PBS, and mounted.

5.5.5 EdU treatment

To label proliferating cells and their progeny we used the Click-iT EdU imaging Kit (C10337, *life technologies*). Freshly dissected nervous systems from swift lousefly pupae were incubated in EdU 1:1000 in PBS at room temperature for 1–3 hr on a shaker, rinsed with PBS and fixed in cold buffered formaldehyde 3.6% in PBS for 30 min. Samples were then stained using the immunohistochemistry protocol described above. The colour reaction for EdU was carried out as instructed by the vendor after the secondary antibodies were washed out.

5.5.6 Generation of undead neuron MARCM clones

To induce mitotic clones of undead neurons, rescued from PCD, we used the mosaic analysis with a repressible cell marker technique [341]. 0–4 hr first instar larvae resulting from crossing females of the genotype *hs-flp*; *TubP-GAL80*, *FRT2A/TM3*, *Sb* with; *TDC2-GAL4*, *UAS-CD8::GFP*, *UAS-TrpA1*; *dronc*^{ΔA8}, *FRT2A/TM6β*, *Tb*, *Hu* males were heat-shocked at 37°C in a plastic food vial placed in a water bath for either 1 hr or 45 min, followed by 45 min at room temperature and a second incubation period at 37°C for 30 min. After heat-shock, larvae were immediately returned to 23°C or 25°C. Cell death was blocked in clones homozygous for the loss-of-function allele of the initiator caspase *Dronc*. Because we used the octopaminergic driver line *TDC2-GAL4* to induce the expression of CD8::GFP and TrpA1, we were able to visualise and thermogenetically activate only postembryonic neurons of hemilineage 0B. A small number of wild-type octopaminergic neurons are born during postembryonic neurogenesis (one in T1 and T3, 4–5 in T2, see [Figure S5.2](#)). To ensure the characterisation of undead neurons only, MARCM clones including a bilaterally symmetrical primary neurite were excluded from analysis.

5.5.7 Thermogenetic activation and video recordings

Prior to recordings, 2–6 day-old males of *Drosophila melanogaster* (*hs-flp*+/+; *TDC2-GAL4*, *UAS-CD8::GFP*, *UAS-dTRPA1*+/+; *dronc*^{ΔA8}, *FRT2A/TubP-GAL80*, *FRT2A*) reared at 23°C or 25°C in a 12 hr:12 hr light:dark cycle were anaesthetised on ice and decapitated using a pair of micro spring scissors in under 3 min. We used males as we found they are more responsive to octopamine release by thermogenetic activation than females (data not shown). The headless flies were brushed back into a food vial placed on its side and left to recover for at least 1 hr. To generate the heat ramp required to thermogenetically activate undead neurons, we used a 12V thermoelectric Peltier plate (model: TEC1-12706, size: 40 mm x 40 mm x 3.6 mm) connected to a DC power supply (HY3005D, Rapid Electronics) set at a constant current of

0.46A, with a variable voltage, calibrated using an infrared laser thermometer (N92FX, Maplin). These settings generated a temperature ramp which lasted 70 s from 22°C to 34°C. Videos were recorded at 25 fps using a Sony NEX-5N digital camera (kindly provided by Ian Wynne) mounted to a stereo microscope. A piece of graph paper was used for spatial calibration. To match the presence of undead neurons with behaviour, each decapitated fly used for thermogenetic activation was indexed and prepared for dissection and immunostaining.

5.5.8 Two-photon calcium imaging in behaving intact flies

The method for in vivo two-photon imaging of the VNC in behaving adult *Drosophila* is described in Chen et al., 2018 [49]. Briefly, flies were anaesthetised through cooling and then mounted onto custom imaging stages. The dorsal thoracic cuticle was removed and indirect flight muscles were left to degrade over the course of 1 hr. Subsequently, the proventriculus and salivary glands were resected to gain optical access to the VNC.

Horizontal sections of the T1 leg ganglion were imaged using galvo-galvo scanning. For control animals, the bifurcation point of TDC-positive neurites were imaged to circumvent ROI disappearances caused by movement. For animals harbouring undead *TDC2-GAL4*-positive neurons, the thickest branch of the axonal bifurcation was chosen because they were most likely to contain undead neurites. Image dimensions ranged between 512×512 and 320×320 , resulting in 1.6 to 3.4 fps data acquisition. Imaging areas ranged between $92 \times 92 \mu\text{m}$ and $149 \times 149 \mu\text{m}$. Laser power was held at 8 mW.

5.5.9 Data analysis for 2-photon imaging in behaving *Drosophila*

Python scripts (modified from Chen et al., 2018 [49]) were used to extract ROI fluorescence traces and to compute spherical treadmill ball rotations. Walking epochs were determined by placing a threshold on ball rotations, which were first converted into anterior-posterior (v_{forward}) and medial-lateral (v_{side}) speeds (one rot $\text{s}^{-1} = 31.42 \text{ mm s}^{-1}$) and into degrees s^{-1} (1 rot $\text{s}^{-1} = 360^\circ \text{ s}^{-1}$) for yaw (v_{rotation}) movements. Thresholds were 0.12 mm, 0.12 mm and 5° , respectively. Periods below these thresholds were considered ‘resting’ while other periods were considered ‘walking’. Fluorescence traces for epochs with the same behaviour were aligned by start point to compute average $\% \Delta R/R$ traces for specific actions.

To calculate fluorescence traces for small subregions-of-interest across neuritic bundles containing both undead and wild-type neurites, images were registered using an optic flow method described in Chen et al., 2018 [49]. This registration served to minimise motion artefacts. Analysis was limited to a period with no warping artefacts and no ROI disappearance. Subregions were manually selected as small circular ROIs across the neuritic bundle of the registered image. Fluorescence values were then computed from each sub-ROI.

5.5.10 Confocal imaging and image processing

Images were acquired using a Zeiss LSM 510 or a Zeiss LSM 800 confocal microscope at a magnification of 20x or 40x with optical sections taken at 1 μm intervals. The resulting images were examined and processed using Fiji (<https://imagej.net/Fiji>). Some images were manually cropped using the Freehand Selection tool to remove debris or to cut out neuronal lineages in *Worniu-GAL4*, *UAS-SR4VH* samples.

5.5.11 Fluorescence intensity plots

To generate fluorescence intensity along Line plots, we used the Plot Profile tool in Fiji to extract raw fluorescence intensity values for the RFP and Venus channels. The values were imported into MATLAB (R2018a, MathWorks) and normalised by dividing all fluorescence intensity values to the maximum value encountered along each Line. In this manner, all fluorescence intensity along Line plots have a common scale from 0 to 1, with one being the highest value encountered along that Line.

5.5.12 Analysis of thermogenetic activation

Decapitated flies were considered to be walking if they covered a distance greater than one body length and moved their legs in a coordinated sequence from T3 to T2 to T1 at least once on each side [104]. Forward, backward and sideway movements were all interpreted as walking when both aforementioned conditions were respected. To generate fly body traces video recordings were imported in MATLAB (R2018a, MathWorks) and the centroid of the decapitated fly (located on the scutellum) was extracted from each frame using a custom-written script which can be found at github.com/sznznp/undead-walking (Pop, 2020 [342]; copy archived at <https://github.com/elifesciences-publications/undead-walking>). Each frame was converted into a greyscale image, its contrast enhanced using contrast-limited adaptive histogram equalisation, filtered using a Gaussian smoothing kernel with a standard deviation of 4, binarised using a custom threshold and the geometric centre of the fly body automatically extracted and stored in an array. To confirm that the centroid detection was accurate, a red dot with the centroid coordinates was superimposed onto each frame of the original recording and the annotated movie was saved for manual inspection.

5.5.13 Quantification of 3A/3B bundle diameters

For calculating 3A/3B hemilineage bundle diameter ratios in fruit flies and bee louseflies, we generated transverse rendered maximum intensity projections of inverted greyscale confocal stacks for the pro- and mesothorax (T1 and T2) and frontal projections for the metathorax (T3). Optical sections were selected to include the common lineage bundle and the individual

hemilineage bundles after their split. Diameter measurements were taken at the widest point within 5 μm of the bundle split using the Straight Line tool in Fiji and ratios were calculated by dividing the diameter of hemilineage 3A to that of 3B.

5.5.14 Statistical analysis

For comparing neuron numbers, 3A/3B bundle diameter and T2/T1 number of neurons, data were tested for normal distribution using the Kolmogorov-Smirnov test and visualisation of Normal Q-Q plots. Differences between groups were analysed using either the independent samples t-test for normally distributed data, Welch's test if data failed to meet the homogeneity of variances assumption or Mann-Whitney t-tests if data failed to meet the normality and homogeneity of variances assumptions of the independent samples t-test.

For comparing the number of flies which walked in each experimental group, we performed a Pearson chi-squared test and interpreted the resulting exact significance if the minimum expected count was greater than 5, or the Fisher's Exact Test 2-sided significance if the minimum expected count was lower than five in at least one cell of the contingency table. To correct for multiple comparisons we performed a Bonferroni correction (i.e. p values were multiplied by 6, the total number of pairwise tests).

All statistical tests were performed in SPSS Statistics 23 (IBM) with an α set at 0.05. In all figures, bars represent means \pm standard deviation; * $p < 0.05$, *** $p < 0.001$, ^{ns} $p =$ not significant.

5.6 Data availability

All data generated or analysed during this study are included in the manuscript and supporting figures.

Figure 7—source data 1 Quantification of T2/T1 number of octopaminergic neurons in fruit flies and swift louseflies.

<https://cdn.elifesciences.org/articles/59566/elifesciences-59566-fig7-data1-v3.xlsx>

[Download elifesciences-59566-fig7-data1-v3.xlsx](#)

Figure 9—source data 1 Quantifications of 3A/3B hemilineage bundle diameter ratios in fruit flies and bee louseflies.

<https://cdn.elifesciences.org/articles/59566/elifesciences-59566-fig9-data1-v3.xlsx>

[Download elifesciences-59566-fig9-data1-v3.xlsx](#)

5.7 Acknowledgments

We would like to thank Richard Benton and Lucia Prieto-Godino for discussions and sharing data. We thank Kristin White and Bloomington *Drosophila* Stock Center (NIH P40OD018537) for sharing flies; Maria Monastirioti, Hermann Aberle, Ilan Davis, Kirsten Gruss, Sean Carroll and Developmental Studies Hybridoma Bank (NICHD of the NIH, University of Iowa) for antibodies. We are indebted to Simon Evans, Richard Newell and Bill Murrells for their kind help in collecting swift lice and Andrew Abrams for sending us bee lice. We are grateful to Andrew M Dacks and Hans-Joachim Pflüger for providing unpublished data on *Manduca* octopaminergic neurons. We would like to thank Ian Wynne for his camera. We also thank Matthias Landgraf, David Shepherd, Jon Clarke and Sanjay Sane for reading the manuscript. Funding: Williams: BBSRC BB/P025552/1 and BB/L022672/1. Ramdya: SNSF Project Grant: 175667; Eccellenza Grant: 181239; R'Equip Grant: 177102.

5.8 Author contributions

Sinziana Pop - Conceptualization, Resources, Data curation, Software, Validation, Investigation, Visualization, Methodology, Writing - original draft, Writing - review and editing

Chin-Lin Chen - Resources, Investigation, Visualization, Methodology, Writing - review and editing

Connor J Sproston - Resources, Investigation, Visualization, Methodology, Writing - review and editing

Shu Kondo - Resources, Validation, Methodology, Writing - review and editing

Pavan Ramdya - Resources, Supervision, Funding acquisition, Visualization, Methodology, Writing - review and editing

Darren W Williams - Conceptualization, Resources, Data curation, Supervision, Funding acquisition, Investigation, Visualization, Methodology, Writing - original draft, Project administration, Writing - review and editing

5.9 Declaration of Interests

The authors declare no competing interests.

5.10 Supplementary Information

5.10.1 Supplementary Figures

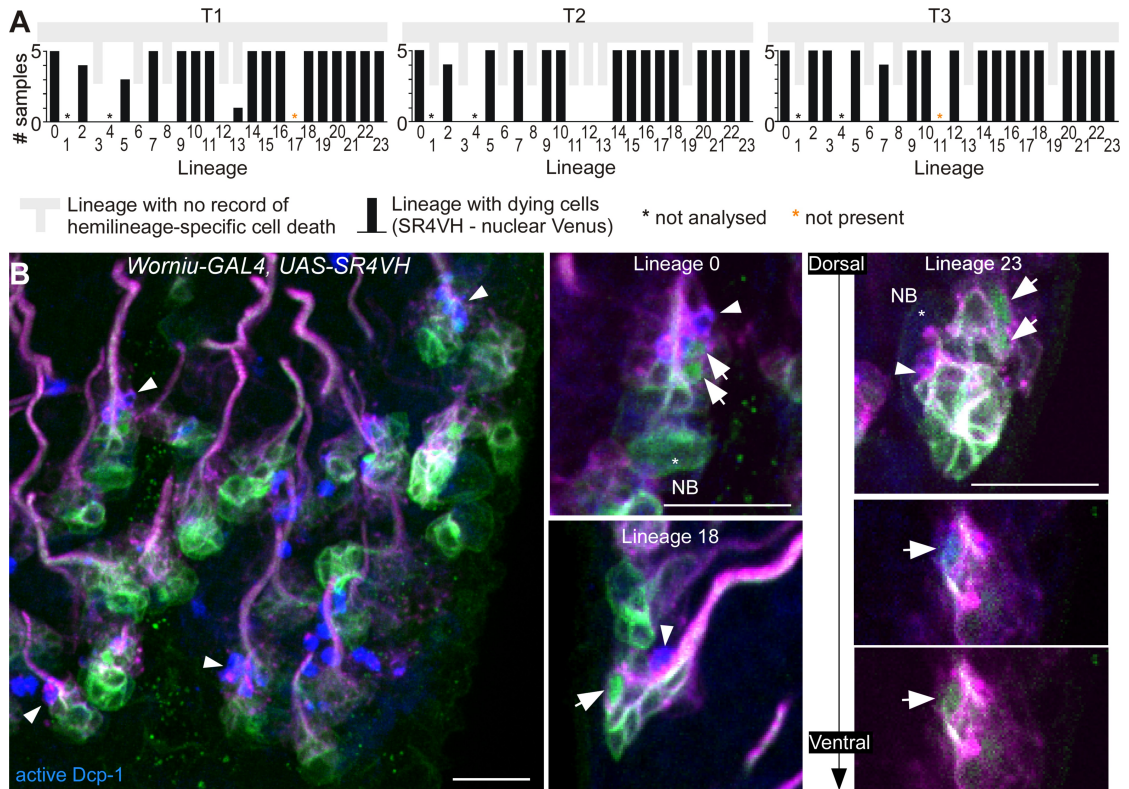


Figure S5.1: **SR4VH reveals successive stages of cell death in lineages with doomed hemilineages.** (A) Quantification of lineages with dying cells as reported with SR4VH in each thoracic segment from 5 wandering 3rd instar larvae. Back bars represent the number of samples in which dying cells were encountered in at least one hemisegment for that lineage. Grey bars represent lineages with no record of hemilineage-specific cell death as reported in Truman et al., 2010 [278]. (B) Antibodies for active Dcp-1 label cells located close to the lineage bundle in doomed lineages from larvae expressing SR4VH driven by *Worniu-GAL4*. Right panels show examples of doomed lineages 0, 18 and 23 containing cells at subsequent stages of cell death. White arrows indicate: nuclear Venus without cleaved Dcp-1 (early stage), Venus and Dcp-1 colocalisation (mid-stage) and pyknotic cell-/dead cell membranes with RFP and cleaved Dcp-1 (late-stage). Scale bars, 10 μ m. n = 7.

Chapter 5. Extensive and Diverse Patterns of Cell Death Sculpt Neural Networks in Insects

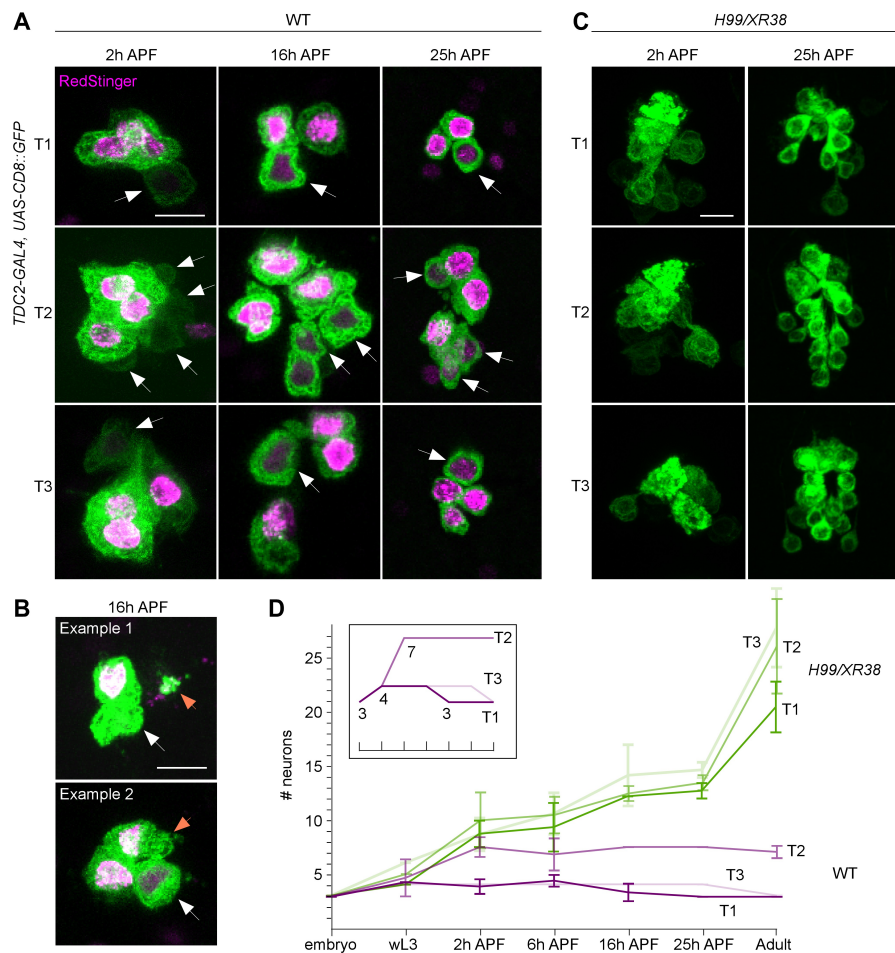


Figure S5.2: Postembryonic development of lineage 0B in wild-type and H99/XR38 flies. (A) CD8::GFP expression driven by *TDC2-GAL4* in octopaminergic neurons from hemilineage 0B in the VNC of wild-type flies in T1 (1st row), T2 (2nd row) and T3 (3rd row) during pupal development at 2 hr after puparium formation (2 hr APF, 1st column), 16 hr APF (2nd column) and 25 hAPF (3rd column). One embryonically born cell is replaced during postembryonic neurogenesis in T1 and T2, while roughly four postembryonic octopaminergic neurons are added in T2. White arrows indicate newly born neurons with faint GFP and no RedStinger visible at 2h APF (arrows). RedStinger fluorescence becomes visible at 16-25h APF, as the protein matures (arrows). Scale bar, 10 μ m. (B) Accumulations of GFP and RedStinger (orange arrow) in the proximity of the prothoracic cell cluster, alongside the presence of one cell with dim RedStinger fluorescence (white arrow) suggest one embryonic cell has died at 16hAPF. Scale bar, 10 μ m. (C) CD8::GFP expression driven by *TDC2-GAL4* in octopaminergic neurons from hemilineage 0B in the VNC of H99/XR38 flies in T1 (1st row), T2 (2nd row) and T3 (3rd row) during pupal development at 2 hr APF (1st column) and 25 hr APF (2nd column). Not all undead neurons present in the adult have matured by 25 hr APF. Scale bar, 10 μ m. (D) Graphical representation of the number of *TDC2-GAL4*-expressing neurons throughout development in wild-type (magenta) and H99/XR38 mutant flies (green), where X represents time and Y represents the number of cells. Individual lines in the graph depict cell numbers in different thoracic segments. Error bars represent standard deviation. The inset represents a compressed

idealised graphical representation for wild-type flies; marks on the X axis are the same; numbers at branch points represent cell numbers. In wild-type flies both T1 and T3 acquire an additional cell at 2 hr APF and lose one by the end of metamorphosis (magenta). Roughly half of undead neurons are present at 25 hAPF, with the other half maturing by the end of metamorphosis (green). **Comment on Figure S5.2:** The implication of additional postembryonic octopaminergic neurons born in the in the wild-type larva. It is well known that there are 3–4 extra octopaminergic neurons generated postembryonically in the wing bearing second (T2) thoracic neuromere in adult flies compared to the 3 cells found in each thoracic segment in larvae [306]. Until our inquiry into the timeline of postembryonic neurogenesis, it was thought that all octopaminergic neurons born in the embryo persist into adulthood, but to our surprise, that is not the case. We noticed that one postembryonic octopaminergic cell is born in wild-type flies in both the first (T1) and third (T3) thoracic segments, bringing the total number of cells to 4 (Figure S5.2A,D). Instead, the total number of 3 cells per cluster in T1 and T3 in adult flies is achieved via *hormonally gated metamorphic cell death of an embryonically born mature neuron* at larval-pupal stages (Figure S5.2A,B,D). We have shown here for the first time that wild-type octopaminergic neurons are produced in lineage 0 in all three thoracic neuromeres during postembryonic neurogenesis. This fits well with our observations that some *Dronc*-null singleton clones generated using MARCM showed bilateral symmetry. As the majority of these were in the mesothorax (see also Figure Figure S5.4A,D), where it is more likely to label wild-type neurons purely by chance (with up to four postembryonic neurons produced here and only one each in T1 and T3), we think these may be indeed wild-type. Furthermore, we only ever encountered mixed MARCM clones containing one bilaterally symmetric and several turning neurites in the mesothorax (see also Figure S5.4A,D). For behavioural experiments we excluded all MARCM *Dronc* clones with bifurcating neurons to ensure that we only interpreted the activity of undead neurons.

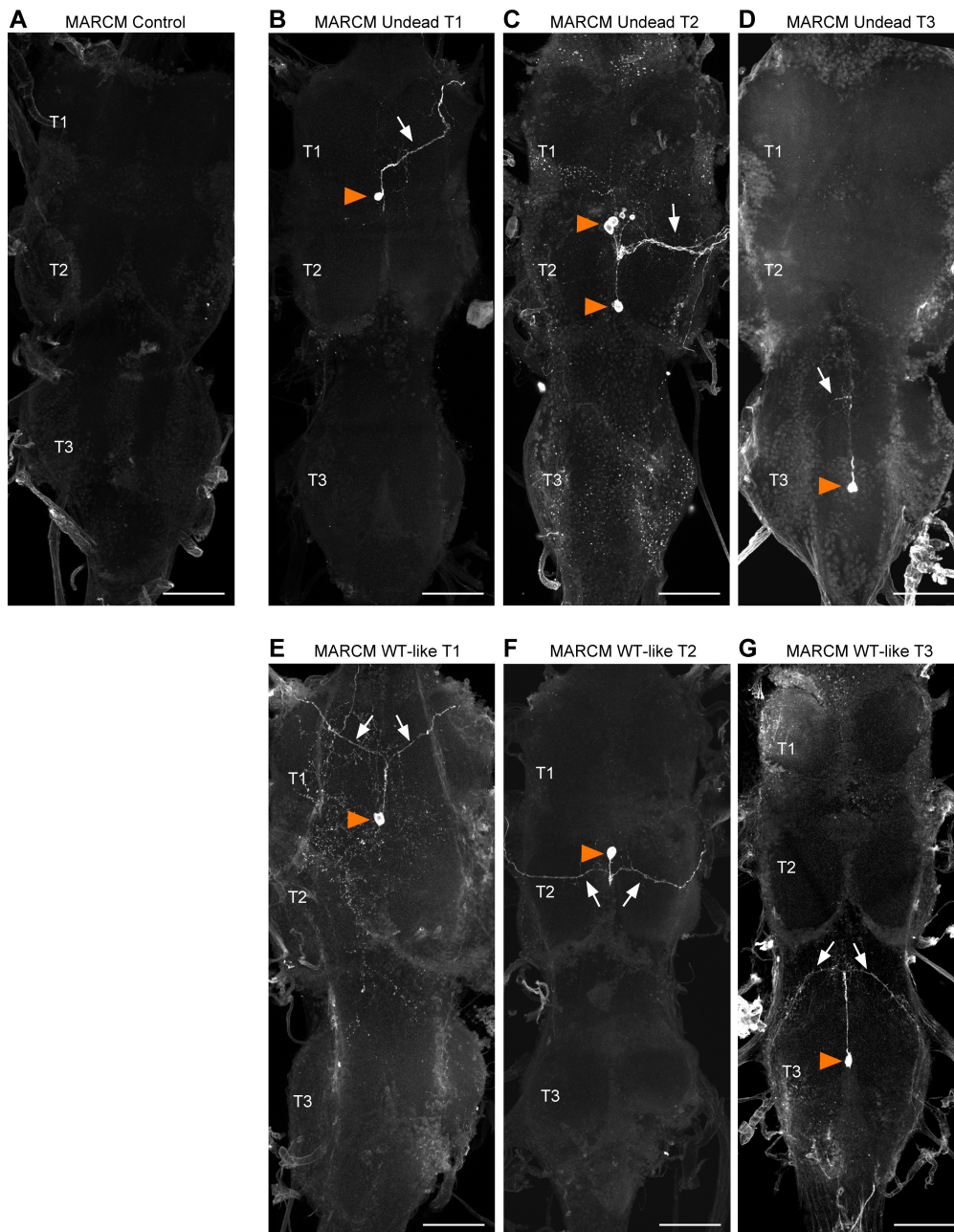


Figure S5.3: **Examples of postembryonic MARCM clones in which cell death is blocked.** (A–G) Ventral nerve cords from flies bearing MARCM clones homozygous for the loss-of-function allele *dronc*^{ΔA8} (in which PCD is blocked); full genotype: *+/+; TDC2-GAL4, UAS-TrpA1, UAS-CD8::GFP / +; dronc*^{ΔA8}/*dronc*^{ΔA8}. (A) MARCM control fly lacking postembryonic clones. (B–D) Undead MARCM clones in the prothorax (B), mesothorax (C) and metathorax (D) with somas located ventrally at the midline (orange arrowhead) and a turning primary neurite (arrow). (E–G) MARCM clones with a wild-type morphology in the prothorax (E), mesothorax (F) and metathorax (G) with somas located ventrally at the midline (orange arrowhead) and a bifurcating primary neurite (arrows). Flies containing undead MARCM clones with a wild-type morphology were excluded from behavioural analysis. Scale bars, 50 μm.

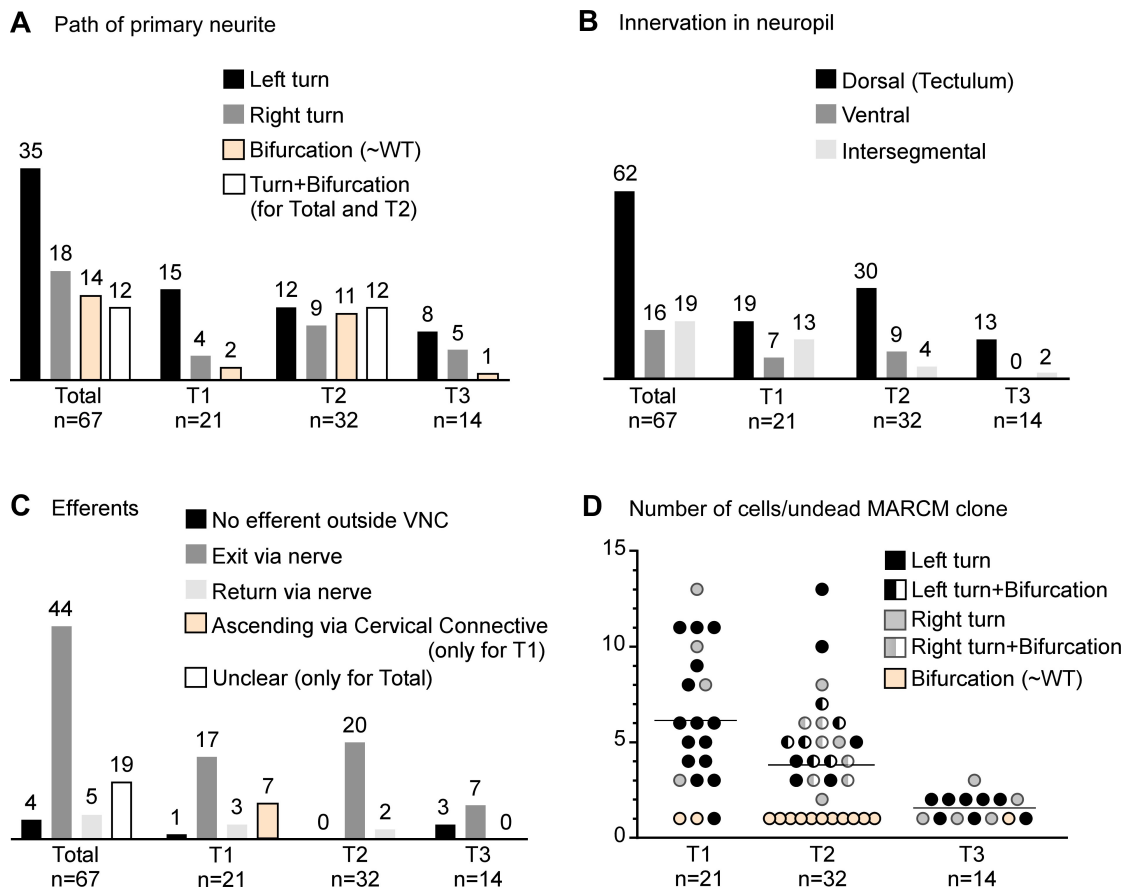


Figure S5.4: Quantification of undead neuron morphology. (A) Quantification of the primary neurite path. Most undead neurons arborise to the left. (B) Quantification of neuropil innervation. Most undead neurons branched extensively in the dorsal neuropil. Undead neurons in T3 never innervated the ventral neuropil. Few undead neurons from each thoracic segment projected neurites into adjacent segments. (C) Quantification of efferent neurites. Most undead neurons joined a thoracic nerve heading towards the periphery. Some undead neurons in T1 sent branches through the cervical connective. (D) Quantification of the number of undead neurons in MARCM clones for each thoracic segment colour-coded by primary neurite path. The number of undead neurons varied across MARCM clones, with up to 13 in T1 and T2 and up to three in T3. Most single-celled MARCM clones contained undead neurons with a wild-type morphology (beige circles) and most undead neurons with a wild-type morphology were encountered in T2. Mixed clones (half-filled circles) made up of one bifurcating neuron and several neurons turning either left or right were encountered only in T2.

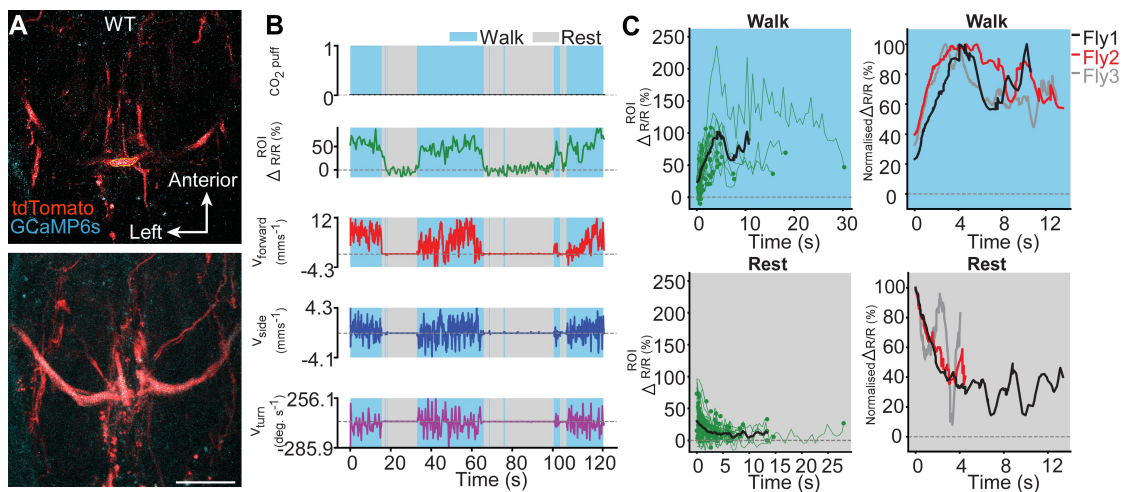


Figure S5.5: **Wild-type octopaminergic neurons are active during walking in intact adult *Drosophila*.** (A) Raw 2-photon image of *TDC2-GAL4*-positive neurons co-expressing tdTomato (red) and GCaMP6s (cyan) in wild-type flies (top). Region-of-interest used to calculate $\% \Delta R/R$ is outlined (yellow). Standard deviation z-projection of a dorsal-ventral image stack of the functional imaging region-of-interest in (B) (bottom). Scale bar, $50 \mu\text{m}$. (B) Representative behavioural and functional imaging data in wild-type flies. Shown are: CO_2 stimulation (black, no stimulation), $\% \Delta R/R$ (ratio of GCaMP6s/tdTomato) signal (green), and ball rotations indicating forward walking (red), sideways walking (blue) and turning (purple). The behaviour of the fly was classified as either walking (light blue), or resting (grey) by applying a threshold on ball rotation speed. (C) (left) Individual (green) and average (black) $\% \Delta R/R$ traces within each behavioural epoch for walking ($n = 77$) and resting ($n = 80$) events processed from 720 s of imaging data. Solid green circles indicate the end of a behavioural epoch. The average trace (black line) was calculated for only periods with four or more traces. (right) Normalised average $\% \Delta R/R$ traces for three different flies during walking and resting. The average (black) trace is the same as in the left panel.

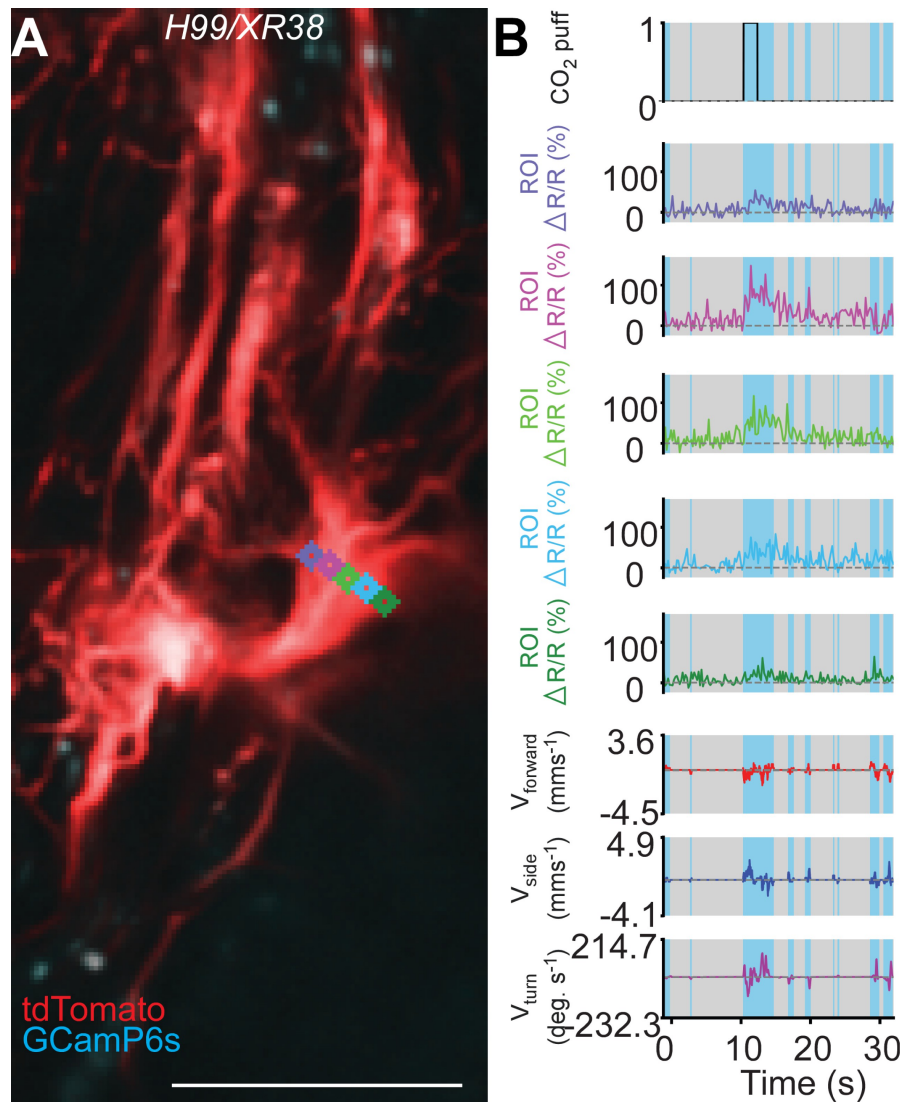


Figure S5.6: **Subregion analysis of calcium signals along the width of a primary neurite in a H99/XR38 animal.** (A) Time-averaged projection of the imaging plane for *TDC2-GAL4*-positive neurons co-expressing tdTomato (red) and GCaMP6s (cyan) in a *H99/XR38* animal. Regions-of-interest used to calculate % $\Delta R/R$ (colour-coded) are overlaid on top of time-projected and optic flow registered 2-photon images. Scale bar, 50 μm . (B) Representative behavioural and functional imaging data for this animal. Shown are: CO₂ stimulation (black), % $\Delta R/R$ (ratio of GCaMP6s/tdTomato) signal (colour-coded for each ROI as in panel a) and ball rotations indicating forward walking (red), side-ways walking (blue) and turning (purple). The behaviour of the fly was classified as either walking (light blue), or resting (grey) by applying a threshold on ball rotation speed.

5.10.2 Supplement Videos

Video S5.1: **Video recordings of control and ‘undead’ decapitated flies during thermogenetic activation.** Examples from each behavioural category showing responses to heat-activation in negative control (**top left**), positive control (**top right**), MARCM control (**bottom left**) and undead neurons (**bottom right**). MARCM control and undead neuron animals were used for extracting the centroid trace provided in **Figure 5.4B,C**. The increase in temperature is displayed in the bottom right corner. Frames represent recordings from 30 to 70 s.

[Download Video S5.1](#)

Video S5.2: **Recording of 2-photon calcium imaging in undead neurons.** Synchronised front and side camera behaviour videography (**bottom right**), and 2-photon imaging data (**top right**) used for the data analysis provided in **Figure 5.5C-E**.

[Download Video S5.2](#)

Video S5.3: **Z-stack of the imaging area for GCaMP6s activity in undead neurons.** A videography showing the imaging plane at different depths of the prothoracic segment corresponding to **Figure 5.5C**. The thicker left branch likely includes mostly undead neurons.

[Download Video S5.3](#)

Video S5.4: **Subregion neuronal activity patterns during walking.** Imaging data used for analysis in **Figure S5.6**. Shown are $\% \Delta R/R$ traces for R.

[Download Video S5.4](#)

6 Conclusion and perspectives

This work overcomes the long-standing difficulty of obtaining optical access to the VNC of a fly from the dorsal thorax while preserving limb movement, as described in [chapter 2](#). Thus, this herein-developed tool allows us to investigate the roots of behavioral control via visualization of the neural mechanism in the motor center housed in the VNC. In several examples, we demonstrated the ability of this VNC imaging technique to validate hypotheses derived from other experiments. For instance, we investigated previous work on the manipulation of neuronal excitability in [chapter 4](#) and [chapter 5](#), where we showed here that both serotonergic and octopaminergic VNC neurons activate during walking, but artificial excitation of both types of neurons actually cause the opposite effect on fly mobility ([Figure 4.2](#), [Figure 5.4](#)). Nevertheless, the contradictory results are exciting and promote a more comprehensive examination of our previous assumptions. With additional measurements of gait pattern and leg coordination, we concluded that serotonergic neurons in the VNC play roles in coordinating leg movement and preventing impulsive movement ([Figure 4.3](#), [Figure 4.4](#)). Conversely, octopaminergic neurons are more likely to initiate locomotion ([Figure 5.4](#), [Figure 5.5](#)). Hence, our VNC imaging technique serves as an indispensable tool to unravel the specific functions of the VNC neurons that ultimately give rise to behavior.

Beyond the local VNC circuit, we show that our VNC imaging technique can interrogate the information exchange that occurs between the brain and the VNC in behavioral control. Here, we demonstrated that interference from local neurons can be avoided with a focus on the axons within the cervical connective, which allows the exclusive recording of brain- or VNC-projecting neurons ([Figure 2.3](#), [Figure 2.4](#), [chapter 3](#)). Until the initial publication of our herein-presented tools in Chen et al., 2018 [49], the function of ANs for behavior control remained largely unclear. Therefore, we performed a large-scale investigation to obtain a more systemic overview of the correlation between AN activity and the subsequent behavior. This involved a focus on the role of the ascending pathway in behavioral control systems where we sought to understand to what extent the information is conveyed to the brain. Our screen results indicate that rather than conveying information such as primary joint angles as

redundant copies of what the SNs encode, ANs encode (i) self-motion states that tell whether the animal is behaving or resting and (ii) different types of ongoing behavior. Additionally, the behavioral state encoded by ANs seems to fit in a hierarchical structure. First, it differentiates whether the animal is moving or not by resting-ANs. Next, the movement is further divided along a spectrum from coarse to specific types of behavior. For example, the general foreleg movement can be further divided into specific type of motion such as eye grooming encoded by a eye grooming-ANs ([Figure 3.6](#)).

Specifically, ANs send information about the self-motion state and type of action states to the multi-sensory hub and action selection center in the brain, respectively. This finding is consistent with the idea of a subsumption structure [48], which uses the state of a robot to determine the next action command [48]. Therefore, understanding the nervous system and how it controls the behavioral state can inspire improvements to robotic control systems [48]. For example, to distinguish the cause of sensory input from self-movement or external stimuli of a robot, a module acting like the resting-ANs tell the brain whether the body is moving or resting can be interesting to be implemented to contextualize the sensory inputs; the ongoing robot behavior can be categorized as the encoded body state by ANs during different types of behavior likely to help assess the current circumstances and optimize the choice of next command.

In summary, our VNC imaging technique can explore the function of different types of VNC neurons in controlling behavior and can validate the outcome of neural network manipulation. To expand studies into the ascending system, future work can start from the resource of AN driver lines and functional screen results to detail which types of neurons correspond to different behaviors. Though this seems like a divergent exploration, it can be reduced by focusing on functional module integration into a low-dimensional representation of the body state in ANs for brain-VNC communication. With guidance from the brain and VNC connectome database [343], our technique and presented results can help constructing a functional map of VNC by visualizing neural dynamics in behavioral control in the VNC at the cellular level.

6.1 A plausible parallel system for efficiently interpreting body state

The high-level behavioral state encoded by ANs is the general representation of ongoing body movement instead of precise information from body compartments, such as joint angles and muscle tension. While seemingly vague, this lack of fine detail in no way makes such information trivial. Instead, it may serve to make the entire information processing system more efficient through its reconstruction of a parallel system to simultaneously inform the brain of high- and low-level body states. In the context of this architecture, the information load required to process and summarize the overwhelming signals received from each sensory neuron is shared by the motor system in the VNC, freeing up computational resources in

the brain. In other words, the VNC implements a natural behavioral classifier to help the brain interpret sensory signals in the context of an additional body-state reference for further sensory feature contextualization and action selection.

Findings from this work are consistent with the idea of the distributed system of behavioral information processing. For example, resting-ANs can differentiate between fly rest or movement but cannot inform the brain about leg position during rest. Hence, we propose that information about joint angles or muscle tension sensed by proprioceptors must be sent to the brain together with resting-state information encoded by ANs to form the complete picture of "the pose during rest". The same interpretation can also be applied to eye grooming behavior, which would likely require both eye-grooming-ANs and tactile sensors to inform the brain of the contact location between legs and eyes. In addition, primary sensory neurons also project axon terminals in the VNC [17], suggesting that ANs can classify their signals into a higher-level representation of body state—behavioral state.

6.2 The role of VNC neurons in neural dynamics

Improving our understanding of how a signal is computed through a neural network can inspire technological advances in neuro-inspired applications [344, 345]. This means that new findings at the circuit level can be emulated in-silico and implemented in various applications. For instance, corollary discharge has been reported to prevent confusion between self-motion-induced sensory input and an external stimulus and is one of the well-understood neural mechanisms for adaptive behavior control within the ascending structure of the motor system. For example, the motor neurons that propel a nematode to move forward also inhibit head sensory neurons [25]; a motor circuit that triggers cricket chirping simultaneously inhibits the auditory neurons via a type of ANs [26]. Overall, these findings can help us improve artificial feedback systems to help the robot integrate the input signals from different sensors.

Additionally, we can ask what role ANs or other local VNC neurons play at the circuit level. Since it has been reported that Moonwalk Ascending Neurons (MAN) helps maintain the duration of backward walking, MAN likely stabilizes the CPG activity to continue the action cycle. Along the same lines, eye-grooming-ANs, rest-ANs, and walk-ANs presented here might also use such a function to maintain ongoing behavior until the next descending command is received because they all develop local axon terminals to compute local information in the VNC (Figure 3.4E,F, Figure 3.5F,G, Figure 3.6K,I). For example, when a fly is posing, a precise muscle tension must be dynamically maintained to resist the natural force of muscle-skeletal mechanics that constantly pull the limbs toward the body. Based on the resting-AN morphology, the neural mechanism can be hypothesized to monitor muscle tone via dendrites that arborize the six leg neuropils and output the command signal for instantaneously applying the precise muscle force via axon terminals in each leg. Hence, this system maintains the muscle tone of a static pose by monitoring the change of muscle tension and then providing

updated feedback to maintain the pose, similar to how "voltage-clamp mode" functions in the patch-clamp technique [346].

Furthermore, both 5HT^{VNC} neurons and puff-ANs of the SS36112 line might be involved in the startle response, since they activate when confronted with a sudden stimulus. We also found PE-ANs might use the recurrent network to filter out sparse PE events to ensure that only deep rest-state-encoding PE trains are encoded (Figure 3.7). Finally, local modulatory neurons, such as octopaminergic neurons, might modulate the weighting of nodes to switch between behaviors.

6.3 Limitations

The nature of acquired data can affect the analysis strategy and how much information can be extracted from the dataset. One factor limiting the temporal details in our data is the temporal resolution, which is determined by the sampling rate or the dynamics of the reporter. The calcium indicators used in this study, OpGCaMP6f or GCaMP6s, usually have slow dynamics in the rising and decay phase compared to the action potential [68]. An additional limitation to our study is the SNR, which is lower and fluctuates more than the electrophysiology recordings. Based on these factors, some information might not be visible to us when using calcium indicators. For example, if the neurons fire sparsely, such as one to two action potentials responding to the ongoing behavior, the calcium signal would be buried within the noise and not detectable. This might explain the silent neurons in the AN functional screen (Table S3.1). Thus, alternative approaches such as voltage indicators or electrophysiological techniques can be applied to check for neurons encoding behavior via sparse firing.

Also, it is common in a large-scale study to question whether the sampled data is representative, and it is especially difficult to judge a fair sampling when dealing with a population of unknown distribution. Therefore, the conclusion drawn in chapter 3 might be suspect if the sampled AN is biased toward certain types of neurons. However, it is challenging to evaluate just how biased the conclusion is before the entire AN population is discovered. For instance, we should consider whether the convergence of brain projection to the GNG and the AVLP results from ANs of a close genetic background.

Nevertheless, two aspects can be examined to exclude some possibility of bias. First, the overlapping level of genetic background between each AN can be evaluated. If their genetic background overlaps significantly, the conclusion is more likely to be biased. By checking the promoters of AD and DBD among the 50 lines shown in the matrices, two AN lines share VT060737-AD, and three AN-lines share VT063643-AD, while three groups each containing two AN-lines share VT028606-DBD, VT033054-DBD, and VT050658-DBD. Among these promoter-sharing lines, PE-ANs of SS30303 and SS25451 lines are redundant to the SS31232 line, which share VT063643-AD. The turn-ANs of the SS29893 line are redundant to the SS34574 line,

which both share VT050658-DBD. Thus, after excluding these with identical labelling ANs, there are eight lines with overlapping genetic backgrounds among the 50 lines. So, we estimate a maximum of around 16% of ANs in the screen experiments partially share the same genetic background.

Second, the innervation of those silent ANs can also be quantified to exclude the possibility that the convergence of projection results from a limited selection of driver lines. If these ANs also show a general projection pattern, the current conclusion should remain plausible. Additionally, the two-photon imaging relies on good SNR, which might cause bias because this includes only lines of strongly expressed promoters. Therefore, the additional use of alternative recording techniques can reduce the bias.

Overall, some potential bias factors can be removed by additional analysis or other experiments. However, they are still limited by our current inability to ensure the population is well sampled, which can only be reduced when we are aware of the entire population of ANs.

6.4 Future works

6.4.1 Scientific part

In this work, we introduced a novel preparation for imaging the VNC in a behaving fly and demonstrated how it could improve studies of the neural mechanism of behavior control. Additionally, the findings about AN behavioral encoding provide genetic resources and implications that can be directly applied to follow-up studies. Thus, any hypothesized model involving local VNC neurons or ANs for behavior control, as presented above, can be tested using existing tools for functional investigation [49, 347] and a shared connectomic resource [343].

Knowing the causal relationship between neural activity and behavior is one of the essential pieces of information for understanding how the neural network operates. However, such information is missing in [chapter 3](#), which is mainly a correlation-based analysis. Therefore, the conclusion that ANs function is to "report" must be considered with appropriate moderation. To obtain the required evidence of a causal relationship, it would be possible to artificially manipulate the excitability of neurons and check the subsequent effect, which is a common approach. Conventionally, tools such as optogenetics [348, 349] and thermogenetics [350] are frequently used to manipulate the neural activity of interest while recording and quantifying the consequent effect on behavior. Since ANs are assumed to report the body state to the brain during behavior, they are not expected to induce any behavior. However, such an assumption may be contradictory to the motor control model, which is hypothesized as a loop ([Figure 1.1](#)). One possibility that might explain why ANs cannot trigger behavior is that artificial activation of an AN that encodes another state may not be strong enough to break the ongoing activity that is formed in the loop of the current state. Thus, the additional ascending information is

blocked or filtered when integrating within the brain circuit. This hypothesis is consistent with the current finding in backward walking, where the MAN cannot induce backward walking, but instead helps maintain the duration [28]. Therefore, if the ANs are artificially silenced [351], the corresponding behavior is expected to be shorter and more fragmented.

Among the ANs found for behavioral encoding, the PE-ANs that display distinct dynamics seem worthy of further investigation. Two questions can be asked to elucidate what and how these ANs encode. First, do they encode the internal state or the motion of the proboscis? Second, what is the neural mechanism that generates ramping activity? The PE train observed in this study might be just a phenotype of an internal state, but our correlation analysis cannot distinguish whether PE-ANs encode the underlying internal state or the motion itself. To clarify this further, we require a manipulation that can induce a non-internal state-related PE. Our unpublished data show that optogenetic excitation of sugar receptor Gr5a can trigger PE. Hence, we can activate the PE apart from the internal state using Gr5a and record the neural activity of PE-ANs. If the PE-ANs remain unresponsive, then these neurons encode a type of internal state that is accompanied by the PE rather than the PE itself. If so, this is consistent with what is known of the waste-clearance state with the PE train [136]. In contrast, if the PE-ANs respond, they will be known to encode the motion of the PE train.

Then we can ask how PE-ANs generate ramping activity. Since we see a ramping of the calcium signal, it might indicate that the neurons are gradually depolarized and fire more frequently through this period. One possibility to explain this excitation is that PE-ANs form an interconnected feedback loop, which is a hypothesis consistent with the preliminary findings in the VNC connectome [343]. To further investigate the mechanism of ramping activity, further physiological data should be obtained. For example, knowledge of the type of transmitter would confirm whether it integrates excitation or disinhibition, and a study of the intrinsic properties could indicate how long PE-ANs can maintain the membrane potential and whether they generate action or graded potential.

Beyond local computation, we also need to know how the information encoded by ANs interacts with brain networks. With the results of the AN screen, we can further dissect the impact of inputs on the behavioral state by activating each type of AN and measuring the effect on different functional modules in the brain, especially in the multi-sensory hub and action selection center (Figure 3.8). For example, one can activate walking-ANs and measure how the signal is modulated in the visual neurons or how it competes with other descending commands. Additionally, whether the synaptic transmission is excitatory or inhibitory should be examined to understand the operation of this inter-module interaction.

6.4.2 Technical part

The VNC imaging technique and analysis pipeline can be further improved to expand its range of applications. For example, a deeper analysis of the specific features of limb motion can expand the range of identified neuron encoding. As we found that walking can only partially predict activity in some ANs, this suggests that ANs encode more specific features during walking, such as leg reaching for exploring the environment. Thus, it is likely worth revisiting behavioral recordings at a higher temporal resolution to improve feature extraction.

Additional measurements together with videography and ball rotation can also help uncover the hidden encoding function of neurons. The results in [chapter 3](#) showing unresponsive ANs suggest that they might encode states that cannot be extracted from videos, such as the visceral nervous response and muscle stiffness. Also, ANs are very likely to encode other flight and social behaviors that require contexts not covered in the current setup. Nevertheless, when mimicking flight by removing the spherical treadmill, this work also found that silent neurons become active when the fly moves without standing on the spherical treadmill ([Figure S3.7](#)). It might also be possible to add a social behavior chamber that surrounds the tethered fly with other flies that can interact socially. The neural plasticity can also be studied with long-term imaging preparation [[143](#)]. Therefore, increasing the novelty and variety of measurements by introducing new apparatuses and detectors can expand the ability of the current setup to study more types of behavior-specific neural mechanisms under more complex scenarios.

Moreover, the neural recording process can also be improved to obtain more neural activity information. First, to obtain dynamic details, the sampling rate can be increased. For example, the scanning speed of two-photon microscopy can be raised using the Galvo-Resonance scanning mirror. However, the higher laser energy required to compensate for the low SNR due to the high scanning frequency may damage the tissue and thus shorten the fly's lifespan during recording. Because some neurons might fire sparsely in response to the behavioral state, genetically encoded voltage indicators can be used to avoid a false-negative readout due to the slow rise and decay of GCaMP [[68](#), [352](#)]. Furthermore, if SNR conditions allow it, this may resolve subthreshold potentials, such as the excitatory postsynaptic potential (EPSP). As an alternative, incorporating electrophysiology recording can improve the study of neural dynamics in terms of the SNR and temporal resolution at the single-cell level, since it has already been widely used in the brain of a tethered fly. The challenge will be the depth of the dissection opening to the VNC, which leaves no working space for the electrode. Therefore, modifications might be required to make the current mounting stage compatible with the dissection procedure to gain more working space for manipulating the electrode.

Though the long-term imaging methodology has been introduced to study neural plasticity [[143](#)], the access window is currently restricted within the T1, limiting some experiments with more posterior targets. For long-term studies of behaviors generated in different areas,

Chapter 6. Conclusion and perspectives

the engineered vector Act88f:Rpr inserted into the fly genome can remove the flight muscles to create a wider space in the thorax from T1 to T2/T3 ([Figure 2.6](#)).

Overall, this work provides an indispensable methodology to subject a fly to VNC imaging along with a library of AN genetic tools with their corresponding functional and morphological characteristics. Beyond the progress made in this work, several technical improvements can be foreseen to enhance the power of this technology, including increasing the temporal resolution, including more kinds of behavioral detectors, modifying the context of behavior, and long-term imaging. The results from a systematic examination of AN encoding can be informative for more in-depth investigations, such as studies of AN local function and AN-encoded behavioral state signals in the action selection center and the multi-sensory module of the brain for generating adaptive behavior.

Bibliography

- [1] E. Marder and D. Bucher, “Central pattern generators and the control of rhythmic movements,” *Current Biology*, vol. 11, no. 23, pp. R986–R996, 2001.
- [2] P. Guertin, “Central pattern generator for locomotion: anatomical, physiological, and pathophysiological considerations,” *Frontiers in Neurology*, vol. 3, 2013.
- [3] I. E. J. Aasebø, M. E. Lepperød, M. Stavrinou, S. Nøkkevangen, G. Einevoll, T. Hafting, and M. Fyhn, “Temporal processing in the visual cortex of the awake and anesthetized rat,” *eNeuro*, vol. 4, no. 4, 2017.
- [4] C. Stringer, M. Pachitariu, N. Steinmetz, C. B. Reddy, M. Carandini, and K. D. Harris, “Spontaneous behaviors drive multidimensional, brainwide activity,” *Science*, vol. 364, no. 6437, p. eaav7893, 2019.
- [5] C. M. Niell and M. P. Stryker, “Modulation of visual responses by behavioral state in mouse visual cortex,” *Neuron*, vol. 65, no. 4, pp. 472–479, 2010.
- [6] S. Musall, M. T. Kaufman, A. L. Juavinett, S. Gluf, and A. K. Churchland, “Single-trial neural dynamics are dominated by richly varied movements,” *Nature Neuroscience*, vol. 22, no. 10, pp. 1677–1686, 2019.
- [7] G. Maimon, A. D. Straw, and M. H. Dickinson, “Active flight increases the gain of visual motion processing in *Drosophila*,” *Nature Neuroscience*, vol. 13, no. 3, pp. 393–399, 2010.
- [8] M. E. Chiappe, J. D. Seelig, M. B. Reiser, and V. Jayaraman, “Walking modulates speed sensitivity in *Drosophila* motion vision,” *Current Biology*, vol. 20, no. 16, pp. 1470–1475, 2010.
- [9] T. Fujiwara, T. L. Cruz, J. P. Bohnslav, and M. E. Chiappe, “A faithful internal representation of walking movements in the *Drosophila* visual system,” *Nature Neuroscience*, vol. 20, pp. 72–81, 2016.
- [10] S. Aimon, T. Katsuki, T. Jia, L. Grosenick, M. Broxton, K. Deisseroth, T. J. Sejnowski, and R. J. Greenspan, “Fast near-whole-brain imaging in adult *Drosophila* during responses to stimuli and behavior,” *PLOS Biology*, vol. 17, no. 2, p. e2006732, 2019.

Bibliography

- [11] K. C. Daly, F. Kalwar, M. Hatfield, E. Staudacher, and S. P. Bradley, “Odor detection in *Manduca sexta* is optimized when odor stimuli are pulsed at a frequency matching the wing beat during flight,” *PLOS ONE*, vol. 8, no. 11, p. e81863, 2013.
- [12] R. Zacarias, S. Namiki, G. M. Card, M. L. Vasconcelos, and M. A. Moita, “Speed dependent descending control of freezing behavior in *Drosophila melanogaster*,” *Nature Communications*, vol. 9, no. 1, p. 3697, 2018.
- [13] V. E. Abraira and D. D. Ginty, “The sensory neurons of touch,” *Neurony*, vol. 79, no. 4, pp. 618–639, 2013.
- [14] L. K. Crawford and M. J. Caterina, “Functional anatomy of the sensory nervous system: updates from the neuroscience bench,” *Toxicologic Pathology*, vol. 48, no. 1, pp. 174–189, 2020.
- [15] D. Purves, G. J. Augustine, D. Fitzpatrick, L. C. Katz, A.-S. LaMantia, J. O. McNamara, and S. M. Williams, “Mechanoreceptors specialized for proprioception,” in *Neuroscience*. Sinauer Associates, Sunderland, MA, USA, 2001, ch. 9.
- [16] C. Chen, S. Agrawal, B. Mark, A. Mamiya, A. Sustar, J. S. Phelps, W.-C. A. Lee, B. J. Dickson, G. M. Card, and J. C. Tuthill, “Functional architecture of neural circuits for leg proprioception in *Drosophila*,” *Current Biology*, vol. 31, pp. 1–13, 2021.
- [17] J. C. Tuthill and R. I. Wilson, “Mechanosensation and adaptive motor control in insects,” *Current Biology*, vol. 26, no. 20, pp. R1022–R1038, 2016.
- [18] A. Tsubouchi, T. Yano, T. K. Yokoyama, C. Murtin, H. Otsuna, and K. Ito, “Topological and modality-specific representation of somatosensory information in the fly brain,” *Science*, vol. 358, no. 6363, pp. 615–623, 2017.
- [19] D. McNeill, L. Quaeghebeur, and S. Duncan, “The man who lost his body,” in *Handbook of Phenomenology and Cognitive Science*, S. D. and G. S., Eds. Springer, Dordrecht., 2010, pp. 519–543.
- [20] T. Akay, W. G. Tourtellotte, S. Arber, and T. M. Jessell, “Degradation of mouse locomotor pattern in the absence of proprioceptive sensory feedback,” *Proceedings of the National Academy of Sciences*, vol. 111, no. 47, pp. 16 877–16 882, 2014.
- [21] C. S. Mendes, I. Bartos, T. Akay, S. Márka, and R. S. Mann, “Quantification of gait parameters in freely walking wild type and sensory deprived *Drosophila melanogaster*,” *eLife*, vol. 2, p. e00231, 2013.
- [22] A. Comitato and R. Bardoni, “Presynaptic inhibition of pain and touch in the spinal cord: From receptors to circuits,” *International Journal of Molecular Sciences*, vol. 22, no. 1, 2021.

- [23] J. C. Tuthill and E. Azim, "Proprioception," *Current Biology*, vol. 28, no. 5, pp. R194–R203, 2018.
- [24] M. Patestas and L. P. Gartner, "Ascending Sensory Pathways," in *A Textbook of Neuroanatomy*, 1st ed. Wiley, 2006, ch. 10, pp. 137–170.
- [25] T. B. Crapse and M. A. Sommer, "Corollary discharge across the animal kingdom," *Nature Reviews Neuroscience*, vol. 9, no. 8, pp. 587–600, 2008.
- [26] J. F. Poulet and B. Hedwig, "New insights into corollary discharges mediated by identified neural pathways," *Trends in Neurosciences*, vol. 30, no. 1, pp. 14–21, 2007.
- [27] K. Stecina, B. Fedirchuk, and H. Hultborn, "Information to cerebellum on spinal motor networks mediated by the dorsal spinocerebellar tract," *The Journal of Physiology*, vol. 591, no. 22, pp. 5433–5443, 2013.
- [28] S. S. Bidaye, C. Machacek, Y. Wu, and B. J. Dickson, "Neuronal control of *Drosophila* walking direction," *Science*, vol. 344, no. 6179, pp. 97–101, 2014.
- [29] J. T. Buchanan and J. F. Einum, "The spinobulbar system in lamprey," *Brain Research Reviews*, vol. 57, no. 1, pp. 37–45, 2008.
- [30] J. C. Tuthill and R. I. Wilson, "Parallel transformation of tactile signals in central circuits of *Drosophila*," *Cell*, vol. 164, no. 5, pp. 1046–1059, 2016.
- [31] M. Talay, E. B. Richman, N. J. Snell, G. G. Hartmann, J. D. Fisher, A. Sorkaç, J. F. Santoyo, C. Chou-Freed, N. Nair, M. Johnson, J. R. Szymanski, and G. Barnea, "Transsynaptic mapping of second-order taste neurons in flies by trans-tango," *Neuron*, vol. 96, no. 4, pp. 783–795.e4, 2017.
- [32] T. Fujiwara, M. Brotas, and M. E. Chiappe, "Walking strides direct rapid and flexible recruitment of visual circuits for course control in *Drosophila*," *bioRxiv*, p. 2021.10.10.4638170, 2021.
- [33] A. J. Kim, J. K. Fitzgerald, and G. Maimon, "Cellular evidence for efference copy in *Drosophila* visuomotor processing," *Nature Neuroscience*, vol. 18, pp. 1247–1255, 2015.
- [34] K. Mann, M. Gordon, and K. Scott, "A pair of interneurons influences the choice between feeding and locomotion in *Drosophila*," *Neuron*, vol. 79, no. 4, pp. 754–765, 2013.
- [35] M. Burrows, "Sensory effect on flying," in *The Neurobiology of An Insect Brain*, 1st ed. Oxford: Oxford University Press, 1996, ch. 11, pp. 541–544.
- [36] L. Ruder, R. Schina, H. Kanodia, S. Valencia-Garcia, C. Pivetta, and S. Arber, "A functional map for diverse forelimb actions within brainstem circuitry," *Nature*, vol. 590, no. 7846, pp. 445–450, 2021.

Bibliography

- [37] M. J. Ferreira-Pinto, H. Kanodia, A. Falasconi, M. Sigrist, M. S. Esposito, and S. Arber, “Functional diversity for body actions in the mesencephalic locomotor region,” *Cell*, vol. 184, no. 17, pp. 4564–4578.e18, 2021.
- [38] S. Namiki, M. H. Dickinson, A. M. Wong, W. Korff, and G. M. Card, “The functional organization of descending sensory-motor pathways in *Drosophila*,” *eLife*, vol. 7, p. e34272, 2018.
- [39] N. Baril, M. Roth, and R. Djouri, *In vivo imaging in mice*. New York, NY: Springer New York, 2015, pp. 119–156.
- [40] J. D. Seelig, M. E. Chiappe, G. K. Lott, A. Dutta, J. E. Osborne, M. B. Reiser, and V. Jayaraman, “Two-photon calcium imaging from head-fixed *Drosophila* during optomotor walking behavior,” *Nature Methods*, vol. 7, no. 7, pp. 535–540, 2010.
- [41] C. Huang, J. R. Maxey, S. Sinha, J. Savall, Y. Gong, and M. J. Schnitzer, “Long-term optical brain imaging in live adult fruit flies,” *Nature Communications*, vol. 9, no. 1, p. 872, 2018.
- [42] G. Nagel, T. Szellas, W. Huhn, S. Kateriya, N. Adeishvili, P. Berthold, D. Ollig, P. Hege-mann, and E. Bamberg, “Channelrhodopsin-2, a directly light-gated cation-selective membrane channel,” *Proceedings of the National Academy of Sciences*, vol. 100, no. 24, pp. 13 940–13 945, 2003.
- [43] S. W. Oh, J. A. Harris, L. Ng, B. Winslow, N. Cain, S. Mihalas, Q. Wang, C. Lau, L. Kuan, A. M. Henry, M. T. Mortrud, B. Ouellette, T. N. Nguyen, S. A. Sorensen, C. R. Slaughterbeck, W. Wakeman, Y. Li, D. Feng, A. Ho, E. Nicholas, K. E. Hirokawa, P. Bohn, K. M. Joines, H. Peng, M. J. Hawrylycz, J. W. Phillips, J. G. Hohmann, P. Wohnoutka, C. R. Gerfen, C. Koch, A. Bernard, C. Dang, A. R. Jones, and H. Zeng, “A mesoscale connectome of the mouse brain,” *Nature*, vol. 508, no. 7495, pp. 207–214, 2014.
- [44] C. Ma, D. F. Donnelly, and R. H. LaMotte, “*In vivo* visualization and functional characterization of primary somatic neurons,” *Journal of Neuroscience Methods*, vol. 191, no. 1, pp. 60–65, 2010.
- [45] B. Graham, A. Brichta, and R. Callister, “An *in vivo* mouse spinal cord preparation for patch-clamp analysis of nociceptive processing,” *Journal of Neuroscience Methods*, vol. 136, no. 2, pp. 221–228, 2004.
- [46] B. Hedwig and M. Burrows, “Presynaptic inhibition of sensory neurons during kicking movements in the locust,” *Journal of Neurophysiology*, vol. 75, no. 3, pp. 1221–1232, 1996.
- [47] U. Bässler and A. Büschges, “Pattern generation for stick insect walking movements—multisensory control of a locomotor program,” *Brain Research Reviews*, vol. 27, no. 1, pp. 65–88, 1998.

- [48] R. A. Brooks, "A robust layered control system for a mobile robot," *IEEE Journal on Robotics and Automation*, vol. 2, no. 1, pp. 14–23, 1986.
- [49] C.-L. Chen, L. Hermans, M. C. Viswanathan, D. Fortun, M. Unser, A. Cammarato, M. H. Dickinson, and P. Ramdya, "Imaging neural activity in the ventral nerve cord of behaving adult *Drosophila*," *Nature Communications*, vol. 9, p. 4390, 2018.
- [50] T. L. Cruz, S. M. Pérez, and M. E. Chiappe, "Fast tuning of posture control by visual feedback underlies gaze stabilization in walking *Drosophila*," *Current Biology*, vol. 31, no. 20, pp. 4596–4607.e5, 2021.
- [51] G. J. Berman, D. M. Choi, W. Bialek, and J. W. Shaevitz, "Mapping the stereotyped behaviour of freely moving fruit flies," *Journal of The Royal Society Interface*, vol. 11, no. 99, p. 20140672, 2014.
- [52] J.-C. Billeter, E. J. Rideout, A. J. Dornan, and S. F. Goodwin, "Control of male sexual behavior in *Drosophila* by the sex determination pathway," *Current Biology*, vol. 16, no. 17, pp. R766–R776, 2006.
- [53] M. M. Aranha and M. L. Vasconcelos, "Deciphering *Drosophila* female innate behaviors," *Current Opinion in Neurobiology*, vol. 52, pp. 139–148, 2018.
- [54] A. Ueda and C.-F. Wu, "Effects of social isolation on neuromuscular excitability and aggressive behaviors in *Drosophila*: altered responses by *hk* and *gsts1*, two mutations implicated in redox regulation," *Journal of neurogenetics*, vol. 23, pp. 378–94, 2009.
- [55] S. J. Certel, M. G. Savella, D. C. F. Schlegel, and E. A. Kravitz, "Modulation of *Drosophila* male behavioral choice," *Proceedings of the National Academy of Sciences*, vol. 104, no. 11, pp. 4706–4711, 2007.
- [56] S. Günel, H. Rhodin, D. Morales, J. Campagnolo, P. Ramdya, and P. Fua, "DeepFly3D, a deep learning-based approach for 3D limb and appendage tracking in tethered, adult *Drosophila*," *eLife*, vol. 8, p. e48571, 2019.
- [57] Z. N. S. J. H. Guo, Li, "Descending neurons coordinate anterior grooming behavior in *Drosophila*," *Current Biology*, vol. 32, no. 4, pp. 823–833.e4, 2022.
- [58] J. C. Simon and M. H. Dickinson, "A new chamber for studying the behavior of *Drosophila*," *PLOS ONE*, vol. 5, no. 1, pp. 1–11, 2010.
- [59] A. Mathis, P. Mamidanna, K. M. Cury, T. Abe, V. N. Murthy, M. W. Mathis, and M. Bethge, "DeepLabCut: markerless pose estimation of user-defined body parts with deep learning," *Nature Neuroscience*, vol. 21, no. 9, pp. 1281–1289, 2018.
- [60] F. van Breugel and M. H. Dickinson, "Plume-tracking behavior of flying *Drosophila* emerges from a set of distinct sensory-motor reflexes," *Current Biology*, vol. 24, no. 3, pp. 274–286, 2014.

Bibliography

- [61] D. Lohr, P. Venkov, and J. Zlatanova, "Transcriptional regulation in the yeast gal gene family: a complex genetic network," *The FASEB Journal*, vol. 9, no. 9, pp. 777–787, 1995.
- [62] J. A. Fischer, E. Giniger, T. Maniatis, and M. Ptashne, "Gal4 activates transcription in *Drosophila*," *Nature*, vol. 332, no. 6167, pp. 853–856, 1988.
- [63] H. Luan, N. C. Peabody, C. R. Vinson, and B. H. White, "Refined spatial manipulation of neuronal function by combinatorial restriction of transgene expression," *Neuron*, vol. 52, no. 3, pp. 425–436, 2006.
- [64] A. Brand and N. Perrimon, "Targeted gene expression as a means of altering cell fates and generating dominant phenotypes," *Development*, vol. 118, no. 2, pp. 401–415, 1993.
- [65] A. Jenett, G. M. Rubin, T.-T. B. Ngo, D. Shepherd, C. Murphy, H. Dionne, B. D. Pfeiffer, A. Cavallaro, D. Hall, J. Jeter, N. Iyer, D. Fetter, J. H. Hausenfluck, H. Peng, E. T. Trautman, R. Svirskas, E. W. Myers, Z. R. Iwinski, Y. Aso, G. M. DePasquale, A. Enos, P. Hulamm, S. C. B. Lam, H.-H. Li, T. R. Lavery, F. Long, L. Qu, S. D. Murphy, K. Rokicki, T. Safford, K. Shaw, J. H. Simpson, A. Sowell, S. Tae, Y. Yu, and C. T. Zugates, "A GAL4-driver line resource for *Drosophila* neurobiology," *Cell Reports*, vol. 2, no. 4, pp. 991–1001, 2012.
- [66] G. Dietzl, D. Chen, F. Schnorrer, K.-C. Su, Y. Barinova, M. Fellner, B. Gasser, K. Kinsey, S. Oettel, S. Scheiblauer, A. Couto, V. Marra, K. Keleman, and B. J. Dickson, "A genome-wide transgenic RNAi library for conditional gene inactivation in *Drosophila*," *Nature*, vol. 448, no. 7150, pp. 151–156, 2007.
- [67] R. Y. Tsien, "The green fluorescent protein," *Annual Review of Biochemistry*, vol. 67, no. 1, pp. 509–544, 1998.
- [68] T.-W. Chen, T. J. Wardill, Y. Sun, S. R. Pulver, S. L. Renninger, A. Baohan, E. R. Schreiter, R. A. Kerr, M. B. Orger, V. Jayaraman, L. L. Looger, K. Svoboda, and D. S. Kim, "Ultrasensitive fluorescent proteins for imaging neuronal activity," *Nature*, vol. 499, no. 7458, pp. 295–300, 2013.
- [69] N. C. Klapoetke, Y. Murata, S. S. Kim, S. R. Pulver, A. Birdsey-Benson, Y. K. Cho, T. K. Morimoto, A. S. Chuong, E. J. Carpenter, Z. Tian, J. Wang, Y. Xie, Z. Yan, Y. Zhang, B. Y. Chow, B. Surek, M. Melkonian, V. Jayaraman, M. Constantine-Paton, G. K.-S. Wong, and E. S. Boyden, "Independent optical excitation of distinct neural populations," *Nature Methods*, vol. 11, no. 3, pp. 338–346, 2014.
- [70] A. Nern, B. D. Pfeiffer, and G. M. Rubin, "Optimized tools for multicolor stochastic labeling reveal diverse stereotyped cell arrangements in the fly visual system," *Proceedings of the National Academy of Sciences of the United States of America*, vol. 112, no. 22, pp. E2967 LP – E2976, 2015.

- [71] J. S. Wu and L. Luo, "A protocol for mosaic analysis with a repressible cell marker (marcm) in *Drosophila*," *Nature protocols*, vol. 1, no. 6, pp. 2583–2589, 2006.
- [72] S.-L. Lai and T. Lee, "Genetic mosaic with dual binary transcriptional systems in *Drosophila*," *Science*, vol. 302, no. 5651, pp. 1765–1768, 2003.
- [73] C. J. Potter and L. Luo, "Using the q system in *Drosophila melanogaster*," *Nature Protocols*, vol. 6, no. 8, pp. 1105–1120, 2011.
- [74] W. Denk, J. H. Strickler, and W. W. Webb, "Two-photon laser scanning fluorescence microscopy," *Science*, vol. 248, no. 4951, pp. 73–76, 1990.
- [75] C. Soeller and M. B. Cannell, "Two-photon microscopy: Imaging in scattering samples and three-dimensionally resolved flash photolysis," *Microscopy Research and Technique*, vol. 47, no. 3, pp. 182–195, 1999.
- [76] K. Svoboda and R. Yasuda, "Principles of two-photon excitation microscopy and its applications to neuroscience," *Neuron*, vol. 50, no. 6, pp. 823–839, 2006.
- [77] B. P. Bean, "The action potential in mammalian central neurons," *Nature Reviews Neuroscience*, vol. 8, no. 6, pp. 451–465, 2007.
- [78] J. Nakai, M. Ohkura, and K. Imoto, "A high signal-to-noise Ca_2^+ probe composed of a single green fluorescent protein," *Nature Biotechnology*, vol. 19, no. 2, pp. 137–141, 2001.
- [79] K. S. Girven and D. R. Sparta, "Probing deep brain circuitry: new advances in *in Vivo* calcium measurement strategies," *ACS Chemical Neuroscience*, vol. 8, no. 2, pp. 243–251, 2017.
- [80] J. Akerboom, J. D. Rivera, M. M. Guilbe, E. C. Malavé, H. H. Hernandez, L. Tian, S. Hires, J. S. Marvin, L. L. Looger, and E. R. Schreiter, "Crystal structures of the gcamp calcium sensor reveal the mechanism of fluorescence signal change and aid rational design *," *Journal of Biological Chemistry*, vol. 284, no. 10, pp. 6455–6464, 2009.
- [81] A. L. Hodgkin and A. F. Huxley, "A quantitative description of membrane current and its application to conduction and excitation in nerve," *The Journal of Physiology*, vol. 117, no. 4, pp. 500–544, 1952.
- [82] M. H. Zhu, J. Jang, M. M. Milosevic, and S. D. Antic, "Population imaging discrepancies between a genetically-encoded calcium indicator (geci) versus a genetically-encoded voltage indicator (gevi)," *Scientific Reports*, vol. 11, no. 1, p. 5295, 2021.
- [83] W. Denk, K. Delaney, A. Gelperin, D. Kleinfeld, B. Strowbridge, D. Tank, and R. Yuste, "Anatomical and functional imaging of neurons using 2-photon laser scanning microscopy," *Journal of Neuroscience Methods*, vol. 54, no. 2, pp. 151–162, 1994.

Bibliography

- [84] H. P. K.K., “Basic principles of photomultiplier tubes,” in *Photomultiplier Tubes—Basic Applications*, 3rd ed., I. World Technical Writing, Ed. Electron Tube Divisions, Hamamatsu Photonics K.K., 2007, ch. 2, p. 13.
- [85] S. S. Bidaye, T. Bockemühl, and A. Büschges, “Six-legged walking in insects: how CPGs, peripheral feedback, and descending signals generate coordinated and adaptive motor rhythms,” *Journal of Neurophysiology*, vol. 119, no. 2, pp. 459–475, 2018.
- [86] R. Court, S. Namiki, J. D. Armstrong, J. Börner, G. Card, M. Costa, M. Dickinson, C. Duch, W. Korff, R. Mann, D. Merritt, R. K. Murphey, A. M. Seeds, T. Shirangi, J. H. Simpson, J. W. Truman, J. C. Tuthill, D. W. Williams, and D. Shepherd, “A systematic nomenclature for the *Drosophila* ventral nerve cord.” *Neuron*, vol. 107, no. 6, pp. 1071–1079.e2, 2020.
- [87] A. Wosnitza, T. Bockemühl, M. Dübber, H. Scholz, and A. Büschges, “Inter-leg coordination in the control of walking speed in *Drosophila*,” *Journal of Experimental Biology*, vol. 216, no. 3, pp. 480–491, 2013.
- [88] J. E. Niven, “Visuomotor control: *Drosophila* bridges the gap,” *Current Biology*, vol. 20, no. 7, pp. R309–R311, 2010.
- [89] G. Card and M. H. Dickinson, “Visually mediated motor planning in the escape response of *Drosophila*,” *Current Biology*, vol. 18, no. 17, pp. 1300–1307, 2008.
- [90] H. J. Pavlou and S. F. Goodwin, “Courtship behavior in *Drosophila melanogaster*: towards a ‘courtship connectome,’” *Current Opinion in Neurobiology*, vol. 23, no. 1, pp. 76–83, 2013.
- [91] L. Zwarts, M. Versteven, and P. Callaerts, “Genetics and neurobiology of aggression in *Drosophila*,” *Fly*, vol. 6, no. 1, pp. 35–48, 2012.
- [92] A. M. Seeds, P. Ravbar, P. Chung, S. Hampel, J. Midgley, Frank M, B. D. Mensh, and J. H. Simpson, “A suppression hierarchy among competing motor programs drives sequential grooming in *Drosophila*,” *eLife*, vol. 3, p. e02951, 2014.
- [93] J. R. Trimarchi and R. K. Murphey, “The shaking-b2 mutation disrupts electrical synapses in a flight circuit in adult *Drosophila*,” vol. 17, no. 12, pp. 4700–4710, 1997.
- [94] K. IKEDA and W. D. KAPLAN, “Neurophysiological genetics in *Drosophila melanogaster*,” *American Zoologist*, vol. 14, no. 3, pp. 1055–1066, 2015.
- [95] N. C. Shaner, R. E. Campbell, P. A. Steinbach, B. N. G. Giepmans, A. E. Palmer, and R. Y. Tsien, “Improved monomeric red, orange and yellow fluorescent proteins derived from *Discosoma* sp. red fluorescent protein,” *Nature Biotechnology*, vol. 22, no. 12, pp. 1567–1572, 2004.

- [96] B. Hedwig and J. F. A. Poulet, "Complex auditory behaviour emerges from simple reactive steering," *Nature*, vol. 430, no. 7001, pp. 781–785, 2004.
- [97] J. Enriquez, L. Venkatasubramanian, M. Baek, M. Peterson, U. Aghayeva, and R. S. Mann, "Specification of Individual Adult Motor Neuron Morphologies by Combinatorial Transcription Factor Codes," *Neuron*, vol. 86, no. 4, pp. 955–970, 2015.
- [98] R. Sen, M. Wu, K. Branson, A. Robie, G. M. Rubin, and B. J. Dickson, "Moonwalker descending neurons mediate visually evoked retreat in *Drosophila*," *Current Biology*, vol. 27, no. 5, pp. 766–771, 2017.
- [99] K. White, M. E. Grether, J. M. Abrams, L. Young, K. Farrell, and H. Steller, "Genetic control of programmed cell death in *Drosophila*," *Science*, vol. 264, no. 5159, pp. 677–683, 1994.
- [100] P. Ramdya, T. Schaffter, D. Floreano, and R. Benton, "Fluorescence behavioral imaging (fbi) tracks identity in heterogeneous groups of *Drosophila*," *PLOS ONE*, vol. 7, no. 11, pp. 1–8, 2012.
- [101] M. C. Reedy, B. Bullard, and J. O. Vigoreaux, "Flightin is essential for thick filament assembly and sarcomere stability in *Drosophila* flight muscles," *Journal of Cell Biology*, vol. 151, no. 7, pp. 1483–1500, 2000.
- [102] R. Lu, W. Sun, Y. Liang, A. Kerlin, J. Bierfeld, J. D. Seelig, D. E. Wilson, B. Scholl, B. Mohar, M. Tanimoto, M. Koyama, D. Fitzpatrick, M. B. Orger, and N. Ji, "Video-rate volumetric functional imaging of the brain at synaptic resolution," *Nature Neuroscience*, vol. 20, no. 4, pp. 620–628, 2017.
- [103] A. A. Robie, J. Hirokawa, A. W. Edwards, L. A. Umayam, A. Lee, M. L. Phillips, G. M. Card, W. Korff, G. M. Rubin, J. H. Simpson, M. B. Reiser, and K. Branson, "Mapping the neural substrates of behavior," *Cell*, vol. 170, no. 2, pp. 393–406.e28, 2017.
- [104] R. M. Harris, B. D. Pfeiffer, G. M. Rubin, and J. W. Truman, "Neuron hemilineages provide the functional ground plan for the *Drosophila* ventral nervous system," *eLife*, vol. 4, p. e04493, 2015.
- [105] M. Markstein, C. Pitsouli, C. Villalta, S. E. Celniker, and N. Perrimon, "Exploiting position effects and the gypsy retrovirus insulator to engineer precisely expressed transgenes," *Nature Genetics*, vol. 40, no. 4, pp. 476–483, 2008.
- [106] U. Nongthomba and N. B. Ramachandra, "A direct screen identifies new flight muscle mutants on the *Drosophila* second chromosome," *Genetics*, vol. 153, no. 1, pp. 261–274, 1999.
- [107] M. C. Viswanathan, A. C. Blice-Baum, W. Schmidt, D. B. Foster, and A. Cammarato, "Pseudo-acetylation of k326 and k328 of actin disrupts *Drosophila melanogaster* indirect flight muscle structure and performance," *Frontiers in Physiology*, vol. 6, 2015.

Bibliography

- [108] J. Schindelin, I. Arganda-Carreras, E. Frise, V. Kaynig, M. Longair, T. Pietzsch, S. Preibisch, C. Rueden, S. Saalfeld, B. Schmid, J.-Y. Tinevez, D. J. White, V. Hartenstein, K. Eliceiri, P. Tomancak, and A. Cardona, “Fiji: An open-source platform for biological-image analysis,” *Nature Methods*, vol. 9, no. 7, pp. 676–682, 2012.
- [109] P. T. Weir and M. H. Dickinson, “Functional divisions for visual processing in the central brain of flying *Drosophila*,” *Proceedings of the National Academy of Sciences of the United States of America*, vol. 112, no. 40, pp. E5523–5532, 2015.
- [110] A. Fayyazuddin and M. H. Dickinson, “Haltere afferents provide direct, electrotonic input to a steering motor neuron in the blowfly, *Calliphora*,” *Journal of Neuroscience*, vol. 16, no. 16, pp. 5225–5232, 1996.
- [111] B. K. Horn and B. G. Schunck, “Determining optical flow,” *Artificial Intelligence*, vol. 17, no. 1, pp. 185–203, 1981.
- [112] T. Brox, A. Bruhn, N. Papenberg, and J. Weickert, “High accuracy optical flow estimation based on a theory for warping,” in *Computer Vision*, 1st ed. Berlin, Heidelberg: Springer, 2004, vol. 3024, ch. ECCV 2004, p. 25–36.
- [113] J. Revaud, P. Weinzaepfel, Z. Harchaoui, and C. Schmid, “Deepmatching: Hierarchical deformable dense matching,” *arXiv*, 2015.
- [114] E. A. Pnevmatikakis and A. Giovannucci, “Normcorre: An online algorithm for piecewise rigid motion correction of calcium imaging data,” *Journal of Neuroscience Methods*, vol. 291, pp. 83–94, 2017.
- [115] S. Boyd, N. Parikh, E. Chu, B. Peleato, and J. Eckstein, “Distributed optimization and statistical learning via the alternating direction method of multipliers,” *Foundation and Trends[®] in Machine Learning*, vol. 3, no. 1, p. 1–122, 2011.
- [116] M. Unser, E. Soubies, F. Soulez, M. McCann, and L. Donati, “Globalbioim: A unifying computational framework for solving inverse problems,” in *Imaging and Applied Optics 2017 (3D, AIO, COSI, IS, MATH, pCAOP)*. Optica Publishing Group, 2017, p. CTu1B.1.
- [117] D. Sun, S. Roth, and M. J. Black, “A quantitative analysis of current practices in optical flow estimation and the principles behind them,” *International Journal of Computer Vision*, vol. 106, no. 2, pp. 115–137, 2014.
- [118] M. Guizar-Sicairos, S. T. Thurman, and J. R. Fienup, “Efficient subpixel image registration algorithms,” *Opt. Lett.*, vol. 33, no. 2, pp. 156–158, 2008.
- [119] P. T. Weir, M. J. Henze, C. Bleul, F. Baumann-Klausener, T. Labhart, and M. H. Dickinson, “Anatomical reconstruction and functional imaging reveal an ordered array of skylight polarization detectors in *Drosophila*,” *Journal of Neuroscience*, vol. 36, no. 19, pp. 5397–5404, 2016.

- [120] Y. Ikegaya, G. Aaron, R. Cossart, D. Aronov, I. Lampl, D. Ferster, and R. Yuste, "Synfire chains and cortical songs: temporal modules of cortical activity," *Science*, vol. 304, no. 5670, pp. 559–564, 2004.
- [121] U. Homberg, "Flight-correlated activity changes in neurons of the lateral accessory lobes in the brain of the locust *Schistocerca gregaria*," *Journal of Comparative Physiology A*, vol. 175, no. 5, pp. 597–610, 1994.
- [122] S. Agrawal, E. S. Dickinson, A. Sustar, P. Gurung, D. Shepherd, J. W. Truman, and J. C. Tuthill, "Central processing of leg proprioception in *Drosophila*," *eLife*, vol. 9, p. e60299, 2020.
- [123] K. Panser, L. Tirian, F. Schulze, S. Villalba, G. S. Jefferis, K. Bühler, and A. D. Straw, "Automatic segmentation of *Drosophila* neural compartments using GAL4 expression data reveals novel visual pathways," *Current Biology*, vol. 26, no. 15, pp. 1943–1954, 2016.
- [124] A. A. M. Mohamed, B. S. Hansson, and S. Sachse, "Third-order neurons in the lateral horn Enhance bilateral contrast of odor inputs through contralateral inhibition in *Drosophila*," *Frontiers in Physiology*, vol. 10, p. 851, 2019.
- [125] E. Matsuo, H. Seki, T. Asai, T. Morimoto, H. Miyakawa, K. Ito, and A. Kamikouchi, "Organization of projection neurons and local neurons of the primary auditory center in the fruit fly *Drosophila melanogaster*," *Journal of Comparative Neurology*, vol. 524, no. 6, pp. 1099–1164, 2016.
- [126] J. S.-Y. Lai, S.-J. Lo, B. J. Dickson, and A.-S. Chiang, "Auditory circuit in the *Drosophila* brain," *Proceedings of the National Academy of Sciences of the United States of America*, vol. 109, no. 7, pp. 2607–2612, 2012.
- [127] A. Kamikouchi, T. Shimada, and K. Ito, "Comprehensive classification of the auditory sensory projections in the brain of the fruit fly *Drosophila melanogaster*," *Journal of Comparative Neurology*, vol. 499, no. 3, pp. 317–356, 2006.
- [128] T. Miyamoto and H. Amrein, "Suppression of male courtship by a *Drosophila* pheromone receptor," *Nature Neuroscience*, vol. 11, no. 8, pp. 874–876, 2008.
- [129] I. Tastekin, J. Riedl, V. Schilling-Kurz, A. Gomez-Marin, J. W. Truman, and M. Louis, "Role of the subesophageal zone in sensorimotor control of orientation in *Drosophila* larva," *Current Biology*, vol. 25, no. 11, pp. 1448–1460, 2015.
- [130] A. Rayshubskiy, S. L. Holtz, I. D'Alessandro, A. A. Li, Q. X. Vanderbeck, I. S. Haber, P. W. Gibb, and R. I. Wilson, "Neural circuit mechanisms for steering control in walking *Drosophila*," *bioRxiv*, p. 2020.04.04.024703, 2020.

Bibliography

- [131] C. Trueta and F. De-Miguel, “Extrasynaptic exocytosis and its mechanisms: a source of molecules mediating volume transmission in the nervous system,” *Frontiers in Physiology*, vol. 3, p. 319, 2012.
- [132] C. J. Edwards, C. J. Leary, and G. J. Rose, “Counting on inhibition and rate-dependent excitation in the auditory system,” *Journal of Neuroscience*, vol. 27, no. 49, pp. 13 384–13 392, 2007.
- [133] R. Naud, D. Houtman, G. J. Rose, and A. Longtin, “Counting on dis-inhibition: a circuit motif for interval counting and selectivity in the anuran auditory system,” *Journal of Neurophysiology*, vol. 114, no. 5, pp. 2804–2815, 2015.
- [134] O. Barak, D. Sussillo, R. Romo, M. Tsodyks, and L. Abbott, “From fixed points to chaos: three models of delayed discrimination,” *Progress in Neurobiology*, vol. 103, pp. 214–222, 2013.
- [135] P. Miller, “Dynamical systems, attractors, and neural circuits,” *F1000Research*, vol. 5, pp. F1000 Faculty Rev–992, 2016.
- [136] B. van Alphen, E. R. Semenza, M. Yap, B. van Swinderen, and R. Allada, “A deep sleep stage in *Drosophila* with a functional role in waste clearance,” *Science Advances*, vol. 7, no. 4, p. eabc2999, 2021.
- [137] G. Bosco and R. Poppele, “Proprioception from a spinocerebellar perspective,” *Physiological Reviews*, vol. 81, no. 2, pp. 539–568, 2001.
- [138] A. Mamiya, P. Gurung, and J. C. Tuthill, “Neural coding of leg proprioception in *Drosophila*,” *Neuron*, vol. 100, no. 3, pp. 636–650.e6, 2018.
- [139] J. Cande, S. Namiki, J. Qiu, W. Korff, G. M. Card, J. W. Shaevitz, D. L. Stern, and G. J. Berman, “Optogenetic dissection of descending behavioral control in *Drosophila*,” *Elife*, vol. 7, p. e34275, 2018.
- [140] S. S. Bidaye, M. Laturney, A. K. Chang, Y. Liu, T. Bockemühl, A. Büschges, and K. Scott, “Two brain pathways initiate distinct forward walking programs in *Drosophila*,” *Neuron*, vol. 108, no. 3, pp. 469–485.e8, 2020.
- [141] S. Hampel, R. Franconville, J. H. Simpson, and A. M. Seeds, “A neural command circuit for grooming movement control,” *eLife*, vol. 4, p. e08758, 2015.
- [142] A. Isakov, S. M. Buchanan, B. Sullivan, A. Ramachandran, J. K. S. Chapman, E. S. Lu, L. Mahadevan, and B. de Bivort, “Recovery of locomotion after injury in *Drosophila melanogaster* depends on proprioception,” *The Journal of Experimental Biology*, vol. 219, no. 11, pp. 1760–1771, 2016.

- [143] L. Hermans, M. Kaynak, J. raun, V. Lobato Ríos, C.-L. Chen, S. Günel, F. Aymanns, M. S. Sakar, and P. Ramdya, “Long-term imaging of the ventral nerve cord in behaving adult *Drosophila*,” *bioRxiv*, p. 2021.10.15.463778, 2021.
- [144] R. Dubuc and S. Grillner, “The role of spinal cord inputs in modulating the activity of reticulospinal neurons during fictive locomotion in the lamprey,” *Brain Research*, vol. 483, no. 1, pp. 196–200, 1989.
- [145] J. Rothwell, “Ascending and descending pathways of the spinal cord,” in *Control of Human Voluntary Movement*. Springer, 1994, pp. 217–251.
- [146] S. Choi, J. Hachisuka, M. A. Brett, A. R. Magee, Y. Omori, D. Zhang, M. M. DeLisle, R. L. Wolfson, L. Bai, C. Santiago *et al.*, “Parallel ascending spinal pathways for affective touch and pain,” *Nature*, vol. 587, no. 7833, pp. 258–263, 2020.
- [147] G. S. Jefferis, C. J. Potter, A. M. Chan, E. C. Marin, T. Rohlfsing, C. R. Maurer, and L. Luo, “Comprehensive maps of *Drosophila* higher olfactory centers: spatially segregated fruit and pheromone representation,” *Cell*, vol. 128, no. 6, pp. 1187–1203, 2007.
- [148] J. A. Bogovic, H. Otsuna, L. Heinrich, M. Ito, J. Jeter, G. Meissner, A. Nern, J. Colonell, O. Malkesman, K. Ito, and S. Saalfeld, “An unbiased template of the *Drosophila* brain and ventral nerve cord,” *PLOS ONE*, vol. 15, no. 12, p. e0236495, 2021.
- [149] V. L. Ríos, P. G. Özdil, S. T. Ramalingasetty, J. Arreguit, S. Clerc Rosset, G. Knott, A. J. Ijspeert, and P. Ramdya, “Neuromechfly, a neuromechanical model of adult *Drosophila melanogaster*,” *bioRxiv*, p. 2021.04.17.440214, 2021.
- [150] J. M. Graving, “behavelet: a wavelet transform for mapping behavior,” 2019.
- [151] G. Ke, Q. Meng, T. Finley, T. Wang, W. Chen, W. Ma, Q. Ye, and T.-Y. Liu, “LightGBM: a highly efficient gradient boosting decision tree,” in *Advances in Neural Information Processing Systems*, I. Guyon, U. V. Luxburg, S. Bengio, H. Wallach, R. Fergus, S. Vishwanathan, and R. Garnett, Eds., vol. 30. Curran Associates, Inc., 2017.
- [152] N. V. Chawla, K. W. Bowyer, L. O. Hall, and W. P. Kegelmeyer, “SMOTE: Synthetic minority over-sampling technique,” *Journal of Artificial Intelligence Research*, vol. 16, pp. 321–357, 2002.
- [153] J. Friedman, T. Hastie, and R. Tibshirani, “Regularization paths for generalized linear models via coordinate descent,” *Journal of Statistical Software*, vol. 33, no. 1, pp. 1–22, 2010.
- [154] N. M. Razali and Y. B. Wah, “Power comparisons of Shapiro-Wilk , Kolmogorov-Smirnov , Lilliefors and Anderson-Darling tests,” *Journal of Statistical Modeling and Analytics*, vol. 2, no. 1, pp. 21–23, 2011.

Bibliography

- [155] O. Ronneberger, P. Fischer, and T. Brox, "U-Net: convolutional networks for biomedical image segmentation," in *Medical Image Computing and Computer-Assisted Intervention (MICCAI)*, ser. LNCS, vol. 9351. Springer, 2015, pp. 234–241.
- [156] C. Payer, D. Štern, T. Neff, H. Bischof, and M. Urschler, "Instance segmentation and tracking with cosine embeddings and recurrent hourglass networks," in *Medical Image Computing and Computer Assisted Intervention – MICCAI 2018*, A. F. Frangi, J. A. Schnabel, C. Davatzikos, C. Alberola-López, and G. Fichtinger, Eds. Cham: Springer International Publishing, 2018, pp. 3–11.
- [157] O. Çiçek, A. Abdulkadir, S. Lienkamp, T. Brox, and O. Ronneberger, "3D U-Net: Learning dense volumetric segmentation from sparse annotation," *arXiv*, p. 1606.06650, 2016.
- [158] P. Wang, N. G. Cuccolo, R. Tyagi, I. Hacihaliloglu, and V. M. Patel, "Automatic real-time CNN-based neonatal brain ventricles segmentation," in *2018 IEEE 15th International Symposium on Biomedical Imaging (ISBI 2018)*, 2018, pp. 716–719.
- [159] S. Ioffe and C. Szegedy, "Batch normalization: accelerating deep network training by reducing internal covariate shift," ser. Proceedings of Machine Learning Research, F. Bach and D. Blei, Eds., vol. 37. Lille, France: PMLR, 2015, pp. 448–456.
- [160] D. P. Kingma and J. Ba, "Adam: A method for stochastic optimization," *arXiv*, p. 1412.6980, 2017.
- [161] T. J. Sørensen, "A method of establishing groups of equal amplitude in plant sociology based on similarity of species content and its application to analyses of the vegetation on danish commons," *Biol. Skar.*, vol. 5, pp. 1–34, 1948.
- [162] L. R. Dice, "Measures of the amount of ecologic association between species," *Ecology*, vol. 26, no. 3, pp. 297–302, 1945.
- [163] A. Buades, B. Coll, and J. M. Morel, "Denoising image sequences does not require motion estimation," in *IEEE Conference on Advanced Video and Signal Based Surveillance, 2005.*, 2005, pp. 70–74.
- [164] G. Bradski, "The OpenCV library," *Dr. Dobb's Journal of Software Tools*, vol. 122-125, p. 120, 2000.
- [165] N. Otsu, "A threshold selection method from gray-level histograms," *IEEE Transactions on Systems, Man, and Cybernetics*, vol. 9, no. 1, pp. 62–66, 1979.
- [166] M. Ankerst, M. M. Breunig, H.-P. Kriegel, and J. Sander, "OPTICS: ordering points to identify the clustering structure," in *Proceedings of the 1999 ACM SIGMOD International Conference on Management of Data*, ser. SIGMOD '99. New York, NY, USA: Association for Computing Machinery, 1999, p. 49–60.

- [167] H. W. Kuhn, "The Hungarian method for the assignment problem," *Naval Research Logistics Quarterly*, vol. 2, no. 1-2, pp. 83–97, 1955.
- [168] S. van der Walt, J. L. Schönberger, J. Nunez-Iglesias, F. Boulogne, J. D. Warner, N. Yager, E. Gouillart, T. Yu, and the scikit-image contributors, "scikit-image: image processing in Python," *PeerJ*, vol. 2, p. e453, 2014.
- [169] M. Guizar, *Efficient subpixel image registration by cross-correlation*, 2020, (<https://www.mathworks.com/matlabcentral/fileexchange/18401-efficient-subpixel-image-registration-by-cross-correlation>), MATLAB Central File Exchange. Retrieved November 9, 2020.
- [170] R. E. Ritzmann and A. Büschges, "Adaptive motor behavior in insects," *Current Opinion in Neurobiology*, vol. 17, no. 6, pp. 629–636, 2007.
- [171] R. E. Ritzmann, R. D. Quinn, and M. S. Fischer, "Convergent evolution and locomotion through complex terrain by insects, vertebrates and robots," *Arthropod Structure Development*, vol. 33, no. 3, pp. 361–379, 2004.
- [172] C. S. Mendes, S. V. Rajendren, I. Bartos, S. Márka, and R. S. Mann, "Kinematic responses to changes in walking orientation and gravitational load in *Drosophila melanogaster*," *PLOS ONE*, vol. 9, no. 10, 2014.
- [173] S. Pick and R. Strauss, "Goal-driven behavioral adaptations in gap-climbing *Drosophila*," *Current Biology*, vol. 15, no. 16, pp. 1473–1478, 2005.
- [174] B. Blaesing and H. Cruse, "Stick insect locomotion in a complex environment: climbing over large gaps," *Journal of Experimental Biology*, vol. 207, no. 8, pp. 1273–1286, 2004.
- [175] R. Strauss and M. Heisenberg, "Coordination of legs during straight walking and turning in *Drosophila melanogaster*," *Journal of comparative physiology. A, Sensory, neural, and behavioral physiology*, vol. 167, no. 3, p. 403–412, 1990.
- [176] E. Couzin-Fuchs, T. Kiemel, O. Gal, A. Ayali, and P. Holmes, "Intersegmental coupling and recovery from perturbations in freely running cockroaches," *Journal of Experimental Biology*, vol. 218, no. 2, pp. 285–297, 2015.
- [177] K. G. Pearson, "Common principles of motor control in vertebrates and invertebrates," *Annual Review of Neuroscience*, vol. 16, no. 1, pp. 265–297, 1993.
- [178] D. Graham, "Pattern and control of walking in insects," ser. *Advances in Insect Physiology*, M. Berridge, J. Treherne, and V. Wigglesworth, Eds. Academic Press, 1985, vol. 18, pp. 31–140.
- [179] L. Venkatasubramanian and R. S. Mann, "The development and assembly of the *Drosophila* adult ventral nerve cord," *Current Opinion in Neurobiology*, vol. 56, pp. 135–143, 2019.

Bibliography

- [180] J. W. Truman, H. Schuppe, D. Shepherd, and D. W. Williams, "Developmental architecture of adult-specific lineages in the ventral CNS of *Drosophila*," *Development*, vol. 131, no. 20, pp. 5167–5184, 2004.
- [181] M. Baek and R. S. Mann, "Lineage and birth date specify motor neuron targeting and dendritic architecture in adult *Drosophila*," *Journal of Neuroscience*, vol. 29, no. 21, pp. 6904–6916, 2009.
- [182] D. J. Brierley, E. Blanc, O. V. Reddy, K. Vijayraghavan, and D. W. Williams, "Dendritic targeting in the leg neuropil of *Drosophila*: the role of midline signalling molecules in generating a myotopic map," *PLoS biology*, vol. 7, no. 9, p. e1000199, 2009.
- [183] R. Murphey, D. Possidente, P. Vandervorst, and A. Ghysen, "Compartments and the topography of leg afferent projections in *Drosophila*," *Journal of Neuroscience*, vol. 9, no. 9, pp. 3209–3217, 1989.
- [184] A. Buschges, "Sensory control and organization of neural networks mediating coordination of multisegmental organs for locomotion," *Journal of neurophysiology*, vol. 93, no. 3, pp. 1127–1135, 2005.
- [185] L. H. Field and T. Matheson, "Chordotonal organs of insects," in *Advances in insect physiology*. Elsevier, 1998, vol. 27, pp. 1–228.
- [186] C. Yellman, H. Tao, B. He, and J. Hirsh, "Conserved and sexually dimorphic behavioral responses to biogenic amines in decapitated *Drosophila*," *Proceedings of the national academy of sciences*, vol. 94, no. 8, pp. 4131–4136, 1997.
- [187] M. Burrows, "Local circuits for the control of leg movements in an insect," *Trends in neurosciences*, vol. 15, no. 6, pp. 226–232, 1992.
- [188] W. Stein, A. Büschges, and U. Bässler, "Intersegmental transfer of sensory signals in the stick insect leg muscle control system," *Journal of neurobiology*, vol. 66, no. 11, pp. 1253–1269, 2006.
- [189] A. Büschges and A. El Manira, "Sensory pathways and their modulation in the control of locomotion," *Current opinion in neurobiology*, vol. 8, no. 6, pp. 733–739, 1998.
- [190] K. G. Pearson, "Proprioceptive regulation of locomotion," *Current opinion in neurobiology*, vol. 5, no. 6, pp. 786–791, 1995.
- [191] S. Grillner and P. Zangger, "On the central generation of locomotion in the low spinal cat," *Experimental brain research*, vol. 34, no. 2, pp. 241–261, 1979.
- [192] A. Bekoff, M. P. Nusbaum, A. L. Sabichi, and M. Clifford, "Neural control of limb coordination. i. comparison of hatching and walking motor output patterns in normal and deafferented chicks," *Journal of Neuroscience*, vol. 7, no. 8, pp. 2320–2330, 1987.

- [193] S. Rossignol, R. Dubuc, and J.-P. Gossard, "Dynamic sensorimotor interactions in locomotion," *Physiological reviews*, vol. 86, no. 1, pp. 89–154, 2006.
- [194] K. Pearson, "Neural adaptation in the generation of rhythmic behavior," *Annual review of physiology*, vol. 62, no. 1, pp. 723–753, 2000.
- [195] E. Marder, "Neuromodulation of neuronal circuits: back to the future," *Neuron*, vol. 76, no. 1, pp. 1–11, 2012.
- [196] P. S. Dickinson, "Neuromodulation of central pattern generators in invertebrates and vertebrates," *Current opinion in neurobiology*, vol. 16, no. 6, pp. 604–614, 2006.
- [197] R. M. Harris-Warrick, "Neuromodulation and flexibility in central pattern generator networks," *Current opinion in neurobiology*, vol. 21, no. 5, pp. 685–692, 2011.
- [198] D. Morton and H. Chiel, "Neural architectures for adaptive behavior," *Trends in neurosciences*, vol. 17, no. 10, pp. 413–420, 1994.
- [199] H. Barbeau and S. Rossignol, "Initiation and modulation of the locomotor pattern in the adult chronic spinal cat by noradrenergic, serotonergic and dopaminergic drugs," *Brain research*, vol. 546, no. 2, pp. 250–260, 1991.
- [200] R. M. Harris-Warrick and A. H. Cohen, "Serotonin modulates the central pattern generator for locomotion in the isolated lamprey spinal cord," *Journal of Experimental Biology*, vol. 116, no. 1, pp. 27–46, 1985.
- [201] D. Parker, "Serotonergic modulation of locust motor neurons," *Journal of neurophysiology*, vol. 73, no. 3, pp. 923–932, 1995.
- [202] S. D. Albin, K. R. Kaun, J.-M. Knapp, P. Chung, U. Heberlein, and J. H. Simpson, "A subset of serotonergic neurons evokes hunger in adult *Drosophila*," *Current Biology*, vol. 25, no. 18, pp. 2435–2440, 2015.
- [203] Z. R. Majeed, E. Abdeljaber, R. Soveland, K. Cornwell, A. Bankemper, F. Koch, and R. L. Cooper, "Modulatory action by the serotonergic system: behavior and neurophysiology in *Drosophila melanogaster*," *Neural plasticity*, vol. 2016, 2016.
- [204] F. Mohammad, S. Aryal, J. Ho, J. C. Stewart, N. A. Norman, T. L. Tan, A. Eisaka, and A. Claridge-Chang, "Ancient anxiety pathways influence *Drosophila* defense behaviors," *Current Biology*, vol. 26, no. 7, pp. 981–986, 2016.
- [205] A. Pooryasin and A. Fiala, "Identified serotonin-releasing neurons induce behavioral quiescence and suppress mating in *Drosophila*," *Journal of Neuroscience*, vol. 35, no. 37, pp. 12 792–12 812, 2015.

Bibliography

- [206] Y. Qian, Y. Cao, B. Deng, G. Yang, J. Li, R. Xu, J. Huang, Y. Rao *et al.*, “Sleep homeostasis regulated by 5ht2b receptor in a small subset of neurons in the dorsal fan-shaped body of *Drosophila*,” *Elife*, vol. 6, p. e26519, 2017.
- [207] O. V. Alekseyenko, C. Lee, and E. A. Kravitz, “Targeted manipulation of serotonergic neurotransmission affects the escalation of aggression in adult male *Drosophila melanogaster*,” *PLoS one*, vol. 5, no. 5, p. e10806, 2010.
- [208] O. V. Alekseyenko, Y.-B. Chan, M. de la Paz Fernandez, T. Bülow, M. J. Pankratz, and E. A. Kravitz, “Single serotonergic neurons that modulate aggression in *Drosophila*,” *Current Biology*, vol. 24, no. 22, pp. 2700–2707, 2014.
- [209] T. Riemensperger, G. Isabel, H. Coulom, K. Neuser, L. Seugnet, K. Kume, M. Iché-Torres, M. Cassar, R. Strauss, T. Preat *et al.*, “Behavioral consequences of dopamine deficiency in the *Drosophila* central nervous system,” *Proceedings of the National Academy of Sciences*, vol. 108, no. 2, pp. 834–839, 2011.
- [210] T. Ueno, N. Masuda, S. Kume, and K. Kume, “Dopamine modulates the rest period length without perturbation of its power law distribution in *Drosophila melanogaster*,” *PLoS One*, vol. 7, no. 2, p. e32007, 2012.
- [211] R. G. Pendleton, A. Rasheed, T. Sardina, T. Tully, and R. Hillman, “Effects of tyrosine hydroxylase mutants on locomotor activity in *Drosophila*: a study in functional genomics,” *Behavior genetics*, vol. 32, no. 2, pp. 89–94, 2002.
- [212] Z. Yang, Y. Yu, V. Zhang, Y. Tian, W. Qi, and L. Wang, “Octopamine mediates starvation-induced hyperactivity in adult *Drosophila*,” *Proceedings of the National Academy of Sciences*, vol. 112, no. 16, pp. 5219–5224, 2015.
- [213] B. Brembs, F. Christiansen, H. J. Pflüger, and C. Duch, “Flight initiation and maintenance deficits in flies with genetically altered biogenic amine levels,” *Journal of Neuroscience*, vol. 27, no. 41, pp. 11 122–11 131, 2007.
- [214] F. Friggi-Grelin, H. Coulom, M. Meller, D. Gomez, J. Hirsh, and S. Birman, “Targeted gene expression in *Drosophila* dopaminergic cells using regulatory sequences from tyrosine hydroxylase,” *Journal of Neurobiology*, vol. 54, no. 4, pp. 618–627, 2003.
- [215] S. H. Cole, G. E. Carney, C. A. McClung, S. S. Willard, B. J. Taylor, and J. Hirsh, “Two functional but noncomplementing *Drosophila* tyrosine decarboxylase genes: distinct roles for neural tyramine and octopamine in female fertility,” *Journal of Biological Chemistry*, vol. 280, no. 15, pp. 14 948–14 955, 2005.
- [216] K. Branson, A. A. Robie, J. Bender, P. Perona, and M. H. Dickinson, “High-throughput ethomics in large groups of *Drosophila*,” *Nature Methods*, vol. 6, no. 6, pp. 451–457, 2009.

- [217] E. Eyjolfsson, S. Branson, X. P. Burgos-Artizzu, E. D. Hoopfer, J. Schor, D. J. Anderson, and P. Perona, "Detecting social actions of fruit flies," in *Computer Vision – ECCV 2014*, D. Fleet, T. Pajdla, B. Schiele, and T. Tuytelaars, Eds. Cham: Springer International Publishing, 2014, pp. 772–787.
- [218] P. Gibert, R. B. Huey, and G. W. Gilchrist, "Locomotor performance of *Drosophila melanogaster*: interactions among developmental and adult temperatures, age, and geography," *Evolution*, vol. 55, no. 1, pp. 205–209, 2001.
- [219] W. Cho, U. Heberlein, and F. Wolf, "Habituation of an odorant-induced startle response in *Drosophila*," *Genes, Brain and Behavior*, vol. 3, no. 3, pp. 127–137, 2004.
- [220] G. Lee and J. H. Park, "Hemolymph sugar homeostasis and starvation-induced hyperactivity affected by genetic manipulations of the adipokinetic hormone-encoding gene in *Drosophila melanogaster*," *Genetics*, vol. 167, no. 1, pp. 311–323, 2004.
- [221] J. S. Yeomans, L. Li, B. W. Scott, and P. W. Frankland, "Tactile, acoustic and vestibular systems sum to elicit the startle reflex," *Neuroscience & Biobehavioral Reviews*, vol. 26, no. 1, pp. 1–11, 2002.
- [222] J. S. Yeomans and P. W. Frankland, "The acoustic startle reflex: neurons and connections," *Brain research reviews*, vol. 21, no. 3, pp. 301–314, 1995.
- [223] G. M. Card, "Escape behaviors in insects," *Current opinion in neurobiology*, vol. 22, no. 2, pp. 180–186, 2012.
- [224] M. Davis, "The mammalian startle response," in *Neural mechanisms of startle behavior*. Springer, 1984, pp. 287–351.
- [225] F. Saudou and R. Hen, "5-hydroxytryptamine receptor subtypes in vertebrates and invertebrates," *Neurochemistry international*, vol. 25, no. 6, pp. 503–532, 1994.
- [226] A. J. Tierney, "Invertebrate serotonin receptors: a molecular perspective on classification and pharmacology," *Journal of Experimental Biology*, vol. 221, no. 19, p. jeb184838, 2018.
- [227] F. Saudou, U. Boschert, N. Amlaiky, J.-L. Plassat, and R. Hen, "A family of *Drosophila* serotonin receptors with distinct intracellular signalling properties and expression patterns." *The EMBO journal*, vol. 11, no. 1, pp. 7–17, 1992.
- [228] P. Witz, N. Amlaiky, J. Plassat, L. Maroteaux, E. Borrelli, and R. Hen, "Cloning and characterization of a *Drosophila* serotonin receptor that activates adenylate cyclase." *Proceedings of the National Academy of Sciences*, vol. 87, no. 22, pp. 8940–8944, 1990.
- [229] W. Blenau, S. Daniel, S. Balfanz, M. Thamm, and A. Baumann, "Dm5-HT2b: pharmacological characterization of the fifth serotonin receptor subtype of *Drosophila melanogaster*," *Frontiers in systems neuroscience*, vol. 11, p. 28, 2017.

Bibliography

- [230] J.-F. Colas, J.-M. Launay, O. Kellermann, P. Rosay, and L. Maroteaux, "Drosophila 5-HT₂ serotonin receptor: coexpression with fushi-tarazu during segmentation," *Proceedings of the National Academy of Sciences*, vol. 92, no. 12, pp. 5441–5445, 1995.
- [231] J. P. Gnerer, K. J. Venken, and H. A. Dierick, "Gene-specific cell labeling using mimic transposons," *Nucleic acids research*, vol. 43, no. 8, pp. e56–e56, 2015.
- [232] S. C. Veasey, C. Fornal, C. Metzler, and B. L. Jacobs, "Response of serotonergic caudal raphe neurons in relation to specific motor activities in freely moving cats," *Journal of Neuroscience*, vol. 15, no. 7, pp. 5346–5359, 1995.
- [233] S. Veasey, C. Fornal, C. Metzler, and B. Jacobs, "Single-unit responses of serotonergic dorsal raphe neurons to specific motor challenges in freely moving cats," *Neuroscience*, vol. 79, no. 1, pp. 161–169, 1997.
- [234] P. A. Correia, E. Lottem, D. Banerjee, A. S. Machado, M. R. Carey, and Z. F. Mainen, "Transient inhibition and long-term facilitation of locomotion by phasic optogenetic activation of serotonin neurons," *Elife*, vol. 6, p. e20975, 2017.
- [235] W. T. Gibson, C. R. Gonzalez, C. Fernandez, L. Ramasamy, T. Tabachnik, R. R. Du, P. D. Felsen, M. R. Maire, P. Perona, and D. J. Anderson, "Behavioral responses to a repetitive visual threat stimulus express a persistent state of defensive arousal in *Drosophila*," *Current Biology*, vol. 25, no. 11, pp. 1401–1415, 2015.
- [236] K. G. Pearson and M. O'Shea, "Escape behavior of the locust," in *Neural mechanisms of startle behavior*. Springer, 1984, pp. 163–178.
- [237] R. E. Ritzmann, "The cockroach escape response," in *Neural mechanisms of startle behavior*. Springer, 1984, pp. 93–131.
- [238] M. Davis and M. H. Sheard, "Habituation and sensitization of the rat startle response: Effects of raphe lesions," *Physiology & behavior*, vol. 12, no. 3, pp. 425–431, 1974.
- [239] P. L. Carlton and C. Advokat, "Attenuated habituation due to parachlorophenylalanine," *Pharmacology Biochemistry and Behavior*, vol. 1, no. 6, pp. 657–663, 1973.
- [240] M. Davis, D. I. Strachan, and E. Kass, "Excitatory and inhibitory effects of serotonin on sensorimotor reactivity measured with acoustic startle," *Science*, vol. 209, no. 4455, pp. 521–523, 1980.
- [241] D. I. Astrachan and M. Davis, "Spinal modulation of the acoustic startle response: The role of norepinephrine, serotonin, and dopamine." *Brain Research*, no. 1, pp. 223–228, 1981.
- [242] J.-F. Perrier and F. Cotel, "Serotonergic modulation of spinal motor control," *Current opinion in neurobiology*, vol. 33, pp. 1–7, 2015.

- [243] M. D. Johnson and C. J. Heckman, "Gain control mechanisms in spinal motoneurons," *Frontiers in neural circuits*, vol. 8, p. 81, 2014.
- [244] G. Cappellini, Y. P. Ivanenko, N. Dominici, R. E. Poppele, and F. Lacquaniti, "Motor patterns during walking on a slippery walkway," *Journal of neurophysiology*, vol. 103, no. 2, pp. 746–760, 2010.
- [245] A. S. Voloshina and D. P. Ferris, "Biomechanics and energetics of running on uneven terrain," *The journal of experimental biology*, vol. 218, no. 5, pp. 711–719, 2015.
- [246] R. G. Kavlie and J. T. Albert, "Chordotonal organs," *Current Biology*, vol. 23, no. 9, pp. R334–R335, 2013.
- [247] R. W. Daniels, M. V. Gelfand, C. A. Collins, and A. DiAntonio, "Visualizing glutamatergic cell bodies and synapses in *Drosophila* larval and adult cns," *Journal of Comparative Neurology*, vol. 508, no. 1, pp. 131–152, 2008.
- [248] E. Ryder, F. Blows, M. Ashburner, R. Bautista-Llacer, D. Coulson, J. Drummond, J. Webster, D. Gubb, N. Gunton, G. Johnson *et al.*, "The drosdel collection: a set of p-element insertions for generating custom chromosomal aberrations in *Drosophila melanogaster*," *Genetics*, vol. 167, no. 2, pp. 797–813, 2004.
- [249] A. Burgos, K. Honjo, T. Ohyama, C. S. Qian, G. J.-e. Shin, D. M. Gohl, M. Silies, W. D. Tracey, M. Zlatic, A. Cardona *et al.*, "Nociceptive interneurons control modular motor pathways to promote escape behavior in *Drosophila*," *Elife*, vol. 7, p. e26016, 2018.
- [250] N. C. Klapoetke, Y. Murata, S. S. Kim, S. R. Pulver, A. Birdsey-Benson, Y. K. Cho, T. K. Morimoto, A. S. Chuong, E. J. Carpenter, Z. Tian *et al.*, "Independent optical excitation of distinct neural populations," *Nature methods*, vol. 11, no. 3, pp. 338–346, 2014.
- [251] R. C. Hardie, P. Raghu, S. Moore, M. Juusola, R. A. Baines, and S. T. Sweeney, "Calcium influx via trp channels is required to maintain pip2 levels in *Drosophila* photoreceptors," *Neuron*, vol. 30, no. 1, pp. 149–159, 2001.
- [252] H. K. Shearin, I. S. Macdonald, L. P. Spector, and R. S. Stowers, "Hexameric gfp and mcherry reporters for the *Drosophila* gal4, q, and lexa transcription systems," *Genetics*, vol. 196, no. 4, pp. 951–960, 2014.
- [253] A. D. Straw and M. H. Dickinson, "Motmot, an open-source toolkit for realtime video acquisition and analysis," *Source code for biology and medicine*, vol. 4, p. 9, 2009.
- [254] T. J. Horder, "Syllabus for an embryological synthesis," in *Complex Organizational Functions: Integration and Evolution in Vertebrates*. John Wiley, New York., 1989, pp. 1–451.

Bibliography

- [255] P. Ramdya and R. Benton, “Evolving olfactory systems on the fly,” *Trends in Genetics*, vol. 26, no. 7, pp. 307–316, 2010.
- [256] S. Herculano-Houzel, P. R. Manger, and J. H. Kaas, “Brain scaling in mammalian evolution as a consequence of concerted and mosaic changes in numbers of neurons and average neuronal cell size,” *Frontiers in neuroanatomy*, vol. 8, p. 77, 2014.
- [257] C. J. Charvet, G. F. Striedter, and B. L. Finlay, “Evo-devo and brain scaling: candidate developmental mechanisms for variation and constancy in vertebrate brain evolution,” *Brain, behavior and evolution*, vol. 78, no. 3, pp. 248–257, 2011.
- [258] L. Biffar and A. Stollewerk, “Conservation and evolutionary modifications of neuroblast expression patterns in insects,” *Developmental Biology*, vol. 388, no. 1, pp. 103–116, 2014.
- [259] P. Rakic, “Evolution of the neocortex: perspective from developmental biology. nat. rev.,” *Nature Reviews Neuroscience*, vol. 10, p. 724–735, 2009.
- [260] J. Truman and E. E. Ball, “Patterns of embryonic neurogenesis in a primitive wingless insect, the silverfish, *Ctenolepisma longicaudata*: comparison with those seen in flying insects,” *Development genes and evolution*, vol. 208, no. 7, pp. 357–368, 1998.
- [261] L. L. Prieto-Godino, A. F. Silbering, M. A. Khallaf, S. Cruchet, K. Bojkowska, S. Pradervand, B. S. Hansson, M. Knaden, and R. Benton, “Functional integration of “undead” neurons in the olfactory system,” *Science advances*, vol. 6, no. 11, p. eaaz7238, 2020.
- [262] C. Bate, “Embryogenesis of an insect nervous system i. a map of the thoracic and abdominal neuroblasts in *Locusta migratoria*,” vol. 35, no. 1, pp. 107–123, 1976.
- [263] R. Booker and J. W. Truman, “Postembryonic neurogenesis in the cns of the tobacco hornworm, *manduca sexta*. i. neuroblast arrays and the fate of their progeny during metamorphosis,” *Journal of Comparative Neurology*, vol. 255, no. 4, pp. 548–559, 1987.
- [264] C. Q. Doe, “Molecular markers for identified neuroblasts and ganglion mother cells in the *Drosophila* central nervous system,” *Development*, vol. 116, no. 4, pp. 855–863, 1992.
- [265] V. Hartenstein and J. A. Campos-Ortega, “Early neurogenesis in wild-type *Drosophila melanogaster*,” *Wilhelm Roux’s archives of developmental biology*, vol. 193, no. 5, pp. 308–325, 1984.
- [266] R. H. Nordlander and J. S. Edwards, “Postembryonic brain development in the monarch butterfly, *danaus plexippus plexippus*, l.” *Wilhelm Roux’Archiv für Entwicklungsmechanik der Organismen*, vol. 162, no. 3, pp. 197–217, 1969.
- [267] D. Shepherd and C. Bate, “Spatial and temporal patterns of neurogenesis in the embryo of the locust (*schistocerca gregaria*),” *Development*, vol. 108, no. 1, pp. 83–96, 1990.

- [268] M. Tamarelle, A. Haget, and A. Ressouches, "Segregation, division, and early patterning of lateral thoracic neuroblasts in the embryos of *Carausius morosus* br.(phasmida: Lonchodidae)," *International Journal of Insect Morphology and Embryology*, vol. 14, no. 5, pp. 307–317, 1985.
- [269] J. W. TRUMAN, "Metamorphosis of the insect nervous system," in *Metamorphosis*. Elsevier, 1996, pp. 1–687.
- [270] J. W. Truman and M. Bate, "Spatial and temporal patterns of neurogenesis in the central nervous system of *Drosophila melanogaster*," *Developmental biology*, vol. 125, no. 1, pp. 145–157, 1988.
- [271] W. M. Wheeler, "Neuroblasts in the arthropod embryo," *Journal of Morphology*, vol. 4, p. 337–343, 1891.
- [272] J. Enriquez, L. Q. Rio, R. Blazeski, S. Bellemin, P. Godement, C. Mason, and R. S. Mann, "Differing strategies despite shared lineages of motor neurons and glia to achieve robust development of an adult neuropil in *Drosophila*," *Neuron*, vol. 97, no. 3, pp. 538–554, 2018.
- [273] H. Lacin and J. W. Truman, "Lineage mapping identifies molecular and architectural similarities between the larval and adult *Drosophila* central nervous system," *Elife*, vol. 5, p. e13399, 2016.
- [274] J. W. Truman, "Metamorphosis of the central nervous system of *Drosophila*," *Journal of neurobiology*, vol. 21, no. 7, pp. 1072–1084, 1990.
- [275] H. Lacin, H.-M. Chen, X. Long, R. H. Singer, T. Lee, and J. W. Truman, "Neurotransmitter identity is acquired in a lineage-restricted manner in the *Drosophila* cns," *Elife*, vol. 8, p. e43701, 2019.
- [276] S. Lin, S.-L. Lai, H.-H. Yu, T. Chihara, L. Luo, and T. Lee, "Lineage-specific effects of notch/numb signaling in post-embryonic development of the *Drosophila* brain," *Development*, vol. 137, no. 1, pp. 43–51, 2010.
- [277] D. Shepherd, V. Sahota, R. Court, D. W. Williams, and J. W. Truman, "Developmental organization of central neurons in the adult *Drosophila* ventral nervous system," *Journal of Comparative Neurology*, vol. 527, no. 15, pp. 2573–2598, 2019.
- [278] J. W. Truman, W. Moats, J. Altman, E. C. Marin, and D. W. Williams, "Role of notch signaling in establishing the hemilineages of secondary neurons in *Drosophila melanogaster*," *Development*, vol. 137, no. 1, pp. 53–61, 2010.
- [279] C. Bertet, X. Li, T. Erclik, M. Cavey, B. Wells, and C. Desplan, "Temporal patterning of neuroblasts controls notch-mediated cell survival through regulation of hid or reaper," *Cell*, vol. 158, no. 5, pp. 1173–1186, 2014.

Bibliography

- [280] A. Kumar, B. Bello, and H. Reichert, "Lineage-specific cell death in postembryonic brain development of *Drosophila*," *Development*, vol. 136, no. 20, pp. 3433–3442, 2009.
- [281] C. Q. Doe and C. S. Goodman, "Early events in insect neurogenesis: I. development and segmental differences in the pattern of neuronal precursor cells," *Developmental biology*, vol. 111, no. 1, pp. 193–205, 1985.
- [282] H. R. Campbell, K. J. Thompson, and M. V. Siegler, "Neurons of the median neuroblast lineage of the grasshopper: a population study of the efferent dum neurons," *Journal of Comparative Neurology*, vol. 358, no. 4, pp. 541–551, 1995.
- [283] X. X. Jia and M. V. Siegler, "Midline lineages in grasshopper produce neuronal siblings with asymmetric expression of engrailed," vol. 129, no. 22, p. 5181–5193, 2002.
- [284] H.-J. Pflüger and P. Stevenson, "Evolutionary aspects of octopaminergic systems with emphasis on arthropods," *Arthropod Structure & Development*, vol. 34, no. 3, pp. 379–396, 2005.
- [285] H. F. Rowell, "The cells of the insect neurosecretory system: constancy, variability, and the concept of the unique identifiable neuron," in *Advances in Insect Physiology*. Elsevier, 1976, vol. 12, pp. 63–123.
- [286] M. V. Siegler and R. R. Pankhaniya, "Engrailed protein is expressed in interneurons but not motor neurons of the dorsal unpaired median group in the adult grasshopper," *Journal of Comparative Neurology*, vol. 388, no. 4, pp. 658–668, 1997.
- [287] M. V. Siegler, P. E. MANLEY JR, and K. J. THOMPSON, "Sulphide silver staining for endogenous heavy metals reveals subsets of dorsal unpaired median (dum) neurones in insects," *The Journal of Experimental Biology*, vol. 157, pp. 565–571, 1991.
- [288] M. V. Siegler, R. R. Pankhaniya, and X. X. Jia, "Pattern of expression of engrailed in relation to gamma-aminobutyric acid immunoreactivity in the central nervous system of the adult grasshopper," *Journal of Comparative Neurology*, vol. 440, no. 1, pp. 85–96, 2001.
- [289] P. A. Stevenson and U. Spörhase-Eichmann, "Localization of octopaminergic neurones in insects," *Comparative Biochemistry and Physiology Part A: Physiology*, vol. 110, no. 3, pp. 203–215, 1995.
- [290] K. J. Thompson and M. V. Siegler, "Anatomy and physiology of spiking local and inter-segmental interneurons in the median neuroblast lineage of the grasshopper," *Journal of comparative neurology*, vol. 305, no. 4, pp. 659–675, 1991.
- [291] J. Witten and J. Truman, "Distribution of gaba-like immunoreactive neurons in insects suggests lineage homology," *Journal of Comparative Neurology*, vol. 398, no. 4, pp. 515–528, 1998.

- [292] S. Sombati and G. Hoyle, "Generation of specific behaviors in a locust by local release into neuropil of the natural neuromodulator octopamine," *Journal of neurobiology*, vol. 15, no. 6, pp. 481–506, 1984.
- [293] J. Rillich, P. A. Stevenson, and H.-J. Pflueger, "Flight and walking in locusts—cholinergic co-activation, temporal coupling and its modulation by biogenic amines," *PLoS One*, vol. 8, no. 5, p. e62899, 2013.
- [294] F. Pinto-Teixeira, N. Konstantinides, and C. Desplan, "Programmed cell death acts at different stages of *Drosophila* neurodevelopment to shape the central nervous system," *FEBS letters*, vol. 590, no. 15, pp. 2435–2453, 2016.
- [295] T. A. Draizen, J. Ewer, and S. Robinow, "Genetic and hormonal regulation of the death of peptidergic neurons in the *Drosophila* central nervous system," *Journal of neurobiology*, vol. 38, no. 4, pp. 455–465, 1999.
- [296] K. Kimura and J. W. Truman, "Postmetamorphic cell death in the nervous and muscular systems of *Drosophila melanogaster*," *Journal of Neuroscience*, vol. 10, no. 2, pp. 403–411, 1990.
- [297] R. H. Nordlander and J. S. Edwards, "Morphological cell death in the post-embryonic development of the insect optic lobes," *Nature*, vol. 218, no. 5143, pp. 780–781, 1968.
- [298] J. K. Lovick, J. J. Omoto, K. T. Ngo, and V. Hartenstein, "Development of the anterior visual input pathway to the *Drosophila* central complex," *Journal of Comparative Neurology*, vol. 525, no. 16, pp. 3458–3475, 2017.
- [299] P.-L. Bardet, G. Kolahgar, A. Mynett, I. Miguel-Aliaga, J. Briscoe, P. Meier, and J.-P. Vincent, "A fluorescent reporter of caspase activity for live imaging," *Proceedings of the National Academy of Sciences*, vol. 105, no. 37, pp. 13 901–13 905, 2008.
- [300] A. M. Allen, M. C. Neville, S. Birtles, V. Croset, C. D. Treiber, S. Waddell, and S. F. Goodwin, "A single-cell transcriptomic atlas of the adult *Drosophila* ventral nerve cord," *Elife*, vol. 9, 2020.
- [301] H. Lacin, Y. Zhu, B. A. Wilson, and J. B. Skeath, "Transcription factor expression uniquely identifies most postembryonic neuronal lineages in the *Drosophila* thoracic central nervous system," *Development*, vol. 141, no. 5, pp. 1011–1021, 2014.
- [302] M. Landgraf, N. Sánchez-Soriano, G. M. Technau, J. Urban, and A. Prokop, "Charting the *Drosophila* neuropile: a strategy for the standardised characterisation of genetically amenable neurites," *Developmental biology*, vol. 260, no. 1, pp. 207–225, 2003.
- [303] C. Peterson, G. E. Carney, B. J. Taylor, and K. White, "reaper is required for neuroblast apoptosis during *Drosophila* development," *Development*, vol. 129, no. 6, p. 1467–1476, 2002.

Bibliography

- [304] C. L. Greer, A. Grygoruk, D. E. Patton, B. Ley, R. Romero-Calderon, H.-Y. Chang, R. Houshyar, R. J. Bainton, A. Diantonio, and D. E. Krantz, "A splice variant of the *Drosophila* vesicular monoamine transporter contains a conserved trafficking domain and functions in the storage of dopamine, serotonin, and octopamine," *Journal of neurobiology*, vol. 64, no. 3, pp. 239–258, 2005.
- [305] S. Kondo, N. Senoo-Matsuda, Y. Hiromi, and M. Miura, "Dronc coordinates cell death and compensatory proliferation," *Molecular and cellular biology*, vol. 26, no. 19, pp. 7258–7268, 2006.
- [306] M. Monastirioti, M. Gorczyca, J. Rapus, M. Eckert, K. White, and V. Budnik, "Octopamine immunoreactivity in the fruit fly *Drosophila melanogaster*," *Journal of Comparative Neurology*, vol. 356, no. 2, pp. 275–287, 1995.
- [307] D. Pauls, C. Blechschmidt, F. Frantzmam, B. El Jundi, and M. Selcho, "A comprehensive anatomical map of the peripheral octopaminergic/tyraminergetic system of *Drosophila melanogaster*," *Scientific Reports*, vol. 8, no. 1, pp. 1–12, 2018.
- [308] T. Roeder, "Tyramine and octopamine: ruling behavior and metabolism," *Annu. Rev. Entomol.*, vol. 50, pp. 447–477, 2005.
- [309] J. C. Bequaert *et al.*, "The hippoboscidae or louse-flies (diptera) of mammals and birds. part i. structure, physiology and natural history." *Entomologica americana*, vol. 33, pp. 211–442, 1953.
- [310] H. R. Hagan, "Embryology of the viviparous insects," *Transactions of the New York Academy of Sciences*, vol. 12, no. 3 Series II, pp. 112–112, 1950.
- [311] A. Hutson, "Keds, flat-flies and bat-flies," in *Handbooks for the Identification of British Insects*. Royal Entomological Socie, London, 1984, pp. 1–40.
- [312] M. Walker and I. Rotherham, "Characteristics of *Crataerina pallida* (diptera: Hippoboscidae) populations; a nest ectoparasite of the common swift, *Apus apus* (aves: Apodidae)," *Experimental parasitology*, vol. 126, no. 4, pp. 451–455, 2010.
- [313] M. D. Walker and I. D. Rotherham, "The common swift louse fly, *Crataerina pallida*: an ideal species for studying host-parasite interactions," *Journal of Insect Science*, vol. 10, no. 1, 2010.
- [314] M. Monastirioti, C. E. Linn Jr, and K. White, "Characterization of *Drosophila* tyramine β -hydroxylase gene and isolation of mutant flies lacking octopamine," *Journal of Neuroscience*, vol. 16, no. 12, pp. 3900–3911, 1996.
- [315] R. Karcavich and C. Q. Doe, "*Drosophila* neuroblast 7-3 cell lineage: a model system for studying programmed cell death, notch/numb signaling, and sequential specification

- of ganglion mother cell identity,” *Journal of comparative neurology*, vol. 481, no. 3, pp. 240–251, 2005.
- [316] A. Rogulja-Ortmann, K. Luer, J. Seibert, C. Rickert, and G. M. Technau, “Programmed cell death in the embryonic central nervous system of *Drosophila melanogaster*,” *Development*, vol. 134, no. 1, pp. 105–116, 2007.
- [317] G. Lee, R. Sehgal, Z. Wang, S. Nair, K. Kikuno, C.-H. Chen, B. Hay, and J. H. Park, “Essential role of grim-led programmed cell death for the establishment of corazonin-producing peptidergic nervous system during embryogenesis and metamorphosis in *Drosophila melanogaster*,” *Biology open*, vol. 2, no. 3, pp. 283–294, 2013.
- [318] M. P. Dekkers and Y.-A. Barde, “Programmed cell death in neuronal development,” *Science*, vol. 340, no. 6128, pp. 39–41, 2013.
- [319] M. Fricker, A. M. Tolkovsky, V. Borutaite, M. Coleman, and G. C. Brown, “Neuronal cell death,” *Physiological reviews*, vol. 98, no. 2, pp. 813–880, 2018.
- [320] D. G. Southwell, M. F. Paredes, R. P. Galvao, D. L. Jones, R. C. Froemke, J. Y. Sebe, C. Alfaro-Cervello, Y. Tang, J. M. Garcia-Verdugo, J. L. Rubenstein *et al.*, “Intrinsically determined cell death of developing cortical interneurons,” *Nature*, vol. 491, no. 7422, pp. 109–113, 2012.
- [321] E. C. Marin, K. E. Dry, D. R. Alaimo, K. T. Rudd, A. R. Cillo, M. E. Clenshaw, N. Negre, K. P. White, and J. W. Truman, “Ultrabithorax confers spatial identity in a context-specific manner in the *Drosophila* postembryonic ventral nervous system,” *Neural Development*, vol. 7, no. 1, pp. 1–15, 2012.
- [322] H. Lacin, W. R. Williamson, G. M. Card, J. B. Skeath, and J. W. Truman, “Unc-4 acts to promote neuronal identity and development of the take-off circuit in the *Drosophila* CNS,” *Elife*, vol. 9, p. e55007, 2020.
- [323] C. Doe, J. Kuwada, and C. Goodman, “From epithelium to neuroblasts to neurons: the role of cell interactions and cell lineage during insect neurogenesis,” *Philosophical Transactions of the Royal Society of London. B, Biological Sciences*, vol. 312, no. 1153, pp. 67–81, 1985.
- [324] J. Y. Kuwada and C. S. Goodman, “Neuronal determination during embryonic development of the grasshopper nervous system,” *Developmental biology*, vol. 110, no. 1, pp. 114–126, 1985.
- [325] D. J. Mellert, W. R. Williamson, T. R. Shirangi, G. M. Card, and J. W. Truman, “Genetic and environmental control of neurodevelopmental robustness in *Drosophila*,” *PloS one*, vol. 11, no. 5, p. e0155957, 2016.

Bibliography

- [326] R. Dudley, "Chapter 6: Evolution of flight and flightlessness," in *The biomechanics of insect flight: Form, function, evolution*. Princeton University Press, Princeton, NJ, 2002, pp. 261–301.
- [327] M. J. Lehane, M. J. Lehane, and M. J. Lehane, *The biology of blood-sucking in insects*. Cambridge University Press, Cambridge, 2005.
- [328] D. S. Petersen, N. Kreuter, L. Heepe, S. Büsse, A. H. Wellbrock, K. Witte, and S. N. Gorb, "Holding tight to feathers—structural specializations and attachment properties of the avian ectoparasite *Crataerina pallida* (diptera, hippoboscidae)," *Journal of Experimental Biology*, vol. 221, no. 13, p. jeb179242, 2018.
- [329] C. Duch and H.-J. Pflüger, "Dum neurons in locust flight: a model system for amine-mediated peripheral adjustments to the requirements of a central motor program," *Journal of Comparative Physiology A*, vol. 184, no. 5, pp. 489–499, 1999.
- [330] M. Eckert, J. Rapus, A. Nürnberger, and H. Penzlin, "A new specific antibody reveals octopamine-like immunoreactivity in cockroach ventral nerve cord," *Journal of Comparative Neurology*, vol. 322, no. 1, pp. 1–15, 1992.
- [331] P. Konings, H. Vullings, M. Geffard, R. Buijs, J. Diederer, and W. Jansen, "Immunocytochemical demonstration of octopamine-immunoreactive cells in the nervous system of locusta migratoria and schistocerca gregaria," *Cell and tissue research*, vol. 251, no. 2, pp. 371–379, 1988.
- [332] M. Schlurmann and K. Hausen, "Mesothoracic ventral unpaired median (mesvum) neurons in the blowfly *Calliphora erythrocephala*," *Journal of Comparative Neurology*, vol. 467, no. 3, pp. 435–453, 2003.
- [333] U. Spörhase-Eichmann, H. G. Vullings, R. M. Buijs, M. Hörner, and F.-W. Schürmann, "Octopamine-immunoreactive neurons in the central nervous system of the cricket, *Gryllus bimaculatus*," *Cell and tissue research*, vol. 268, no. 2, pp. 287–304, 1992.
- [334] P. Stevenson, H.-J. Pflüger, M. Eckert, and J. Rapus, "Octopamine immunoreactive cell populations in the locust thoracic-abdominal nervous system," *Journal of Comparative Neurology*, vol. 315, no. 4, pp. 382–397, 1992.
- [335] K. J. Thompson and M. Siegler, "Development of segment specificity in identified lineages of the grasshopper cns," *Journal of Neuroscience*, vol. 13, no. 8, pp. 3309–3318, 1993.
- [336] W. Kutsch and O. Breidbach, "Homologous structures in the nervous systems of arthropoda," in *Advances in Insect Physiology*. Elsevier, 1994, vol. 24, pp. 1–113.

- [337] J. B. Thomas, M. J. Bastiani, M. Bate, and C. S. Goodman, "From grasshopper to *Drosophila*: a common plan for neuronal development," *Nature*, vol. 310, no. 5974, pp. 203–207, 1984.
- [338] E. McAlister, *The secret life of flies*. Natural History Museum London, 2017.
- [339] R. E. Campbell, O. Tour, A. E. Palmer, P. A. Steinbach, G. S. Baird, D. A. Zacharias, and R. Y. Tsien, "A monomeric red fluorescent protein," *Proceedings of the National Academy of Sciences*, vol. 99, no. 12, pp. 7877–7882, 2002.
- [340] A. Mahr and H. Aberle, "The expression pattern of the *Drosophila* vesicular glutamate transporter: a marker protein for motoneurons and glutamatergic centers in the brain," *Gene Expression Patterns*, vol. 6, no. 3, pp. 299–309, 2006.
- [341] T. Lee and L. Luo, "Mosaic analysis with a repressible cell marker for studies of gene function in neuronal morphogenesis," *Neuron*, vol. 22, no. 3, pp. 451–461, 1999.
- [342] S. Pop, "Undead-walking, version v3.0," *Undead-Walking*, 2020. [Online]. Available: <http://github.com/sznpp/undead-walking>
- [343] J. S. Phelps, D. G. C. Hildebrand, B. J. Graham, A. T. Kuan, L. A. Thomas, T. M. Nguyen, J. Buhmann, A. W. Azevedo, A. Sustar, S. Agrawal *et al.*, "Reconstruction of motor control circuits in adult *Drosophila* using automated transmission electron microscopy," *Cell*, vol. 184, no. 3, pp. 759–774, 2021.
- [344] L. Alzubaidi, J. Zhang, A. J. Humaidi, A. Al-Dujaili, Y. Duan, O. Al-Shamma, J. Santamaría, M. A. Fadhel, M. Al-Amidie, and L. Farhan, "Review of deep learning: concepts, cnn architectures, challenges, applications, future directions," *Journal of Big Data*, vol. 8, no. 1, p. 53, 2021.
- [345] A. Vanarse, A. Osseiran, and A. Rassau, "A review of current neuromorphic approaches for vision, auditory, and olfactory sensors," *Frontiers in Neuroscience*, vol. 10, 2016. [Online]. Available: <https://www.frontiersin.org/article/10.3389/fnins.2016.00115>
- [346] B. G. Kornreich, "The patch clamp technique: Principles and technical considerations," *Journal of Veterinary Cardiology*, vol. 9, no. 1, pp. 25–37, 2007.
- [347] L. J. Macpherson, E. E. Zaharieva, P. J. Kearney, M. H. Alpert, T.-Y. Lin, Z. Turan, and C.-H. Lee, "Dynamic labelling of neural connections in multiple colours by trans-synaptic fluorescence complementation," *Nature Communications*, vol. 6, no. 1, p. 10024, 2015.
- [348] K. Deisseroth, "Optogenetics," *Nature Methods*, vol. 8, pp. 26–29, 2011.
- [349] H. K. Inagaki, Y. Jung, E. D. Hoopfer, A. M. Wong, N. Mishra, J. Y. Lin, R. Y. Tsien, and D. J. Anderson, "Optogenetic control of *Drosophila* using a red-shifted channelrhodopsin reveals experience-dependent influences on courtship," *Nature Methods*, vol. 11, pp. 325–332, 2014.

Bibliography

- [350] J. G. Bernstein, P. A. Garrity, and E. S. Boyden, "Optogenetics and thermogenetics: technologies for controlling the activity of targeted cells within intact neural circuits," *Current Opinion in Neurobiology*, vol. 22, no. 1, pp. 61–71, 2012.
- [351] M. Mahn, L. Gibor, P. Patil, K. Cohen-Kashi Malina, S. Oring, Y. Printz, R. Levy, I. Lampl, and O. Yizhar, "High-efficiency optogenetic silencing with soma-targeted anion-conducting channelrhodopsins," *Nature Communications*, vol. 9, no. 1, p. 4125, 2018.
- [352] Y. Xu, P. Zou, and A. E. Cohen, "Voltage imaging with genetically encoded indicators," *Current Opinion in Chemical Biology*, vol. 39, pp. 1–10, 2017, molecular Imaging Chemical Genetics and Epigenetics.
- [353] S. E. McGuire, P. T. Le, A. J. Osborn, K. Matsumoto, and R. L. Davis, "Spatiotemporal rescue of memory dysfunction in *Drosophila*," *Science*, vol. 302, no. 5651, pp. 1765–1768, 2003.
- [354] I. S.-K. F. S. Kim Hyeonhui, Kim Minki, "Mouse cre-loxp system: general principles to determine tissue-specific roles of target genes," *Laboratory Animal Research*, vol. 34, no. 4, pp. 147–159, 2018.
- [355] O. V. Alekseyenko, Y.-B. Chan, R. Li, and E. A. Kravitz, "Single dopaminergic neurons that modulate aggression in *Drosophila*," *Proceedings of the National Academy of Sciences*, vol. 110, no. 15, pp. 6151–6156, 2013.
- [356] H. Barlow, "Redundancy reduction revisited." *Network (Bristol, England)*, vol. 12, no. 3, pp. 241–253, 2001.
- [357] G. R. Sterne, H. Otsuna, B. J. Dickson, and K. Scott, "Classification and genetic targeting of cell types in the primary taste and premotor center of the adult *Drosophila* brain," *Elife*, vol. 10, p. e71679, 2021.
- [358] R. M. Harris-Warrick and E. Marder, "Modulation of neural networks for behavior," *Annual Review of Neuroscience*, vol. 14, no. 1, pp. 39–57, 1991.
- [359] R. Hengstenberg, "The effect of pattern movement on the impulse activity of the cervical connective of *Drosophila melanogaster*," *Zeitschrift für Naturforschung C*, vol. 28, no. 9-10, pp. 593–596b, 1973.
- [360] C. E. Howard, C.-L. Chen, T. Tabachnik, R. Hormigo, P. Ramdya, and R. S. Mann, "Serotonergic modulation of walking in *Drosophila*," *Current Biology*, vol. 29, no. 24, pp. 4218–4230.e8, 2019.
- [361] A. Imms, "On *Braula coeca nitsch* and its affinities," *Parasitology*, vol. 34, no. 1, pp. 88–100, 1942.

- [362] H. Kim, C. Kirkhart, and K. Scott, “Long-range projection neurons in the taste circuit of *Drosophila*,” *eLife*, vol. 6, p. e23386, 2017.
- [363] N. S. Narayanan, E. Y. Kimchi, and M. Laubach, “Redundancy and synergy of neuronal ensembles in motor cortex,” *The Journal of Neuroscience*, vol. 25, no. 17, pp. 4207 LP – 4216, 2005.
- [364] D. Shepherd, R. Harris, D. W. Williams, and J. W. Truman, “Postembryonic lineages of the *Drosophila* ventral nervous system: Neuroglial expression reveals the adult hemilineage associated fiber tracts in the adult thoracic neuromeres,” *Journal of Comparative Neurology*, vol. 524, no. 13, pp. 2677–2695, 2016.
- [365] J. W. Truman, W. S. Talbot, S. E. Fahrbach, and D. S. Hogness, “Ecdysone receptor expression in the cns correlates with stage-specific responses to ecdysteroids during *Drosophila* and *Manduca* development,” *Development*, vol. 120, no. 1, pp. 219–234, 1994.

List of abbreviations

5HT: serotonin	CO₂: carbon dioxide
α'L: adult mushroom body alpha'-lobe	CPG: central pattern generator
αL: adult mushroom body alpha-lobe	CRE: adult crepine
β'L: adult mushroom body beta'-lobe	cs: campaniform sensilla
βL: adult mushroom body beta-lobe	CTr: coxa-trochanter
γL: adult mushroom body gamma-lobe	DBD: DNA-binding domain
Ab: abdominal gut	DFT: discrete fourier transform
AD: activation domain	DLM: dorsal longitudinal IFM
AL: adult antennal lobe	DN: descending neuron
AME: accessory medulla	Dor: dormicum
AMMC: antennal mechanosensory and motor center	dpe: day post-eclosion
AMNm: accessory mesothoracic neuromere	DRG: dorsal root ganglion
AN: ascending neuron	EB: ellipsoid body
ANm; AS: abdominal neuromere; abdominal segment	EPA: epaulette
AOTU: anterior optic tubercle	es: external sensilla
APF: after puparium formation	FB: fan-shaped body
ATL: antler	FeCO: femoral chordotonal organ
ATR: all-trans-retinal	FLA: flange
AVLP: anterior ventrolateral protocerebrum	FTi: femur-tibia
BSA: bovine serum albumin	GA: gall
BU: bulb	GECI: genetically-encoded calcium indicator
CA: calyx of adult mushroom body	GEVI: genetically-encoded voltage indicator
cAMP: cyclic adenosine monophosphate	GFP: green fluorescence protein
CAN: cantle	GMC: ganglion mother cell
CD: corollary discharge	GNG: adult gnathal ganglion
ChAT: choline acetyltransferase	GOR: gorget
CNS: central nervous system	gs: gustatory sensilla
co: chordotonal organ	GUI: graphical user interface
	HTct: Haltere tectulum
	HTMR: high-threshold mechanoreceptor

Bibliography

IB: inferior bridge
ICL: inferior clamp
IFM: Indirect flight muscles
IntTct: Intermediate tectulum
IPS: inferior posterior slope
IQR: interquartile range
Iso: Isoflurane
Ket: ketamine
Kir: Inward-rectifier potassium channel
LAL: adult lateral accessory lobe
LH: adult lateral horn
LO: lobula
LOP: lobula plate
LSM: laser scanning microscopy
LTct: lower tectulum
LTMR: low-threshold mechanoreceptor
MAN: moonwalker ascending neuron
MARCM: mosaic analysis with a repressive cell marker
MCFO: multi-color flip-out
md: multidendritic neuron
MDN: moonwalker descending neuron
ME: medulla
MN: motor neuron
MNB: median neuroblast
mVAC: medialventral association center
NB: neuroblasts
NO: nodulus
NTct: neck tectulum
PB: protocerebral bridge
PBS: phosphate buffered saline
PC: principle component
PCD: programmed cell death
PE: proboscis extension
PED: pedunculus of adult mushroom body
PLP: posterior lateral protocerebrum
PMT: photomultiplier tube
PRW: prow
Pv: proven-triculus
PVLP: posterior ventrolateral protocerebrum
R²: explained variance
RA: rapidly adapting
RFP: red fluorescent protein
ROB: adult round body
ROI: region-of-interest
rpr: reaper
RUB: rubus
SA: slowly adapting
SAD: saddle
SB: stratum basalis
SC: stratum corneum
SCL: superior clamp
SG: stratum granulosum
SIP: superior intermediate protocerebrum
SLP: superior lateral protocerebrum
SMP: superior medial protocerebrum
SN: sensory neuron
SNR: signal-to-noise ratio
SPS: superior posterior slope
sr: stretch receptor
SS: stratum spinosum
T1; proNm: prothoracic segment
T2; mesoNm: mesothoracic segment
T3; metaNm: metathoracic segment
Tdc2: tyrosine decarboxylase 2
TH: tyrosine hydroxylase
Trh: tryptophan hydroxylase
TRP: transient receptor potential cation channel
UAS: upstream activation sequence
VAC: ventral association center
VES: vest
Vg: vestigial
VGLuT: vesicular Glutamate Transporter
VNC: ventral nerve cord
WED: wedge
WT: wild type
WTct: wing tectulum
Xyl: xylazine
Z.T.: zeitgeber time

CHIN-LIN CHEN

PhD STUDENT IN NEUROSCIENCE

✉ chinlin.chen1312@gmail.com [in https://www.linkedin.com/in/chin-lin-chen-45b68a96/](https://www.linkedin.com/in/chin-lin-chen-45b68a96/)

☎ 0787285920 🏠 92 avenue du Tir-Fédéral, 1024 Ecublens, Switzerland 🌐 Taiwanese

EDUCATION

PhD

Ecole Polytechnique Fédérale de Lausanne (EPFL)

📅 August 2017 - ongoing 📍 Lausanne, Switzerland

Thesis topic: Uncovering the neural encoding of behavior in the adult Drosophila motor system.

- Conceptualized research project and designed the corresponding experiments.
- Developed a surgery procedure to allow *in-vivo* two-photon imaging in the spinal cord equivalent-VNC of tethered fruit flies.
- Performed large-scale functional screen of ascending neurons to characterize their behavioral encoding and innervation with our newly developed preparation
- Performed in-depth neural morphology analysis by random-expression genetic tools (MCFO) and confocal laser scanning microscopy (LSM).
- Analyzed the neural activity variance explained by behavior via general linear model (GLM) in the large-scale screen dataset by Python programming.
- Analyzed neural activity event-based behavior via a semi-auto event detector in the large-scale screen dataset by Python programming.
- Quantified the morphological patterning via ROI segmentation with SNT of FIJI plugins and computing innervated areas among brain and VNC regions by Python scripts.
- Developed a semi-auto classifier to identify proboscis extension by integrating DeepLabCut and Python programs for labeling landmarks and detecting events.
- Post-hoc synchronization between the signals and the derivatives from different sensors implemented in the functional recording setup and raw data visualization.
- Led interns and coordinated with colleagues of stronger analytic expertise and the supervisor to assist with the data acquisition and analysis pipeline integration in the large-scale screen project.
- Cooperated with collaborators in joint projects for providing specific assistance.
- Lectured courses regarding neurophysiology and the animal behavior-inspired robot action simulation in the Webot.

Master in Brain and Mind Sciences

National Taiwan University

📅 September 2011 - June 2013 📍 Taipei, Taiwan

Thesis topic: The persistent sodium current in rat locus coeruleus neurons

- Used patch-clamp technique to measure persistent sodium current and the resting membrane potential with pharmacological applications.
- Acute rate and mouse brain slice preparation.
- Assisted Taiwan-Japan international neuroscience training camp by lecturing the electrophysiological techniques, pharmacological experiments, data analysis, and anatomy experiments.

Bachelor in Forestry and Agriculture

National Taiwan University

📅 September 2007 - June 2011 📍 Taipei, Taiwan

- Reviewed literature focusing on modeling the cost of the supplied chain system of biofuel infrastructure.
- Simulated the cost of a simplified supplied chain system.
- Majored specifically in wood product, chemistry, and carbon deposit
- Basic statistics and genetics.

OBJECTIVE

From experience obtained from studying neuron's functions, I developed a skill set from designing and conducting experiments to quantitatively analyzing the large dataset. I am motivated to apply these skills in industrial research projects that realize the science from the bench to real-world use in bio-data science and clinical research.

SKILLS

Experimental techniques:

Two-photon imaging, patch-clamp, immunohistochemistry (IHC), mouse and fly's central nervous system dissection, fly thoracic surgery for *in-vivo* recording, optogenetic manipulation, reagent buffer preparation, fly strains maintenance, acute brain preparation, confocal microscopy, PCR,

Analytic tools:

Bio-statistics, general linear regression, signal event detection, ROI segmentation, FIJI, DeepLabCut, OpenCV, data visualization.

Soft skills:

Creative thinking, a keen eye for detail, scientific writing, communication, problem-solving, project management, task planing and scheduling

IT

Programming: Major in Python and FIJI-macro, minor in R, C languages, and Java.

Software: LaTeX, Adobe Illustrator, Blender, Prism, Microsoft Word, Excel, and Powerpoint.

Experimental software: ThorImage, ThorSync, Clampex, Clampfit, Singal, Spike2.

Electronics: experience in Arduino and Phidget

STRENGTH

Hard-working

Systemic

Fast learner

Dedicated

Proactive

Open-mind

WORK EXPERIENCE

Electrophysiology specialist

National Yang Ming Chiao Tung University

📅 November 2014 - July 2017

📍 Taipei, Taiwan

- Conducted a joint project and communicated between project leaders and technicians.
- Measured the electrophysiological effect of neuropeptide in memory-related neurons via the patch-clamp technique in ex-vivo fly brains.
- Measured the synaptic transmission between memory-related neurons by simultaneous whole-cell recording.

Second Lieutenant of Political Warfare Officer

Taiwan Army

📅 September 2013 - August 2014

📍 Taiwan

- Consulted with soldiers and helped them integrate into the teams.
- Monitored mental health and discipline violation issues on the company.
- Led a small team to execute the assigned political warfare projects.

Research Intern

Academia Sinica

📅 July 2009 - August 2009

📍 Taipei, Taiwan

- Learned the basic molecular biology experiment techniques for plants, including DNA extraction, PCR, electrophoresis, Western blot, Northern blot.
- Used an extended version of PCR--Amplified Fragment Length Polymorphism (AFLP) to profile the genome polymorphism across different varieties of broccoli *Brassica oleracea*.

PUBLICATIONS

- "Ascending neurons convey behavioral state to integrative sensory and action selection centers in the brain." **Chin-Lin Chen**, Florian Aymanns, Ryo Minegishi, Victor D. V. Matsuda, Nicolas Talabot, Semih Günel, Barry J. Dickson, Pavan Ramdya. *bioRxiv* 2022.02.09.479566, 2022
- "Imaging neural activity in the ventral nerve cord of behaving adult *Drosophila*." **Chin-Lin Chen**¹, Laura Hermans¹, Meera C Viswanathan, Denis Fortun, Florian Aymanns, Michael Unser, Anthony Cammarato, Michael H Dickinson, Pavan Ramdya. *Nature Communications*, vol.9, p.4390, 2018
- "Long-term imaging of the ventral nerve cord in behaving adult *Drosophila*." Laura Hermans, Murat Kaynak, Jonas Braun, Victor Lobato-Rios, **Chin-Lin Chen**, Semih Günel, Florian Aymanns, Mahmut Selman Sakar, Pavan Ramdya. *bioRxiv*, 2021.10.15.463778, 2021
- "Extensive and diverse patterns of cell death sculpt neural networks in insects." Sinziana Pop, **Chin-Lin Chen**, Connor J Sproston, Shu Kondo, Pavan Ramdya, Darren W Williams. *eLife*, vol.9, p.e59566, 2020
- "Serotonergic modulation of walking in *Drosophila*." Clare E Howard, **Chin-Lin Chen**, Tanya Tabachnik, Rick Hormigo, Pavan Ramdya, Richard S Mann. *Current Biology*, vol.29, no.23, p.4218-4230, 2019
- "Causal evidence for the role of specific GABAergic interneuron types in entorhinal recruitment of dentate granule cells." Cheng-Ta Lee, Min-Hua Kao, Wen-Hsien Hou, Yu-Ting Wei, **Chin-Lin Chen**, Cheng-Chang Lien. *Scientific Reports*, vol.6, no.1, pp.1-13, 2016

INTERESTS

- Neuroscientific research
- Entrepreneurship
- Start-ups
- Tennis
- Snowboarding
- Biking
- Travelling

Languages

Chinese: Native proficiency

English: Full professional proficiency

French: Elementary proficiency

Japanese: Elementary proficiency